PACIFIC EARTHQUAKE ENGINEERING
RESEARCH CENTER

Probabilistic Seismic Demand Analysis Using Advanced Ground Motion Intensity Measures, Attenuation Relationships, and Near-Fault Effects

Polsak Tothong

and

C. Allin Cornell

Stanford University

PEER 2006/11
MARCH 2007

Probabilistic Seismic Demand Analysis Using Advanced Ground Motion Intensity Measures, Attenuation Relationships, and Near-Fault Effects

Polsak Tothong
Department of Civil and Environmental Engineering
Stanford University

C. Allin Cornell
Department of Civil and Environmental Engineering
Stanford University

PEER Report 2006/11
Pacific Earthquake Engineering Research Center
College of Engineering
University of California, Berkeley

March 2007

ABSTRACT

In performance-based earthquake engineering (PBEE), evaluating the seismic performance (or seismic risk) of a structure at a designated site has gained major attention, especially in the past decade. One of the objectives in PBEE is to quantify the seismic reliability of a structure due to future random earthquakes at a site. For that purpose, probabilistic seismic demand analysis (PSDA) is utilized as a tool to estimate the mean annual frequency of exceeding a specified value of a structural demand parameter (e.g., interstory drift ratio).

This report focuses on applying *advanced* scalar ground motion intensity measures (*IM*s), specifically inelastic spectral displacement (S_{di}) and S_{di} with a higher-mode factor denoted as $IM_{1I\&2E}$, when assessing the seismic performance of structures. The results obtained by using these advanced *IM*s are compared with a *conventional elastic*-based *scalar IM* (i.e., pseudo-spectral acceleration, S_a) and the *vector IM* (i.e., S_a with epsilon, denoted as $<S_a, \varepsilon>$). The advantages of applying advanced *IM*s are (1) "sufficiency" or more accurate evaluations of seismic performance, while eliminating the need to perform detailed ground motion record selection for the nonlinear dynamic structural analyses, (2) "efficiency" or smaller variability of structural responses, and (3) "scaling robustness," which implies that ground motion records can be scaled without introducing a bias in the structural responses. For ordinary records, using the advanced *IM*s (S_{di} and $IM_{1I\&2E}$) leads to the same conclusions obtained using the vector *IM*, $<S_a, \varepsilon>$. However, using advanced *IM*s to evaluate the structural performance for *near-source* pulse-like records is found to be *more accurate* than using the elastic-based *IM*s (i.e., S_a and $<S_a, \varepsilon>$).

For structural demands that are dominated by the first mode of vibration, using S_{di} can be advantageous relative to the conventionally used S_a and $<S_a, \varepsilon>$. We demonstrate that this is true for *ordinary* and for *near-source* pulse-like earthquake records; the latter cannot be adequately characterized by either S_a alone or $<S_a, \varepsilon>$. For structural demands with significant higher-mode contributions (under either of the two types of ground motions), an advanced scalar *IM* that incorporates higher modes needs to be utilized.

ACKNOWLEDGMENTS

This work was supported in part by the Earthquake Engineering Research Centers Program of the National Science Foundation under award number EEC-9701568 through the Pacific Earthquake Engineering Research (PEER) Center.

Any opinions, findings, and conclusions or recommendations expressed in this material are those of the author(s) and do not necessarily reflect those of the National Science Foundation.

CONTENTS

LIST OF FIGURES

LIST OF TABLES

LIST OF SYMBOLS

CDF	Cumulative distribution function
CCDF	Complementary cumulative distribution function
$E[X]$	Expected value of the random variable X
EDP	Engineering demand parameter
F_e	Strength required for the oscillator to remain elastic
$\hat{F}_e$	Predicted median strength required for the oscillator to remain elastic
F_y	Yield strength of an oscillator
G	Complementary cumulative distribution function
IM	Ground motion intensity measure
$IM_{1E\&2E}$	Intensity measure incorporating first- and second-mode S_{de}
$IM_{1I\&2E}$	Intensity measure incorporating first-mode S_{di} and second-mode S_{de}
MAF	Mean annual frequency
MDOF	Multi-degree-of-freedom
M_w	Earthquake moment magnitude
NGA	Next Generation Attenuation of Ground Motions project
$P[\cdot]$	Probability of $[\cdot]$
PBEE	Performance-based earthquake engineering
P_C	Probability of collapse
PDF	Probability density function
PEER	Pacific Earthquake Engineering Research Center
PGA	Peak ground acceleration
PGV	Peak ground velocity
PSDA	Probabilistic seismic demand analysis
PSHA	probabilistic seismic hazard analysis
R	Strength-reduction factor (Chapters 3 and 4) or source-to-site distance
$\hat{R}$	Predicted median strength-reduction factor
R_{rup}	Closest distance from the site to the rupture plane
S_a	Pseudo-spectral acceleration
$S_{a\text{-}AVG}$	Geometric mean of S_a at a specified period range
S_{de}	Elastic spectral displacement
S_{di}	Inelastic spectral displacement
SDOF	Single-degree-of-freedom
T, T_n	Natural period of vibration of a structure
T_{eff}	Effective period for elastic oscillator
T_p	Pulse period
UHS	Uniform hazard spectra
$\bar{X}$	Estimated mean value of the random variable X
$\hat{X}$	Predicted median value of the random variable X

d_y	Yield displacement
f_X	Probability density function of the random variable X
$f_{X,\,Y}$	Joint probability density function of random variables X and Y
$f_{Y\mid X}$	Conditional probability density function of random variable Y given X
$\ln(\cdot)$	Natural logarithm of $(\cdot)$
$\Phi(\cdot)$	Standard Gaussian cumulative distribution function
Γ_n	n^{th}-mode modal participation factor
α	Hardening stiffness ratio
α_c	Post-capping stiffness ratio
δ_c	Displacement associated with the peak strength
δ_y	Yield displacement parameter
ε	Ground motion epsilon
ϕ_n	n^{th}-mode modal shape function
$\gamma_{s,c,k,a}$	Cyclic deterioration parameter
λ_X	Mean annual frequency of X
μ	Ductility
θ_i	Peak (over time) interstory drift ratio
$\theta_{\max}$	Peak (over time) maximum (over the height of a structure) interstory drift ratio
$\rho_{X,\,Y}$	Linear correlation function between random variables X and Y
σ_X	Dispersion (or standard deviation) of the random variable X
ω	Natural circular frequency of vibration
ζ	Viscous damping ratio

1 Introduction

1.1 OVERVIEW

Performance-based earthquake engineering (PBEE) has recently gained significant attention, especially after past earthquakes (1989 Loma Prieta and 1994 Northridge, California, and 1995 Kobe, Japan) in which the affected communities realized that sometimes building only to prevent collapse (or just life safety) is simply insufficient. In these events, there was significant damage to buildings as well as to contents, creating substantial losses both financial (including business interruption) and human (fatalities and casualties). As a result, there is a need for better-designed structures to minimize damage and to ensure that buildings remain functional after earthquakes. PBEE has been documented in recent guidelines (e.g., ATC-40 1996; FEMA-273 1997; Vision-2000 1995; and SAC/FEMA-350 2000). These documents require that a building be designed to assure specific performance objectives under frequent earthquakes typically resulting in little or no damage, and in rare but potentially catastrophic seismic events that may occur during its service life. In the context of PBEE, the seismic demands of structures need to be evaluated accurately for comparison with the target (i.e., acceptable) performance objectives.

Earthquakes are low-probability, large-consequence, and large-uncertainty hazards (Wen 2000). Due to the randomness of earthquakes and the many uncertainties involved in evaluating a structure's seismic performance, estimations of future earthquakes can be completed only in a probabilistic way. According to modern guidelines (cited above) and in work by the Pacific Earthquake Engineering Research (PEER) Center (Cornell and Krawinkler 2000; Moehle and Deierlein 2004), evaluations of structural performance (or seismic risks) can be expressed in terms of the mean annual frequency (MAF) of exceeding a given level of response, for example, x, denoted as $\lambda_{EDP}(x)$ (in the PEER context, the response parameter is termed an engineering demand parameter, *EDP*). $\lambda_{EDP}(x)$ is a direct measure of a structure's seismic performance because it is related to the probability of experiencing the event $EDP > x$ within the lifetime of a structure (e.g., 50 years). This will be briefly described in the next subsection. Note that attention in this report is limited to predicting probabilities of structural responses, and it is presumed that their translation to loss estimations is a direct, sufficiently accurate, and straight-forward task.

1.1.1 Brief Review of Probabilistic Seismic Demand Analysis

To evaluate the seismic performance of structures at a designated site, the uncertainties in the ground motions and nonlinear structural responses need to be considered. Monte-Carlo simulation can be utilized, but this approach requires computationally intensive analyses to evaluate $\lambda_{EDP}(x)$ (e.g., Collins et al. 1996; Han and Wen 1997; Jalayer et al. 2004; Wen 2000). For a given fault *i*, this method requires a computation of $\nu_i \cdot P[EDP > x \mid fault\ i]$, where ν_i is the mean annual rate of occurrence of an earthquake above a threshold magnitude of fault *i*, and $P[EDP > x \mid fault\ i]$ is the probability of exceeding the response or *EDP* level *x* given an event on fault *i*. This term can be calculated from nonlinear dynamic analysis results from, for example, synthetic records of random magnitude and location on the fault. The summation from all the sources in the region is (assuming that earthquake faults occur independently)

$$\lambda_{EDP}(x) = \sum_i \nu_i \cdot P[EDP > x \mid fault\ i] \tag{1.1}$$

Given that the dispersion of responses for a fault (or simply given magnitude, M_w, and source-to-site distance, R) is about 0.8 or more, the required sample size is $(0.8/0.1)^2 = 64$ to estimate the median *EDP* within a standard error of 10%. The computation also requires at least 20 or more M_w and R pairs (i.e., collectively exhaustive and mutually exclusive) to adequately cover the seismic source contributions in the region. This procedure ultimately requires thousands of records to be simulated and analyzed through the structure in order to obtain accurate estimates of the extreme responses and ground motions. To improve the efficiency in the calculation, Wen and co-workers utilize a "de-aggregation" method, which selects only magnitudes, M_w, and sources-to-site distances, R, that contribute most to the λ_{EDP}.

Another approach to calculate the seismic performance of structures is to use a structure- and response-specific attenuation relationship as a function of M_w and R. The concept is similar to the conventional probabilistic seismic hazard analysis (PSHA); merely the ground motion attenuation relationship is replaced with the more structure-specific one, i.e.,

$$\lambda_{EDP}(x) = \sum_i \nu_i \cdot \iint P[EDP > x \mid m_w, r] \cdot f_{M_w,R}(m,r) \cdot dr \cdot dm \tag{1.2}$$

where $f_{M_w,R}(m_w,r)$ is the joint probability density function of M_w and R of a given fault. Many suites of records (from various M_w, R, fault mechanisms, etc.) are needed to obtain an accurate structure-specific attenuation model, which is found by regression analysis of *EDP* upon M_w and R. The implicit assumptions in this method are (1) the functional form of the regression equation, (2) the lack of dependence of *EDP* on the source characteristics not contained in the vector of independent variables (e.g., rupture duration), and (3) the lack of dependence of *EDP* on the geometry of the fault relative to the site (Cornell 1996b; McGuire and Cornell 1974; Sewell 1989). Drawbacks are that this method still needs hundreds of analyses to obtain a reliable estimate for the structure- and response-specific attenuation model. On the other hand, the number of records is relatively small as compared to those of the simulation-based method. There are, however, sufficient real records in the catalogs to avoid the use of synthetic records.

Cornell and co-workers (e.g., Bazzurro 1998; Luco 2002; Shome 1999) simplified the problem further by decoupling the ground motion hazard and nonlinear dynamic analyses via the intermediate variable known as the ground motion intensity measure (*IM*). A conventional *IM* is the peak ground acceleration (PGA) or, a little more structure-specific, the pseudo-spectral acceleration at the first-mode period (denoted as $S_a(T_1)$ or simply S_a). The benefit of this method is that the number of records needed can be substantially reduced because most of the uncertainties in *EDP* are concentrated in λ_{IM}, which is found by conventional PSHA, leaving a small variation of *EDP* given *IM* to be estimated from the dynamic analyses (while still obtaining the accurate estimates for the marginal *EDP* distribution of the structure at a site). The typical value for the dispersion of an *EDP*-conditioned *IM* associated with large ductility levels is about 0.3–0.4, implying that the necessary sample size is in the order of 10 (i.e., $0.35/0.1)^2$ records to estimate the median *EDP* within a standard error of 10%. Assuming that 5 to 6 *IM* levels need to be analyzed, the total number of analyses required is about 50–60. By using the total probability theorem (Benjamin and Cornell 1970), $\lambda_{EDP}(x)$ representing all M_w and R scenarios from the causative faults can be expressed as

$$\lambda_{EDP}(x) = \int P[EDP > x \mid im] \cdot d\lambda_{IM}(im) \tag{1.3}$$

where $d\lambda_{IM}(im) = \lambda_{IM}(im) - \lambda_{IM}(im + dim)$ is the differential of the ground motion hazard curve in terms of *IM*. λ_{IM} is typically carried out by seismologists. It is approximately the MAF of *IM* = *im*, where *dim* is a small increment in the ground motion intensity. Note that this site-specific seismic hazard reflects all of the M_w and *R* scenarios. Therefore, it captures a major portion of the specific nature at the site. Still to be determined are which *IM* to select and its ground motion hazard computability. These topics will be discussed further in following chapters. This seismic performance assessment approach is known as the *IM*-based probabilistic seismic demand analysis (PSDA).

Note that this PSDA has been applied in various fields in diverse degrees. For example, the U.S. nuclear power industry has applied the seismic probabilistic risk assessments (PRAs) for more than two decades to all plants (Hickman 1983). This framework is also implemented in the probabilistic assessment of steel moment-resisting frames (SAC/FEMA-350) and in other recent guidelines (e.g., ATC-40; Vision-2000).

The principal assumption (for the *IM*-based PSDA) is the "sufficiency" property of the *IM* (Luco 2002), which requires that the probability distribution of the structural response of interest given an *IM* is *conditionally independent* of the other ground motion parameters (i.e., M_w, distance, epsilon, fault mechanism, etc.). This assumption ultimately implies that a detailed record selection is *not* necessary (i.e., any ground motion records from any M_w, distance, epsilon, fault mechanism, etc., can be selected). If the selected *IM* is not sufficient, a full conditional probability distribution of *EDP* needs to be used to ensure the accuracy of PSDA.

$$\begin{aligned}\lambda_{EDP}(x) = \iint & P\left[EDP > x \mid im, m_w, r, \varepsilon, etc.\right] \cdot \ldots \\ & f_{M_w,R,\varepsilon,etc.|IM}\left(m_w, r, \varepsilon, etc. \mid im\right) \cdot d\left(m_w, r, \varepsilon, etc.\right) \cdot d\lambda_{IM}(im)\end{aligned} \tag{1.4}$$

where ground motion epsilon (ε) is a proxy for the deviation of an *IM* (e.g., S_a) of as-recorded ground motion relative to the predicted (median) value calculated from the attenuation model. $f_{M_w,R,\varepsilon,etc.|IM}$ is the joint probability distribution function of M_w, *R*, ε, and other ground motion parameters at a given *IM* level, which can be obtained from the result of PSHA disaggregation. If an insufficient *IM* is used, and the selected records do not represent the hazard at the site, the seismic performance estimation will be biased. Therefore, the choice of an appropriate *IM* is *essential* in obtaining an accurate estimate for the seismic performance of structures. The efficiency, the sufficiency, and the bias in the responses when scaling records depend upon the chosen *IM*. With a sufficient *IM*, however, evaluating the seismic performance of a structure can be estimated using Equation 1.3, simply because $P[EDP > x \mid im, m_w, r, \varepsilon, etc.]$ is *functionally independent* of the ground motion parameters (e.g., M_w, distance, epsilon, fault mechanism, etc.).

Two other important properties of an *IM* are the "efficiency" and "scaling robustness." The former implies that a more efficient *IM* can reduce the number of nonlinear dynamic analyses but still achieve the same accuracy in seismic performance estimation. The latter implies that no statistically strong relationship exists between the structural responses and the scale factors used in scaling the amplitude of the records. By definition extreme ground motions are scarce. The real (as-recorded) ground motions will, instead, be used and scaled. The effect of scaling records on the responses of structures will be studied in Chapters 2 and 5.

An *IM* is introduced to quantify the scaling of ground motion records. Scaling records to a common *elastic* value (i.e., using elastic-based *IM*s) can result in the spectral shape being largely influenced by ε, M_w, soil type, etc., which impact the nonlinear responses of structures (see Chapters 2 and 3). If scaling factors are, however, determined using inelastic-based *IM*s (i.e., inelastic spectral displacement), the influence from the spectral shape (vis-à-vis ε and M_w) will be less prominent. This is mainly because the positive slope (relative to the median spectra) of more aggressive records will be scaled less than the negative slope (more benign) records[1] (see, e.g., Chapters 2, 3, and 5) to achieve a common structural response level.

It should be noted here that with structural capacity information, the PSDA results can be used to compute the MAF of exceeding a specified limit state (*LS*). Typically, a limit state is composed of the capacity and demand random variables with the same units. A limit state is simply the probability that the (random) capacity is less than the (random) demand, and can be expressed as

$$\lambda_{LS} = \int P[LS \mid EDP = x] \cdot d\lambda_{EDP}(x) \tag{1.5}$$

where $d\lambda_{EDP}(x)$ is defined similar to the $d\lambda_{IM}(im)$, but in terms of *EDP*. $P[LS \mid EDP = x]$ is simply $P[EDP_{Capacity} < EDP_{Demand} \mid EDP = x]$ vis-à-vis $P[EDP_{Capacity} < x]$. Estimating the dynamic capacities is not within the scope of this study. The limit states considered are simply the deterministic values of $EDP_{Capacity}$; as a result, the $P[LS \mid EDP = x]$ is simply a binary function ($I_{EDP_{Capacity} < x}$, equal to unity if x is greater than the specified deterministic capacity and zero

[1] Ground motion records with positive slope (aggressive) spectral shape (relative to the median shape determined from an attenuation model), on average impose stronger inelastic responses than those having negative slope (benign) spectral shape.

otherwise). This process simplifies Equation 1.5 from λ_{LS} to an equivalent λ_{EDP} at a specified *EDP* level.

1.2 FOCUS OF THIS STUDY

In this report, the approach known as probabilistic seismic demand analysis (PSDA) is applied and used as a framework to study and estimate the seismic risk of the structures at a designated site using advanced *IM*s. The studies are focused on the effects of "ordinary" and "near-source" pulse-like earthquake ground motions records on single-degree-of-freedom (SDOF) and multi-degree-of-freedom (MDOF) structures.

This report focuses on applying *advanced* ground motion *IM*s (specifically, inelastic spectral displacement (S_{di}) and S_{di} with a higher-mode factor, denoted as $IM_{1I\&2E}$) to assess the seismic performance of structures. The results are compared with conventional elastic-based *IM*s (such as S_a) and the *vector IM* (S_a with epsilon denoted as $<S_a, \varepsilon>$). The latter has been known to improve the PSDA results for *ordinary* (non-near-source) ground motions. The use of $<S_a, \varepsilon>$ is driven by the insufficiency of the basic *IM*, S_a. As will be shown, for ordinary records, the advanced *IM*s (i.e., S_{di} and $IM_{1I\&2E}$) provide statistically identical results to those computed using a vector *IM*. Use of advanced *IM*s to evaluate the structural performance for *near-source* pulse-like records is shown to be more accurate than using the elastic-based *IM*s (i.e., S_a and $<S_a, \varepsilon>$).

The shortcoming of using an advanced *IM in the past* has been the computability of the ground motion hazard in terms of this *IM*. To be able to implement the *IM*-based PSDA using an advanced *IM*, the ground motion prediction model (i.e., attenuation relationship) for S_{di} and $IM_{1I\&2E}$ are developed. The attenuation relationships for S_{di} and $IM_{1I\&2E}$ can be easily implemented in the PSHA programs to generate site-specific results or the national seismic hazard maps (similar to those of S_a from the U.S. Geological Survey; http://earthquake.usgs.gov/research/hazmaps/).

Lastly, the seismic performance of structures using an *IM*-based PSDA is compared with the simulation-based results to validate its effectiveness and accuracy. The results are statistically equivalent. The main advantage of the *IM*-based method is then confirmed and its accuracy is verified.

1.3 ORGANIZATION

All chapters are intended to be self-contained because they have been or will be published as individual journal papers. As a result, there may be some repetition of background material, and apologies are made for any distraction this may cause.

Chapters 2 and 3 of this report discuss structural performance evaluation under ordinary ground motions. The efficiency, sufficiency, and scaling robustness are discussed for the advanced *IM*s and compared to the results of the elastic-based *IM*s (i.e., S_a and S_a with epsilon, denoted as $<S_a, \varepsilon>$). One important aspect of using the advanced *IM*s is the computability of the ground motion hazard in terms of the *IM*. This is illustrated in Chapter 3. The second half of the report focuses on the effect of pulse-like ground motions on both structural behavior and ground motion hazard. Due to the lack of proper hazard estimation and identification for sites located close to faults, the seismic risk evaluation of a structure may be over- or underestimated. The last chapter of this report validates the *IM*-based PSDA results with the simulation-based approach, which is considered to be an "exact" result and serves as a basis for comparison. Details of earthquake records used in this report are explained in the final Appendix.

In Chapter 2, PSDA is utilized as a tool to investigate and demonstrate the efficiency, sufficiency, and scaling robustness of the advanced *IM*s subjected to ordinary ground motions. The advanced *IM*s considered are the inelastic spectral displacement (S_{di}) and S_{di} incorporating a higher-mode factor (denoted as $IM_{1I\&2E}$). The results are compared with the elastic-based *IM*s, i.e., S_a and $<S_a, \varepsilon>$. The former was shown to be biased for tall, long-period structures (Shome 1999). The latter was shown to improve the PSDA results for ordinary ground motions (Baker and Cornell 2005a). Sixteen generic frames are used to draw a general conclusion. The advantages of using the advanced *IM*s compared to the *vector IM* are demonstrated and discussed.

One of the concerns in implementing the advanced *IM*s in the past has been the computability of the ground motion hazard curves in terms of the *IM*s. In Chapter 3, ground motion prediction models (i.e., attenuation relationships) for S_{di} and $IM_{1I\&2E}$ are developed in order to construct their ground motion hazard curves via a conventional PSHA. The attenuation relationship for S_{di} is developed based on the inelastic displacement ratio (S_{di}/S_{de}) concept. This is largely because (1) this ratio is a proxy for the spectral-shape information and (2) the ratio should depend less on ground motion properties (i.e., M_w, distance, soil type, etc.) as compared to S_{de} or S_{di} itself. The ground motion hazard developed in this chapter is applied with the PSDA demonstrated in Chapters 2 and 5.

In Chapter 4, a new dimension to PSHA is introduced to estimate the seismic hazard at sites located close to the faults to directly incorporate the effect of near-source pulse-like ground motions. The new concept of assigning the probability of expecting a pulse-like record based on a site-source configuration is introduced and implemented in the proposed PSHA framework. The importance of the relative values for the modal periods of the structure and the pulse period are shown to be significant parameters that affect inelastic responses (see Chapter 5). It would be meaningful to be able to capture this information in the seismic hazard identification. To do this, first, the ground motion hazard analysis is separated into non-near-source and near-source cases based on the distance parameter. Then for the near-source case, the analysis is further divided into two pieces: hazards (1) with and (2) without pulse-like ground motions via attenuation relationships. An example for a characteristic event is presented to demonstrate the effect of sites located near/close to the faults. The seismic hazard disaggregation on the probability of expecting a pulse and pulse period (in addition to M_w, distance, and ε) can be directly estimated.

In Chapter 5, advanced *IM*s are applied to estimate the seismic performance of structures under pulse-like ground motions. This type of ground motion is known to cause severe damage in structures. In the situation where low-hazard (i.e., extreme) ground motions are of interest, pulse-like records may be selected. Their effects on the behavior of structures are briefly illustrated. The results are compared with the elastic-based *IM*s (S_a and $\langle S_a, \varepsilon \rangle$), which have been shown to be *ineffective* to capture pulse-like ground motion effects (Baker and Cornell 2005b; Luco 2002). Using inelastic-based *IM*s can ensure the accuracy of seismic performance evaluation of a structure susceptible to near-source pulse-like ground motions. The results from pulse-like records are further compared with those of ordinary records to illustrate that the sufficiency property of the *IM* is preserved.

In Chapter 6, the PSDA results using the *IM*-based approach are validated with the results of simulation. A stochastic-method simulation (SMSIM) (Boore 1983, 2003) is utilized to generate ground motions for a scenario earthquake. PSDA results using S_a, $\langle S_a, \varepsilon \rangle$, and S_{di} are compared and discussed. The ground motion hazard is computed directly using the simulated ground motions for a scenario earthquake (i.e., M_w 6.9 and a distance parameter of about 18 km). A total of 55,000 records have been simulated and utilized to obtain the “exact” results, while a subset of only 40 records have been used for the *IM*-based PSDA. The *IM*-based results are compared directly with the results of nonlinear dynamic analyses obtained from the simulated ground motions. The chapter ends with interesting findings on how the spectral (auto-) correlation function of $\ln S_a$ at two periods influences the effectiveness of $<S_a, \varepsilon>$, and how this correlation function can be used to determine the goodness of the simulated ground motions as compared to the real (as-recorded) ground motions.

Chapter 7 summarizes the most important contributions and findings of this report. It also provides the overall conclusions and the limitations of this study. Future research directions are discussed at the end.

2 Probabilistic Seismic Demand Analysis Using Advanced Ground Motion Intensity Measure

2.1 SUMMARY

One of the objectives in performance-based earthquake engineering is to quantify the seismic reliability of a structure at a site. For that purpose, PSDA is utilized as a tool to estimate the MAF of exceeding a specified value of a structural demand parameter (e.g., interstory drift ratio). This chapter compares and contrasts the use, in PSDA, of certain *advanced scalar* versus *vector* and *conventional scalar* ground motion intensity measures (*IM*s). One of the benefits of using a well-chosen *IM* is that more accurate evaluations of seismic performance are achieved without the need to perform detailed ground motion record selection for the nonlinear dynamic structural analyses involved in PSDA (e.g., record selection with respect to seismic parameters such as earthquake magnitude, source-to-site distance, and ground motion epsilon). For structural demands that are dominated by a first mode of vibration, using inelastic spectral displacement (S_{di}) can be advantageous relative to the conventionally used elastic spectral acceleration (S_a) and the *vector IM* consisting of S_a and epsilon (ε). We demonstrate that this is true for *ordinary* and for *near-source* pulse-like earthquake records. The latter ground motions cannot be adequately characterized by either S_a alone or the vector of S_a and ε. For structural demands with significant higher-mode contributions (under either of the two types of ground motions), using S_{di} alone is not sufficient, so we use an advanced scalar *IM* that additionally incorporates higher modes.

2.2 INTRODUCTION

Performance-based seismic evaluation is a process that results in a realistic understanding of the quantified risk due to future earthquakes for a proposed design/upgrade of a new/existing structure. One of the objectives in performance-based seismic evaluation can be to estimate the MAF of exceeding a specified structural demand (or response) level of interest for a given structure and site. Probabilistic seismic demand analysis (e.g., Cornell 1996a; Cornell and Krawinkler 2000; FEMA-355 2000; Luco 2002; Shome 1999; Younan et al. 2001) is an approach for estimating this MAF quantity and for assessing the structural performance under future seismic hazards. As described in more detail later in this chapter, PSDA combines a site-specific ground motion hazard curve with structural responses of interest from nonlinear dynamic analyses of the given structure. Analogous to a ground motion hazard curve computed by PSHA (Cornell 1968; Frankel et al. 2000), the final result of PSDA is a structural response hazard curve for multiple levels of seismic demands (i.e., from elastic to collapse behavior), which is useful for multi-objective structural performance evaluations, for example. The ground motion intensity measure (*IM*) used in PSDA is, from the engineering perspective, the quantification of the characteristics of a ground motion that are important to the nonlinear structural response, e.g., the amplitude and frequency content, or spectral shape (response spectral ordinates at multiple periods), of the ground motion. Therefore, an advanced *IM* that contains information about spectral shape, as well as information about the structure, can be expected to be preferable and to lead to more appropriate scale factors when scaling (in amplitude) ground motions to target values of the *IM*, as discussed further below. (Note that scaling earthquake records is often needed because, by definition, the rare earthquake events considered in structural design and evaluation are scarce, and therefore few of them have been recorded by seismometers.) From a seismology perspective, on the other hand, the *IM* is used to quantify the ground motion hazard at a site due to seismicity in the region; hence, the feasibility of computing this seismic hazard in terms of an advanced *IM* must also be considered.

A commonly used *IM* is the pseudo-spectral acceleration at or near the first-mode period of the structure for a damping ratio of 5% ($S_a(T_1)$, or simply S_a here for the sake of brevity). S_a is widely used because hazard curves in terms of spectral acceleration are available from the U.S. Geological Survey (USGS; http://earthquake.usgs.gov/research/hazmaps/) and the Southern California Earthquake Center (SCEC); http://www.opensha.org/). However, due to the limited spectral-shape information in S_a alone, structural responses to ground motion records scaled to target S_a levels have been identified to depend on how the records are selected, i.e., on their characteristics such as earthquake magnitude (M_w) and ground motion epsilon (ε), etc. (e.g., Baker and Cornell 2005b; Luco and Bazzurro 2004; Luco and Cornell 2006). Note that epsilon, ε, measures the number of the standard deviation of S_a for an as-recorded ground motion from the median (geometric mean) S_a calculated from an attenuation relationship, or ground motion prediction equation (e.g., Abrahamson and Silva 1997).

A vector *IM* consisting of S_a and response spectral values at other-than-first-mode periods has been shown to improve structural response prediction and hence to reduce the dependence on other ground motion record characteristics (Baker and Cornell 2005b; Bazzurro and Cornell 2002; Luco et al. 2005; Shome 1999; Vamvatsikos and Cornell 2004); however, for use in PSDA, this vector *IM* requires a vector-valued probabilistic seismic hazard analysis (Bazzurro and Cornell 2002) to obtain the joint hazard information, an analysis tool which has not yet been commonly applied. In contrast, the joint hazard between S_a and ε — i.e., the components of a vector *IM* denoted hereafter as $<S_a, \varepsilon>$ — can be obtained by using the conventional disaggregation results of PSHA (Baker and Cornell 2005a; Bazzurro and Cornell 2002; Luco and Cornell 2006). This vector *IM*, $<S_a, \varepsilon>$, has been thoroughly investigated by Baker and Cornell (2005a). The effectiveness of using ε when selecting ground motion records and predicting inelastic responses of multi-degree-of-freedom (MDOF) structures has been shown to be significantly greater than that of S_a alone for *ordinary* ground motions, as discussed further below.

Because of their simplicity relative to *vector IM*s, this chapter focuses on applying PSDA using *advanced scalar IM*s, specifically (1) inelastic spectral displacement (S_{di}) and (2) S_{di} with higher-mode modification ($IM_{1I\&2E}$) (Luco 2002; Luco and Cornell 2006). The latter is needed for structural responses with significant higher-mode contributions. An attenuation relationship for S_{di} that is now available (Chapter 3; see also Tothong and Cornell 2006) is used in this chapter to construct the S_{di} hazard curves needed for PSDA. The approximate attenuation relationship for $IM_{1I\&2E}$ that is used can be found in Chapter 3. The PSDA results using these *advanced IM*s are compared with those using the *conventional IM*, S_a, and the *vector IM*, $<S_a, \varepsilon>$.

2.3 REVIEW OF PROBABILISTIC SEISMIC DEMAND ANALYSIS

As mentioned above, PSDA assesses the performance of a structure by probabilistically predicting the structural response under future (random) earthquake ground motions, and combining this information with seismic hazard analysis results. Borrowing from the terminology of the Pacific Earthquake Engineering Research Center, in PSDA the structural response is quantified via an engineering demand parameter (*EDP*). The *EDP* values for future (random) ground motions can be predicted via incremental dynamic analysis (IDA) (Vamvatsikos and Cornell 2002a), i.e., by nonlinear dynamic analysis of the structure under records that are incrementally scaled to different levels of the *IM*. The ground motion hazard at the site is typically calculated using PSHA (Cornell 1968; Frankel et al. 2000). This site-specific ground motion hazard curve for an *IM* (λ_{IM}) — whether it be S_a, S_{di}, or $IM_{1I\&2E}$ — can then be combined with the structural response information to obtain the MAF of exceeding a specified level of response, or *EDP* value (λ_{EDP}), calculated as

$$\lambda_{EDP}(x) = \int_{all\ ims} P[EDP > x \mid IM = im] \cdot \left| d\lambda_{IM}(im) \right| \tag{2.1}$$

where $P[EDP > x| IM = im]$ is the probability of exceeding a specified *EDP* level x, given a level of $IM = im$. Throughout this chapter, uppercase denotes random variables, and lowercase indicates realizations or specific values of those random variables. The differential of the ground motion hazard curve, $d\lambda_{IM}(im) = \lambda_{IM}(im) - \lambda_{IM}(im + dim)$, is approximately the MAF of $IM = im$, where *dim* is a small increment in the ground motion intensity. $\lambda_{EDP}(x)$ is a direct measure of the performance of a structure because it relates to the probability of experiencing the event $EDP > x$ within the next, approximately, 50 years. Note that the *IM* provides a connection between site-specific seismic hazard (from seismologists) and structural analyses (by engineers). Next, a methodology to predict structural responses using a scalar *IM* will be demonstrated.

By using IDA (Vamvatsikos and Cornell 2002a), i.e., scaling the amplitudes of ground motions to a target ground motion intensity (e.g., $IM = im$), and performing nonlinear dynamic analyses of a structure to obtain the structural response of interest, the variation of responses due to earthquake excitations at each *im* level can be obtained. At a specified intensity level, a fraction of ground motions will cause collapse in a structure. For non-collapse data (denoted *NC*), the conditional responses on *im* have been shown to follow a lognormal distribution (Shome 1999). The sample (from the sample earthquake records) mean and standard deviation of lnEDP (denoted $\hat{\propto}_{\ln EDP|im}$ and $\hat{\sigma}_{\ln EDP|im}$, respectively) can be estimated from the responses of records scaled to an *im* level using a method of moments (Benjamin and Cornell 1970); note that ln(·) denotes the natural logarithm of (·) throughout). The probability of an *EDP* exceeding a given level *x* at a given intensity level, e.g., *im*, for non-collapse data is

$$P\left[EDP > x \mid IM = im, NC\right] = 1 - \Phi\left(\frac{\ln x - \hat{\propto}_{\ln EDP|im}}{\hat{\sigma}_{\ln EDP|im}}\right) \tag{2.2}$$

where $\Phi(\cdot)$ is the standard Gaussian cumulative distribution function.

Next consider the collapse data (denoted *C*), indicated by non-convergence of dynamic analysis or a large increment in structural deformations with a small increment in intensity. If a relatively large number of records are used, the probability of collapse at each *im* level ($P_{C|IM}$) can be empirically estimated as

$$P_{C|IM=im} = \frac{\text{no. of records causing collapse at } IM \leq im}{\text{total no. of records}} \tag{2.3}$$

This estimated probability of collapse (which can be represented with a *collapse fragility* curve) can also be calculated from a parametric distribution by fitting a lognormal distribution to the intensity levels of ground motions that cause the collapse of a structure (IM^{CAP}).

$$P_{C|IM=im} = \Phi\left(\frac{\ln im - \hat{\propto}_{\ln IM^{CAP}}}{\hat{\sigma}_{\ln IM^{CAP}}}\right) \tag{2.4}$$

where $\hat{\propto}_{\ln IM^{CAP}}$ and $\hat{\sigma}_{\ln IM^{CAP}}$ are the estimated mean and standard deviation of the collapse capacity in terms of *IM* (lnIM^{CAP}). Using the total probability theorem (Benjamin and Cornell 1970) to combine non-collapse and collapse data, the probability of an *EDP* exceeding a specified intensity level is

$$P\left[EDP > x \mid IM = im\right] = \left(1 - \Phi\left(\frac{\ln x - \hat{\propto}_{\ln EDP|im}}{\hat{\sigma}_{\ln EDP|im}}\right)\right) \cdot \left(1 - P_{C|im}\right) + P_{C|im} \tag{2.5}$$

Equation 2.5 can then be substituted into Equation 2.1 to estimate the seismic performance of a structure (i.e., λ_{EDP}).

As alluded to in the introduction, recent research (e.g., Baker and Cornell 2005a; Luco and Cornell 2006; Luco et al. 2005) has shown that using S_a (or equivalently S_{de}[1], where S_{de} =

[1] Throughout this chapter, S_{de} is used interchangeably with S_a, simply for direct comparison with S_{di}. The results and conclusions are the same.

$(T/2\pi)^2 \times S_a$) alone as the *IM* is not optimal in characterizing the ground motion intensity, as evidenced by the variability in structural responses for a given S_a. This is because S_a does not take into consideration the spectral ordinates at other periods (i.e., spectral shape), which have an impact on inelastic (due to period lengthening) as well as higher-mode responses of MDOF structures. Baker and Cornell (2005a) have found that ε (defined above) is a proxy for spectral shape and thereby an effective *IM* when coupled with S_a. Hence, Baker and Cornell proposed using the *vector IM* $<S_a, \varepsilon>$ to estimate λ_{EDP} via the following modified version of Equation 2.1:

$$\lambda_{EDP}(x) = \int_{all\ s_a} \int_{all\ e} P\left[EDP > x \mid S_a = s_a, \varepsilon = e\right] \cdot \left| d\lambda_{S_a,\varepsilon}(s_a, e) \right| \tag{2.6}$$

where $d\lambda_{S_a,\varepsilon}$ is the joint MAF of the S_a and ε values (within some small increment). Using the definition of conditional probability, $d\lambda_{S_a,\varepsilon}(s_a, e)$ can be expressed as $f_{\varepsilon=e|S_a=s_a} \cdot de \cdot d\lambda_{S_a}(s_a)$, where $f_{\varepsilon=e|S_a=s_a}$ reflects the likelihood of observing different ε values at the s_a level, and *de* is a small increment in epsilon value. Conveniently, $f_{\varepsilon=e|S_a=s_a}$ can be obtained from PSHA disaggregation results. To estimate the first factor in Equation 2.6, one needs to first scale records to a given $S_a = s_a$ level, then perform nonlinear dynamic analysis. The additional steps, which take into account the effect of ε on response prediction, are separated into two: for collapse and non-collapse data. To estimate the probability of collapse given a S_a level and ε, a logistic regression (McCullagh and Nelder 1990) can be utilized. The estimated probability of collapse is

$$P_{C|S_a=s_a,\varepsilon=e} = \frac{1}{1 + \exp\left[-\left(\hat{\beta}_{0,C} + \hat{\beta}_{1,C} \cdot e\right)\right]} \tag{2.7}$$

where $\hat{\beta}_{0,C}$ and $\hat{\beta}_{1,C}$ are estimated regression coefficients using logistic regression on binary (collapse and non-collapse) responses of records scaled to $S_a = s_a$ intensity level. Collapse and non-collapse data (indicated by 1 and 0, respectively, in the figure) along with the estimated probability of collapse are shown, for example, in Figure 2.1a.

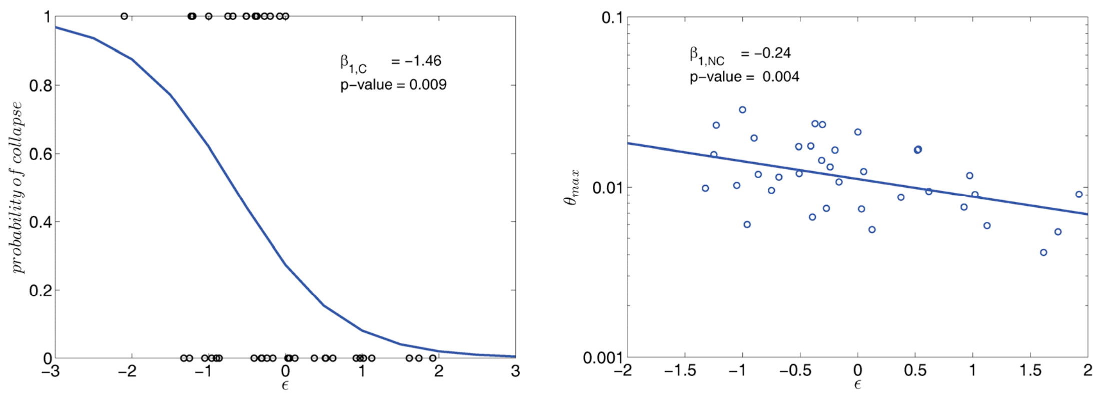

(a) (b)

Fig. 2.1 Analysis of data of 40 records using *S_a* (or *S_{de}*) *IM*: (a) prediction of probability of collapse using logistic regression applied to binary (collapse and non-collapse) data as a function of epsilon; (b) prediction of responses for non-collapse data using linear regression.

For non-collapse data, at a given S_a level, the distribution of responses can be modeled using linear regression analysis to estimate ln*EDP*. The estimated mean of ln*EDP* on ε ($\hat{\propto}_{\ln EDP|\varepsilon}$) is shown to be well represented by $\hat{\beta}_{0,NC} + \hat{\beta}_{1,NC} \cdot \varepsilon$ (Baker and Cornell 2005a), where $\hat{\beta}_{0,NC}$ and $\hat{\beta}_{1,NC}$ are the estimated regression coefficients from the regression analysis shown in Figure 2.1b.

The p-values shown in the figures indicate the significance of the estimated parameter $\hat{\beta}_{1,C}$ and $\hat{\beta}_{1,NC}$. The p-value is defined here as the likelihood of observing the slope coefficient equal to or greater than (in absolute value) $\hat{\beta}_{1,C}$ or $\hat{\beta}_{1,NC}$ if the underlying (true) value of $\beta_{1,C}$ or $\beta_{1,NC}$ is in fact zero (Benjamin and Cornell 1970). Hence, a small p-value (e.g., less than a 5% significant level) indicates that it is very unlikely to observe $\hat{\beta}_{1,C}$ or $\hat{\beta}_{1,NC}$ to be different from zero (if the true value is zero); therefore, ε is statistically significant in predicting the responses. The estimated dispersion (standard deviation of the natural logarithm) of *EDP* given ε ($\hat{\sigma}_{\ln EDP|\varepsilon}$) can be calculated from the residuals between observed data and predicted values (i.e., $\ln EDP - \widehat{\ln EDP}$). The residuals have been shown to follow a normal distribution. With the assumed lognormal distribution, the probability of *EDP* exceeding a specified value x, given $S_a = s_a$, $\varepsilon = e$, and non-collapse can be expressed as

$$P\left[EDP > x \mid S_a = s_a, \varepsilon = e, NC\right] = 1 - \Phi\left(\frac{\ln x - \left(\hat{\beta}_{0,NC} + \hat{\beta}_{1,NC} \cdot e\right)}{\hat{\sigma}_{\ln EDP|\varepsilon}}\right) \tag{2.8}$$

The collapse and non-collapse data can then be combined via the total probability theorem (Benjamin and Cornell 1970), shown as follows:

$$P\left[EDP > x \mid S_a = s_a, \varepsilon = e\right] = \left(1 - \Phi\left(\frac{\ln x - \left(\hat{\beta}_{0,NC} + \hat{\beta}_{1,NC} \cdot e\right)}{\hat{\sigma}_{\ln EDP|\varepsilon}}\right)\right) \cdot \left(1 - P_{C|s_a,e}\right) + P_{C|s_a,e} \tag{2.9}$$

where $P_{C|S_a=s_a,\varepsilon=e} = 1\Big/\left(1+\exp\left[-\left(\hat{\beta}_{0,C} + \hat{\beta}_{1,C} \cdot e\right)\right]\right)$. Note that the estimated regression coefficients ($\hat{\beta}_{0,NC}$, $\hat{\beta}_{1,NC}$, $\hat{\beta}_{0,C}$, $\hat{\beta}_{1,C}$, and $\hat{\sigma}_{\ln EDP|\varepsilon}$) are calculated from responses of records scaled to $S_a = s_a$. Equation 2.9 can then be substituted into Equation 2.6 to calculate the MAF of exceeding a specified value of *EDP*. A more detailed explanation of how to estimate λ_{EDP} using $<S_a, \varepsilon>$ can be found in Baker and Cornell (2005a, b); also described there is how the double integration for this vector *IM* (Eq. 2.6) can be avoided by properly selecting ground motions with ε values that match its conditional probability distribution (from PSHA disaggregation) at specified S_a levels. The selection must be redone for each S_a level. This disaggregation-based method has also been used to reduce the number of analyses when performing simulation-based PSDA, where thousands of earthquake records are generated to represent seismicity at a site and used to analyze the structural response probabilistically (Collins et al. 1996; Wen 2000).

2.4 STRUCTURES, GROUND MOTION RECORDS, AND INELASTIC SPECTRAL DISPLACEMENT PARAMETERS CONSIDERED

2.4.1 Structures and Ground Motion Records

Sixteen generic moment-resisting frames with a variety of structural properties are considered in this study. The structures were modeled and analyzed by Ibarra and Krawinkler (2005). They vary in number of stories, first-mode period, and hysteretic model parameters. The peak-oriented hysteretic model considered (used at the beam ends and at the bases of columns) incorporates stiffness and strength deterioration (Ibarra et al. 2005; see Fig. 2.2).

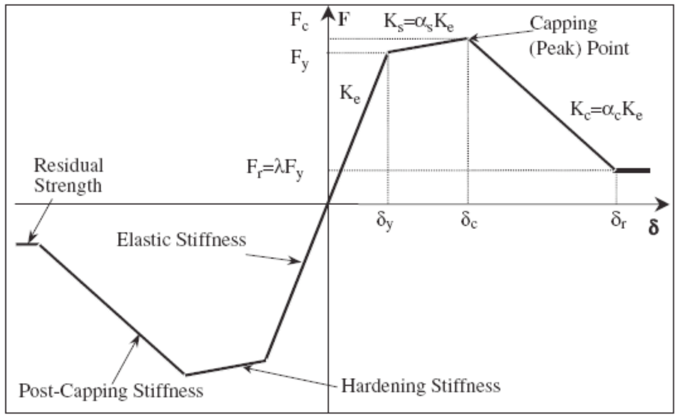

Fig. 2.2 Backbone curve for hysteretic models (adapted from Ibarra et al. 2005).

The model utilizes energy-based deterioration through a cyclic deterioration parameter ($\gamma_{s,c,k,a}$), as well as the following backbone curve parameters: the strain-hardening stiffness ratio (set equal to 3%), which is relative to the elastic stiffness (K_e); the capping ductility (δ_c/δ_y) (set equal to four), which is defined as the displacement at the peak strength (δ_c) divided by the yield displacement (δ_y); and the post-capping stiffness ratio (α_c), relative to K_e. A detailed description of this hysteretic model can be found in Ibarra et al. (2005).

The 16 structures considered are summarized in Table 2.1. To distinguish between these structures, a four-number code is adopted. The first two numbers indicate the number of stories, and the last two numbers indicate the first-mode period of vibration. Each structure has a single bay with story stiffnesses and strengths chosen to be representative of typical structures. Accounting for P-Δ effects, Ibarra and Krawinkler (2005) subjected each structural model to 40 historical earthquake ground motion records (or "records," for short) with magnitudes from 6.5 to 6.9 and distances from 13 to 40 km. This set of records was compiled by Medina and Krawinkler (2003). The resulting structural demand parameter considered in this chapter is the peak maximum interstory drift ratio ($\theta_{\max}$; peak over response time and maximum over the height of the structure).

Table 2.1 Generic frames considered and their hysteretic model properties: first-mode period of vibration (T_1); capping ductility (δ_c/δ_y), defined as displacement at peak strength (δ_c) divided by yield displacement (δ_y); post-capping stiffness ratio (α_c); and cyclic deterioration parameter ($\gamma_{s,c,k,a}$).

Structure Code	Number of Stories	T_1	δ_c / δ_y	α_c	$\gamma_{s,c,k,a}$
0303	3	0.3	4	-0.05	50
0303	3	0.3	4	-0.10	∞
0306	3	0.6	4	-0.05	50
0306	3	0.6	4	-0.10	∞
0606	6	0.6	4	-0.05	50
0606	6	0.6	4	-0.10	∞
0612	6	1.2	4	-0.05	50
0612	6	1.2	4	-0.10	∞
0909	9	0.9	4	-0.05	50
0909	9	0.9	4	-0.10	∞
0918	9	1.8	4	-0.05	50
0918	9	1.8	4	-0.10	∞
1515	15	1.5	4	-0.05	50
1515	15	1.5	4	-0.10	∞
1530	15	3.0	4	-0.05	50
1530	15	3.0	4	-0.10	∞

The primary structure considered in this chapter has nine stories and a first-mode period of vibration equal to 0.9 sec, with $\gamma_{s,c,k,a}$= 50; it is referred to as structure 0909. The base shear strength coefficient for this structure is 15% of its total weight. To illustrate higher-mode effects, the 1515 structure with $\gamma_{s,c,k,a}=\infty$ (and base shear strength equal to 20% of its weight) is also used. These generic frames are especially sensitive to higher-mode excitations due to the way in which they have been designed, i.e., to have a straight-line first-mode shape.

2.5 INELASTIC SPECTRAL DISPLACEMENT PARAMETERS

For computing the inelastic spectral displacement, S_{di}, the single-degree-of-freedom (SDOF) hysteretic model used in this study is bilinear with a 5% post-yield hardening stiffness ratio and a 5% damping ratio. This bilinear hysteresis model is used because it has been previously utilized to develop an attenuation relationship for S_{di} (Chapter 3 and also Tothong and Cornell 2006); as a result, site-specific ground motion hazard curves for the S_{di} of this hysteresis model can be calculated, which is necessary for PSDA. The period (T) and yield displacement (d_y) of the bilinear SDOF system used to compute S_{di} can be estimated from the results of a nonlinear static pushover analysis of the MDOF structure under evaluation (Fajfar 2000; Goel and Chopra 2004); however, for structures with degrading strength (either from post-capping stiffness or cyclic deterioration), these estimates of the parameters will result in a well-suited S_{di} only when the structure behaves linearly or mildly inelastically (i.e., when strength degradation does not contribute significantly). In order to maintain the effectiveness of S_{di} near linear elastic behavior, we set the period parameter equal to the first-mode period of vibration, T_1. In order to relate better to structural responses up to global dynamic instability, the yield displacement is established by minimizing the dispersion of the IM values at which the structure exhausts its capacity to resist global dynamic instability ($\sigma_{\ln IM^{CAP}}$), determined via incremental dynamic analysis of the structure for the set of 40 records considered. Interestingly, for each of the 16 MDOF structures considered in this study, the d_y that minimizes $\sigma_{\ln IM^{CAP}}$ (d_y^*, where * indicates the optimal value) is about half the d_y estimated via static pushover analysis. Given that the strength at or right before collapse is less than the initial yield strength of each of these strength-degrading MDOF structures, it is intuitive to choose an SDOF system with a reduced d_y (i.e., d_y^*) to capture the MDOF response at or near collapse. The corresponding inelastic spectral displacement $S_{di}(T_1, d_y^*)$, or S_{di} for short, is used throughout this chapter.

For the 0909 structure, the bilinear backbone curve used for S_{di} is shown in Figure 2.3a. Also shown is the static pushover curve of the 0909 structure, along with the bilinear backbone curve that would be used if the conventional method of establishing T and d_y based on the pushover analysis were applied. Figure 2.3b is a contour plot of $\sigma_{\ln IM^{CAP}}$ for the 0909 structure (and the set of 40 records considered) as a function of T and d_y for a range of bilinear SDOF systems that could be used for S_{di}. The values of $\sigma_{\ln IM^{CAP}}$ for $S_{de}(T_1)$ and for S_{di} with parameters based on pushover analysis (i.e., $T = T_1$ and $d_y = 1.6$ in. from Fig. 2.3a) are 0.39 and 0.31, respectively, meaning that not much dispersion reduction is gained when using the pushover-based parameters. In fact, $\sigma_{\ln IM^{CAP}}$ for the optimal *elastic* SDOF system, or $S_{de}(T^*)$, is 0.30 (at T^* = 1.8 sec, twice the first-mode period, a factor consistent with other studies, e.g., Haselton and Baker 2006).

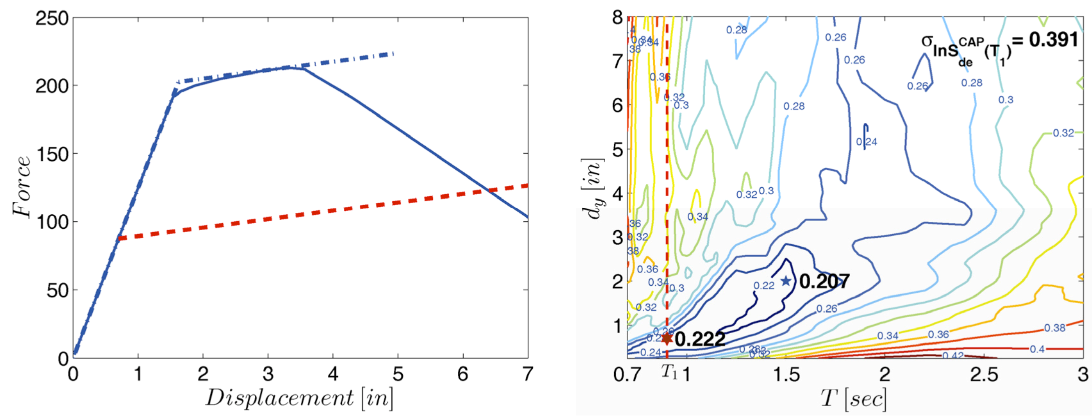

(a) (b)

Fig. 2.3 For the "0909 structure" ($\gamma_{s,c,k,a}$= 50), (a) nonlinear static pushover curve (solid line) and two options for bilinear backbone curve used for S_{di}, and (b) contours of dispersion of IM^{CAP} for different T and d_y combinations.

The bilinear SDOF system used in this chapter (i.e., $S_{di}(T_1, d_y^* = 0.75 \text{ in.})$, as shown in Fig. 2.3a) results in $\sigma_{\ln IM^{CAP}} = 0.22$, an approximately 50% reduction in capacity dispersion compared to using $S_{de}(T_1)$. The minimum $\sigma_{\ln IM^{CAP}}$ is only 0.21 at T^* = 1.5 sec and $d_y{}^*$ = 2 inches. While these parameters obtained by simultaneously optimizing T and d_y result in the smallest $\sigma_{\ln IM^{CAP}}$, the inelastic spectral displacement $S_{di}(T^*, d_y^*)$ will poorly explain the variation of MDOF responses near the elastic regime (i.e., at low ground motion intensities) because T^* is different than T_1. By maintaining T_1 and only optimizing d_y, $S_{di}(T_1, d_y^*)$ captures both the elastic and collapse-level responses of structures. Note that all of the optimized SDOF systems described above seem to work in such a way that they aim to intersect a reduced strength on the static pushover curve, possibly the point at which the structure has (on average) lost its lateral capacity and incipient collapse is reached.

It should be noted that with respect to the bilinear SDOF model used here for S_{di}, the strength-limited bilinear model developed by Ibarra et al. (2005) would further reduce $\sigma_{\ln IM^{CAP}}$, based on the fact that its application by Han and Chopra (2006) dramatically improved the modal pushover analysis procedure (Chopra and Goel 2002). In order to use the strength-limited bilinear model for an IM, however, one would need to determine how the inelastic spectral displacement of the strength-limited bilinear model depends on attenuation relationship parameters such as M_w and R_{rup}. Furthermore, if the seismic hazard in terms of the strength-limited bilinear model were to be made as readily available as the current spectral acceleration hazard curves, the USGS would need to compute the hazard for a much larger number of model parameters, i.e., many combinations of ductility, post-capping stiffness, strength-deterioration rate, etc., in addition to the current periods. The simple bilinear model appears to be a good compromise, especially if the d_y is chosen to be at or near the optimal value.

2.6 REVIEW OF EPSILON AND HOW IT AFFECTS STRUCTURAL RESPONSES

Epsilon, ε, measures the deviation of S_a for an as-recorded ground motion from the median (geometric mean) S_a calculated from an attenuation relationship (e.g., Abrahamson and Silva 1997). More specifically, ε is the difference between the natural logarithms of the two S_a values, normalized by the standard deviation of $\ln(S_a)$ from the attenuation relationship. Note that in this chapter the standard deviation of $\ln(S_a)$ is for a randomly oriented horizontal component of ground motion, which is larger than the dispersion reported by Abrahamson and Silva (1997) for the geometric mean of the two horizontal components of a ground motion. In addition to calculating ε values, this inflated dispersion is used in generating the ground motion hazard curves. The latter is done to ensure consistency when combining, via PSDA, the hazard curves with structural responses. The responses are calculated based on individual randomly oriented record properties, not the geometric mean across two horizontal components (Baker and Cornell 2006c).

Baker and Cornell (2005a) have shown that records with the same S_a level (at the same period, T_1) but different ε values can excite an MDOF structure differently, causing different inelastic responses. This is because ε is a proxy for *average* spectral shape (where the average is over a number of records with the same ε value) despite that, strictly speaking, it contains only *local* spectral-shape information at T_1 (where local refers to not only the proximity to T_1, but also that ε is calculated for a particular record). Among records with a given ε value, there are variations in their individual spectral shapes, but the average spectral shape for positive versus negative ε values is systematically different. Around T_1, positive ε records tend to have a "peak" spectral shape (e.g., Fig. 2.4a) whereas negative ε records tend to have a "valley" spectral shape (e.g., Fig. 2.4b). When these two different types of records have (or are scaled to) the same S_a level, those with the valley spectral shape will, on average, have higher spectral ordinates at periods other than T_1 (e.g., Fig. 2.4c). The higher spectral values at shorter periods will more strongly excite higher-mode responses of MDOF structures. Likewise, the higher spectral values at longer periods will cause stronger inelastic responses of MDOF structures (because when structures behave nonlinearly, the lateral stiffness will soften, thus resulting effectively in period elongation). In other words, the structural responses resulting from records that have a common (i.e., the same) S_a value will depend on the ε values of the selected records, i.e., the numbers of peak records versus valley records. Baker and Cornell (2005a) capture this dependence by including ε in the vector $IM < S_a, \varepsilon >$. As will be discussed in the next section, using S_{di} as the IM eliminates the need to add this additional element to the vector.

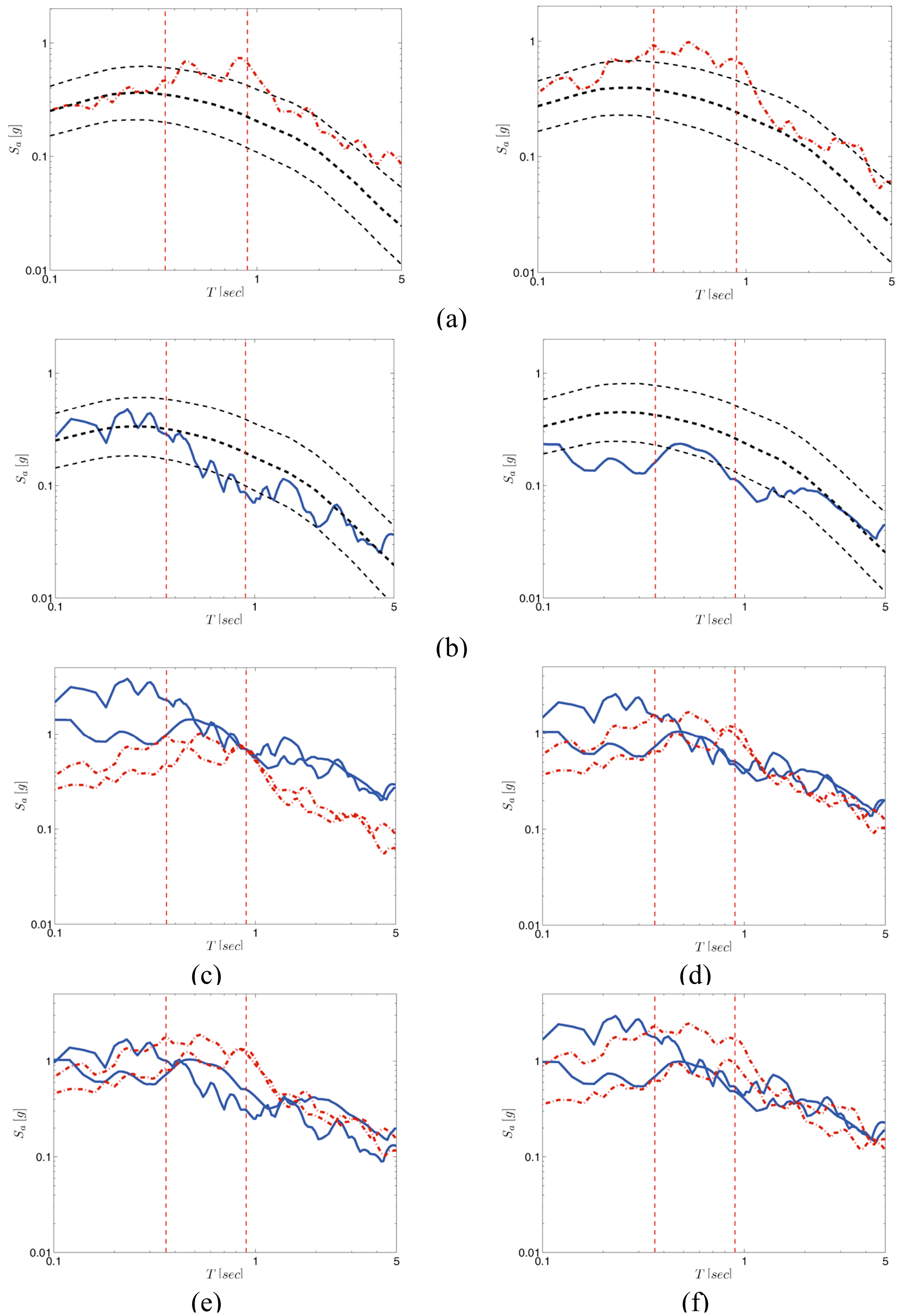

Fig. 2.4 Response spectra of (a) two "peak" records and (b) two "valley" records, and their response spectra when scaled to common value of (c) S_a (or S_{de}), (d) S_{di} (or $S_{di}(T_1, d_y^*)$, (e) $S_{di}(T^*, d_y^*)$, or (f) $S_{de}(T^*)$. Vertical dotted lines indicate first- and second-mode periods of 0909 structure, 0.9 and 0.36 sec, respectively.

2.7 HOW INELASTIC SPECTRAL DISPLACEMENT REDUCES EFFECT OF EPSILON

In contrast to S_a, S_{di} implicitly captures the spectral shape at periods longer than T_1 because the spectral values at those periods directly affect S_{di} (due to period elongation). As a result, the response spectra of records that have (or are scaled to) a common value of S_{di} can be expected to produce less record-to-record variability in the response spectra at $T > T_1$. Figure 2.4d illustrates this greater similarity in the response spectra of the aforementioned *peak* (Fig. 2.4a) and *valley* (Fig. 2.4b) records after they are scaled to a common value of S_{di}. (Note: For all of the figures in this chapter that show results for records scaled to a common value of an *IM*, the value is that associated with a (counted-median) θ_{max} value of about 1.3%, as obtained from the incremental dynamic analysis results for the structure.) By using S_{di} as the *IM*, higher-scale factors are assigned to the peak (positive epsilon) records and vice versa for the valley (negative epsilon) records, both relative to the scale factors that are assigned when S_a is used as the *IM*. With a common value of S_{di} and thereby smaller record-to-record variability among response spectra at $T > T_1$, the (scaled) records can be expected to result in comparable inelastic responses of MDOF structures that are *independent* of the ε values of the records. Such independence with respect to ε (or "sufficiency" of S_{di}) is demonstrated quantitatively in the next section for the first-mode-dominated 0909 structure. Because S_{di} does not capture the ground motion frequency content at higher-mode periods, however, a modification factor that accounts for the second mode of vibration (and results in $IM_{1I\&2E}$, as discussed later) is needed in order to achieve more accurate PSDA results for higher-mode-sensitive structures.

To further illustrate the effectiveness of S_{di}, Figure 2.5a displays $\sigma_{\ln S_a(T)}$, the conditional (on a given value of each *IM*) dispersion, of the response spectra scaled like those shown in Figure 2.4c–f, but now for all 40 of the records. (The heavy solid lines show the dispersion for only the 7 largest ε records scaled to a common S_a. These results represent the use of the $<S_a, \varepsilon>$ with special record selection to reflect the ε component.) First note that in Figure 2.5a and elsewhere in this chapter, S_{de} is used interchangeably with S_a, simply for direct comparison with S_{di}. Since they are proportional to each other, the results and conclusions for the two *IM*s (i.e., S_{de} and S_a) are the same. As revealed by the figure, using S_{di} can reduce the variation in the response spectra at $T > T_1$, as can $<S_a, \varepsilon>$ but not (to the same extent) S_a. This reduction in $\sigma_{\ln S_a(T)}$ is indicative of the relative efficiency (Luco 2002; Luco and Cornell 2006) of S_{di} and $<S_a, \varepsilon>$ for first-mode-dominated structures, as discussed in the next section. The relatively large $\sigma_{\ln S_a(T)}$ at shorter (than first-mode) periods when S_{di} is the *IM*, on the other hand, is indicative of its relative inefficiency for higher-mode-sensitive structures. As mentioned above, this weakness can be alleviated by using $IM_{1I\&2E}$. Also note from Figure 2.5a that the two largest dispersions at T_1 result from using $S_{di}(T^*, d_y^*)$ and $S_{de}(T^*)$, which capture inelastic structural responses well, but not the responses of near-elastic behavior (as mentioned earlier in the chapter). As seen in Figure 2.4e and f, the records have been scaled to a nearly exact common spectral ordinate for $S_{di}(T^*, d_y^*)$ and $S_{de}(T^*)$ respectively, creating large amplitudes deviation at T_1.

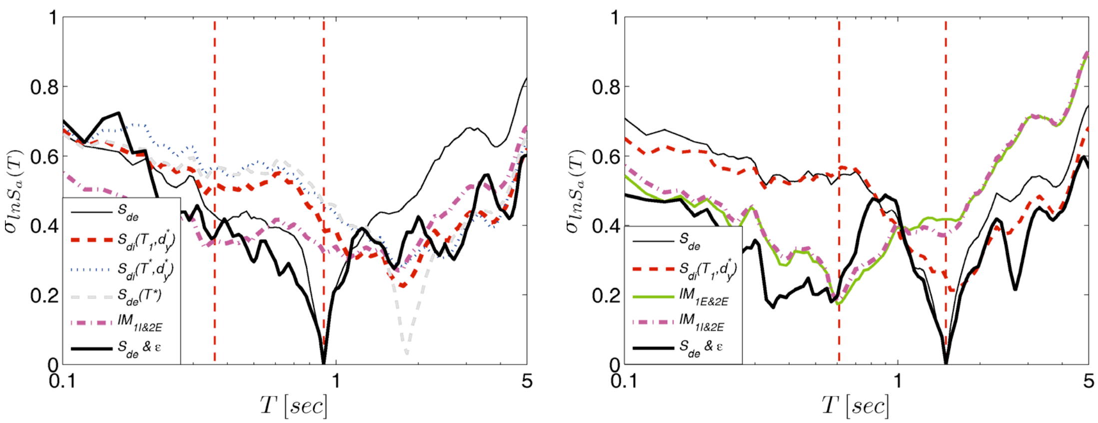

(a) (b)

Fig. 2.5 Dispersions of response spectra of 40 records (7 largest *ε* records for <S_a, *ε*> results) scaled to a common value of each *IM*. Vertical dotted lines show first- and second-mode periods for (a) 0909 structure, namely 0.9 and 0.36 sec, respectively, and (b) 1515 structure, namely 1.5 and 0.61 sec.

As can be seen in Figure 2.5a, $\sigma_{\ln S_a(T)}$ of these two systems shows the two largest values at T_1. The large $\sigma_{\ln S_a(T)}$ at shorter periods will make the *IM* inefficient and insufficient for structures sensitive to higher-mode frequencies. The $IM_{1I\&2E}$ needs to be used in such a case, discussed further in the next section. On the other hand, the proposed system, $S_{di}(T_1, d_y^*)$ performs relatively well at $T > T_1$ (for large responses) as well as near the elastic response regions (for smaller seismic demands).

2.8 DESIRABLE GROUND MOTION *IM* PROPERTIES

For ensuring accuracy in assessing structural performance via PSDA (Eq. 2.1), desirable *IM* properties include efficiency, sufficiency, (Luco 2002; Luco and Cornell 2006), and scaling robustness, each which are discussed in this section. An *IM* that exhibits these properties will tend to be structure specific, recognizing both the important modes of vibration and effects of nonlinear behavior as well as the relative frequency content of the earthquake records. At the limit, the *IM* itself would be the structural response of interest. In this extreme case, however, computing the ground motion hazard curve (which would also be the structural response hazard curve) would require hundreds, if not thousands, of nonlinear dynamic analyses under ground motions that are (1) simulated to represent the seismicity at the site (Collins et al. 1996; Wen 2000) or (2) used to develop an attenuation relationship for the structural response. Hence, a desirable *IM* is also one for which it is feasible to compute the seismic hazard. In this section, the above three properties of the conventional *IM*, S_a, the vector *IM*, $<S_a, \varepsilon>$, and the advanced *IM*, S_{di}, are compared for the first-mode-dominated 0909 structure. The desirable properties of $IM_{1I\&2E}$ for higher-mode-sensitive structures will be discussed later in the chapter.

2.8.1 Efficiency

An efficient *IM* is defined as one that results in relatively small variability of structural responses for a given *IM* level ($\sigma_{\ln EDP|IM}$), as well as relatively small $\sigma_{\ln IM^{CAP}}$. A small $\sigma_{\ln EDP|IM}$ (or analogously, $\sigma_{\ln IM^{CAP}}$) is desirable because the standard error of the sample mean of ln*EDP* for a specified *IM* level ($\sigma_{\ln EDP|IM} / \sqrt{n}$, where n is the number of records that have been sampled; Benjamin and Cornell 1970) is proportional to $\sigma_{\ln EDP|IM}$, and the sample mean of ln*EDP*|*IM* is typically the first-order information used in quantifying the first integrand in the PSDA integral (Eq. 2.1).

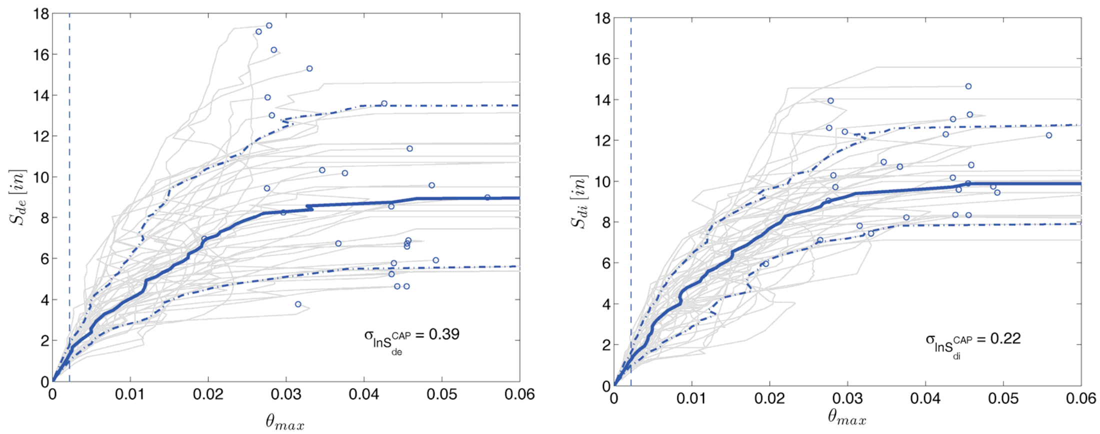

(a) (b)

Fig. 2.6 Incremental dynamic analysis results using (a) S_{de} (or equivalently S_a) or (b) S_{di} as *IM* for 40 records and 0909 structure. Dashed vertical line represents drift level at yielding, determined from static pushover analysis. Circles indicate where global dynamic instability of structure is reached. Counted-median and 16% and 84% fractiles shown with solid and dashed-dotted lines, respectively.

Since the standard error is inversely proportional to $\sqrt{n}$, a reduction in $\sigma_{\ln EDP|IM}$ also reduces the number of records needed to achieve an accurate estimate of the mean ln*EDP*|*IM* and thereby reliable PSDA results. For first-mode-dominated structures like 0909, the use of S_{di} as the *IM* can substantially reduce $\sigma_{\ln EDP|IM}$ and $\sigma_{\ln IM^{CAP}}$. Figure 2.6 indicates that $\sigma_{\ln IM^{CAP}}$ is reduced by about 50% when using S_{di} in lieu of S_a, implying that the number of records needed to achieve the same accuracy in estimating the mean ln*EDP*|*IM* can be reduced by a factor of four. The corresponding reductions in $\sigma_{\ln EDP|IM}$ can also be observed in Figure 2.6, by comparing the distances between the 16th and 84th percentiles of θ_{max} (the peak maximum interstory drift ratio, recall) for a given S_{di} versus S_a level, both obtained via incremental dynamic analysis (Vamvatsikos and Cornell 2002a). As one might expect, including ε in the vector *IM* $\langle S_a, \varepsilon \rangle$ also increases the efficiency (i.e., reduces $\sigma_{\ln EDP|IM}$) relative to S_a alone (Baker and Cornell 2005a).

2.8.2 Sufficiency

A sufficient *IM* is one for which the conditional probability distribution of *EDP* given *IM* (i.e., the first integrand in Eq. 2.1, denoted here as $G_{EDP|IM}$) is independent of the other parameters involved in computing the seismic hazard, mainly ε, M_w, and R_{rup}. A sufficient *IM* is desirable because it implies that any set of ground motions selected for nonlinear dynamic analysis of the structure will result in approximately the same $G_{EDP|IM}$ (i.e., $G_{EDP|IM} \cong G_{EDP|IM,\varepsilon,M_w,R_{rup}}$). If an IM is not sufficient, the estimate of $G_{EDP|IM}$ will depend to some degree on which earthquake records are selected, thus ultimately altering the estimated seismic performance of the structure (i.e., $\lambda_{\theta_{\max}}$).

Previous research has demonstrated that S_a can be insufficient (in addition to inefficient) with respect to M_w and/or R_{rup} for tall, long-period structures (Shome 1999) and for near-source ground motions (Luco 2002; Luco and Cornell 2006). Baker and Cornell (2005a) have found that S_a can be particularly insufficient with respect to the ground motion parameter ε, as demonstrated here in Figure 2.7a, a plot of $\ln\theta_{\max}$ versus ε for the 0909 structure subjected to records scaled to a given S_a level. Note that the slope of the linear trend between $\ln\theta_{\max}$ and ε is statistically significant, as indicated by the small (0.9%) p-value for the estimated slope coefficient ($\hat{\beta}_{1,NC}$). The p-value is defined as the likelihood of observing a slope coefficient equal to or greater than (in absolute value) $\hat{\beta}_{1,NC}$ if the underlying (true) value of $\beta_{1,NC}$ is in fact zero (Benjamin and Cornell 1970).

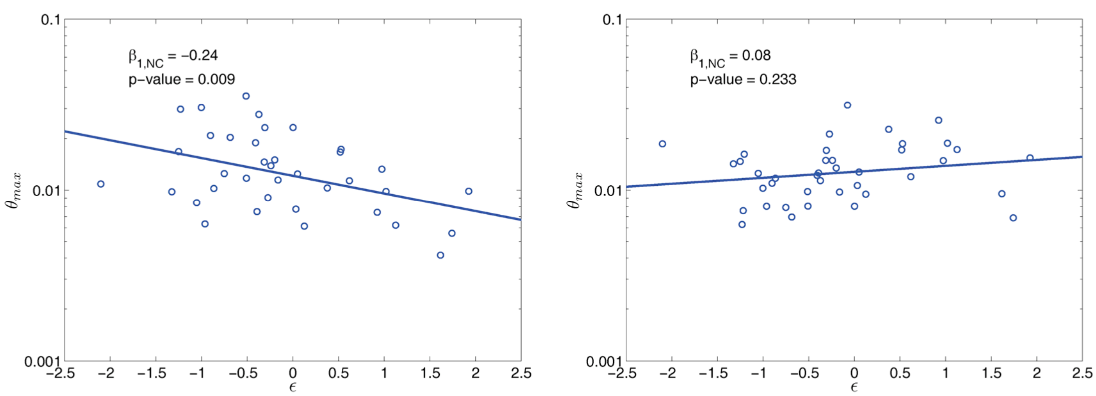

(a) (b)

Fig. 2.7 Dependence of maximum interstory drift ratio (θ_{max}; for non-collapse cases) on ground motion ε for common value of (a) S_a or (b) S_{di}. Solid lines show the regression fits. Example is for 0909 structure.

Hence, a small p-value (e.g., less than a 5% significance level) indicates that it is very unlikely that the true value of $\beta_{1,NC}$ is zero. Here this means that ε has a statistically significant effect on the structural responses. By replacing S_a with S_{di} (i.e., scaling to a comparable S_{di} level instead), the linear trend between $\ln\theta_{\max}$ and ε is rendered statistically *insignificant* in Figure

2.7b. Although not shown here, S_{di} has also been demonstrated to be sufficient with respect to M_w and R_{rup}, as has <S_a, ε> (Baker and Cornell 2005b).

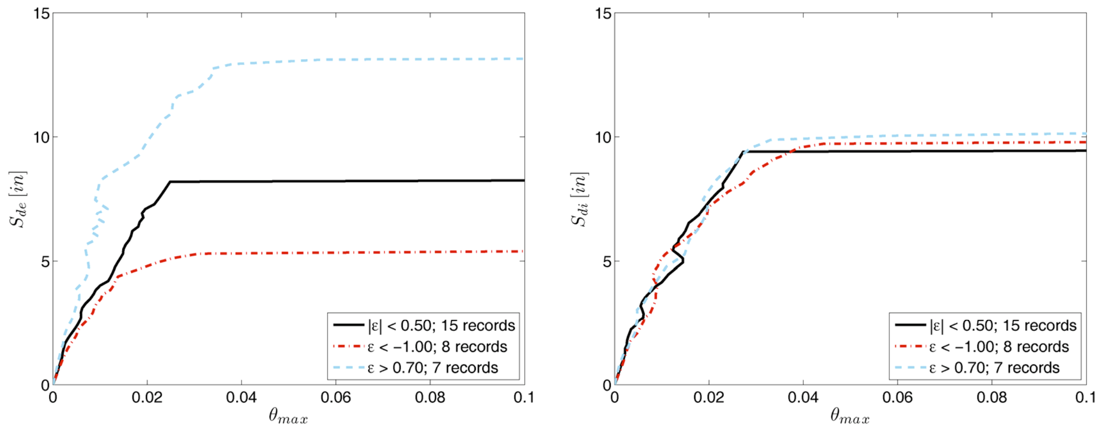

(a) (b)

Fig. 2.8 Counted-median incremental dynamic analysis curves for 0909 structure using records grouped by epsilon and (a) S_{de} (or equivalently S_a) or (b) S_{di} as *IM*.

To further demonstrate the sufficiency of S_{di} with respect to ε for other (higher and lower) levels of the *IM*, the ground motion records are partitioned into three epsilon bins: (1) $|\varepsilon| < 0.5$, (2) $\varepsilon < -1.0$, and (3) $\varepsilon > 0.7$; representing the median, the valley-like, and the peak-like spectral shapes, respectively. (The bin widths are chosen to provide separation in the ε values and to maintain an adequate number of records in each bin.) The results of incremental dynamic analysis of the 0909 structure for these three epsilon bins are shown in Figure 2.8a for S_a and Figure 2.8b for S_{di}. Once again, the dependence of the structural responses ($\theta_{\max}$ medians) on ε is substantially reduced by using S_{di}, rather than S_a, as the *IM*. Thus, S_{di} avoids the need to include ε in a vector *IM*, unlike S_a.

2.8.3 Scaling Robustness

Another desirable *IM* property is that scaling records to a value of the *IM* results in unbiased structural responses compared to the analogous responses obtained from as-recorded (unscaled) ground motions. That is, the responses for records scaled to different amounts but to the same resulting *IM* level should not show a trend in responses versus scale factors. Such scaling robustness is important because scaled records are often (including in this chapter) used in PSDA to establish the first integrand in Equation 2.1 via incremental dynamic analysis. An example of an *IM* that does not exhibit scaling robustness is S_a (Luco and Bazzurro 2004).

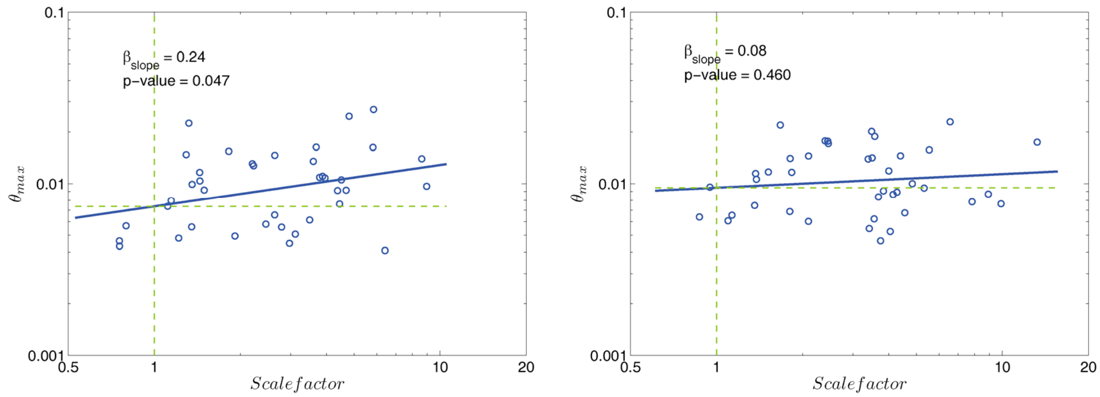

(a) (b)

Fig. 2.9 Maximum interstory drift ratio ($\theta_{\max}$) versus scale factor for records scaled to common value of (a) S_a or (b) S_{di}. Solid lines show the regression fits, and dashed lines pinpoint median $\theta_{\max}$ predicted for unscaled records. Example is for 0909 structure.

For the first-mode-dominated 0909 structure, Figure 2.9 demonstrates that scaling records to a value of S_a tends to result in biased structural responses that increase with increasing scale factors. In contrast, when using S_{di} as the *IM* (Fig. 2.9b), no statistically significant trend exists between $\ln\theta_{\max}$ and ln(Scale factor), indicating that S_{di} is robust with respect to scaling. This observation can be explained by the fact that records with large-scale factors tend to be smaller epsilon cases, and the effect of epsilon on responses has been shown above (Fig. 2.7). Baker and Cornell (2006b) have demonstrated that by considering epsilon-binned sets of records like those described in the preceding subsection, $<S_a, \varepsilon>$ also exhibits scaling robustness (at least for ordinary records).

2.8.4 PSDA Results Using Inelastic Spectral Displacement as *IM*

As previously mentioned, the desirable *IM* properties of efficiency, sufficiency, and scaling robustness help to ensure the accuracy of a PSDA structural performance assessment. To demonstrate this, PSDA results using the conventional *IM*, S_a, the vector *IM*, $<S_a, \varepsilon>$, and the advanced *IM*, S_{di}, are compared in this section for the first-mode-dominated 0909 structure hypothetically located at a site in Van Nuys, California. First the collapse fragility curves needed (as the first factor in the PSDA integral, Eq. 2.1) to compute the MAF of structural collapse are compared, followed by the structural response (drift) hazard curves that demonstrate the end result of PSDA. Note that the latter results involve PSHA (in order to compute the second factor in the PSDA integral). The PSHA for the site was conducted using software provided by Dr. Norman Abrahamson and modified to compute ground motion hazard curves in terms of S_{di} (using a S_{di} attenuation model explained in Chapter 3) and $<S_a, \varepsilon>$, in addition to S_a. Since the attenuation relationship used for S_{di} (and for $IM_{1I\&2E}$, which will be discussed in a subsequent section) is an extension of the existing attenuation relationship for S_a (specifically Abrahamson and Silva 1997), the computed S_{di} hazard curve is consistent with those for S_a and $<S_a, \varepsilon>$.

2.8.5 Collapse Fragility

In order to compute the MAF of collapse of a given structure at a specified site, PSDA (Eq. 2.1) couples the *IM* seismic hazard curve for the site with the collapse fragility for the structure. The collapse limit state fragility function (or curve) is defined as the conditional probability of structural collapse for a given *IM* level, denoted here as $P_{C|IM}$. Based on incremental dynamic analysis results for the structure subjected to a selected set of ground motion records, $P_{C|IM}$ can be estimated via a logistic regression (McCullagh and Nelder 1990; Shome 1999) of a collapse/no collapse binary indicator variable on *IM* (Eq. 2.7). Using the vector *IM*, $<S_a, \varepsilon>$, Figure 2.10a shows the collapse fragility *surface* (as a function of the two dimensions S_a and ε) for the 0909 structure. As revealed by the graph, the collapse fragility *curves* that are a function of S_a only (i.e., $P_{C|S_a}$) can be strongly dependent on ε. This observation demonstrates that S_a is not a sufficient *IM* for collapse estimation.

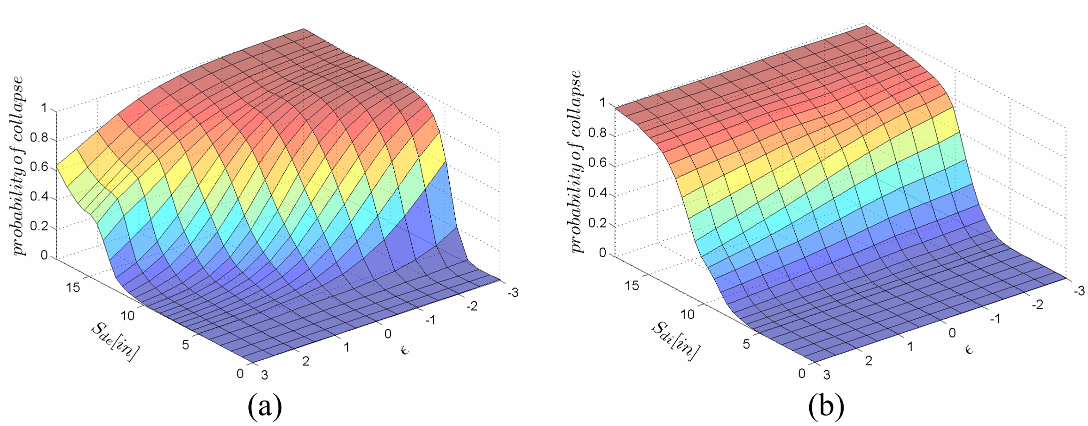

Fig. 2.10 Collapse fragility for 0909 structure as function of (a) S_{de} (or equivalently S_a) and ε or (b) S_{di} and ε.

In contrast, Figure 2.10b demonstrates that collapse fragility curves that are a function of S_{di} (i.e., $P_{C|S_{di}}$) rather than S_a are not significantly dependent (statistically) on ε — i.e., that S_{di} *is* sufficient with respect to ε. Hence, using S_{di} as the *IM* in PSDA would result in practically the same estimate of the MAF of collapse regardless of the ε values of the selected earthquake records. The same can be said for $<S_a, \varepsilon>$, although in that case the MAF of collapse is computed by coupling the fragility surface with a vector seismic hazard (Eq. 2.6).

2.8.6 Structural Response (Drift) Hazard Curve

To evaluate multi-objective structural performance (i.e., more than collapse prevention alone), the MAF of exceeding structural drift levels (denoted here as $\lambda_{\theta_{max}}$, the so-called drift hazard curve) can be calculated via PSDA, i.e., Equations 2.1 and 2.6 using S_{di} or S_a and $<S_a, \varepsilon>$, respectively. Recall that this involves (1) computing a ground motion hazard curve in terms of S_{di}, S_a, or $<S_a, \varepsilon>$ via PSHA and (2) performing incremental dynamic analysis of the structure using the respective *IM*. Drift hazard curves, $\lambda_{\theta_{max}}$, computed using S_{di} (dashed line), the conventional S_a (thin solid line), and the vector $<S_a, \varepsilon>$ (thick solid line) are shown in Figure 2.11.

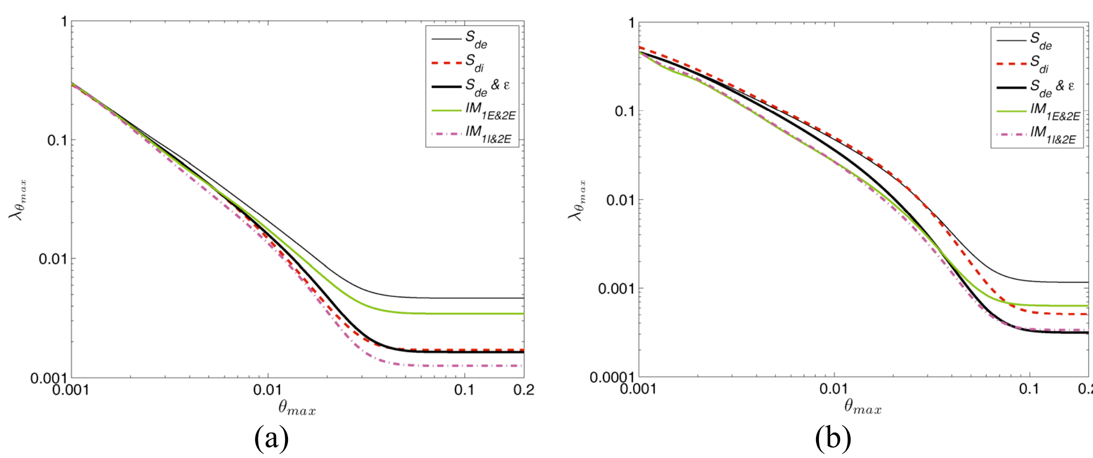

Fig. 2.11 Structural response hazard curves for (a) first-mode-dominated 0909 and (b) higher-mode-sensitive 1515 structure computed using various *IM*s.

Table 2.2 PSDA results, namely (1) MAF of exceeding a θ_{max} value that corresponds to a ductility of about four and (2) MAF of collapse, computed using different *IM*s. Percentage reductions with respect to results using S_a as *IM*. MAF values in table are normalized by 10^{-4}. Blank line separates first-mode-dominated structures from those more sensitive to higher modes.

Structure Analyzed	MAF (% Reduction) at ductility of four						MAF (% Reduction) at collapse					
	S_a & ε		S_{di}		$IM_{1I\&2E}$		S_a & ε		S_{di}		$IM_{1I\&2E}$	
0303 $\gamma_{s,c,k,a}$ = 50	6.7	(-66)	8.1	(-59)	7.7	(-61)	2.3	(-84)	4.0	(-73)	3.7	(-74)
0303 $\gamma_{s,c,k,a}$ = Inf	10.5	(-58)	9.4	(-62)	9.1	(-64)	3.4	(-81)	4.0	(-78)	3.8	(-79)
0306 $\gamma_{s,c,k,a}$ = 50	6.6	(-59)	10.2	(-37)	8.2	(-50)	1.3	(-86)	4.8	(-49)	3.6	(-62)
0306 $\gamma_{s,c,k,a}$ = Inf	5.3	(-62)	9.1	(-34)	6.4	(-54)	2.5	(-72)	3.8	(-58)	2.6	(-70)
0606 $\gamma_{s,c,k,a}$ = 50	5.0	(-57)	9.7	(-16)	6.0	(-49)	0.3	(-91)	0.9	(-72)	0.4	(-87)
0606 $\gamma_{s,c,k,a}$ = Inf	4.7	(-50)	6.4	(-32)	4.2	(-55)	0.3	(-88)	0.5	(-77)	0.2	(-89)
0612 $\gamma_{s,c,k,a}$ = 50	41.5	(-41)	61.0	(-13)	42.6	(-39)	4.1	(-74)	7.0	(-55)	4.3	(-73)
0612 $\gamma_{s,c,k,a}$ = Inf	35.2	(-43)	47.8	(-22)	32.0	(-48)	4.4	(-71)	5.1	(-67)	3.0	(-80)
0909 $\gamma_{s,c,k,a}$ = 50	192	(-21)	182	(-25)	163	(-33)	16.4	(-65)	17.0	(-63)	12.5	(-73)
0909 $\gamma_{s,c,k,a}$ = Inf	153	(-24)	141	(-29)	120	(-40)	19.2	(-58)	15.3	(-66)	12.1	(-73)
0918 $\gamma_{s,c,k,a}$ = 50	27.0	(-47)	56.4	(11)	20.3	(-60)	2.9	(-54)	4.1	(-35)	2.2	(-65)
0918 $\gamma_{s,c,k,a}$ = Inf	24.0	(-44)	47.6	(10)	16.4	(-62)	4.8	(-24)	4.1	(-35)	3.1	(-51)
1515 $\gamma_{s,c,k,a}$ = 50	181	(-34)	292	(06)	142	(-48)	2.2	(-81)	4.8	(-58)	3.2	(-72)
1515 $\gamma_{s,c,k,a}$ = Inf	165	(-35)	269	(06)	123	(-52)	3.1	(-73)	5.1	(-56)	3.4	(-71)
1530 $\gamma_{s,c,k,a}$ = 50	24.5	(-74)	94.6	(-2)	46.8	(-50)	0.7	(-88)	5.7	(-8)	4.9	(-22)
1530 $\gamma_{s,c,k,a}$ = Inf	21.1	(-75)	89.0	(-7)	41.1	(-51)	1.8	(-70)	6.1	(0)	5.7	(-8)

For the first-mode-dominated 0909 structure (Fig. 2.11a), this $\lambda_{\theta_{max}}$ comparison confirms that using S_{di} as the *IM* results in a drift hazard curve that is comparable to that obtained by using the vector *IM*, $<S_a, \varepsilon>$, which are both different than the S_a-based result at larger structural response levels. To further support this conclusion, PSDA results for the other 15 structures considered in this study are computed, with the results shown in Table 2.2. For the first-mode-dominated structures and a large nonlinearity level (collapse), the tabulated MAF values computed using $<S_a, \varepsilon>$ and S_{di} are *not* statistically significantly different. The statistical significant test is performed via the bootstrap technique (explained below) to evaluate the difference in the logarithmic values of $\lambda_{\theta_{max}}$ using either S_{di} or $IM_{1I\&2E}$ relative to those of $<S_a, \varepsilon>$. Table 2.3 reports such p-values for all of the structures considered using advanced *IM*s relative to $<S_a, \varepsilon>$.

For the first-mode-dominated structures and a lower nonlinearity level (ductility of about four), the MAF values calculated using S_{di} are only statistically different from those using $<S_a, \varepsilon>$ for one of the first-mode-dominated structures (i.e., the 0612 structure with $\gamma_{s,c,k,a}$=50). This is likely due to the fact that the higher-mode contributions to the response at the lower nonlinearity level are relatively strong for this structure. As discussed further later in the chapter, S_{di} modified by a higher-mode factor (i.e., $IM_{1I\&2E}$) can be employed to obtain comparable drift hazard curve results for higher-mode-sensitive structures (e.g., preview Table 2.3 and Fig. 2.11b for the 1515 structure).

To compare the standard error (S.E.) of each of the $\lambda_{\theta_{max}}$ estimates obtained using the different *IMs*, the bootstrap method (Efron and Tibshirani 1993) can be applied. The bootstrap method is used here at the ground motion selection step, to generate "bootstrap samples" of the record set that is used for nonlinear dynamic analysis. The 40 records in each bootstrap sample are selected randomly with replacement (such that a record may be sampled more than once or not at all) from the original 40 ground motions. With each of these new record sets, $\lambda_{\theta_{max}}$ is calculated as usual (via PSDA), generating a series of $\lambda_{\theta_{max}}$ curves for the bootstrap samples. The median and the median plus/minus one standard deviation (i.e., the S.E.) of $\lambda_{\theta_{max}}$ across the samples are shown in Figure 2.12.

Table 2.3 P-values from t-test to test hypothesis that using advanced *IM*s results in (statistically) same structural response hazard curves as those of $<S_a, \varepsilon>$. Blank line separates first-mode-dominated structures from those more sensitive to higher modes. Bold values indicate statistically significant results (at 5% significant level).

Structure Analyzed	P-values at ductility of four		P-values at collapse	
	S_{di}	$IM_{1I\&2E}$	S_{di}	$IM_{1I\&2E}$
0303 $\gamma_{s,c,k,a}$ = 50	0.53	0.56	0.95	0.96
0303 $\gamma_{s,c,k,a}$ = Inf	0.65	0.67	0.89	0.92
0306 $\gamma_{s,c,k,a}$ = 50	0.30	0.46	0.06	0.11
0306 $\gamma_{s,c,k,a}$ = Inf	0.23	0.42	0.45	0.69
0606 $\gamma_{s,c,k,a}$ = 50	0.13	0.48	0.06	0.55
0606 $\gamma_{s,c,k,a}$ = Inf	0.44	0.92	0.55	0.78
0612 $\gamma_{s,c,k,a}$ = 50	**0.01**	0.19	0.46	0.22
0612 $\gamma_{s,c,k,a}$ = Inf	0.06	0.18	0.46	0.49
0909 $\gamma_{s,c,k,a}$ = 50	0.85	0.57	0.36	0.96
0909 $\gamma_{s,c,k,a}$ = Inf	0.94	0.10	0.94	0.42
0918 $\gamma_{s,c,k,a}$ = 50	**0.04**	0.30	0.72	0.60
0918 $\gamma_{s,c,k,a}$ = Inf	0.05	0.76	0.72	0.63
1515 $\gamma_{s,c,k,a}$ = 50	**0.02**	0.25	0.94	0.87
1515 $\gamma_{s,c,k,a}$ = Inf	**0.01**	**0.03**	0.28	0.97
1530 $\gamma_{s,c,k,a}$ = 50	**0.00**	**0.02**	0.57	0.60
1530 $\gamma_{s,c,k,a}$ = Inf	**0.00**	**0.01**	0.53	0.55

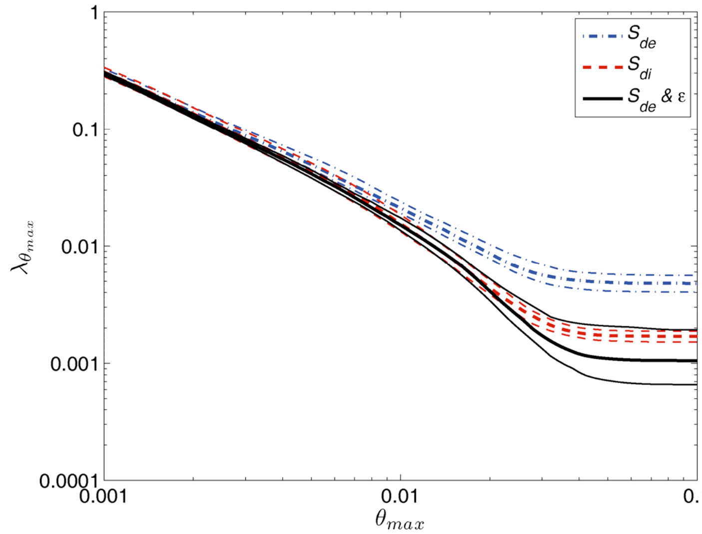

Fig. 2.12 Bootstrap results estimating median (heavier lines) and its plus/minus one standard error bands (lighter lines) for drift hazard curves computed using various *IM*s. Example is for 0909 structure.

The larger S.E. when using <S_a, ε> is due to the larger number of parameters in the *IM*, which results in "over-fitting" of the structural response data, or a bias-variance tradeoff (Hastie et al. 2001). The relatively large S.E. when using <S_a, ε> becomes even larger when, due to, e.g., many records causing collapse, a smaller number of records are used to determine the relationship between structural responses (here $\theta_{\max}$) and the *IM*.

2.8.7 Drift Hazard Curves for Epsilon-Binned Records

Using the records that (as introduced earlier in the chapter) are partitioned into three epsilon bins: (1) $|\varepsilon| < 0.5$, (2) $\varepsilon < -1.0$, and (3) $\varepsilon > 0.7$; representing the median, valley-like, and peak-like spectral shapes, respectively — the corresponding drift hazard curves, $\lambda_{\theta_{\max}}$, obtained using S_a, <S_a, ε>, and S_{di} are shown in Figure 2.13a, b, and c, respectively (all for the first-mode-dominated 0909 structure).

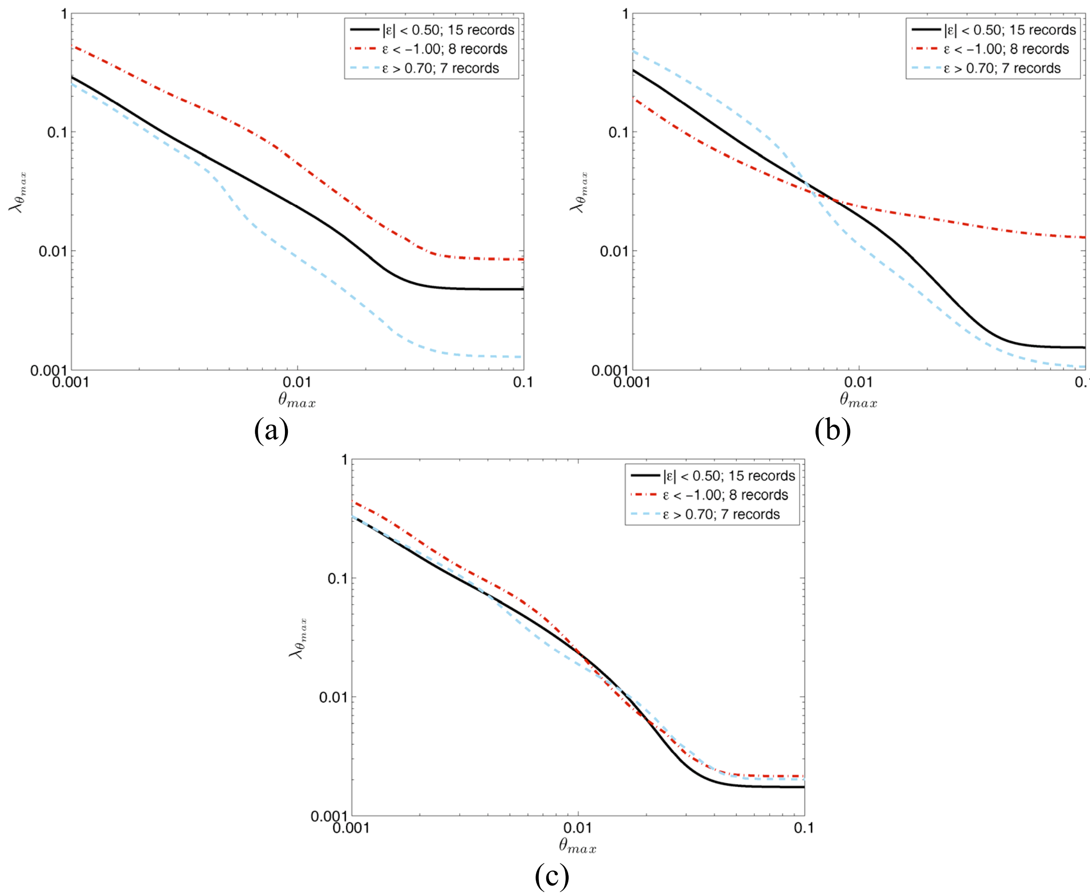

Fig. 2.13 Structural response hazard curves for 0909 structure computed using records grouped by epsilon and (a) S_a, (b) <S_a, ε>, or (c) S_{di} as *IM*.

When using S_a as the *IM*, the drift hazard curves for the three epsilon bins are significantly different, due primarily to the insufficiency of S_a. The differences observed when using the vector <S_a, ε> (Fig. 2.13b), on the other hand, are primarily due to the relatively large statistical uncertainty that results from using an additional parameter in the *IM* in conjunction with the small number of records within each narrow range of epsilon values. Otherwise, using <S_a, ε> or S_{di}, results in approximately the same structural performance, $\lambda_{\theta_{\max}}$, for the three subsets of these *ordinary* ground motions (compare Fig. 2.13b and c). We conclude that the results obtained using S_{di} are more stable (with respect to record selection) than those for the vector <S_a, ε>, especially when a small number of records is used.

2.8.8 Drift Hazard Curves for Pulse-Like Records

To demonstrate an additional advantage of S_{di} relative to <S_a, ε> (not to mention S_a), the seismic performance of the 0909 structure is evaluated using a set of 70 near-source pulse-like ground motions described in Chapters 4 and 5 (see also, Tothong et al. 2007). Past research (e.g., Alavi and Krawinkler 2001; Fu 2005; Mavroeidis et al. 2004; Tothong et al. 2007; and also Chapters 4 and 5) has shown that pulse-like records with $T_p/T_1 \cong 2$ (where T_p is the pulse period of the near-source record) tend to cause relatively severe damage in MDOF structures, whereas records with $T_p/T_1 \cong 1$ do not.

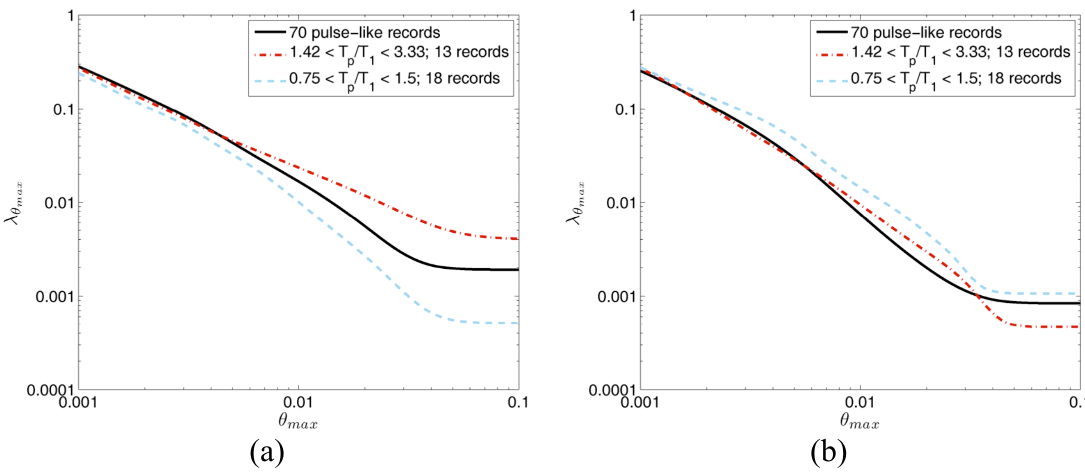

Fig. 2.14 Structural response hazard curves for 0909 structure computed using three different sets of pulse-like records and (a) <S_a, ε> or (b) S_{di} as *IM*.

Therefore, three sets of the pulse-like records are considered: (1) all 70 of the records, (2) only the records with $1.42<T_p/T_1<3.33$ (the "aggressive" set), and (3) the records with $0.75<T_p/T_1<1.50$ (the "benign" set). The drift hazard curves, $\lambda_{\theta_{\max}}$, calculated using <S_a, ε> and S_{di} are shown in Figure 2.14a and Figure 2.14b, respectively. As seen in Figure 2.14a, using <S_a, ε> as the *IM* yields significantly different $\lambda_{\theta_{\max}}$ results for the three pulse-like record sets; in contrast, $\lambda_{\theta_{\max}}$ calculated using S_{di} is comparable for the three different pulse-like record sets (Fig. 2.14b), and the results roughly match those using ordinary ground motions (recall Fig. 2.11a). Again, we conclude that the use of S_{di} leads to results which are insensitive to the record set used, even in this extreme case of pulse-like records. The discrepancy for <S_a, ε> can be explained by the fact that, while this *IM* does encapsulate the average spectral shape (as reviewed earlier in the chapter), it does not necessarily contain information about the local (for each record) spectral shape near T_p, especially if T_p is far from T_1. S_{di}, on the other hand, implicitly captures the local spectral shape at the periods longer than T_1 that directly affect the inelastic response (through period elongation), including T_p (if $T_p > T_1$). Note that this is possible because S_{di}, unlike $\langle S_a, \varepsilon \rangle$, takes into account the strength of the MDOF structure being evaluated (through d_y); as such, S_{di} can distinguish the amount of period elongation (or the level of inelasticity) induced by the record, e.g., that the effective period of a weak structure might elongate to T_p, whereas that of a stronger structure might not (Bazzurro and Luco 2006). PSDA results for pulse-like ground motions using S_{di} as the *IM* are discussed in more detail in Chapter 5.

2.9 PSDA RESULTS USING $IM_{1I\&2E}$

For higher-mode-sensitive structures such as the 0918, 1515, and 1530 frames considered in this chapter (or other tall, long-period buildings), S_{di} is not as efficient and sufficient as it is for first-mode-dominated structures like the 0909 frame (Luco 2002; Luco and Cornell 2006), nor is it likely to be as robust with respect to scaling. These shortcomings (i.e., undesirable *IM* properties) are largely due to the fact that using S_{di} alone does not capture the ground motion frequency content at higher-mode periods, as demonstrated in Figure 2.5b for example, where the dispersion of $S_a(T_2)$ for the 1515 structure is relatively large when the record set is scaled to a common value of S_{di}. The shortcomings of S_{di} explain why, as shown in Figure 2.11b, the structural drift hazard curve computed (via PSDA) using S_{di} for the 1515 structure is different than that computed using $\langle S_a, \varepsilon \rangle$ (especially at a lower nonlinearity level, see Tables 2.2 and 2.3), which reflects spectral shape not only at longer-than-first-mode periods but at shorter periods (higher modes) as well. Presented in this section are results of PSDA using $IM_{1I\&2E}$, which (as explained below) incorporates second-mode effects via a scalar modification of S_{di}.

As developed by Luco (2002) and Luco and Cornell (2006) and furthered by Mori et al. (2004) (who approach the problem from a predictor or simplified analysis perspective, rather than an *IM* perspective), the ground motion intensity measure $IM_{1I\&2E}$ is calculated from a square-root-of-sum-of-squares (SRSS) modal combination reasoning as a function of $S_{di}(T, d_y)$ (where $T = T_1$ and $d_y = d_y^*$ here, but other options can be used), $S_{de}(T_2)$, and the elastic participation factors of the first two modes of the structure of interest, i.e.,

$$IM_{1I\&2E} = S_{di}\left(T, d_y\right) \cdot \sqrt{1 + \left[\frac{PF_2^{[2]} \cdot S_{de}\left(T_2\right)}{PF_1^{[2]} \cdot S_{di}\left(T, d_y\right)}\right]^2} \tag{2.10}$$

where $PF_n^{[2]}$ is the n^{th}-mode *effective* participation factor for interstory drift ratio (i.e., $\Gamma_n \cdot \frac{\phi_{n,i} - \phi_{n,i-1}}{h_i}$) that corresponds to the story of the structure at which $\sqrt{\left[PF_1^{[2]} \cdot S_{di}\left(T, d_y\right)\right]^2 + \left[PF_2^{[2]} \cdot S_{de}\left(T_2\right)\right]^2}$ is maximized (for $\theta_{\max}$; Luco 2002; Luco and Cornell 2006). In the expression for $PF_n^{[2]}$, h_i is the height of the i^{th} story (above the i^{th} floor), $\phi_{n,i}$ is the i^{th}-floor element of the n^{th}-mode shape vector, and Γ_n is the n^{th}-mode participation factor, as defined in Chopra (2001). Note that here we have adopted the equation for $IM_{1I\&2E}$ put forth by Mori et al. (2004), which is slightly different than the original equation proposed by Luco (2002) and Luco and Cornell (2006); the latter uses $S_{de}(T_1)$ in the denominator of the square root term, thereby involving three different spectral displacement parameters. In either case, the square root term serves as a higher-mode modification factor for S_{di}.

Using a first-order mean-centered Taylor's series expansion of the natural logarithm of Equation 2.10 in conjunction with existing attenuation relationships for S_{di} (Tothong and Cornell 2006, see also Chapter 3) and S_{de} (e.g., Abrahamson and Silva 1997), an attenuation relationship for $IM_{1I\&2E}$ is described in Chapter 3. Here we use this attenuation relationship to compute (via PSHA) ground motion hazard curves in terms of $IM_{1I\&2E}$. Still for the same Van Nuys site considered throughout the chapter, but now for the higher-mode-sensitive 1515 structure, the drift hazard curve computed (via PSDA) using $IM_{1I\&2E}$ is shown in Figure 2.11b. Via comparison with the results of using $<S_a, \varepsilon>$ as the *IM*, the figure illustrates that the accuracy of using $IM_{1I\&2E}$ in PSDA for higher-mode-sensitive structures is about the same as that using $<S_a, \varepsilon>$, at least at the larger drift levels. Although not shown here (see Chapter 5), the standard error of the drift hazard curve obtained using $IM_{1I\&2E}$ is comparable to that for S_{di} (and S_{de}), and less than that for $<S_a, \varepsilon>$ (see Fig. 2.12).

For comparison purposes, the corresponding drift hazard curve computed using $IM_{1E\&2E}$, which is similar to $IM_{1I\&2E}$ but does not reflect inelasticity (i.e., S_{di} is replaced with S_{de}), is also shown in Figure 2.11b. Note that like S_{di} alone the fully elastic but second-mode-inclusive $IM_{1E\&2E}$ does not lead to an accurate (relative to using $IM_{1I\&2E}$) drift hazard curve at larger drift levels, although it does at smaller drifts; it appears that the combination, namely $IM_{1I\&2E}$, is needed to ensure the accuracy of the drift hazard curve at all drift levels. Similar conclusions can be drawn from the results shown in Tables 2.2 and 2.3 for other higher-mode-sensitive structures, at least relative to $<S_a, \varepsilon>$. The second-mode modification factor included in $IM_{1I\&2E}$

helps characterize responses at low-drift levels (sensitive to the higher modes), whereas S_{di} improves the PSDA result at near-collapse levels, perhaps because the collapse behavior is governed by a first-mode-like pattern (i.e., collapse at or near the bottom story). This is consistent with the often-seen behavior of $\theta_{\max}$ migrating from the top story down to the bottom story as the ground motion intensity increases. For one of the 1515 and the two 1530 structures that are the most (of the structures considered) sensitive to higher modes, though, note that in Table 2.2 the MAF values at the ductility of four calculated using $IM_{1I\&2E}$ are statistically significantly different than that using $<S_a, \varepsilon>$ (see Table 2.3). This difference (for a lower nonlinearity level) might imply a need to incorporate the third mode into $IM_{1I\&2E}$, which is conceptually straightforward (Mori et al. 2004).

The apparent accuracy of the PSDA results described above bolsters previous findings (Luco 2002; Luco and Cornell 2006) that $IM_{1I\&2E}$ is efficient and sufficient, and suggests that $IM_{1I\&2E}$ is also likely robust with respect to scaling (likewise for $IM_{1E\&2E}$ at low $\theta_{\max}$ levels). Briefly, Figure 2.5b demonstrates why incorporating the second-mode term in $IM_{1I\&2E}$ (or $IM_{1E\&2E}$) leads to an increase in the efficiency, i.e., because it reduces the conditional dispersion of the response spectra, $\sigma_{\ln S_a(T)}$, at lower (than the first-mode) periods. In Figure 2.5b neither $IM_{1E\&2E}$ nor $IM_{1I\&2E}$ results in smaller $\sigma_{\ln S_a(T)}$ at higher periods because the level of nonlinearity (drift) considered in the figure is relatively low. As discussed in the preceding paragraph, the $\theta_{\max}$ response is more sensitive to higher modes in this case, and therefore the second-mode portion of $IM_{1I\&2E}$ dominates (due to the effective participation factors). Although not shown here, at larger levels of nonlinearity using $IM_{1I\&2E}$ will result in smaller $\sigma_{\ln S_a(T)}$. This is reflected in Figure 2.11b, where using $IM_{1I\&2E}$ results in a relatively accurate $\lambda_{\theta_{\max}}$ at larger drift levels, as does using $IM_{1E\&2E}$ at lower drifts levels.

Even for first-mode-dominated structures (e.g., the 0909 generic frame), we speculate that computing $\lambda_{\theta_{\max}}$ using $IM_{1I\&2E}$ may be more accurate than using either S_{di} or $<S_a, \varepsilon>$ (we speculate because we lack an absolute, correct value for $\lambda_{\theta_{\max}}$). We suspect this because, first, using $IM_{1I\&2E}$ changes the $\lambda_{\theta_{\max}}$ computed using S_{di} by about the same amount that using $IM_{1E\&2E}$ changes the results for S_a (see Fig. 2.11a), suggesting that the second mode may indeed be contributing (e.g., due to some records causing collapse in the higher-mode-sensitive upper stories). Secondly, $\lambda_{\theta_{\max}}$ computed using $IM_{1I\&2E}$ for the (40) ordinary records (Fig. 2.11a) is similar to that for the (70) pulse-like records (not shown here, but not significantly different than the $\lambda_{\theta_{\max}}$ computed using S_{di}, shown in Fig. 2.14b), more so than when using S_{di} (comparing Figs. 2.11a and 2.14b). Lastly, the PSDA results in Table 2.2 and Table 2.3 indicate that for most of the first-mode-dominated structures considered the MAF values using $IM_{1I\&2E}$ are more similar (although perhaps not statistically speaking) to those using $\langle S_a, \varepsilon \rangle$ than are the S_{di} results. Direct computations of $\lambda_{\theta_{\max}}$ by means of Monte Carlo simulation (e.g., Collins et al. 1996; Wen 2000) will identify which of the *IM*s yields the most accurate estimates of $\lambda_{\theta_{\max}}$. This comparison will be investigated in Chapter 6.

2.10 CONCLUSIONS

We have demonstrated the feasibility and relative accuracy of using advanced scalar *IM*s, namely S_{di} and $IM_{1I\&2E}$, in probabilistic evaluations of the seismic performance of structures (PSDA). Using S_{di} for first-mode-dominated structures (e.g., the 0909 generic frame) and $IM_{1I\&2E}$ for higher-mode-sensitive structures (e.g., 1515) results in both IDAs and structural response (drift) hazard curves that are comparable to those obtained using the vector *IM*, $\langle S_a, \varepsilon \rangle$, for ordinary (i.e., non-near-source) ground motions — e.g., see Figure 2.11, and Tables 2.2–2.3.

For near-source pulse-like ground motions, using S_{di} (or perhaps even more so, $IM_{1I\&2E}$) again results in comparable IDAs and drift hazard curves for the 0909 structure (and other structures in Chapter 5), whereas using $\langle S_a, \varepsilon \rangle$ as the *IM* leads to drift hazard curves that are dependent on which (of three considered) set of pulse-like ground motion records is used for the incremental dynamic analyses of the structure — see Figure 2.14. This insensitivity of the response versus *IM* curves to the records used ensures that the results will not be sensitive to the record selection and scaling. Another observed advantage of S_{di} (and $IM_{1I\&2E}$, although not shown explicitly in this chapter, see Chapter 5) is a smaller standard error of the drift hazard curve computed using the scalar *IM* versus the vector $\langle S_a, \varepsilon \rangle$, as demonstrated in Figure 2.12 for the 0909 structure and ordinary ground motions. Using the conventional *IM*, S_a, results in drift hazard curves that are different than those for S_{di}, $IM_{1I\&2E}$, and $\langle S_a, \varepsilon \rangle$ (again, see Fig. 2.11), and dependent on the ground motion ε values of the records used, unlike S_{di} and $\langle S_a, \varepsilon \rangle$ (see Fig. 2.13 for the 0909 structure). Note that each of these PSDA applications involves a PSHA for the site in terms of the *IM* used. The requisite (for PSHA) attenuation relationship for S_{di} is already available (e.g., Chapter 3 and Tothong and Cornell 2006) and an attenuation for $IM_{1I\&2E}$ is described in Chapter 3.

The relative accuracy of the PSDA results summarized above, and of PSDA results in general, is linked to the efficiency and sufficiency of the *IM* used (Luco 2002; Luco and Cornell 2006), as well as to its robustness with respect to scaling. An *IM* that exhibits these three desirable properties will tend to be structure specific, recognizing in a compact way the important modes of vibration and effects of nonlinear behavior, in addition to the frequency content of the earthquake records. In this chapter we have explicitly demonstrated that S_{di}, unlike S_a, exhibits all three of these desirable *IM* properties for the first-mode-dominated 0909 structure subjected to the ordinary ground motions. As documented by Baker and Cornell (2005b), the same can be said for $<S_a, \varepsilon>$ because like S_{di} (and $IM_{1I\&2E}$), it contains spectral-shape information (as evidenced by Fig. 2.5, which shows a reduced variability in the response spectra upon scaling to a value of each *IM*). For the pulse-like ground motions, however, the aforementioned likeness between the drift hazard curves for the 0909 structure computed using S_{di}, and their differences when using $<S_a, \varepsilon>$, suggests that S_{di} does, but $<S_a, \varepsilon>$ does not, exhibit the three desirable *IM* properties. (Indeed, Baker and Cornell 2005b have noted a residual dependence on pulse period when using $<S_a, \varepsilon>$ for near-source records, implying insufficiency of the *IM*.) This is because S_{di}, unlike S_a or $<S_a, \varepsilon>$, takes into account the strength of the MDOF structure being evaluated; therefore, S_{di} can distinguish the amount of period elongation (i.e., the level of inelasticity) induced by a record. For example, the effective period of a weak structure might elongate to T_p, whereas that of a stronger structure might not.

Making use of an advanced scalar *IM* like S_{di} or $IM_{1I\&2E}$ in PSDA requires minimal effort in switching from the conventional *IM*, S_a. The record scaling process in incremental dynamic analysis is changed to handle the two inelastic *IM*s, but conceptually it remains the same. The selection of records for these analyses is actually simplified, with random selection (e.g., of records with any ε, M_w, R_{rup}) becoming an option that maintains accurate PSDA results. Provided that an attenuation relationship for the advanced *IM* is available, the PSHA component of PSDA remains virtually unchanged as compared to when S_a is employed. In this case, for example, the USGS could simply apply S_{di} or $IM_{1I\&2E}$ attenuation models in lieu of those for S_a (Frankel et al. 2000), thereby generating national seismic hazard maps for S_{di} or $IM_{1I\&2E}$. The demonstrated advantages of the advanced *IM*s in probabilistic structural performance evaluations serve as motivation for doing so.

2.11 APPENDIX: GROUND MOTION ATTENUATION RELATIONSHIP FOR *$IM_{1I\&2E}$*

Using the first-order mean-centered Taylor's series expansion of the natural logarithm of Equation 2.10 for $IM_{1I\&2E}$, an attenuation relationship for $\ln IM_{1I\&2E}$ is developed by combining existing attenuation models for $\ln S_{di}(T, d_y)$ (Chapter 3; see also Tothong and Cornell 2006) and $\ln S_{de}(T_2)$ (e.g., Abrahamson and Silva 1997); recall that an attenuation relationship gives the mean value and variance of the random variable as a function of seismic parameters such as M_w and R_{rup}, etc. The mean value of $\ln IM_{1I\&2E}$ is obtained by simply evaluating the natural logarithm of Equation 2.10, i.e.,

$$g = \ln IM_{1I\&2E} = \ln S_{di}\left(T, d_y\right) + \frac{1}{2} \cdot \ln\left(1 + \left[\frac{PF_2^{[2]} \cdot \exp\left[\ln S_{de}\left(T_2\right)\right]}{PF_1^{[2]} \cdot \exp\left[\ln S_{di}\left(T, d_y\right)\right]}\right]^2\right) \tag{2.11}$$

at the mean values of the two log spectral displacement random variables. The variance of $\ln IM_{1I\&2E}$ is as follows:

$$\begin{aligned} VAR\left[\ln IM_{1I\&2E}\right] = & \left[\left(\frac{\partial g}{\partial \ln S_{di}\left(T, d_y\right)}\right) \cdot \sigma_{\ln S_{di}\left(T, d_y\right)}\right]^2 + \left[\left(\frac{\partial g}{\partial \ln S_{de}\left(T_2\right)}\right) \cdot \sigma_{\ln S_{de}\left(T_2\right)}\right]^2 + \ldots \\ & 2 \cdot \rho_{\ln S_{di}\left(T, d_y\right), \ln S_{de}\left(T_2\right)} \cdot \left(\frac{\partial g}{\partial \ln S_{di}\left(T, d_y\right)}\right) \cdot \left(\frac{\partial g}{\partial \ln S_{de}\left(T_2\right)}\right) \cdot \sigma_{\ln S_{di}\left(T, d_y\right)} \cdot \sigma_{\ln S_{de}\left(T_2\right)} \end{aligned} \tag{2.12}$$

where $\dfrac{\partial g}{\partial \ln S_{di}\left(T, d_y\right)} = 1 - \dfrac{b \cdot Y^2}{1 + b \cdot Y^2}$ and $\dfrac{\partial g}{\partial \ln S_{de}\left(T_2\right)} = \dfrac{b \cdot Y^2}{1 + b \cdot Y^2}$, with b = $\left(\dfrac{PF_2^{[2]}}{PF_1^{[2]}}\right)^2$ and Y = $\exp[\ln S_{de}(T_2) - \ln S_{di}(T, d_y)]$ but evaluated at the mean values of the two log spectral displacements. The variances $\sigma_{\ln S_{di}\left(T, d_y\right)}$ and $\sigma_{\ln S_{de}\left(T_2\right)}$, like the mean values, are obtained from the attenuation models. Strictly speaking, $\rho_{\ln S_{di}\left(T, d_y\right), \ln S_{de}\left(T_2\right)}$ is the correlation between $\ln S_{di}(T, d_y)$ and $\ln S_{de}(T_2)$. This correlation has, however, been approximated by taking advantage of the well-known equal displacement rule (Veletsos and Newmark 1960) for moderate- to long-period structures, which are also the structures for which higher-mode contributions become significant and $IM_{1I\&2E}$ is needed. $\rho_{\ln S_{di}\left(T, d_y\right), \ln S_{de}\left(T_2\right)}$ is simply approximated with $\rho_{\ln S_{de}\left(T\right), \ln S_{de}\left(T_2\right)}$ because models for $\rho_{\ln S_{de}\left(T\right), \ln S_{de}\left(T_2\right)}$ are available (e.g., Baker and Cornell 2006a; Inoue and Cornell 1990). As can be seen in Chapter 3, the difference between these two correlations is at most 0.13, and the effect on the total variance is negligible. Note that, the variance of $\ln IM_{1I\&2E}$ (Eq. 2.12) approaches the variance of $\ln S_{di}(T, d_y)$ for first-mode-dominated structures and vice versa for purely second-mode-dominated structures, as easily shown by taking the limit of Equation 2.12 as b approaches zero and infinity, respectively.

3 Empirical Ground Motion Attenuation Relationship for Inelastic Spectral Displacement and $IM_{1I\&2E}$

3.1 ABSTRACT

This chapter presents an empirical ground motion prediction model (attenuation relationship) for inelastic (as opposed to elastic) spectral displacement (S_{di}) for ground motions without forward-directivity effects. It is a function of two earthquake parameters, moment magnitude (M_w) and the closest distance to rupture (R_{rup}), and two bilinear oscillator parameters, an undamped elastic period (T) and a yield displacement (d_y). The latter, d_y, is introduced via the predicted median strength-reduction factor ($\hat{R}$), a proxy for the ratio of elastic spectral displacement (S_{de}) to d_y, which is identical to the familiar strength-reduction factor (R). The proxy $\hat{R}$ recognizes that R can only be estimated indirectly because it implicitly contains the random variable, S_{de}, which cannot be known *a priori*; therefore, the median estimate or predicted median $\left(\hat{S}_{de}\right)$ from a conventional (elastic) ground motion prediction model is used instead to calculate $\hat{R} = \hat{S}_{de}/d_y$. For enhanced generality, the inelastic spectral displacement prediction model here is based on a ratio concept, that is, the total model is a (any) conventional elastic prediction model coupled with a new inelastic displacement *ratio* prediction model, with proper statistical correlation between the two. We empirically consider the dependence of this ratio on source and path effects (i.e., M_w and R_{rup}) and find that M_w is significant, but R_{rup} is not. The resulting prediction model can easily be added to existing probabilistic seismic hazard analysis (PSHA) software packages with only one extra structure-specific parameter, d_y of the oscillator. In practical engineering applications, this will likely have been estimated from the conventional static pushover analysis of the multi-degree-of-freedom (MDOF) structure under consideration.

The resulting PSHA product is a hazard curve for S_{di}, the inelastic spectral displacement of a nonlinear oscillator. Such a curve can provide a more direct hazard-based "target displacement" for nonlinear static procedures (FEMA-356 2000) and/or a basic input function for new probabilistic seismic demand analyses that is based on S_{di} (as opposed to S_{de}) as an efficient and sufficient intensity measure (*IM*). This new attenuation relationship will be particularly useful in evaluating the performance of existing structures and specified designs with known lateral strength. In particular, unlike most past studies, it does not pre-fix the ductility level.

3.2 INTRODUCTION

Most ground motion prediction models ("attenuation relations") today are used to predict the pseudo-spectral acceleration (S_a) of an elastic oscillator. However, S_a or S_{de} does not correlate well with inelastic responses of multi-degree-of-freedom (MDOF) structures (Bazzurro and Luco 2004; Luco and Cornell 2006; Luco et al. 2005), resulting in highly uncertain seismic demand prediction. The objective of this chapter is to present an empirical attenuation model for inelastic spectral displacement (S_{di}) for bilinear oscillators with a given natural period (T) and yield displacement (d_y). The prediction is made as a function of earthquake parameters such as magnitude (M_w) and distance between site and rupture zone (R_{rup}). This model can be used to produce S_{di} hazard curves and "uniform hazard spectra" (UHS) for such oscillators. These in turn can be used to provide an improved input into the deterministic and probabilistic assessment of structures. This chapter focuses on the latter role.

One approach to this problem would be simply to provide an array of attenuation models for S_{di} for a very large number of (T, d_y) combinations (McGuire and Cornell 1974). The approach adopted here focuses on developing a new prediction model for the *ratio* of inelastic to elastic spectral displacement, or "inelastic displacement ratio" (S_{di}/S_{de}). This approach is used because many attenuation relationships already exist for elastic spectral displacement. Usually these models are prepared in terms of the elastic pseudo-spectral acceleration, S_a. However, S_a is simply a constant, $(2\pi/T)^2$, multiplied by S_{de}. Further, it can be anticipated from many previous studies that the inelastic displacement ratio will have comparatively mild dependence on independent variables such as M_w and R_{rup}, simplifying the development of the net S_{di} prediction model.

In this study of the inelastic displacement ratio, S_{di}/S_{de}, the authors also use the well-known strength-reduction factor (R) to introduce, in a continuous manner, the structural parameter d_y. R is defined here as the ratio of *elastic* spectral displacement to the yield displacement, d_y. This ratio is identical to the ratio of the strength required for the oscillator to remain elastic (F_e) to the yield strength (F_y) of the oscillator (Chopra 2001; see Fig. 3.1). Note as defined herein, R is similar to but distinct from the strength-reduction factor defined in building codes to define the design seismic base shear as a fraction of the spectral acceleration associated with the design earthquake.

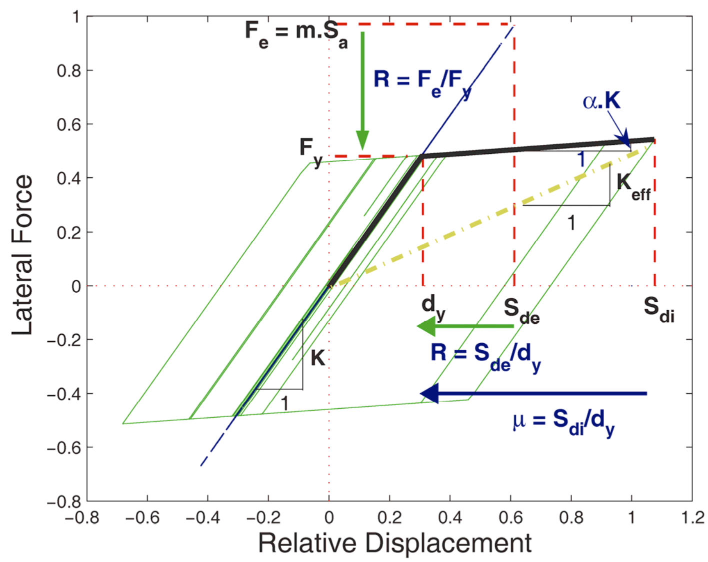

Fig. 3.1 Force displacement behavior of bilinear oscillator with 5% hardening stiffness ratio.

This effective normalization of d_y by S_{de} permits us to focus on a limited parameter range, for example $1 \leq R \leq 8$. Further, past research (Chintanapakdee and Chopra 2003; Miranda 2000; Miranda and Bertero 1994; Nassar and Krawinkler 1991; Qi and Moehle 1991; Ruiz-García and Miranda 2003) has carefully investigated how S_{di}/S_{de} depends on R for all period ranges. As a result, the dependence of S_{di}/S_{de} versus R and T is well understood. This ratio is, on average, close to unity for moderate periods where the "equal displacement rule" applies (Veletsos and Newmark 1960), greater than unity for shorter periods, where it grows with R, and somewhat less than unity for longer periods. This information can be used when developing empirical attenuation relationships.

The S_{di} attenuation relationship developed here differs from previous models. First, most of these are models for constant-ductility oscillators (Bozorgnia et al. 2006; Chakraborti and

Gupta 2005; Lawson 1996; Miranda 2000; Miranda and Bertero 1994; Nassar and Krawinkler 1991; Sewell 1989). By contrast, the objective here is not to achieve a given ductility level in design, but rather to evaluate the behavior of oscillators with given structural properties, in particular d_y. Ruiz-García and Miranda (2003) note that using the constant-ductility inelastic displacement ratio to estimate S_{di} for systems with known lateral strengths or yield displacements will underestimate the peak responses as well as the statistical variation. This last observation is intuitively clear because in the first case S_{di} is constrained to certain values in order to achieve specified target ductilities, whereas in the second case S_{di} itself is random. Second, although previous studies (Chintanapakdee and Chopra 2003; Chopra and Chintanapakdee 2004; Ruiz-García and Miranda 2003) have developed predictions of S_{di}/S_{de} for oscillators for a specified d_y (for known S_{de}), they have assumed that S_{di}/S_{de} is independent of ground motion record properties (i.e., independent of M_w and distance). Even though these models can be used to estimate an S_{di} hazard curve (Ruiz-García and Miranda 2005) by using the total probability theorem to convolve the conventional S_{de} hazard curve and the probability distribution of S_{di}/S_{de}, this approach will be inaccurate to the degree that this ratio displays, for example, magnitude dependence because it fails to distinguish between hazard generated by small versus large earthquake magnitude events. As seen in the following section, we do detect this M_w dependence. Using the proposed ground motion prediction models, one can produce the S_{di} hazard curve directly by conventional PSHA software, avoiding the need for a subsequent convolution.

Our use of the R factor, S_{de}/d_y, to assist in the prediction of S_{di}/S_{de} is not as straightforward as it might appear, however. In contrast to the studies of S_{di}/S_{de} versus R, where the ground motion records are available and known, in the prediction mode only earthquake parameters such as M_w and distance are known, whereas the value of S_{de} of the future record is unknown. As a result, one does not know *a priori* what the value of $R = S_{de}/d_y$ will be. Therefore, a new variable called the *predicted* strength-reduction factor ($\hat{R}$, the hat denoting predicted median value throughout) is defined, which is based on the predicted value of S_{de} (denoted $\hat{S}_{de}$) rather than on S_{de}. This predicted value, $\hat{S}_{de}$, is the median value from a standard attenuation model for S_{de} versus M_w, R_{rup}, and other source and site parameters (e.g., Abrahamson and Silva 1997). Therefore, $\hat{S}_{de}$ and $\hat{R}$ are known *a priori*. One other repercussion is that past results for

S_{di}/S_{de} versus R cannot be directly applied. Instead, a new relationship for S_{di}/S_{de} versus $\hat{R}$ must be developed. The implications of this change will be illustrated subsequently.

Once the model for the geometric mean of S_{di}/S_{de} versus earthquake parameters is obtained, the ratio can be multiplied by that for $\hat{S}_{de}$ to obtain the median value for S_{di}. In applications, models are based on the means of the natural logarithms of S_{de} and S_{di}/S_{de}, implying simple addition of the two coefficients on the independent variables, for example, magnitude.

To complete the description of attenuation relationship, a model for dispersion (the standard deviation of the natural logarithm) of S_{di} ($\sigma_{\ln S_{di}}$) must be developed. This model must reflect both dispersion in the prediction of S_{de} and dispersion in the inelastic displacement ratio, S_{di}/S_{de}. Further, it must consider the correlation between these two random variables. As a result, we have chosen to develop an empirical model for the *total* standard deviation for $\ln S_{di}$ ($\sigma_{\ln S_{di}}$). This $\sigma_{\ln S_{di}}$ model approaches $\sigma_{\ln S_{de}}$ for large values of d_y or small values of $\hat{R}$.

The need for a S_{di} attenuation relationship is based on recent research. Earlier studies (Bazzurro and Luco 2004; Luco 2002; Luco and Cornell 2006; Luco et al. 2005) have shown that S_{di} provides better nonlinear response prediction of MDOF structures than a prediction based on the elastic pseudo-spectral acceleration ($S_a(T_1)$) at the fundamental period, T_1, of a structure or a prediction based on the structure-independent peak ground acceleration (PGA). In addition, S_{di} should intuitively reduce the so-called peak-valley effects (Baker and Cornell 2005a). These authors show that records with a spectral peak at the first-mode period tend to cause less than the average nonlinear response induced by all records with the same $S_a(T_1)$. This happens because the effectively elongated period of the oscillators "drifts" off the spectral peak into a weaker valley. They also found that this effect can largely be "corrected" by coupling ε with $S_a(T_1)$ in a *vector* intensity measure (*IM*) for seismic demand prediction, where ε is the number of standard deviations that the ground motion deviates from the predicted elastic median attenuation relationship. S_{di} is also capable of resolving the peak-valley problem because it captures the period drift as structures behave inelastically. As a result, S_{di} "senses" which ground motions will tend to cause benign or aggressive inelastic responses on structures, in contrast to S_{de}. In fact, it has been shown that scaling a ground motion with respect to S_{di} reduces the predictive power of ε, at least for first-mode-dominated structures (see Chapter 2, and also Tothong and Luco 2007); therefore, the predictor ε is not statistically significant when S_{di} is employed as an *IM*. Importantly too, using S_{di} can reduce the potential bias in scaling the amplitude of ground motions (see Chapter 2, and also Tothong and Luco 2007), thus simplifying the record selection by avoiding strong emphasis on other ground motion record properties such as ε, M_w, and distance, etc.

A S_{di} attenuation relationship will be particularly useful in assessing the performance of existing and proposed design structures with known lateral strength both in the deterministic nonlinear static procedure described in FEMA-356 (2000) and in the PSDA underlying advanced performance-based earthquake engineering (Cornell and Krawinkler 2000; Moehle and Deierlein 2004). If the MDOF structures are assumed to have simplified bilinear moment-rotation relations and to have small influence from the global P-delta effect, the empirical model here can be directly applied to estimate the inelastic target roof displacement needed to perform both conventional NSP described in FEMA-356 (2000) and modal pushover analysis, for example, in Chopra and Goel (2002) and Mori et al. (2004). Studies using S_{di}-based PSDA include Luco (2002), and additional studies as illustrated in Chapter 2. All of these procedures require a S_{di} ground motion hazard curve, which in turn requires a S_{di} attenuation relationship.

3.3 OBJECTIVE

The objective of this chapter is to develop the S_{di} ground motion prediction model via a model for the ratio S_{di}/S_{de} for ground motions without forward-directivity effects. This ratio can then be coupled with an existing S_{de} attenuation relationship to "convert" the elastic spectral ordinate into an inelastic one. This S_{di} attenuation model is constructed based on bilinear oscillator responses with a 5% hardening stiffness ratio (α) and 5% (of the critical) damping ratio (ζ). In addition to the natural period, T, one extra structure-specific parameter is needed to generate S_{di} hazard curves, namely the yield displacement d_y of an oscillator which can be estimated from a conventional static pushover analysis of a MDOF structure. Note that many references on finding equivalent SDOF systems exist in the literature: (e.g., Chopra 2001; Collins et al. 1996; Fajfar; FEMA-356 2000; Luco and Cornell 2006; Tothong and Luco 2007).

3.4 NONLINEAR OSCILLATOR RESPONSE BACKGROUND

The inelastic responses of oscillators have been studied for decades (Veletsos and Newmark 1960; Veletsos et al. 1965), and more intensively in the past two decades (including Chopra and

Chintanapakdee 2004; Miranda 2000; Miranda 2001; Miranda and Bertero 1994; Nassar and Krawinkler 1991; Riddell et al. 2002; Sewell 1989; among others). With past work as guidance, our objective is the probability distribution of S_{di} as a function of source, path, and site characteristics (i.e., M_w, R_{rup}, soil type, fault mechanism, etc.) as well as two structural parameters (i.e., T and d_y). To limit the number of structural parameters required to define the hysteretic behavior of an inelastic oscillator, a simple bilinear SDOF system with 5% post-yield stiffness ratio (without strength and stiffness degradation) was chosen. Despite the simplicity of this bilinear system, it can provide improved seismic demand prediction for a broad range of nonlinear structures with properly chosen parameters T and d_y (see Chapter 2, and also Tothong and Luco 2007).

Typically, previous researchers relied on a conventional elastic-perfectly-plastic (α=0) system. We have chosen to use a 5% hardening stiffness ratio because of the well-known differences in the peak responses between elastic-perfectly-plastic and bilinear (α>0) oscillators. Previous work has shown that 0% hardening of an elastic-perfectly-plastic system yields a larger record-to-record variability as well as a more conservative inelastic response, in particular, in the short-period region (Chintanapakdee and Chopra 2003; Chopra and Chintanapakdee 2004; Riddell et al. 2002; Veletsos et al. 1965). According to Chopra and Chintanapakdee (2004), "… ignoring the post-yield stiffness in estimating deformation is too conservative for seismic evaluation of existing structures with known lateral strength in the acceleration-sensitive region." We believe that the bilinear oscillator is better than the elastic-perfectly-plastic system at representing and estimating the inelastic seismic demand of actual MDOF structures; the sequence of plastic hinge formation in MDOF structures does not occur simultaneously, resulting in progressive softening of the lateral stiffness of the structures and more nearly bilinear-like behavior.

For the limiting case in which the period approaches zero for an SDOF system, the difference between S_{di}/S_{de} for the elastic-perfectly-plastic (α=0) case versus the bilinear (α>0) oscillator case is particularly significant even with a slight positive hardening stiffness ratio, α (Chintanapakdee and Chopra 2003; Veletsos et al. 1965). As shown in Equation 3.1, first derived by Chintanapakdee and Chopra (2003), the inelastic displacement ratio for zero period (for a specified R) is equal to infinity in the elastic-perfectly-plastic case and to a finite constant in the bilinear oscillator case.

$$\frac{S_{di}}{S_{de}} = \frac{1}{R} \cdot \left(1 + \frac{R-1}{\alpha}\right) \tag{3.1}$$

Differences are also apparent in the dispersions of S_{di}/S_{de} between elastic-perfectly-plastic and bilinear oscillators. Chopra and Chintanapakdee (2004) showed that this dispersion is infinite for the elastic-perfectly-plastic and zero for the bilinear oscillators as the period T approaches zero. The differences between elastic-perfectly-plastic and bilinear oscillators decrease as the period increases, but are still significant in the period range of structural engineering interest. For the value of the hardening stiffness ratio, α, past studies (Chintanapakdee and Chopra 2003; Nassar and Krawinkler 1991; Ruiz-García and Miranda 2003) showed that S_{di}/S_{de} is insensitive to α in the 3 to 10% range. Therefore, the precise non-zero α value to be used is not critical, at least for periods greater than 0.2 sec.

Past research (Farrow and Kurama 2004; Foutch and Shi 1998) has also shown that, aside from strength reduction, the influence of the hysteretic behavior on the peak responses of nonlinear oscillators and MDOF structures is minimal. Thus, because of its simplicity, the bilinear oscillator is a reasonable choice for a common generic oscillator for S_{di} prediction purposes. To remain consistent with elastic attenuation models, the inelastic displacement ratio developed here is also based on a 5% damping ratio. The inelastic force-displacement behavior of the chosen bilinear oscillator is shown in Figure 3.1.

Next, the dependence of S_{di}/S_{de} on R and T is summarized. This information provides direction when later replacing R by $\hat{R}$. The median (geometric mean) values of S_{di}/S_{de} as a function of R (for *known* S_{de}) for specified periods from a suite of earthquake ground motions are shown in Figure 3.2. The results shown in this figure are based on 291 earthquake records (discussed in the next section).

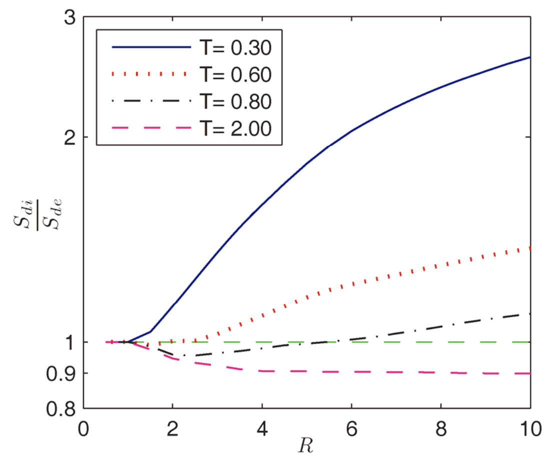

Fig. 3.2 Empirical geometric mean values of inelastic displacement ratio, S_{di}/S_{de}, with 5% post-yield stiffness ratio (with known S_{de}) for short (0.3 sec), moderate (0.6 and 0.8 sec), and long (2.0 sec) periods (based on total dataset).

These results are representative of those found by past researchers cited previously. As shown in Figure 3.2, a central value curve for the moderate-period range ($0.6 \leq T < 1.2$) does not vary monotonically as it does for short ($T < 0.6$) and long ($T \geq 1.2$) periods. Note that for shorter periods, the median ratio increases monotonically as R increases and may reach values of two or greater. For longer periods, within the range $R \leq 8$, the median ratio decreases monotonically but does not fall far below unity. For moderate-period ($0.6 \leq T < 1.2$) oscillators, the median curve does not vary monotonically. Finding a functional form to capture both this non-monotonic behavior for moderate periods and the increasing and decreasing monotonic behavior for short and long periods with relatively few parameters becomes a challenging task. This non-monotonic behavior has also been reported in the software *Static Pushover to Incremental Dynamic Analysis* (Vamvatsikos and Cornell 2002b). However, past research has normally assumed the central value of S_{di}/S_{de} to simply be equal to one in that problematic period range, which may be adequate for the mean, if not for the median. Further, some investigators have identified at least some degree of dependence of the central value of the ratio on magnitude (Ruiz-García and Miranda 2003). We too shall see that the median of S_{di}/S_{de} depends not only on the range of period, but also on M_w, which adds further complexity in the fitting process. This study makes use of the geometric mean in order to remain consistent with standard attenuation models. For very large, perhaps practically unrealistic values of R, such as R>10, there tends to be a saturation effect. Therefore, we limit our predictions to $R \leq 10$.

Figure 3.3 indicates that the dispersion of S_{di}/S_{de} for all periods increases as R (for *known* S_{de}) increases. Although the dispersion of S_{di}/S_{de} increases as the nonlinearity level increases, $\sigma_{\ln S_{di}}$ (for a given M_w and R_{rup}) does not always increase. Curiously, this dispersion decreases slightly (below $\sigma_{\ln S_{de}}$) for values of R between 1.3 and about 2.0 (this reduction in $\sigma_{\ln S_{di}}$ implies a negative correlation between $\ln S_{de}$ and $\ln S_{di}/S_{de}$). Beyond that range it exceeds $\sigma_{\ln S_{de}}$ and grows with R. $\sigma_{\ln S_{di}}$ exceeds $\sigma_{\ln S_{de}}$ by lesser amounts for longer periods.

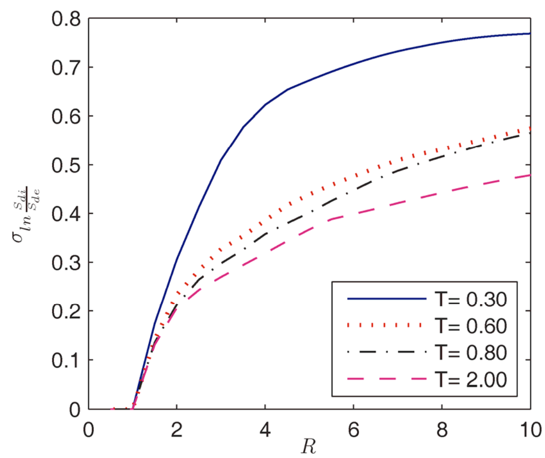

Fig. 3.3 Dispersion of S_{di}/S_{de} (with known S_{de}) for four periods.

3.5 GROUND MOTION RECORDS

The S_{di} attenuation relationship presented here is intended to be used for ordinary earthquake ground motions. The maximum R_{rup} was limited to 95 km to avoid potential effects of (regionally differing) anelastic attenuation on spectral shape, and hence S_{di}/S_{de}, in the regime of less intense ground motions that are unlikely to cause significant inelastic behavior. Near-source ground motions with forward-directivity effects were largely excluded by restricting the closest distance to rupture (R_{rup}) to be greater than 15 km (SEAOC 1999). An S_{di} attenuation model for the near-source environment is under development by the authors. The S_{di} model is expected to be coupled with the anticipated narrowband modification factors for the elastic attenuation relationships to be developed by the Next Generation Attenuation of Ground Motions (NGA) project (2005). Free-field-like ground motions recorded on deep, stiff soil from all faulting styles were used in the analysis. More precisely, from the NGA flatfile (NGA 2005), we used Geomatrix-C1 (Instrument Housing) classes I, A, and B, and Geomatrix-C3 (Geotechnical Subsurface Characteristics) classes C and D. One randomly oriented (i.e., arbitrary) horizontal component was selected. The implications of using one component rather than the geometric mean of both horizontal components are discussed below. The band-pass filter frequencies were selected to be less than 0.25 Hz and greater than 20 Hz, for high- (f_{HP}) and low-pass (f_{LP}) filter frequencies, respectively; thus, the minimum usable low frequency is 0.3125 (=0.25×1.25) Hz, as suggested by Dr. Walter Silva (http://peer.berkeley.edu/smcat/process.html). Therefore, for the total dataset, the longest usable period for *elastic* analysis is approximately 3.2 seconds. As discussed below, we use a restricted dataset ($f_{HP} \leq$ 0.10 Hz; leaving 169 ground motions) for longer periods when fitting the regression model.

Originally, ground motions outside of California were excluded from the development of the model. However, this constraint limits the maximum M_w to 7.3 (i.e., the Landers earthquake), which has an impact when extrapolating the empirical model to larger M_w events. As a result, we later assembled a larger dataset that includes earthquake events outside California, which contains a significant number of large M_w events. Figure 3.4 shows the latter ensemble of ground motions used in this study, which comprises 291 strong earthquake ground motions from 28 historical earthquakes with M_w ranging from 5.65 to 7.90. Table 3.1 shows the earthquake events considered in this study.

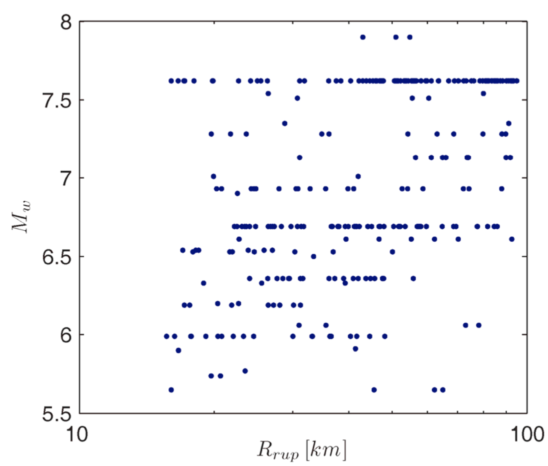

Fig. 3.4 Total ground motion record dataset used in this study.

Table 3.1 Earthquake events considered in this study.

Earthquake ID	Earthquake Name	Date	Time	Earthquake Magnitude (M_w)	Fault Mechanism	No. of Records
0025	Parkfield	28-Jun-1966	04:26	6.19	Strike-Slip	1
0030	San Fernando	09-Feb-1971	14:00	6.61	Reverse	7
0040	Friuli, Italy-01	06-May-1976	20:00	6.50	Reverse	1
0043	Friuli, Italy-02	15-Sep-1976	03:15	5.91	Reverse	1
0046	Tabas, Iran	16-Sep-1978	15:35	7.35	Reverse	2
0048	Coyote Lake	06-Aug-1979	17:05	5.74	Strike-Slip	2
0050	Imperial Valley-06	15-Oct-1979	23:16	6.53	Strike-Slip	7
0064	Victoria, Mexico	09-Jun-1980	03:28	6.33	Strike-Slip	3
0068	Irpinia, Italy-01	23-Nov-1980	19:34	6.90	Normal	1
0069	Irpinia, Italy-02	23-Nov-1980	19:35	6.20	Normal	2
0073	Westmorland	26-Apr-1981	12:09	5.90	Strike-Slip	1
0076	Coalinga-01	02-May-1983	23:42	6.36	Reverse	20
0090	Morgan Hill	24-Apr-1984	21:15	6.19	Strike-Slip	7
0101	N. Palm Springs	08-Jul-1986	09:20	6.06	Reverse/Oblique	4
0102	Chalfant Valley-01	20-Jul-1986	14:29	5.77	Strike-Slip	1
0103	Chalfant Valley-02	21-Jul-1986	14:42	6.19	Strike-Slip	4
0113	Whittier Narrows-01	01-Oct-1987	14:42	5.99	Reverse/Oblique	19
0116	Superstition Hills-02	24-Nov-1987	13:16	6.54	Strike-Slip	6
0118	Loma Prieta	18-Oct-1989	00:05	6.93	Reverse/Oblique	18
0123	Cape Mendocino	25-Apr-1992	18:06	7.01	Reverse	2
0125	Landers	28-Jun-1992	11:58	7.28	Strike-Slip	11
0127	Northridge-01	17-Jan-1994	12:31	6.69	Reverse	55
0136	Kocaeli, Turkey	17-Aug-1999	00:01	7.51	Strike-Slip	3
0137	Chi-Chi, Taiwan	20-Sep-1999	17:47	7.62	Reverse/Oblique	95
0142	St Elias, Alaska	28-Feb-1979	21:27	7.54	Reverse	2
0152	Little Skull Mtn,NV	29-Jun-1992	10:14	5.65	Normal	4
0158	Hector Mine	16-Oct-1999	09:46	7.13	Strike-Slip	9
0169	Denali, Alaska	03-Nov-2002	22:12	7.90	Strike-Slip	3

The full list of the 291 earthquake ground motions can be found in Table A.3. The first, smaller ground motion dataset (180 ground motions from 20 earthquakes) was selected from the Pacific Earthquake Engineering Research (PEER) strong ground motion database as of summer 2003 (Silva 2003). The second, larger dataset (used in the analysis) was selected from the PEER NGA (2005) database. The effect of the larger dataset used here and how it improves large M_w event prediction is discussed in Section 3.11.

3.6 FORMAL MODEL

The objective of our formulation is to develop a prediction model for the inelastic displacement ratio, S_{di}/S_{de}, to be multiplied with an S_{de} attenuation model (Abrahamson and Silva 1997) as follows:

$$S_{di}\left(M_w, R_{rup}, etc.\right) = S_{de}\left(M_w, R_{rup}, etc.\right) \cdot \frac{S_{di}}{S_{de}}\left(M_w, R_{rup}, etc.\right) \tag{3.2}$$

As mentioned earlier, S_{di}/S_{de} will be constructed as a function of the familiar strength-reduction factor, R ($=F_e/F_y = S_{de}/d_y$). R, however, requires knowledge of S_{de}, which is not known *a priori* because it depends on the ground motion of future earthquakes. Hence, we replace the real S_{de} by its *predicted* median value $\hat{S}_{de}$ obtained from an existing elastic ground motion prediction model, yielding the predicted median strength-reduction factor ($\hat{R}$), as shown in Equation 3.3 where $\hat{S}_{de} = 1/\omega^2 \cdot \hat{S}_a$ and $\omega = 2\pi/T$.

$$\hat{R} = \frac{\hat{S}_{de}\left(M_w, R_{rup}, etc.\right)}{d_y} \tag{3.3}$$

Note that although the Abrahamson and Silva (1997) model was used in the quantitative analysis that follows, we believe that the resulting model for S_{di}/S_{de} can be used effectively with any other such modern or future S_{de} attenuation model (in Eq. 3.2 and $\hat{R}$ in Eq. 3.3). The net model for the random predicted value of S_{di} is given by

$$\ln S_{di} = \ln \hat{S}_{de} + \ln \frac{\hat{S}_{di}}{S_{de}}\left(\hat{R}\right) + \varepsilon_{\ln S_{de}} + \varepsilon_{\ln(S_{di}/S_{de})} \tag{3.4}$$

In this equation, where the dependence on ground motion parameters (i.e., M_w, distance, etc.) is suppressed in the notation, the median or predicted value of $\ln S_{di}$ is given by $\ln \hat{S}_{de} + \ln \frac{\hat{S}_{di}}{S_{de}}\left(\hat{R}\right)$, where $\hat{R}$ is $\hat{S}_{de}/d_y$. Both S_{de} and S_{di}/S_{de} have associated random terms $\varepsilon_{\ln S_{de}}$ and $\varepsilon_{\ln(S_{di}/S_{de})}$. The random variables $\varepsilon_{\ln S_{de}}$ and $\varepsilon_{\ln(S_{di}/S_{de})}$ shown in Equation 3.4 have zero means and variances equal to $\sigma^2_{\ln S_{de}}$ and $\sigma^2_{\ln(S_{di}/S_{de})}$, respectively. Note that $\varepsilon_{\ln S_{de}}$ is identical to $\varepsilon_{\ln S_a}$ (i.e., $\varepsilon_{\ln S_{de}} = \ln S_{de} - \ln \hat{S}_{de} = \ln\left(S_a/\omega^2\right) - \ln\left(\hat{S}_a/\omega^2\right) = \varepsilon_{\ln S_a}$).

One implication of using $\hat{S}_{de}$ instead of the real S_{de} is that S_{di}/S_{de} will not necessarily be equal to one when $\hat{R}$ is equal to one or less. This characteristic distinguishes this work from the previously cited studies of S_{di}/S_{de} where the value of S_{de} and hence R were known. In such studies, the ratio always equals one when $R \leq 1$. The effect on S_{di}/S_{de} is discussed in the next section.

3.7 OBSERVED BEHAVIOR OF S_{di}/S_{de} versus $\hat{R}$

The behavior of the inelastic displacement ratio, S_{di}/S_{de}, versus R is, as discussed earlier, well studied (see, e.g., Figs. 3.2–3.3). But the dependence of the ratio on $\hat{R}$ is not. To study this dependence, the following steps were taken.

First, for a given period and accelerogram i, i = 1, 2, …, 291, the value of the predicted median value of $\hat{S}_{de}^{(i)}$ was obtained from the elastic attenuation (i.e., ground motion prediction) model for the magnitude, $M_w^{(i)}$, rupture distance, $R_{rup}^{(i)}$, faulting style$^{(i)}$, site condition$^{(i)}$, and other ground motion parameters associated with the event causing the recorded accelerogram. Next, a set of bilinear oscillators with yield displacements, $d_y^{(i,j)}$, for j = 1, 2, …, n, were established such that n pre-selected values of $\hat{R}^{(j)}$ were obtained, that is $d_y^{(i,j)} = \hat{S}_{de}^{(i)} / \hat{R}^{(j)}$. The $S_{de}^{(i)}$ of each record is known from a linear dynamic analysis. Finally, nonlinear dynamic analyses of all these oscillator and record pairs were carried out, resulting in 291 values of S_{di}/S_{de} for each selected $\hat{R}^{(j)}$ value. The results form a set of "stripes" of ln(S_{di}/S_{de}) values at each $\hat{R}^{(j)}$ value, as shown in Figure 3.5 (for T = 0.6 sec).

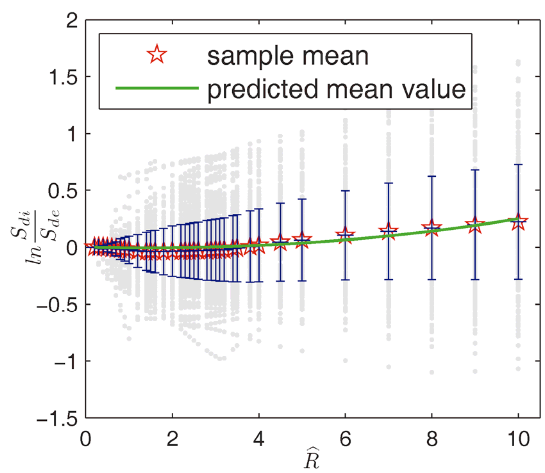

Fig. 3.5 Predicted mean values and ln(S_{di}/S_{de}) data for T = 0.6 sec.

The sample mean and the standard deviation of ln(S_{di}/S_{de}) were calculated for each stripe, as shown. We will discuss these and other results systematically next, but one sees at first glance that the geometric mean and dispersion of S_{di}/S_{de} versus $\hat{R}$ are not qualitatively different from those of S_{di}/S_{de} versus R (Figs. 3.2–3.3) except in one area near $\hat{R} = 1$.

As stated previously the inelastic displacement ratio, S_{di}/S_{de}, does not need to be unity for $\hat{R} \le 1$ (as it is for $R \le 1$) because, owing to the uncertainty in S_{de}, $\hat{S}_{de}/d_y \le 1$ does not imply that $S_{de}/d_y \le 1$. Note that, first, inelastic displacement, S_{di}, can be smaller or greater than elastic displacement, S_{de}, when structures behave inelastically. Second, $\hat{R} \le 1$ implies $\hat{S}_{de} \le d_y$ or, using the more familiar strength concept, $\hat{F}_e \le F_y$ where $\hat{F}_e$ is the predicted median elastic strength required for the oscillator to remain elastic. In reality when $F_y = \hat{F}_e$, about 50% of earthquake records will have its F_e smaller or larger than this $\hat{F}_e$ value. Ground motions with F_e values larger than F_y will cause an oscillator to behave inelastically. For F_e values smaller than F_y, an oscillator will remain elastic. The probability distribution of S_{di}/S_{de} near $\hat{R} = 1$ is, in fact, very unusual but quite understandable (see Fig. 3.6). For illustration, consider the case where $\hat{R}$ is precisely one, implying that $\hat{S}_{de} = d_y$ (or $\hat{F}_e = F_y$). As $\hat{S}_{de}$ ($\hat{F}_e$) is the predicted median value of S_{de} (F_e), we anticipate that about 50% of observed values of S_{de} (F_e) will lie below d_y (F_y), leading to elastic behavior, and S_{di}/S_{de} will equal one. On the other hand about 50% of observed S_{de} (F_e) will lie above d_y (F_y), leading to inelastic behavior, in which case S_{di}/S_{de} may be greater or less than one. Indeed, given the dispersion values of typical attenuation models, which may be 0.6 or larger, the observed values of S_{de} (F_e) may be as high as twice d_y (F_y) or more. The resulting observed histogram and the predicted probability distribution of $\ln(S_{di}/S_{de})$ values for $\hat{R} = 1$ will have, in short, a "spike" of 50% probability mass at zero and 50% of the mass spread over an interval about zero (see Fig. 3.6b). The resulting mean value of $\ln(S_{di}/S_{de})$ may be above or below zero. For values of $\hat{R}$ less than one (larger F_y), we expect a larger fraction of the S_{de} (F_e) values to be less than d_y (F_y) leading to a spike of $\ln(S_{di}/S_{de})$ at zero greater than 50% in value (Fig. 3.6a), and approaching unity as $\hat{R}$ approaches zero. For $\hat{R}$ values greater than unity, the spike will fade to zero (Fig. 3.6c–d). The observed frequency of data points with $\ln(S_{di}/S_{de})=0$ (i.e., linear behavior) is 271, 175, 96, and 48 for $\hat{R} = 0.5, 1.0$, 1.5, and 2.0, respectively, for $T = 0.3$ sec.

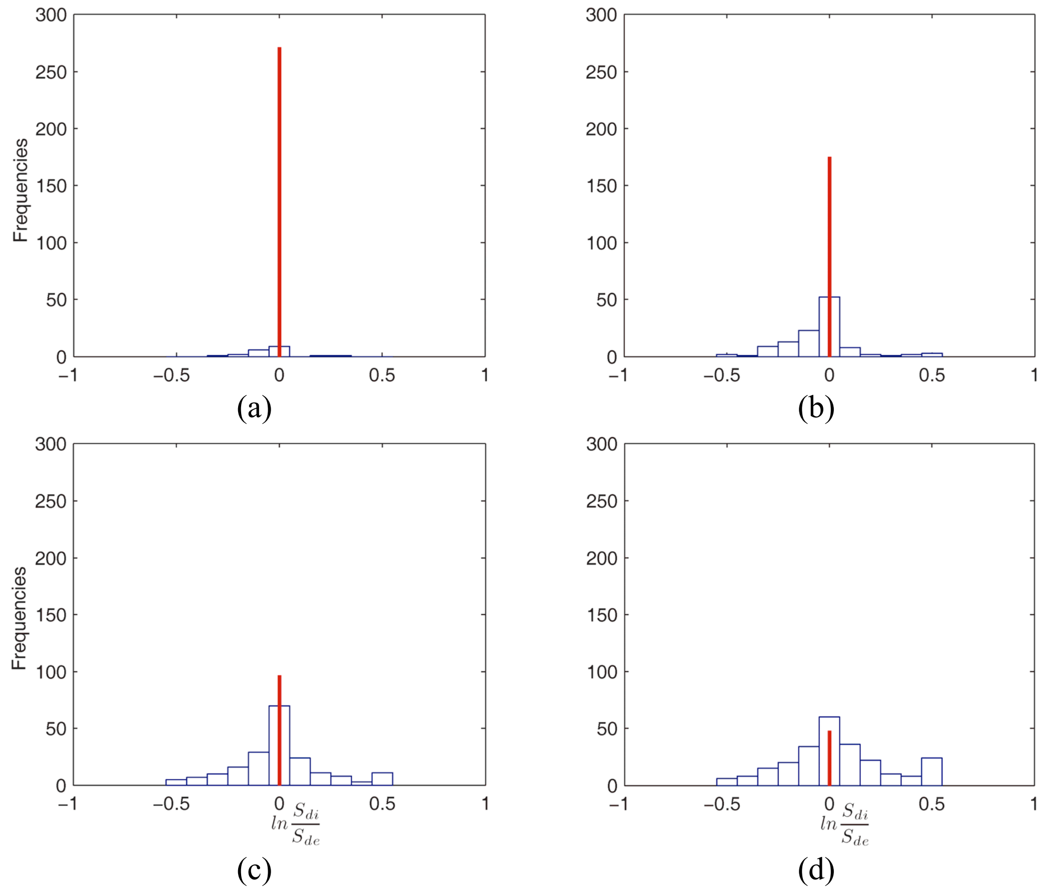

Fig. 3.6 Observed histograms of ln(S_{di}/S_{de}) for (a) $\hat{R} = 0.5$, (b) $\hat{R} = 1.0$, (c) $\hat{R} = 1.5$, and (d) $\hat{R} = 2.0$ for a 0.3 second oscillator. In each plot, solid line represents observed frequencies of ln(S_{di}/S_{de}) when $S_{de}/d_y \leq 1$ (elastic behavior), and histogram bars represent the frequencies of ln(S_{di}/S_{de}) when $S_{de}/d_y > 1$ (inelastic behavior).

This unusual behavior of the sample data and probability distribution of S_{di}/S_{de} are perhaps reasons why it has been difficult and uncommon to study and to model S_{di}/S_{de} as a function of magnitude and distance for the case of fixed d_y (F_y) (rather than fixed ductility, $\propto$, or fixed R for *known* S_{de}). The unique nature of the probability distribution of S_{di}/S_{de} can be largely ignored in what follows, a benefit of modeling the distribution of S_{di} itself, and not that of the ratio. Note here (from Fig. 3.6) that the histogram of ln(S_{di}/S_{de}), especially for $\hat{R} \leq 1$, will predominantly have S_{di}/S_{de} values less than unity for ground motion records with S_{de} (F_e) greater than d_y (F_y). This occurs because these ground motion records are positive ε ground motions, which on average tend to cause comparatively benign inelastic response. After this point, the strength notation (i.e., $\hat{F}_e$, F_e , and F_y) will be omitted for the sake of brevity.

Before turning our attention to the geometric mean of S_{di}/S_{de}, it is worth noting a second, quantitative difference between S_{di}/S_{de} versus $\hat{R}$ (Fig. 3.5) and S_{di}/S_{de} versus R (Figs. 3.2–3.3): the dispersion is substantially larger for the former case, especially for lower values of $\hat{R}$. For example at $\hat{R} = 2$ (Fig. 3.5), the dispersion is about 0.5, whereas at $R = 2$ (Fig. 3.3) the dispersion is less than 0.3. For $R \leq 1$ the dispersion is naturally zero, whereas this is not the case for $\hat{R} \leq 1$. The cause of this larger dispersion is simply the additional uncertainty caused by not knowing S_{de} precisely in the $\hat{R}$ $(= \hat{S}_{de}/d_y)$ case.

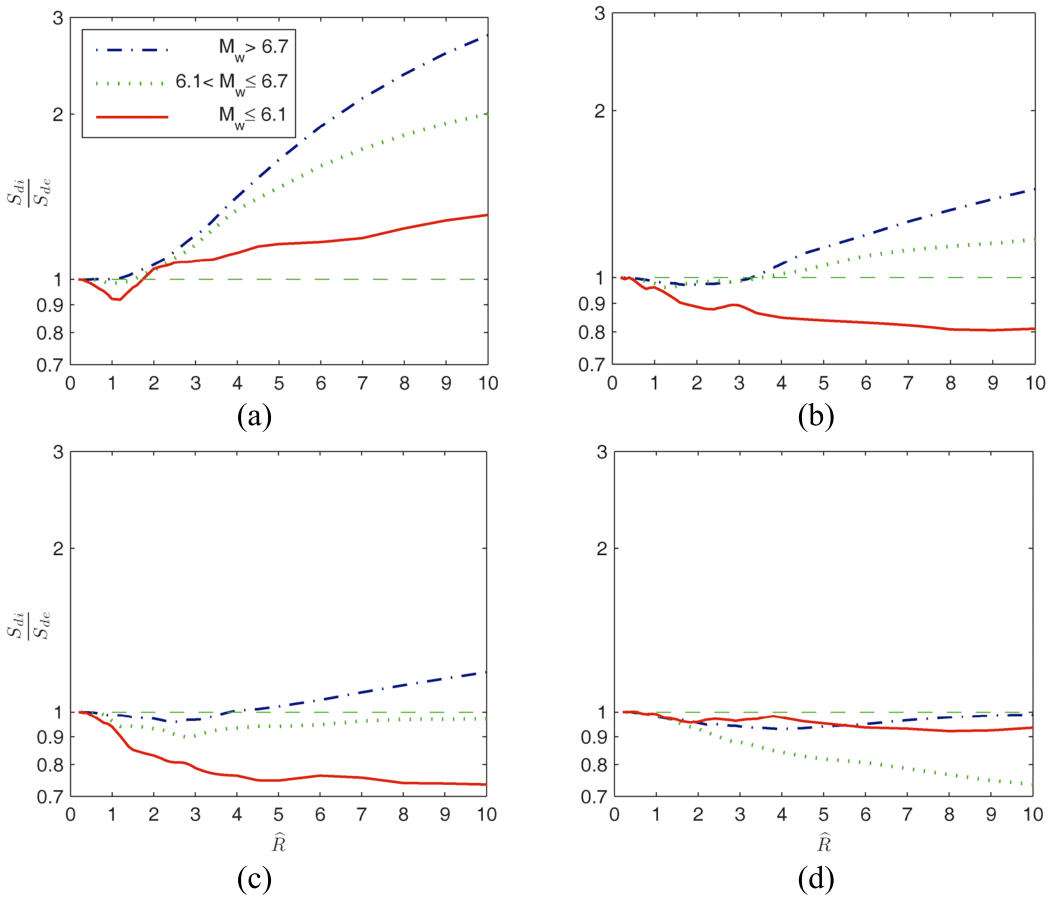

Fig. 3.7 **Geometric mean of inelastic displacement ratio, S_{di}/S_{de}, as a function of $\hat{R}$ grouped into three M_w bins for (a) $T = 0.3$, (b) $\underline{T} = 0.6$, (c) $T = 0.8$, and (d) $T = 2.0$ sec (based on total dataset).**

Fortunately the characteristic of the geometric mean of S_{di}/S_{de} versus $\hat{R}$ is not ill-behaved, although it is no longer expected to be precisely unity for $\hat{R} \leq 1$. We discuss the empirically observed geometric mean of S_{di}/S_{de} versus $\hat{R}$ next and return to the dispersion and probability distribution in a following section. Based on the numerical data, we observed three characteristic behavior patterns of S_{di}/S_{de} versus $\hat{R}$ in three different period ranges discussed subsequently. Further, within each period range, it was observed that S_{di}/S_{de} generally depends on M_w (see Fig. 3.7).

3.7.1 For Short-Period Structures: (0.2 < *T* < 0.6 sec)

For the short-period range, as the level of nonlinearity ($\hat{R}$) increases, the inelastic displacement ratio also increases (see Fig. 3.7a). This "short-period effect" has been attributed to the inability of such oscillators to dissipate energy efficiently (Foutch and Shi 1998). As the nonlinearity increases past a certain value of $\hat{R}$, however, S_{di}/S_{de} stays approximately constant (i.e., there tends to be saturation as $\hat{R}$ increases). The dependence of the geometric mean of S_{di}/S_{de} versus $\hat{R}$ is similar to that anticipated by the observations of this ratio versus R (as discussed earlier).

Within this short-period range, the authors also observed that the geometric mean of S_{di}/S_{de} depends strongly on M_w for values of $\hat{R} > 4$. In Figure 3.7, the geometric mean of S_{di}/S_{de} is plotted for records from three distinct M_w bins. This dependence can likely be explained by the differing slopes of the response spectrum.

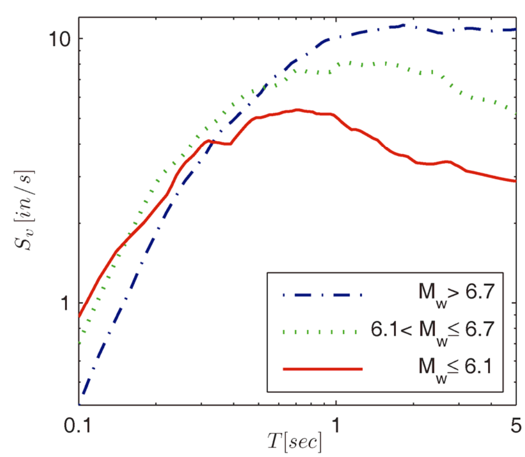

Fig. 3.8 Median elastic response spectra grouped by M_w bins of ensemble ground motions.

As seen from Figure 3.8, the slope of the elastic spectral velocity (S_v) of a large M_w bin is steeper than that for moderate and for small M_w bins. By using the observation that S_{di}/S_{de} depends on the slope of the elastic response spectrum (Kennedy et al. 1984; Sewell 1989), we can anticipate S_{di}/S_{de} to be largest for the large M_w bin and smallest for the small M_w bin (for the same $\hat{R}$ value). Figure 3.7a confirms that S_{di}/S_{de} increases with increasing M_w.

3.7.2 For Moderate-Period Structures: (0.6 ≤ T < 1.2 sec)

We may expect the "equal displacement rule" to apply in this moderate-period range (Veletsos and Newmark 1960). Although this rule is roughly true, more precisely, oscillators in this period range, in general, will first experience "hardening" at a low-nonlinearity level and then "soften" at a higher nonlinearity level, where hardening means $S_{di}<S_{de}$ and softening means $S_{di}>S_{de}$. This is the same non-monotonic dependence of S_{di}/S_{de} on the degree of nonlinearity that we discussed previously. Figure 3.7b–c shows this effect in plots of the geometric mean of S_{di}/S_{de} versus $\hat{R}$. As seen from Figure 3.7b–c, in this period range, S_{di}/S_{de} also depends strongly on the M_w level for $\hat{R}>4$. Response spectrum slopes may again explain this observation. Figure 3.8 shows that the effective slope of the response spectrum (Kennedy et al. 1984) associated with the nonlinear oscillator in this moderate-period range increases with magnitude largely because the corner period (i.e., the period at which the elastic response spectrum changes from the constant spectral acceleration domain to the constant spectral velocity domain) increases with M_w. The assumption of previous studies (e.g., Chopra and Chintanapakdee 2004; Miranda and Bertero 1994; Ruiz-García and Miranda 2003) that S_{di}/S_{de} is independent of M_w oversimplifies the model. Maintaining this M_w dependence is important when a site is dominated by earthquake magnitudes different from the average M_w in the dataset.

3.7.3 For Long-Period Structures: (1.2 ≤ T < 5.0 sec)

In general for a simple long-period bilinear oscillator (with no influence from the global P-delta effect and with no stiffness/strength deterioration), as $\hat{R}$ increases, the geometric mean of S_{di}/S_{de} decreases (see Fig. 3.7d). As $\hat{R}$ increases to a certain value, the geometric mean of S_{di}/S_{de} stays approximately constant (i.e., it experiences "saturation" as $\hat{R}$ increases). This can be explained by the fact that as $\hat{R}$ increases, the "effective" period (roughly speaking $T\sqrt{\propto}$, for which ductility, $\propto = S_{di}/d_y$, and the stiffness of an effective period, K_{eff}, shown in Fig. 3.1) of the structure will elongate and eventually approach a point where $S_{di} = S_{de} =$ peak ground displacement.

For the same reason, in this period range, the spectral slope is less significant when compared with that of short- and moderate-period ranges. Therefore, there is relatively little dependence on M_w.

3.8 EMPIRICAL MODEL FOR GEOMETRIC MEAN OF INELASTIC DISPLACEMENT RATIO

An empirical functional form for each oscillator period has been developed that is designed to be flexible enough to capture the three different behaviors for the three different period ranges presented previously, as well as the spectral slope effect from different magnitudes. The final model was chosen after many trial functional forms, some of which had been used in past research. For example, to estimate the geometric mean of S_{di}/S_{de}, we considered the cubic polynomials, the Gumbel complementary cumulative distribution function (CCDF), power laws, and functional forms developed by Nassar and Krawinkler (1991) and Ruiz-García and Miranda (2003). However, these functional forms do not capture all three different period-range characteristics.

Only the cubic polynomial and the model developed by Nassar and Krawinkler (1991) can capture the hardening effect of bilinear oscillators that we observed in the moderate-period range. However, these general forms do not capture the "fine detail" that can be observed from the empirical data, where oscillators experience first "hardening" and then "softening" behavior as ground motion intensity increases. The final functional form we have developed is robust enough to capture the three characteristic period-range behaviors and the M_w dependencies.

An empirical function for the predicted geometric mean value of S_{di}/S_{de} was developed using a two-stage regression (Joyner and Boore 1982; Sewell 1989). The two-stage approach was used in order to reduce the potential bias due to uneven numbers of ground motion records for each earthquake. In the first stage (for a given M_w event), ridge regression (Hastie et al. 2001) was used with a weighting scheme on $\ln(S_{di}/S_{de})$ for a given structural period. This type of biased estimation effectively reduces the potential correlation between independent variables, whereas the weighting scheme was used to reduce the non-constant variance of $\ln(S_{di}/S_{de})$ versus $\hat{R}$ (see Fig. 3.5). This weighting scheme was necessary to ensure that the homoscedasticity assumption is not severely violated, thus allowing valid conclusions to be drawn from hypothesis testing (Hastie et al. 2001). Using this method in the first stage, the estimated α_j coefficients can be obtained for each $M_{w,j}$ event on $\hat{R}$ and $\hat{R} \cdot \ln \hat{R}$ without including the predictor M_w:

$$\ln \frac{S_{di}}{S_{de}} = \left(\sum_{j=1}^{N_{EQ}} \alpha_j \cdot E_{ij} \right) \cdot \hat{R} + \left(\sum_{j=1}^{N_{EQ}} \alpha'_j \cdot E_{ij} \right) \cdot \hat{R} \cdot \ln\left(\hat{R}\right) + \beta_5 \cdot \hat{R}^{2.5} + \tilde{\varepsilon} \tag{3.5}$$

where $\tilde{\varepsilon}$ is the random error term in the prediction of $\ln(S_{di}/S_{de})$, N_{EQ} is the number of earthquakes in the ensemble database, and E_{ij} is defined as follows:

$$E_{ij} = \begin{cases} 1\ ; if\ record\ i\ is\ from\ earthquake\ j \\ 0\ ; otherwise \end{cases}$$

The power 2.5 on the last predictor in Equation 3.5 was initially determined from nonlinear regression using Levenberg-Marquardt algorithms (Bates and Watts 1988), which combines the steepest descent (at early iterations) and the Newton's method (near the solution point).

In the second stage, all of the estimated α coefficients from the first stage are regressed on M_w to obtain coefficients $\beta_1, \beta_2, \beta_3,$ and β_4 in Equation 3.6:

$$\begin{aligned} \alpha_j &= \beta_1 + \beta_2 \cdot M_{w,j} + \varepsilon';\quad for\ j = 1\ to\ N_{EQ} \\ \alpha'_j &= \beta_3 + \beta_4 \cdot M_{w,j} + \varepsilon'';\quad for\ j = 1\ to\ N_{EQ} \end{aligned} \tag{3.6}$$

where ε' and ε'' are the random error terms. A quadratic form for the second-stage regression was found to be statistically insignificant, so only a linear form was used. Finally, we refit the data using $\beta_1, \beta_2, \beta_3,$ and β_4 from the second stage to obtain a better estimate for β_5 and an estimate for β_6 in Equation 3.7, using weighted regression with the same weighting scheme used in the first stage.

$$\ln \frac{S_{di}}{S_{de}} = \begin{cases} 0 & ;\quad \hat{R} \le 0.2 \\ g_1\left(\hat{R}, M_w\right) + g_2\left(\hat{R}\right) \cdot (M_w - 6.5) - g_1\left(0.2, M_w\right) + \varepsilon_{\ln(S_{di}/S_{de})} & ; 0.2 \le \hat{R} \le 10 \end{cases} \tag{3.7}$$

where

$$g_1\left(\hat{R}, M_w\right) = \left(\beta_1 + \beta_2 \cdot M_w\right) \cdot \hat{R} + \left(\beta_3 + \beta_4 \cdot M_w\right) \cdot \hat{R} \cdot \ln\left(\hat{R}\right) + \beta_5 \cdot \hat{R}^{2.5}$$

$$g_2\left(\hat{R}\right) = \begin{cases} 0 & ;\quad \hat{R} \le 0.3 \\ 0.37 \cdot \beta_6 \cdot \left(\hat{R} - 0.3\right) & ; 0.3 \le \hat{R} \le 3 \\ \beta_6 & ;\quad 3 \le \hat{R} \le 10 \end{cases}$$

The third term, $g_1\left(0.2, M_w\right)$, ensures that the function is zero at $\hat{R} = 0.2$. Note that if $\hat{R}$ is greater than 10, then an $\hat{R}$ value equal to 10 should be used because our results are limited to $\hat{R} \le 10$.

The regression coefficients $(\beta's)$ are given in Table 3.2 for each period value. Interpolation of results for periods not in Table 3.2 can be performed, but extrapolation is not recommended. Preferably, this attenuation relationship should be used only for structures with periods less than *three* seconds because the effective period will lengthen as the system behaves nonlinearly. As a result, the effective period may be greater than the longest usable period for *elastic* analysis (as discussed earlier). Therefore, the regression coefficients for oscillators with $T \geq 1.5$ sec were determined from the ground motion records with $f_{HP} \leq 0.10$ Hz. This is discussed further in the conclusion.

Table 3.2 Regression coefficients for geometric mean value of S_{di}/S_{de} (β_1 through β_6) and standard deviation $\sigma_{\ln Sdi}$ (a, b, and c_1 through c_4).

T (sec)	β_1	β_2	β_3	β_4	β_5	β_6	c_1	c_2	c_3	c_4	a	b
0.30	-0.1037	0.0138	-0.0059	0.0105	-0.0022	-0.074	0.002	-0.010	0.096	-0.077	0.9	3.8
0.40	0.1226	-0.0197	-0.0696	0.0160	-0.0008	0.013	0.008	-0.040	0.095	-0.045	0.7	3.8
0.50	0.0449	-0.0073	-0.0489	0.0106	-0.0007	0.017	0.006	-0.028	0.075	-0.036	0.9	3.0
0.60	0.1116	-0.0211	-0.0953	0.0178	-0.0003	0.037	0.008	-0.040	0.065	-0.010	1.0	2.9
0.70	-0.0759	0.0066	-0.0350	0.0076	-0.0003	0.050	0.007	-0.033	0.059	-0.013	1.8	5.0
0.75	-0.1307	0.0157	-0.0156	0.0038	0	0.030	0.006	-0.030	0.056	-0.012	1.8	4.5
0.80	-0.3233	0.0434	0.0568	-0.0069	0	-0.025	0.009	-0.047	0.048	0.016	1.2	2.0
0.85	-0.3798	0.0504	0.0971	-0.0117	-0.0004	-0.050	0.011	-0.056	0.037	0.035	1.2	1.8
0.90	-0.3791	0.0489	0.0913	-0.0102	-0.0005	-0.050	0.014	-0.072	0.046	0.041	1.2	1.4
1.00	-0.3800	0.0515	0.0660	-0.0084	-0.0005	-0.061	0.013	-0.064	0.073	0.007	1.4	3.4
1.10	-0.3324	0.0444	0.0378	-0.0051	0	-0.050	0.011	-0.056	0.078	-0.008	1.8	5.0
1.25	-0.3582	0.0463	0.0796	-0.0112	0.0006	-0.020	0.012	-0.062	0.039	0.037	1.4	2.0
1.50	-0.4244	0.0561	0.1125	-0.0157	0.0005	0	0.008	-0.040	0.020	0.038	1.0	2.2
2.00	-0.1304	0.0130	-0.0042	0.0009	0.0010	0	0.008	-0.041	0.045	0.014	1.4	3.5
2.50	-0.2275	0.0264	0.0537	-0.0072	0.0009	0	0.008	-0.038	0.053	-0.006	1.6	5.0
3.00	0.0693	-0.0195	-0.0603	0.0120	0.0001	0	0.013	-0.067	0.085	-0.009	1.2	2.0
4.00	*-0.1692*	*0.0161*	*0.0348*	*-0.0038*	*0.0004*	*0*	*0.018*	*-0.088*	*0.091*	*-0.005*	*1.0*	*4.5*
5.00	*-0.4170*	*0.0517*	*0.0788*	*-0.0108*	*0*	*0*	*0.035*	*-0.177*	*0.165*	*0.017*	*0.8*	*5.0*

Originally, $\hat{R}$, M_w, $\ln R_{rup}$, and $M_w \cdot \ln R_{rup}$, were used as predictors. After performing statistical analyses to test for the statistical significance of each variable, we concluded that only $\hat{R}$ and M_w are important in the prediction of $\ln(S_{di}/S_{de})$. This conclusion is intuitive, because S_{di}/S_{de} is expected to depend strongly only on the spectral shape. We anticipate that there will be little influence from a distance parameter on the spectral shape for records with distance less than 95 km. Therefore, even though the distance parameter, R_{rup}, was found to be statistically significant for moderate periods (from 0.8 to 1.5 sec), it was excluded in order to reduce model complexity. For this same reason, parameters such as faulting style have also not been included in the regression model. Note that faulting styles on modern attenuation models can have some effect on changing the spectral shape. Therefore, it may have an influence on S_{di}/S_{de}.

3.9 EMPIRICAL FUNCTIONAL FORM FOR TOTAL STANDARD DEVIATION OF 1nS_{di}

The *total* residual, $\varepsilon_{\ln S_{di}}$, is defined as the sum of the two random variables $\varepsilon_{\ln S_{de}}$ and $\varepsilon_{\ln(S_{di}/S_{de})}$ for a given $\hat{R}$ value and for a given period (Eq. 3.4). Therefore, the correlation between these two random variables is implicitly taken into account. The random variable $\varepsilon_{\ln S_{di}}$ is assumed to have zero mean and variance equal to $\sigma^2_{\ln S_{di}}$. To validate the lognormality assumption for the total residual, $\varepsilon_{\ln S_{di}}$, the standardized residuals (i.e., transformed to have mean zero and unit variance) were plotted on standard normal probability paper (Fig. 3.9), which shows that the lognormal distribution assumption for $\varepsilon_{\ln Sdi}$ is justified.

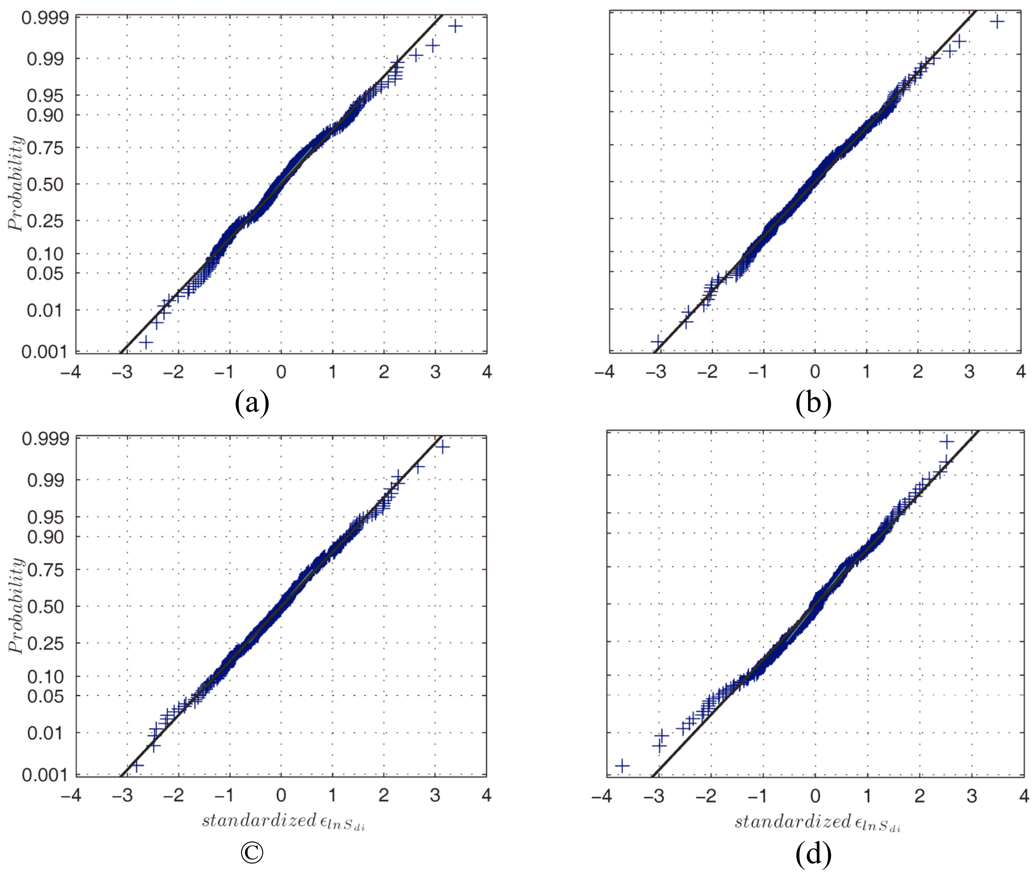

Fig. 3.9 Normal probability plots of standardized $\varepsilon_{\ln S_{di}}$ at $\hat{R}$ = 5 for (a) T = 0.3, (b) T = 0.6, (c) T = 0.8, and (d) T = 2.0 sec.

The linear spline (continuous piecewise linear) functional form (Hastie et al. 2001) is used to model the total standard deviation of ln S_{di}, $\sigma_{\ln S_{di}}$. For simplicity, the shape of $\sigma_{\ln S_{di}}$ (for a given T) with respect to $\hat{R}$ is assumed to be invariant with respect to M_w, while its absolute value still depends on M_w. The $\sigma_{\ln S_{di}}$ is adjusted to match the standard deviation calculated from the elastic attenuation relationship, $\sigma_{\ln S_{de}}$, (at $\hat{R}$ equal to 0.2) to avoid any inconsistency due to the differences in the ground motion datasets used in this study and those used to develop the elastic attenuation relationships. The functional form for the arbitrary component $\sigma_{\ln S_{di}}$ is shown in Equation 3.8:

$$\sigma_{\ln S_{di}} = \begin{cases} \sigma_{\ln S_{de}} & ; \quad \hat{R} \le 0.2 \\ \sigma_{\ln S_{de}} + c_1 + c_2 \cdot \hat{R} + c_3 \cdot \left(\hat{R} - a\right)_+ + c_4 \cdot \left(\hat{R} - b\right)_+ & ; \; 0.2 \le \hat{R} \le 10 \end{cases} \tag{3.8}$$

where $(x)_+$ denotes the "positive part" of x and is defined as

$$(x)_+ = \begin{cases} x; \; x > 0 \\ 0; \; otherwise \end{cases}$$

In Equation 3.8, *a*, *b*, and the $c's$ are regression coefficients.

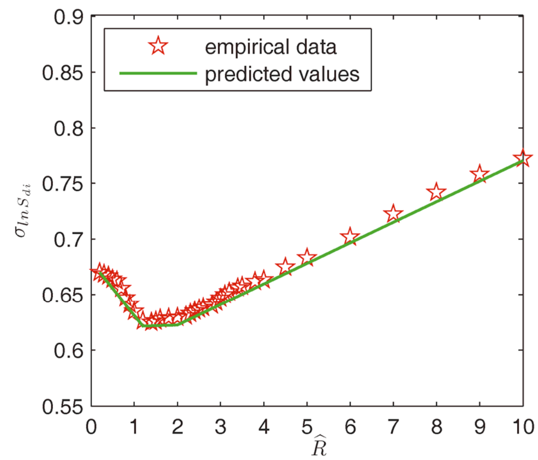

Fig. 3.10 Dispersion of S_{di} and its fitted values for a 0.8 sec oscillator.

For this S_{di} attenuation relationship to be used with other elastic spectral ordinate empirical models (while still providing a smooth transition between elastic and inelastic spectral displacement), Equation 3.8 has been written with an arbitrary $\sigma_{\ln S_{de}}$, and the values of c_1 and c_2 are selected such that the equation is continuous at $\hat{R} = 0.2$. (We presume that most elastic ground motion prediction relationships provide roughly the same median result as that of Abrahamson and Silva (1997), which was used here to compute the S_{de} residuals.) The empirical dispersion of S_{di} and its fitted model (for T = 0.8 sec) are shown in Figure 3.10. The coefficients (*a*, *b*, and $c's$) for the *total* standard deviation, $\sigma_{\ln S_{di}}$, are also provided in Table 3.2.

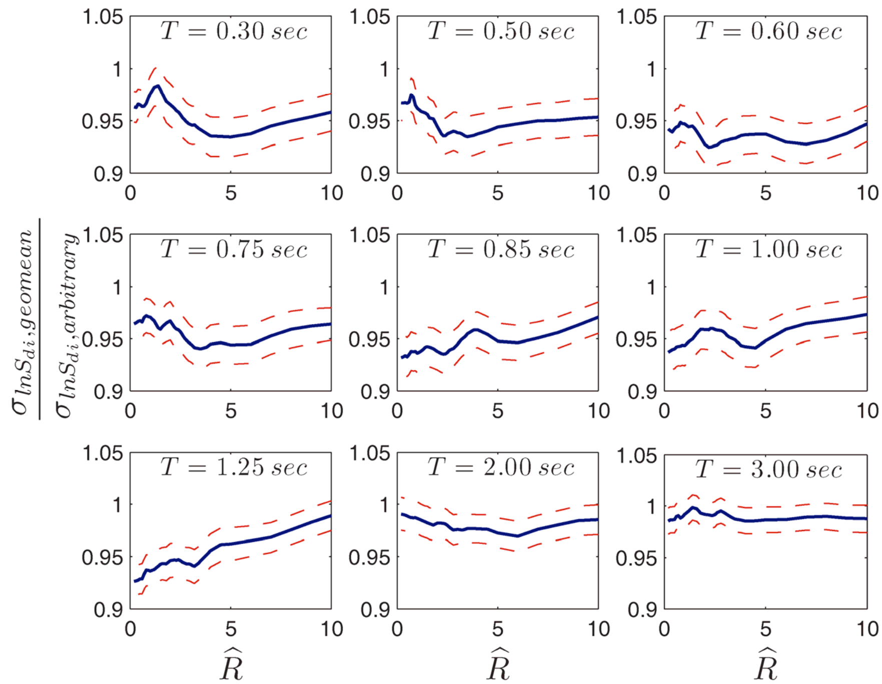

Fig. 3.11 Median ratio of $\sigma_{\ln S_{di}}$ for geometric mean of two horizontal components to $\sigma_{\ln S_{di}}$ for arbitrary component (solid line) and its one standard error bands (dashed lines) estimated from 1000 bootstrap samples (Efron and Tibshirani 1993; based on total dataset).

As stated previously, the ground motion attenuation relationship presented here was developed for a random horizontal component. It can also be used for predicting the geometric mean of the two horizontal components. The median prediction is unchanged. The $\sigma_{\ln S_{di}}$ must be reduced, however. The typical S_{de} dispersion reduction is about 5% (Boore 2005). We have assumed the general form is that of Equation 3.8. The ratio results shown in Figure 3.11 can be used to obtain the standard deviation of the geometric mean. Standard errors of estimation are visually small.

Note that the reduction of $\sigma_{\ln S_{di}}$ is also typically about 5%. To a first approximation, we may simply replace the arbitrary component $\sigma_{\ln S_{de}}$ (in Eq. 3.8) by the geometric mean $\sigma_{\ln S_{de}}$ to obtain the geometric mean $\sigma_{\ln S_{di}}$. To validate this approximation that $\sigma_{\ln S_{di}, geometric\ mean} / \sigma_{\ln S_{di}, arbitrary}$ is not statistically different from $\sigma_{\ln S_{de}, geometric\ mean} / \sigma_{\ln S_{de}, arbitrary}$, the median ratio of $\sigma_{\ln S_{di}, geometric\ mean} / \sigma_{\ln S_{di}, arbitrary}$ is plotted together with its one standard error (16th and 84th percentiles) bands; see Figure 3.11. The two percentiles were estimated from 1000 bootstrap samples (Efron and Tibshirani 1993). As seen from Figure 3.11, $\sigma_{\ln S_{di}, geometric\ mean} / \sigma_{\ln S_{di}, arbitrary}$ is not statistically different from $\sigma_{\ln S_{de},geometric\ mean} / \sigma_{\ln S_{de},arbitrary}$. This implies that we need only input the geometric mean or arbitrary component $\sigma_{\ln S_{de}}$ to obtain the geometric mean or arbitrary component $\sigma_{\ln S_{di}}$, respectively.

3.10 NUMERICAL EXAMPLES FOR S_{di} ATTENUATION MODEL AND S_{di} HAZARD CURVES

Based on the empirical functional forms for lnS_{di}, that is, Equation 3.4, we formed the scenario-based examples for four periods and for M_w ranging from 5.8 to 7.9, shown in Figure 3.12. These figures are based on strike-slip events with the Geomatrix site class C and R_{rup} = 30 km. Note that as M_w increases, $\hat{S}_{de}$ also increases, resulting in increasing ground motion intensity and, ultimately, to nonlinear behavior. The effect of d_y is also shown to contrast with the elastic case.

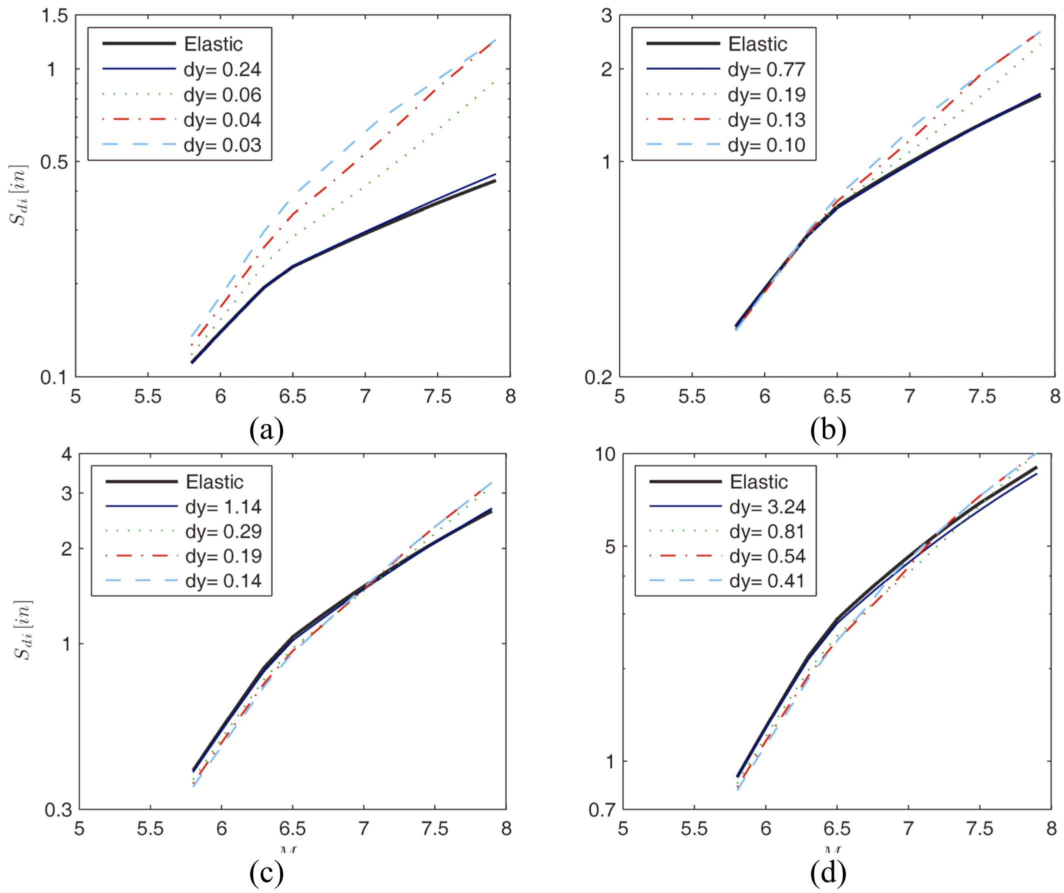

Fig. 3.12 Predicted median values from S_{di} ground motion prediction model for different T and d_y pairs: (a) T = 0.3, (b) T = 0.6, (c) T = 0.8, and (d) T = 2.0 sec (for strike-slip mechanism, R_{rup} = 30 km, and Geomatrix site class C; based on f_{HP} < 0.1 Hz dataset for T > 1.5 sec).

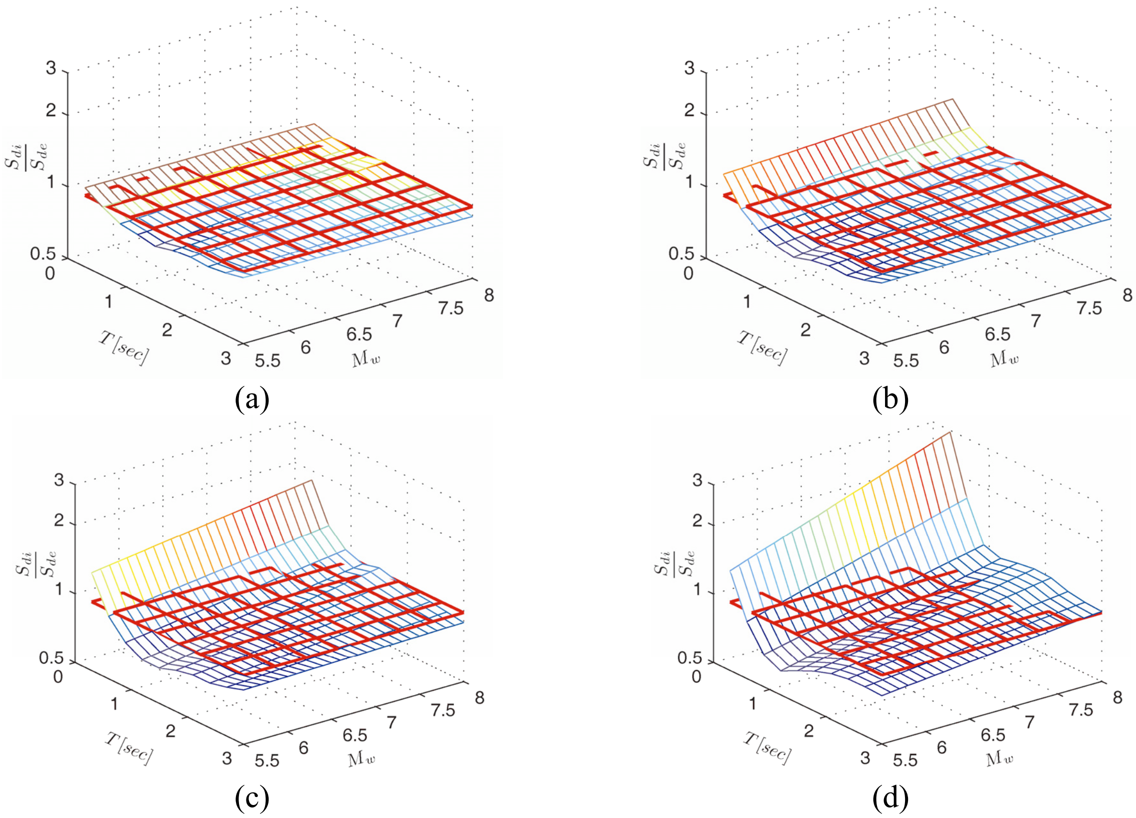

Fig. 3.13 Predicted median values from S_{di}/S_{de} ground motion prediction model for (a) $\hat{R} = 2$, (b) $\hat{R} = 4$, (c) $\hat{R} = 6$, and (d) $\hat{R} = 10$ (based on f_{HP} < 0.1 Hz dataset for T > 1.5 sec).

As explained earlier, the dependence of S_{di}/S_{de} on M_w is stronger for shorter T (for the same $\hat{R}$ value), and the dependence of S_{di}/S_{de} on M_w increases as $\hat{R}$ increases (see Fig. 3.13).

Examples of the S_{di} ground motion hazard curves, computed via conventional PSHA (Cornell 1968; Frankel et al. 1996), for a Stanford University site surrounded by 10 major earthquake faults in the San Francisco Bay Area are illustrated in Figure 3.14 for different combinations of T and d_y values. The differences between elastic and inelastic spectra are, of course, greater for shorter periods and smaller mean annual frequencies of exceedance.

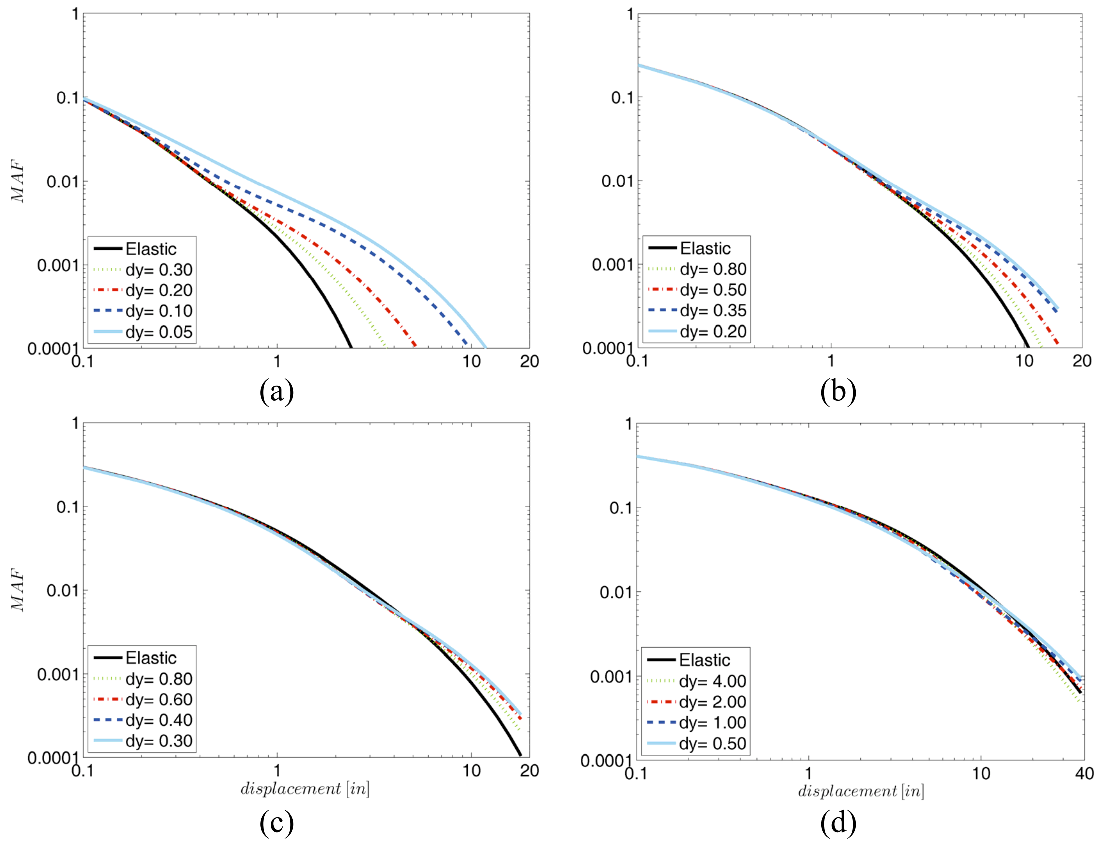

Fig. 3.14 Representative S_{di} ground motion hazard curves for different T and d_y pairs at Stanford University site: (a) $T = 0.3$, (b) $T = 0.6$, (c) $T = 0.8$, and (d) $T = 2.0$ sec. MAF of exceedance versus displacement (based on $f_{HP} < 0.1$ Hz dataset for $T > 1.5$ sec).

3.11 COMMENTS AND CONCLUSIONS FOR S_{di} ATTENUATION MODEL

An inelastic spectral displacement ground motion prediction model ("attenuation relationship") as a function of $\hat{R}$ and M_w was developed for bilinear oscillators ($\alpha = 5\%$ and $\zeta = 5\%$) for specified values of T and d_y, the latter via a proxy $\hat{R}$. The predicted median strength-reduction factor, $\hat{R}$, was introduced because the real S_{de} is not known *a priori* for given ground motion record properties (i.e., M_w, R_{rup}, fault mechanism, soil type, etc.). The S_{di} attenuation relationship developed here can be used to predict the S_{di} probability distribution for free-field, non-near-fault earthquake ground motions on firm soil sites and of distance less than 95 km. In addition, the proposed S_{di} attenuation relationship can also be used to obtain the probability distribution for either the arbitrary or the geometric mean component, provided that one has used the proper

$\sigma_{\ln S_{de}}$ for each case. In addition, we have illustrated that the lognormal assumption for the $\varepsilon_{\ln S_{di}}$ is justified even at a high-nonlinearity level. Our S_{di}/S_{de} study is limited to $\hat{R} \leq 10$.

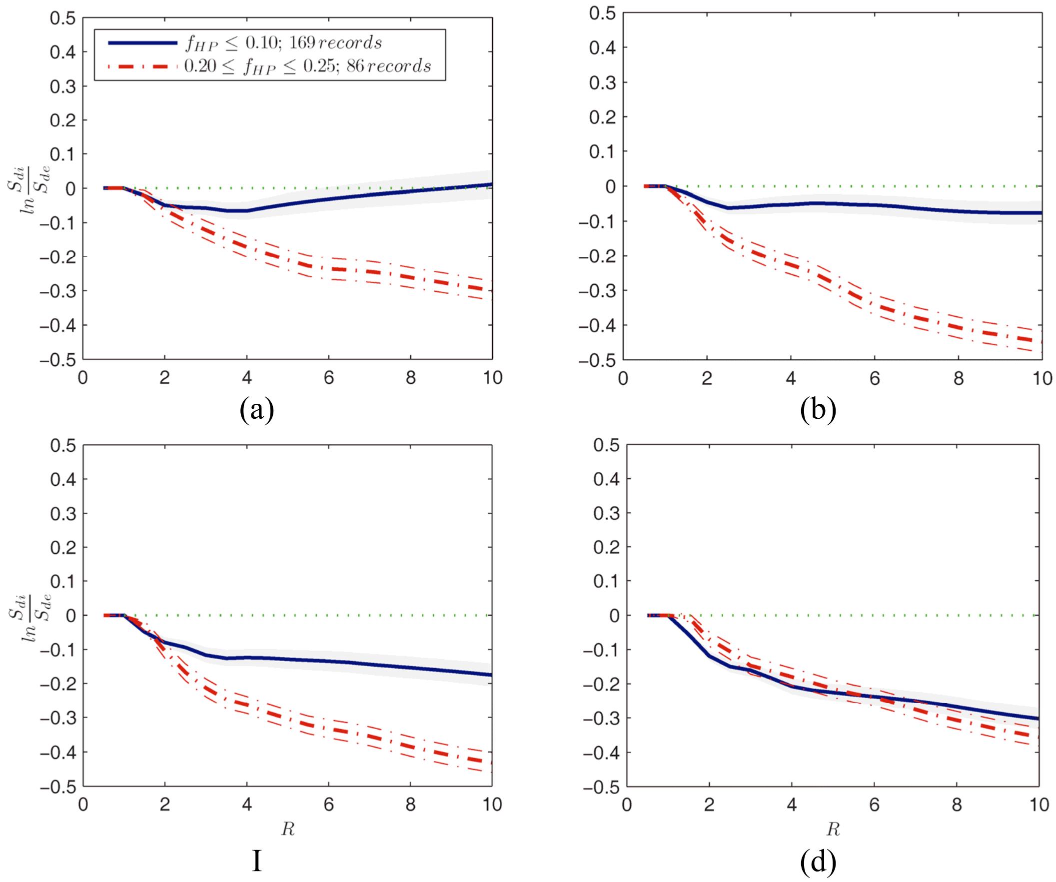

Fig. 3.15 Mean and one standard error bands of ln(S_{di}/S_{de}) as function of R grouped into two f_{HP} bins for (a) T = 2.0, (b) T = 3.0, (c) T = 4.0, and (d) T = 5.0 sec.

The oscillator response data used here are based on the processed accelerograms made available by strong motion seismologists. However, seismologists face a problem in estimating the wave forms of accelerograms at lower frequencies. This is because the raw recorded ground motions need to be filtered to remove noise and correct for instrument bandwidth limitation. This has consequences when estimating the elastic responses of the long-period oscillators (Akkar and Bommer 2006; Bazzurro et al. 2004; Boore and Bommer 2005). For this same reason, it is difficult to obtain a reliable estimate of inelastic response, such as S_{di}. To illustrate this problem, Figure 3.15 shows the mean of ln(S_{di}/S_{de}) for two subsets of 291 records: one with the $f_{HP} \leq 0.1$ Hz and the other with $0.20 < f_{HP} < 0.25$ Hz. The latter record set produces apparently unconservative results for large R values. Therefore, for $T > 1.5$ sec, one note of caution is made when using the model for "effective periods" (loosely speaking $T\sqrt{R}$ for long-period systems) greater than 10 sec (or 8 sec according to Silva's recommendation). Recall, for this period range, we have restricted to records (when fitting the regression model) with $f_{HP} \leq 0.1$ Hz (leaving 169 earthquake records). Once more broadband digitized recordings become available, these models may be more refined. Synthetic ground motions may also help to fill in this lack of low-frequency ground motions. Note that this problem with respect to f_{HP} also occurred when scaling the amplitude of earthquake ground motions. The scaling process is commonly performed in the PEER framework in performance-based earthquake engineering.

The dependence of S_{di}/S_{de} on M_w is significant, in particular, for short-period structures. As a result, assuming no dependence on M_w can lead to a biased estimate of the site S_{di} seismic hazard, especially if the site hazard is dominated by a M_w different from the average M_w in the dataset used in developing the S_{di}/S_{de} model. We assembled a larger ground motion dataset beyond that in the Silva (2003) database, which helped to improve the median prediction for S_{di} for large M_w events. We observed that the difference in the predicted median value for S_{di} from the two datasets for M_w smaller than 7 is negligible (within 3–5%). However, we observed quite different results when predicting the median value of S_{di} for large M_w events, that is, greater than 7. This difference is due to the extrapolation necessary when using a smaller dataset. The smaller dataset, because of its lack of large M_w events, tended to either over- or underestimate the predicted median value for S_{di} by about 20–40% for short and long periods, respectively. It should be pointed out that this observation implies that the functional form is robust with respect to different datasets for small to moderate M_w cases. Note that we have not included the slight dependence of S_{di}/S_{de} on $\ln R_{rup}$. Even though it is mildly statistically significant, it is of negligible practical importance because its corresponding coefficient is relatively small.

As anticipated, the model predicts that short-period oscillators display softening (i.e., $S_{di}/S_{de}>1$). The proposed model can also capture the "hardening" and "softening" behavior of S_{di}/S_{de} observed in the moderate-period range, as well as the "hardening" behaviors for structures with long periods.

Even though this S_{di} ground motion prediction model was developed for bilinear oscillators, it can still be used as an effective intensity measure, *IM*, for the systems that experience severe stiffness and strength degradation, that are near collapse, with "smartly" chosen SDOF parameters based on the procedures described in Chapter 2 and in Tothong and Luco (2007).

The development of the S_{di}/S_{de} empirical model has benefited from prior work done by Kennedy et al. (1984) and Sewell (1989). Their descriptions of how the inelastic displacement ratio, S_{di}/S_{de}, varies from record to record as a function of the slope of the response spectrum guided the model development described earlier. Based on the three-period ranges, we observed that the dependence of S_{di}/S_{de} on M_w becomes less significant for structures with longer periods. As expected, S_{di}/S_{de} for short periods is more influenced by the response spectrum slope (Kennedy et al. 1984; Sewell 1989). For long-period structures, S_{di}/S_{de} falls into the descending branch of the S_v spectrum; however, the spectral slope concept still holds. As can be seen from Figure 3.8, at the two-second period, the S_v slope of the small and moderate M_w bins is steeper (in absolute value) than that of the large M_w bin, resulting in lower S_{di}/S_{de}. The influence of M_w on a structure with a comparatively long period ($T > 2$ sec) is relatively small compared with that for a short-period system. For example, in the case of a two-second period oscillator with $\hat{R} = 4$, the difference in S_{di}/S_{de} for large and moderate M_w is about 10%, whereas it is about 50% for a short period of 0.3 sec (see Fig. 3.7d and Fig. 3.7a, respectively). As a result, even though the M_w parameter is statistically significant for long-period systems, it may not be significant in practice.

This S_{di} ground motion prediction model can be directly and easily implemented in existing PSHA programs. The engineering community will then be able to develop structural demand hazard curves using S_{di} as an *IM* (as opposed to S_{de}), which improves the accuracy of PSDA because the sufficiency assumption is fulfilled (Bazzurro 1998; Jalayer 2003; Luco 2002; Shome 1999; Vamvatsikos 2002). In addition, for deterministic response prediction approaches, once an S_{di} hazard curve is developed, the target displacement required for NSP (FEMA-356 2000) can be directly obtained for a specified site.

For higher-mode sensitive structures, an *IM* that incorporates a higher-mode factor (see Chapter 2; and also Luco and Cornell 2006; Tothong and Luco 2007) is needed. This in turns requires developing new attenuation relations, which will be discussed in the next section.

This chapter can be viewed as a general basis for developing such S_{di} attenuation relationships. A more complex S_{di}/S_{de} model, including other ground motion parameters (e.g., source mechanism, soil type – site shear wave velocity, surface rupture, etc.), could be developed which may reduce the total variation. However, such improvements may be negligible compared with the overall aleatory uncertainties presented in ground motions. Note that the S_{di}/S_{de} model prepared here can be used with current or future S_{de} (or S_a) models that include dependence on such factors. Finally, this model is not recommended for circumstances such as shallow soft soil sites or directivity-induced pulses that introduce a systematic change in the spectral shape.

3.12 APPENDIX: GROUND MOTION ATTENUATION RELATIONSHIP FOR $IM_{1I\&2E}$

For higher-mode-sensitive structures (i.e., tall, long-period buildings), S_{di} is not as efficient and sufficient as it is for first-mode-dominated structures (discussed in Chapter 2; see also Luco 2002; Luco and Cornell 2006), nor is it likely to be as robust with respect to scaling. These shortcomings (i.e., undesirable *IM* properties discussed in Chapter 2) are largely due to the fact that using S_{di} alone does not capture the ground motion frequency content at higher-mode periods. As mentioned in Chapter 2 for high-mode-sensitive structures, S_{di} with higher-mode factor (denoted as $IM_{1I\&2E}$) needs to be utilized (as explained below).

As developed by Luco (2002) and Luco and Cornell (2006) and furthered by Mori et al. (2004) (who approach the problem from a predictor or simplified analysis perspective, rather than an *IM* perspective), the ground motion intensity measure $IM_{1I\&2E}$ is calculated as a function of $S_{di}(T, d_y)$, $S_{de}(T_2)$, and the elastic participation factors of the first two modes of the structure of interest (note that T_2 is typically the second-mode period of the structure), i.e.,

$$IM_{1I\&2E} = S_{di}\left(T, d_y\right) \cdot \sqrt{1 + \left[\frac{PF_2^{[2]} \cdot S_{de}\left(T_2\right)}{PF_1^{[2]} \cdot S_{di}\left(T, d_y\right)}\right]^2} \tag{3.9}$$

where $PF_n^{[2]}$ is the n^{th}-mode *effective* participation factor for interstory drift ratio (i.e., $\Gamma_n \cdot \frac{\phi_{n,i} - \phi_{n,i-1}}{h_i}$) that corresponds to the story of the structure at which $\sqrt{\left[PF_1^{[2]} \cdot S_{di}\left(T, d_y\right)\right]^2 + \left[PF_2^{[2]} \cdot S_{de}\left(T_2\right)\right]^2}$ (which considers two modes) is maximized (for $\theta_{\max}$; Luco 2002; Luco and Cornell 2006). In the expression for $PF_n^{[2]}$, h_i is the height of the i^{th} story (above the i^{th} floor), $\phi_{n,i}$ is the i^{th}-floor element of the n^{th}-mode shape vector, and Γ_n is the n^{th}-mode participation factor, as defined in Chopra (2001). Note that here we have adopted the equation for $IM_{1I\&2E}$ put forth by Mori et al. (2004), which is slightly different than the original equation proposed by Luco (2002) and Luco and Cornell (2006); the latter uses $S_{de}(T_1)$ in the denominator of the square root term, thereby involving three different spectral displacement parameters. In either case, the square-root term serves as a higher-mode modification factor for S_{di}.

Applying a first-order mean-centered Taylor's series expansion of the natural logarithm of Equation 3.9 in conjunction with the existing attenuation relationship for S_{di} (see above and also Tothong and Cornell (2006) and S_{de} (e.g., Abrahamson and Silva 1997)), an attenuation relationship for $\ln IM_{1I\&2E}$ can be developed. This attenuation model can be directly utilized to compute (via PSHA) ground motion hazard curves in terms of $IM_{1I\&2E}$. Recall that an attenuation relationship gives the mean value and variance of the random variable as a function of seismic parameters such as M_w, R_{rup}, faulting styles, etc. The mean value of $\ln IM_{1I\&2E}$ can be estimated by simply evaluating the natural logarithm of Equation 3.9, i.e.,

$$g = \ln IM_{1I\&2E} \cong \ln S_{di}\left(T, d_y\right) + \frac{1}{2} \cdot \ln\left(1 + \left[\frac{PF_2^{[2]} \cdot \exp\left[\ln S_{de}\left(T_2\right)\right]}{PF_1^{[2]} \cdot \exp\left[\ln S_{di}\left(T, d_y\right)\right]}\right]^2\right) \tag{3.10}$$

at the mean values of $\ln S_{di}(T, d_y)$ and $\ln S_{de}(T_2)$. The variance of $\ln IM_{1I\&2E}$ can be estimated as

$$\begin{aligned}\sigma^2_{\ln IM_{1I\&2E}} = & \left[\left(\frac{\partial g}{\partial \ln S_{di}\left(T, d_y\right)}\right) \cdot \sigma_{\ln S_{di}\left(T, d_y\right)}\right]^2 + \left[\left(\frac{\partial g}{\partial \ln S_{de}\left(T_2\right)}\right) \cdot \sigma_{\ln S_{de}\left(T_2\right)}\right]^2 + \ldots \\ & 2 \cdot \rho_{\ln S_{di}\left(T, d_y\right), \ln S_{de}\left(T_2\right)} \cdot \left(\frac{\partial g}{\partial \ln S_{di}\left(T, d_y\right)}\right) \cdot \left(\frac{\partial g}{\partial \ln S_{de}\left(T_2\right)}\right) \cdot \sigma_{\ln S_{di}\left(T, d_y\right)} \cdot \sigma_{\ln S_{de}\left(T_2\right)}\end{aligned} \tag{3.11}$$

where $\dfrac{\partial g}{\partial \ln S_{di}\left(T, d_y\right)} = 1 - \dfrac{b \cdot Y^2}{1 + b \cdot Y^2}$ and $\dfrac{\partial g}{\partial \ln S_{de}\left(T_2\right)} = \dfrac{b \cdot Y^2}{1 + b \cdot Y^2}$, with $b = \left(\dfrac{PF_2^{[2]}}{PF_1^{[2]}}\right)^2$ and $Y = \exp[\ln S_{de}(T_2) - \ln S_{di}(T, d_y)]$ are evaluated at the mean values of the logarithm of the two spectral displacements. The variances $\sigma_{\ln S_{di}\left(T, d_y\right)}$ and $\sigma_{\ln S_{de}\left(T_2\right)}$, like the mean values, are obtained from the attenuation models.

3.12.1 Approximated Correlation Function between $\ln S_{di}$ and $\ln S_{de}$

Strictly speaking, to estimate the variance for $\ln IM_{1I\&2E}$ (i.e., Eq. 3.11), the correlation function between $\ln S_{di}(T, d_y)$ and $\ln S_{de}(T_2)$, $\rho_{\ln S_{di}\left(T, d_y\right), \ln S_{de}\left(T_2\right)}$ needs to be developed. There is not yet an existing correlation model for this pair of random variables. We have, instead, approximated this function by taking advantage of the well-known equal displacement rule (Veletsos and Newmark 1960) for moderate- to long-period structures, which are also the structures for which higher-mode contributions become significant and $IM_{1I\&2E}$ is needed. Assuming then that $S_{di}(T_2, d_y) \cong S_{de}(T_2)$, it implies that $\rho_{\ln S_{di}\left(T, d_y\right), \ln S_{de}\left(T_2\right)}$ is approximated by $\rho_{\ln S_{de}(T), \ln S_{de}\left(T_2\right)}$. Models for

$\rho_{\ln S_{de}(T),\ln S_{de}(T_2)}$ are available (e.g., Baker and Cornell 2006a; Inoue and Cornell 1990). The approximation is confirmed by selected empirical estimates in Figure 3.16. The difference between these two correlations is at most 0.13 for the second-mode period (T_j)—less than about two thirds of the first-mode period (T); as a result, the effect on the total variance (Eq. 3.11) due to this approximation is negligible. These empirical correlation functions are estimated from the 291 ground motion records explained above. Note that in this figure, the correlation function is shown up to T_j = 10 sec. As discussed previously, because the high-pass filter frequency for this database is selected to be less than 0.25 Hz, the spectral ordinates (or $\rho_{\ln S_{de}(T),\ln S_{de}(T_2)}$) for periods longer than 3.25 sec may not be representative.

In general, $\rho_{\ln S_{di}(T,d_y),\ln S_{de}(T_2)}$ is smaller than $\rho_{\ln S_{de}(T),\ln S_{de}(T_2)}$ (for T_j less than T) because once the systems behave inelastically, the effective period for elastic oscillator (T_{eff}) elongates increasing the period ratio (T_{eff}/T_j), hence reducing the correlation values. On the other hand for $T_j>T$, $\rho_{\ln S_{di}(T,d_y),\ln S_{de}(T_2)}$ is larger than $\rho_{\ln S_{de}(T),\ln S_{de}(T_2)}$ presumably because the period ratio of the effective period and T_j (T_{eff}/T_j) will be closer to unity than T/T_j. The result is an asymmetric shape for the correlation function of $\ln S_{di}(T, d_y)$ and $\ln S_{de}(T_2)$. Note that this correlation function of $\ln S_{di}(T, d_y)$ and $\ln S_{de}(T_2)$ can be utilized to develop the conditional *median* (i.e., geometric mean) spectra given a specified level of S_{di} (see Chapter 6, for example).

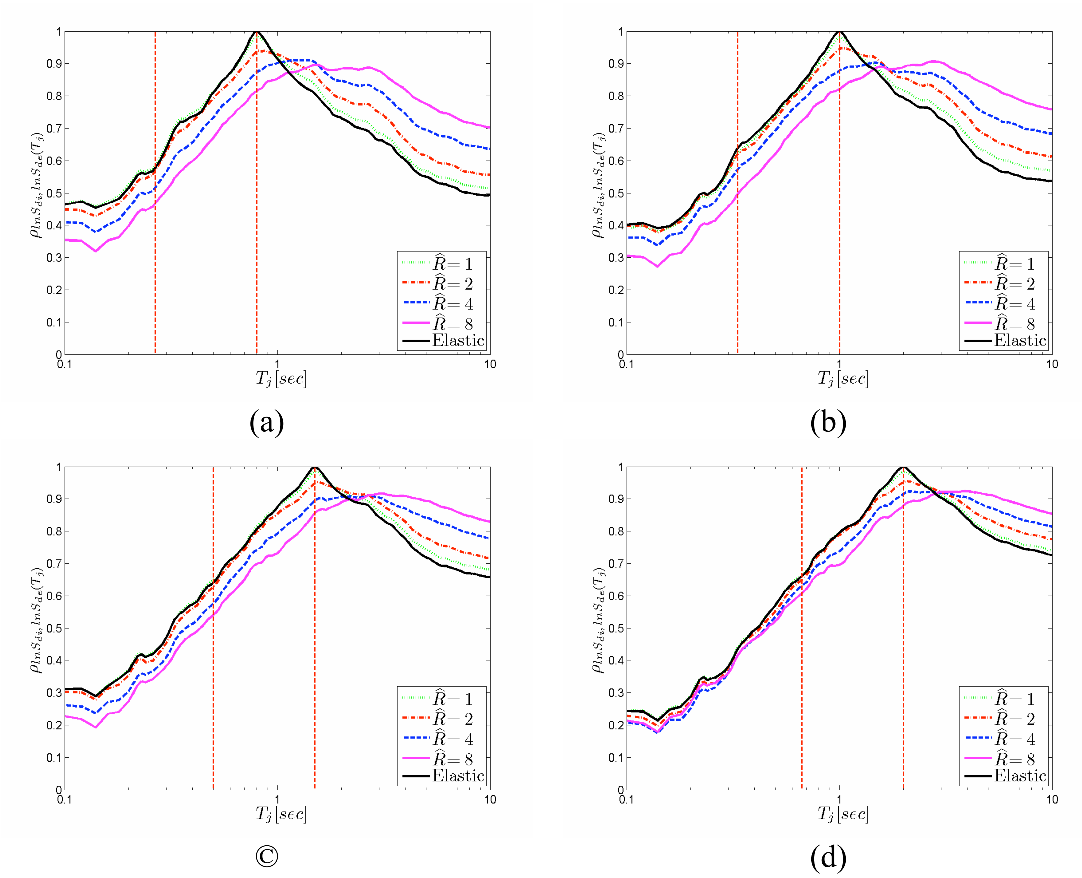

Fig. 3.16 Empirical spectral correlation functions for lnS_{di}(T, d_y) and lnS_{de}(T_j) for T equal to (a) 0.8 sec, (b) 1.0 sec, (c) 1.5 sec, and (d) 2.0 sec. Yield displacement, d_y, is chosen to be same for all 291 ordinary records and associated with *median* S_{de}/d_y of 1, 2, 4, and 8. Correlation functions between lnS_{de}(T) and lnS_{de}(T_j) are also superimposed for comparison (elastic case). Vertical dashed lines represent hypothetical first- and second-mode periods; latter is typically about one-third of first-mode period.

3.12.2 Limiting Cases for Approximated $IM_{1I\&2E}$ Attenuation Relationship

The variance of ln$IM_{1I\&2E}$ (Eq. 3.11) approaches the variance of ln$S_{di}(T, d_y)$ for the first-mode-dominated structures and vice versa for purely second-mode-dominated structures. This can be easily shown by taking the limit of b in Equation 3.11 approaching zero and infinity, respectively. Note that for the statement to follow $[\cdot]\big|_{\tilde{X}}$ implies evaluating $[\cdot]$ at the mean values of $\underline{X}$, where $\underline{X}$ is a vector of random variables.

For first-mode-dominated structures; $b = \left(\frac{PF_2^{[2]}}{PF_1^{[2]}} \right)^2 \to 0$

$$\lim_{b \to 0} \left(\left. \frac{\partial g}{\partial \ln S_{di}} \right|_{\tilde{X}} \right) = \lim_{b \to 0} \left(1 - \left. \frac{b \cdot Y^2}{1 + b \cdot Y^2} \right|_{\tilde{X}} \right) = \lim_{b \to 0} \left(\left. \frac{1}{1 + b \cdot Y^2} \right|_{\tilde{X}} \right) = 1$$

$$\lim_{b \to 0} \left(\left. \frac{\partial g}{\partial \ln S_{de}} \right|_{\tilde{X}} \right) = \lim_{b \to 0} \left(\left. \frac{b \cdot Y^2}{1 + b \cdot Y^2} \right|_{\tilde{X}} \right) = 0$$

$$\therefore \sigma^2_{\ln IM_{1I2E}} = \sigma^2_{\ln S_{di}}$$

For second-mode-dominated structures; $b = \left(\frac{PF_2^{[2]}}{PF_1^{[2]}} \right)^2 \to \infty$

$$\lim_{b \to \infty} \left(\left. \frac{\partial g}{\partial \ln S_{di}} \right|_{\tilde{X}} \right) = \lim_{b \to \infty} \left(1 - \left. \frac{b \cdot Y^2}{1 + b \cdot Y^2} \right|_{\tilde{X}} \right) = \lim_{b \to \infty} \left(\left. \frac{1}{1 + b \cdot Y^2} \right|_{\tilde{X}} \right) = 0$$

$$\lim_{b \to \infty} \left(\left. \frac{\partial g}{\partial \ln S_{de}} \right|_{\tilde{X}} \right) = \lim_{b \to \infty} \left(\left. \frac{b \cdot Y^2}{1 + b \cdot Y^2} \right|_{\tilde{X}} \right) = 1$$

$$\therefore \sigma^2_{\ln IM_{1I2E}} = \sigma^2_{\ln S_{de}(T_2)}$$

It should also be noted here that $\sigma_{\ln IM_{1I\&2E}}$ is *always* smaller or equal to $\sigma_{\ln S_{di}}$. This is because $\sigma_{\ln S_{de}}$ always increases from short- to long-period oscillators (e.g., Abrahamson and Silva 1997). Therefore with a stronger higher-mode contribution, $\sigma_{\ln IM_{1I\&2E}}$ will be smaller than $\sigma_{\ln S_{di}}$. This can be shown as follows.

Given that $\left. \frac{\partial g}{\partial \ln S_{di}} \right|_{\tilde{X}} + \left. \frac{\partial g}{\partial \ln S_{de}} \right|_{\tilde{X}} = 1.0$ and $\left. \frac{\partial g}{\partial \ln S_{di}} \right|_{\tilde{X}} = a$. For short, $\sigma_{\ln S_{de}(T_2)}$, $\sigma_{\ln S_{di}(T, d_y)}$, and $\rho_{\ln S_{di}(T, d_y), \ln S_{de}(T_2)}$ will be simplified as $\sigma_{\ln S_{de}}$, $\sigma_{\ln S_{di}}$, and ρ, respectively. The total variance, $\sigma^2_{\ln IM_{1I2E}}$, can then be written as $a^2 \sigma^2_{\ln S_{di}} + (1-a)^2 \sigma^2_{\ln S_{de}} + 2a(1-a)\rho \sigma_{\ln S_{di}} \sigma_{\ln S_{de}}$. By dividing this equation by $\sigma^2_{\ln S_{di}}$, one can obtain $a^2 + (1-a)^2 \left(\frac{\sigma_{\ln S_{de}}}{\sigma_{\ln S_{di}}} \right)^2 + 2a(1-a)\rho \frac{\sigma_{\ln S_{de}}}{\sigma_{\ln S_{di}}}$. Assuming further that ρ is unity (maximum), the equation can be simplified further as $\left(a + (1-a)\left(\sigma_{\ln S_{de}} / \sigma_{\ln S_{di}} \right) \right)^2$. From the fact that $\sigma_{\ln S_{de}(T_2)} < \sigma_{\ln S_{di}(T, d_y)}$, this factor is always equal to or less than unity implying $\sigma^2_{\ln IM_{1I2E}} \le \sigma^2_{\ln S_{di}}$.

3.12.3 Effect of M_w on $IM_{1I\&2E}$ Attenuation Model

In this section, we demonstrate the effect of M_w (i.e., spectral shape) on the $IM_{1I\&2E}$ attenuation relationship. Three M_w values (i.e., 5, 6, and 8) are chosen to represent three different spectral shapes. Figure 3.17a shows the median spectral shape and the +/- one standard deviation bands for the three M_w scenarios. The source-to-site distance parameters were chosen such that the spectral ordinate at the first-mode period (i.e., 2 sec for this example) is approximately the same for all cases. As expected, smaller M_w has higher spectral ordinates at higher frequencies (implying stronger higher-mode contributions) than those of larger M_w. For example, shown below, the second-mode period is assumed to be one third of the first-mode period. The effective modal shape function for the first-two modes are shown in Figure 3.17b. The total number of stories is 10.

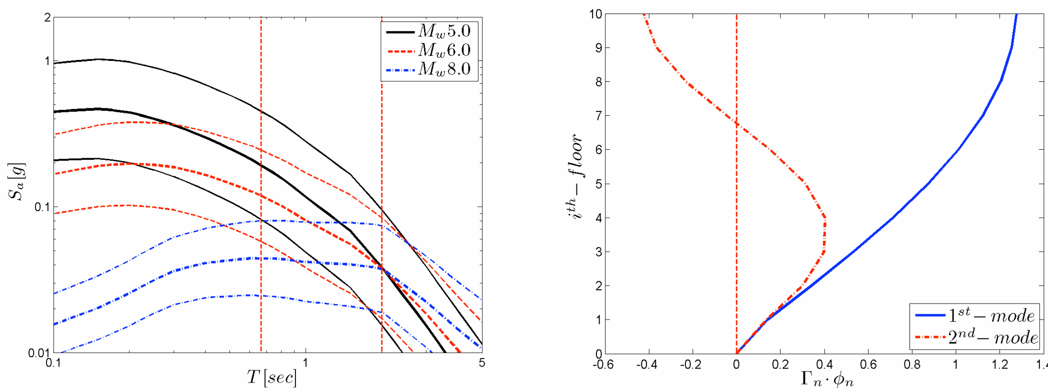

(a) (b)

Fig. 3.17 (a) Median response spectra for three M_w cases along with +/- one standard deviation bands. Vertical dashed lines indicate first- and second-mode periods, i.e., 2.0 and 0.67 sec (for this example). (b) Effective modal shape functions for example structure.

The higher-mode contribution factors (i.e., the second factor in Eq. 3.9) are calculated for the three scenarios. The differences in the mean and the standard deviation ratios (between ln$IM_{1I\&2E}$ and lnS_{di}) are calculated and shown in Figure 3.18.

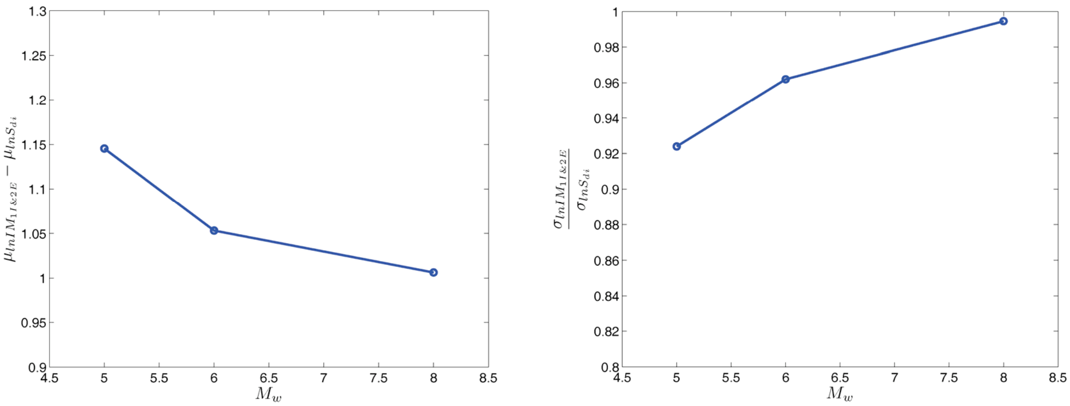

(a) (b)

Fig. 3.18 Influence of M_w (vis-à-vis spectral shape) on $IM_{1I\&2E}$ attenuation model in terms of (a) difference in mean and (b) standard deviation of ln $IM_{1I\&2E}$.

Note that the main contribution to both mean and standard deviation of $\ln IM_{1I\&2E}$ is primarily from the terms associated with the $\ln S_{di}$ itself. The stronger contribution is from the second mode (either from higher $S_{de}(T_2)$ or higher $PF_2^{[2]}$), the higher the deviation from the S_{di} properties. Figure 3.18 shows how much the higher-mode factor due to different M_w values can change the median (i.e., geometric mean) and the dispersion values of S_{di}.

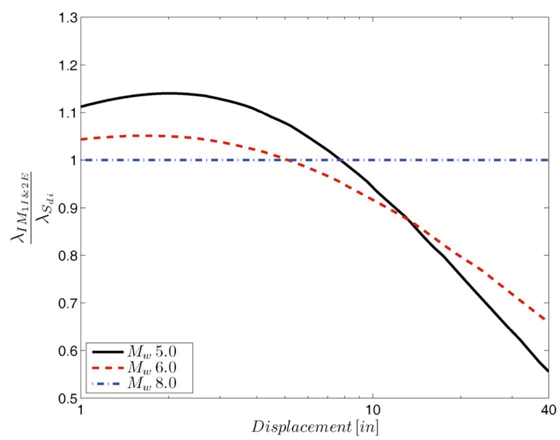

Fig. 3.19 Influence of M_w (vis-à-vis spectral shape) on ground motion hazard curves in terms of $IM_{1I\&2E}$. Results are normalized by normalized hazard for M_w 8.0.

As expected, given the same level of $S_a(T_1)$, small M_w records contribute a stronger effect on the mean and standard deviation of $\ln IM_{1I\&2E}$. For this simple case, the mean value of $\ln IM_{1I\&2E}$ is increased by 15% and the standard deviation is decreased by 10% (for small M_w) relative to the large M_w values. Figure 3.19 shows the influence of M_w on the ground motion hazard curves in terms of $IM_{1I\&2E}$. The plots are normalized with respect to that of large M_w to highlight the effect of spectral shape due to M_w. As seen in the figure, $IM_{1I\&2E}$ can capture the difference in the hazard at a site due to different earthquakes.

4 Explicit Directivity-Pulse Inclusion in Probabilistic Seismic Hazard Analysis

4.1 ABSTRACT

Probabilistic seismic hazard analysis (PSHA) is widely used to estimate the ground motion intensity that should be considered when assessing a structure's performance. Disaggregation of PSHA is often used to identify representative ground motions, in terms of magnitude and distance, for structural analysis. Forward-directivity-induced velocity pulses that may occur in near-fault (or near-source) motions are known to cause relatively severe elastic and inelastic response in structures of certain periods. Here, the principles of PSHA are extended to incorporate the possible occurrence of such a velocity pulse in a near-fault ground motion. For each magnitude and site-source geometry, the probability of occurrence of a pulse is considered along with the probability distribution of the pulse period given that a pulse does occur. A near-source "narrowband" S_a modification to predict ground motion amplitude is utilized which takes advantage of this additional pulse period information. Further, disaggregation results provide the probability that a given level of ground motion intensity is caused by a pulse-like ground motion, as well as the conditional probability distribution of pulse periods associated with that ground motion. These extensions improve the accuracy of PSHA for sites located near faults, as well as provide a rational basis for selecting appropriate near-fault ground motions to be used in the dynamic analyses of a structure.

4.2 INTRODUCTION

In principle, when an earthquake fault ruptures and propagates toward a site at a speed close to the shear wave velocity, the generated waves will arrive at the site at approximately the same time generating a “distinct” velocity pulse in the ground motion time history in the strike-normal direction (Singh 1985; Somerville et al. 1997). This intense velocity pulse usually occurs at the beginning of a record. This is referred to as the forward-directivity effect, which has been known for more than a decade to have the potential to cause severe damage in a structure (for example, Aagaard et al. 2000; Aagaard et al. 2001; Alavi and Krawinkler 2001; Bertero et al. 1978; Hall 1998; Hall and Aagaard 1998; Hall et al. 1995; Iwan 1999; Iwan et al. 2000; MacRae et al. 2001; Singh 1985; Wald and Heaton 1998). The question of how to estimate the ground motion hazard for a site that may experience such a forward-directivity effect is raised because not all observed earthquake ground motions exhibit distinct velocity pulses when they are expected. Thus, probabilistic methods are used to quantify the effects of pulses in any given seismic environment. In the past, only a few available spectral acceleration attenuation relationships that account for the forward-directivity effect have been developed, e.g., Somerville et al. (1997), later modified by Abrahamson (2000). (It should be noted here that later, when we refer to that of Somerville et al. 1997, we actually mean the attenuation model modified by Abrahamson 2000.) However, due to the limited samples of ground motions with distinct velocity pulses, such relationships were developed for a “broadband” rupture-directivity model. This broadband model simply decreases or increases the amplitudes of the spectral ordinates monotonically with respect to increasing period. Further, Somerville et al. (1997) used a data set consisting of both pulse-like records and others, smearing out the effect of the former.

Recent studies (e.g., Alavi and Krawinkler 2001; Baker and Cornell 2005b; Fu 2005; Mavroeidis and Papageorgiou 2003; Somerville 2003; see also Chapter 5) have shown that a ground motion with a distinct velocity pulse tends to cause heightened elastic response only in a narrow period range of structures, namely those with a natural period close to the pulse period (T_p). As a result, it is important to develop a “narrowband” ground motion attenuation relationship, in which only spectral amplitudes around T_p are modified, in order to better characterize this special class of ground motions and its statistical properties. This chapter describes and demonstrates an approach for PSHA that explicitly addresses records with such narrowband characteristics. Records without such pulses are treated separately. The chapter also highlights the information that needs to be developed and modified for this procedure.

This chapter focuses on the pulse effect from forward directivity, and not on the permanent static ground motion displacement (“fling”), which is predicted to occur, for example, in the parallel component of a strike-slip mechanism. In reality, forward directivity and fling are coupled depending on the orientation of the fault and faulting style (Bray and Rodriguez-Marek 2004; Mavroeidis and Papageorgiou 2002).

4.3 GROUND MOTION RECORDS

The pulse-like ground motion recordings used in this study are a collection of the pulse motions identified by Mavroeidis and Papageorgiou (2003), Fu and Menun (2004), and Bazzurro and Luco (2004). The first two pairs of authors visually selected recordings deemed to contain a pulse in the velocity trace. Bazzurro and Luco (2004) selected records whose location relative to the fault rupture suggested that a velocity pulse was likely to occur, rather than directly identifying a velocity pulse in the record. As a result, we visually selected only the subset of their record set which appeared to contain a pulse. The first two author pairs fit a simple wave form with a modulating function to estimate the T_p, while Bazzurro and Luco (2004) used empirical mode decomposition (Loh et al. 2001) to estimate the T_p. The processed records, in the fault-normal direction, were obtained from the Next Generation Attenuation database as of March 2005 (NGA 2006). Ground motion records were selected from both firm soil and rock (based on Geomatrix site classes) for all faulting styles. This pooling of site and faulting sets is justifiable here because we expect that the pulse-like nature of these motions will dominate the spectral shape, and the spectral shape effects induced by other ground motion properties will be less influential.

It should be pointed out that the identification of pulse ground motions is not unique, varying from one researcher to another. In the interest of obtaining a larger sample size, we have included the pulse-like set of any recording that at least one of these authors has identified as such. A total of 70 pulse-like records is contained in the resulting sample. These recordings are listed in Table A.2. These data are used here only to demonstrate the effects of such recordings and the application of the proposed PSHA procedure; the data set here does not affect the procedure per se. More systematic pulse identification methods (Baker 2007) are under development for the purpose of developing numerical estimates of the pulse probabilities and narrowband attenuation relationships necessary for practical implementation of this method.

4.4 BACKGROUND

A near-fault (or near-source) pulse-like ground motion differs from a far-field motion by its "distinct" pulse in the velocity time history. Figure 4.1 shows an example ground motion recording that displays the forward-rupture-directivity effect in the fault-normal direction during the 1992 Landers earthquake.

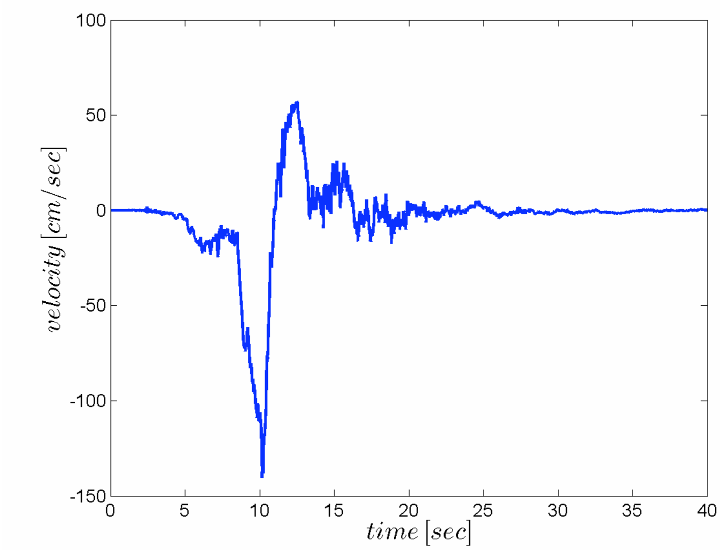

Fig. 4.1 The velocity time history at Lucerne station in the fault-normal direction during the 1992 Landers earthquake, demonstrating forward-rupture-directivity effect.

This velocity record shows a clear low-frequency (long-period) wave form of the pulse. It should be pointed out that estimating the pulse period (T_p) is in itself a challenging problem due to noise present in accelerograms (Mavroeidis and Papageorgiou 2002). Rather than attempt to measure T_p by fitting a function to the velocity time history, we define T_p here as the period at the peak of the response spectral velocity (S_v) with 5% damping ratio. Past research has shown that this T_p value generally provides a good estimate of the period of the primary pulse present in the ground motion velocity time history (e.g., Alavi and Krawinkler 2001; Fu and Menun 2004; Sinan et al. 2005). This estimation procedure ensures a common definition of T_p for the entire record set.

It has been shown that only structures within a narrow range of periods will be affected by a pulse record with a given T_p; thus, it is desirable to incorporate T_p in ground motion studies and structural analyses. It is also meaningful to know the relative value between the period of the structure and the pulse period of the ground motion (Alavi and Krawinkler 2001; Fu 2005;

Mavroeidis et al. 2004). Given this systematic behavior, it should prove valuable to incorporate T_p into PSHA. Including T_p as an extra variable will require some modifications in standard PSHA, as will be explained below.

The pulse-like ground motions were grouped into T_p bins (e.g., $0.25 \le T_p < 0.65$, $0.65 \le T_p < 1.5$, $1.5 \le T_p < 2.5$, $2.5 \le T_p < 3.5$, $3.5 \le T_p < 4.5$) to illustrate the narrowband characteristics. The estimated mean values of T_p ($\bar{T}_p$) in each bin are about 0.4, 1.0, 1.9, 3.1, and 4.0 sec, and the number of records in each bin are 13, 20, 8, 10, and 9, respectively. These periods will be used below to indicate the specific bin used to generate data for plots and numerical examples. Figure 4.2 shows the estimated median (geometric mean) response spectra of the pulse-like motions from two different T_p bins. Also plotted in Figure 4.2 are median predictions of these spectra obtained from ordinary (Abrahamson and Silva 1997) and directivity-adjusted (Somerville et al. 1997) ground motion prediction models. As can be seen from Figure 4.2, the median curves of the response spectra for the narrow T_p bins show peaks at periods around T_p and flatten back downward toward the median values of ordinary records as the periods move away from T_p, exhibiting the so-called narrowband effect. This is a characteristic of forward-rupture-directivity ground motions, as confirmed by observations from recent large earthquakes (Somerville 2003). In contrast, the "broadband" model for these ground motions predicts larger response spectral values at a wide range of periods, rather than just a narrow range around T_p. When comparing the median curves in Figure 4.2 with the predicted median curves using the Somerville broadband model (Somerville et al. 1997), where all periods are monotonically modified, it is clear that there is an important difference. This observation emphasizes that pulse-like ground motions cannot be adequately described by the monotonic broadband scaling.

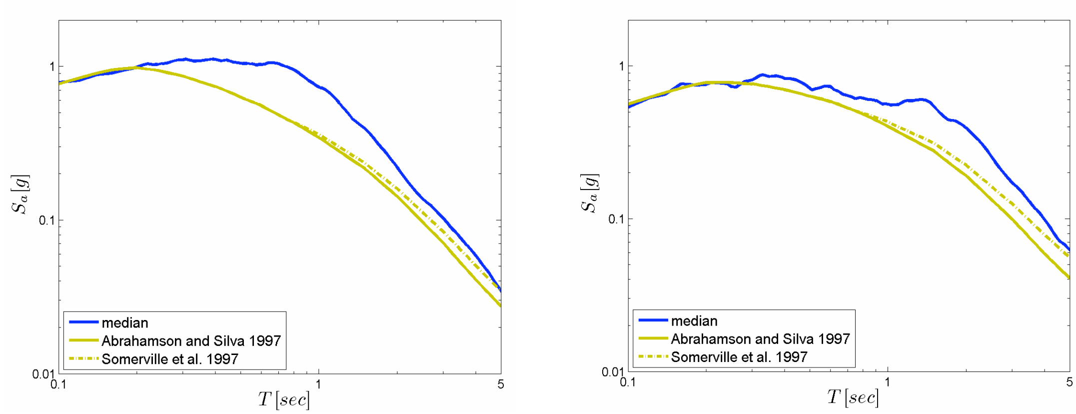

(a) (b)

Fig. 4.2 Empirical median response spectra of pulse-like records along with medians estimated from Abrahamson and Silva (1997) for ordinary records and from Somerville et al. (1997) for forward-directivity effect in fault-normal direction. T_p bins: (a) $\bar{T}_p$ =1.0 and (b) $\bar{T}_p$ =1.9. (Strictly, predicted median curves are median of *n* estimated medians as each record (*i*= 1, …, *n*) has its own earthquake magnitude, source-to-site distance, and median).

To demonstrate the narrowband directivity spectrum, we plotted the median acceleration and velocity spectra of the pulse-like ground motions that have been grouped into T_p bins. Figure 4.3 shows that only spectral periods near T_p are significantly amplified, while spectral periods further away from T_p are amplified less.

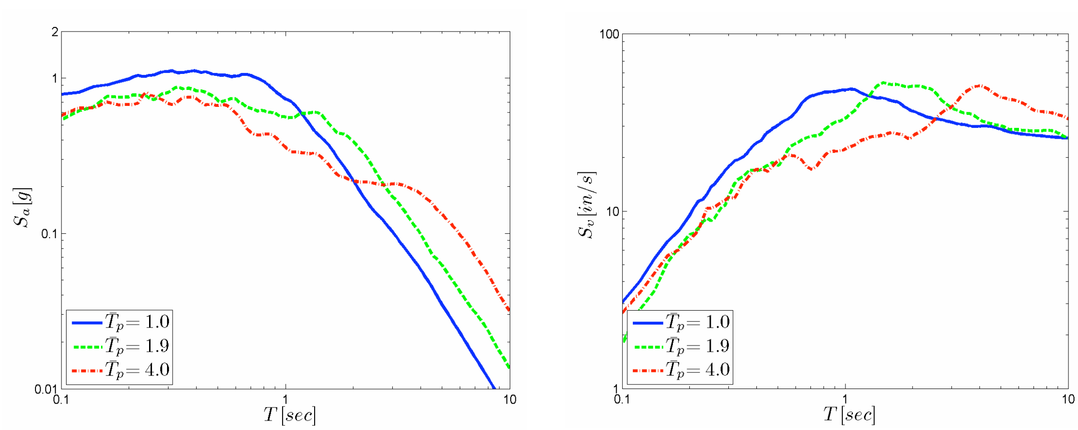

(a) (b)

Fig. 4.3 Median (a) acceleration spectra and (b) velocity spectra of pulse-like ground motions from three T_p bins. For illustration, only three of five bins shown.

Figure 4.4 shows the estimated mean value of the normalized residuals (ε) of the pulse-like data (for four T_p bins) along with its +/- one standard deviation bands calculated using the conventional attenuation relationship (i.e., Abrahamson and Silva 1997 model shown in solid line and shaded area, respectively) and the attenuation model accounting for the forward-directivity effect in the fault-normal component (dotted line; Somerville et al. 1997). Epsilon, ε, is defined as the number of standard deviations that the ground motion deviates from the predicted median attenuation model. The horizontal axis is the normalized period (T/T_p). The large deviation of ε from zero (here about 1.5 at T/T_p near unity) indicates the lack of fit when using a current attenuation model to estimate ground motion amplitudes of the pulse-like motions. The systematic deviation of ε from zero is clear, suggesting that T_p is a good indicator for predicting the spectral ordinates of pulse-like motions.

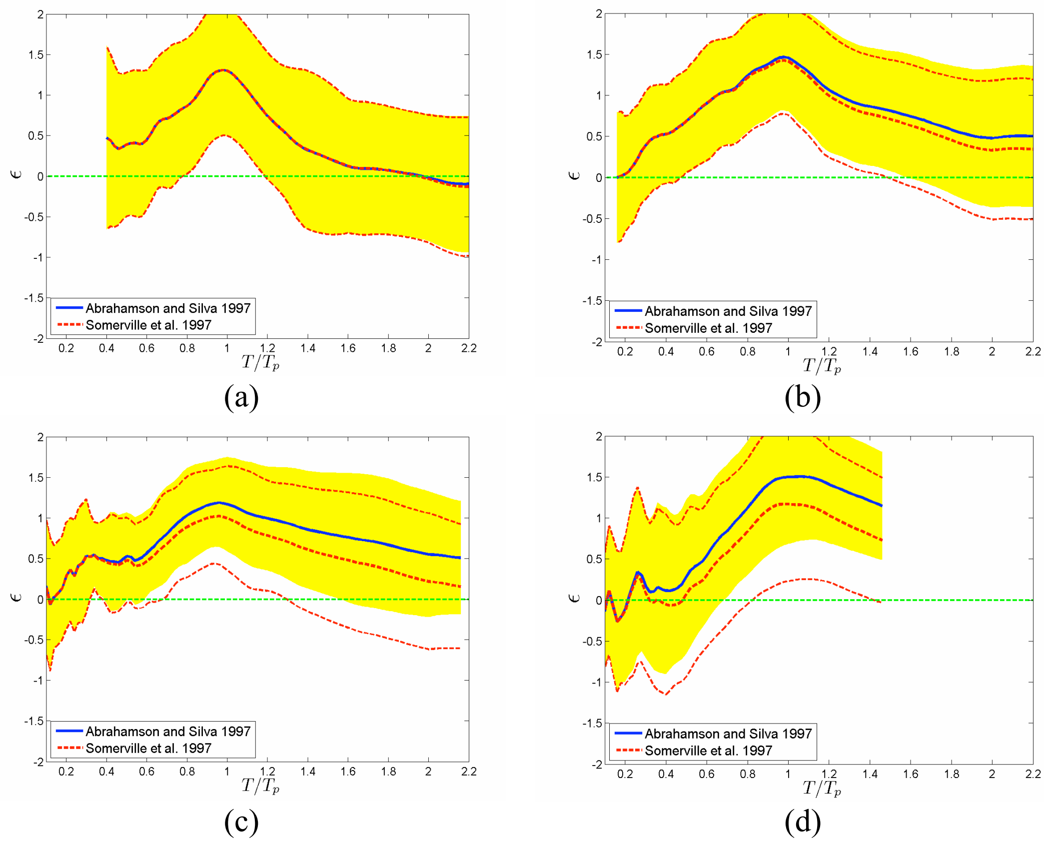

Fig. 4.4 ε values plotted versus T/T_p grouped by T_p bins: (a) $\bar{T}_p$=0.4, (b) $\bar{T}_p$=1.0, (c) $\bar{T}_p$=1.9, and (d) $\bar{T}_p$=3.1. Solid and dotted lines are medians of normalized residuals with respect to Abrahamson and Silva (1997) and Somerville et al. (1997) attenuation models, respectively. Shaded area and thinner dotted lines are +/- one standard deviation bands using Abrahamson and Silva (1997) and Somerville et al. (1997) attenuation models, respectively. Bin with $\bar{T}_p$=4.0 sec is similar.

The mean estimate of the normalized residuals decays to zero as oscillator periods shift away from T_p. It should also be pointed out that ε calculated using Somerville et al. (1997) fails to capture the narrowband effect, as expected. Using Somerville's modification factor simply monotonically shifts the median ε toward zero, while the shape remains virtually unchanged. This figure confirms what is expected from the narrowband effect as pointed out by Somerville (2003). The T_p bin grouping demonstrates that the effect is similar for short-, intermediate-, and long-period pulses.

Figure 4.5 shows the histogram of the epsilon value, ε (cross-section of Fig. 4.4 at a specified T/T_p) using Abrahamson and Silva's model (1997), of both pulse-like and ordinary ground motions. The latter ground motion set was compiled by Tothong and Cornell (2006) (see Table A.3). From Figure 4.5, we notice that pulse-like ground motions tend to have higher positive ε values than the ordinary records. This is because pulse-like ground motions are relatively strong for T/T_p=1.0 as compared to ordinary ground motions.

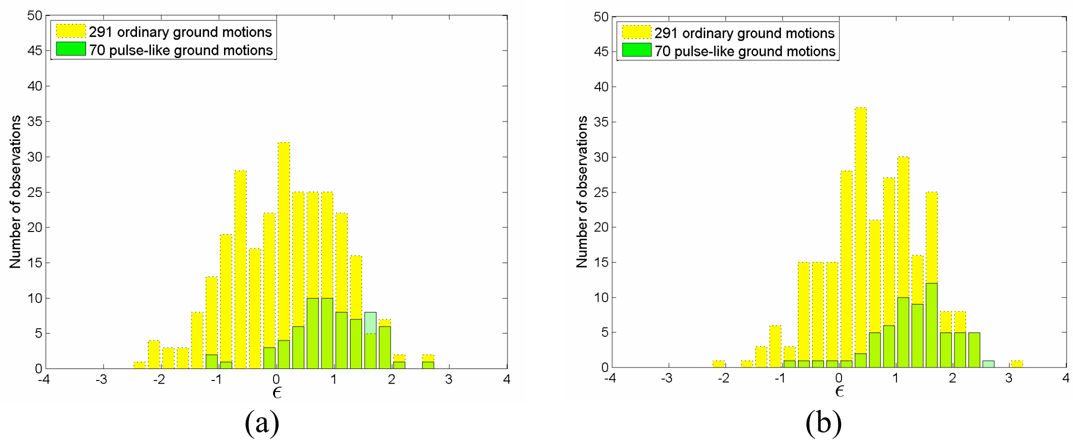

Fig. 4.5 Histogram of epsilon at (a) T/T_p = 0.75 and (b) T/T_p = 1.0 for the pulse-like ground motion data set superimposed with that of ordinary earthquake records.

It should also be pointed out here that among the records typically identified as near-source, based on their proximity to the fault, only a fraction will display a clear-cut identifiable pulse-like behavior. Iervolino and Cornell (2007) find this fraction to depend upon magnitude and geometry but seldom to exceed 30%. Therefore recent statistical studies seeking to identify and quantify this narrowband effect out of the body of all near-source records have proven largely ineffective, i.e., the residuals show no significant T/T_p dependence. The large fraction of non-pulse-like records in the near-source regime, together with the broad scatter in the value of T_p tend to "smear out" and dampen the narrowband effect when looked at this way. In contrast, here we look only at the subset of records pre-identified as being pulse-like, when the effects are clear and quantifiable.

4.5 EFFECT OF PULSE-LIKE GROUND MOTIONS ON NONLINEAR STRUCTURAL RESPONSE

To validate the importance of T_p and the differences between ordinary and near-field pulse-like motions, the inelastic displacement ratio (S_{di}/S_{de}) of nonlinear oscillators for both ground motion sets versus the absolute spectral period, T, are plotted. Interested readers are referred to, for example, Chapter 3 or Tothong and Cornell (2006) for further explanation of S_{di}/S_{de} and its significance. The bilinear oscillator (with 5% hardening stiffness and damping ratio) responses, given by the inelastic spectral displacement (S_{di}) normalized by its elastic spectral value (S_{de}) at the same initial elastic period, are plotted in Figure 4.6 for a strength-reduction factor equal to four.

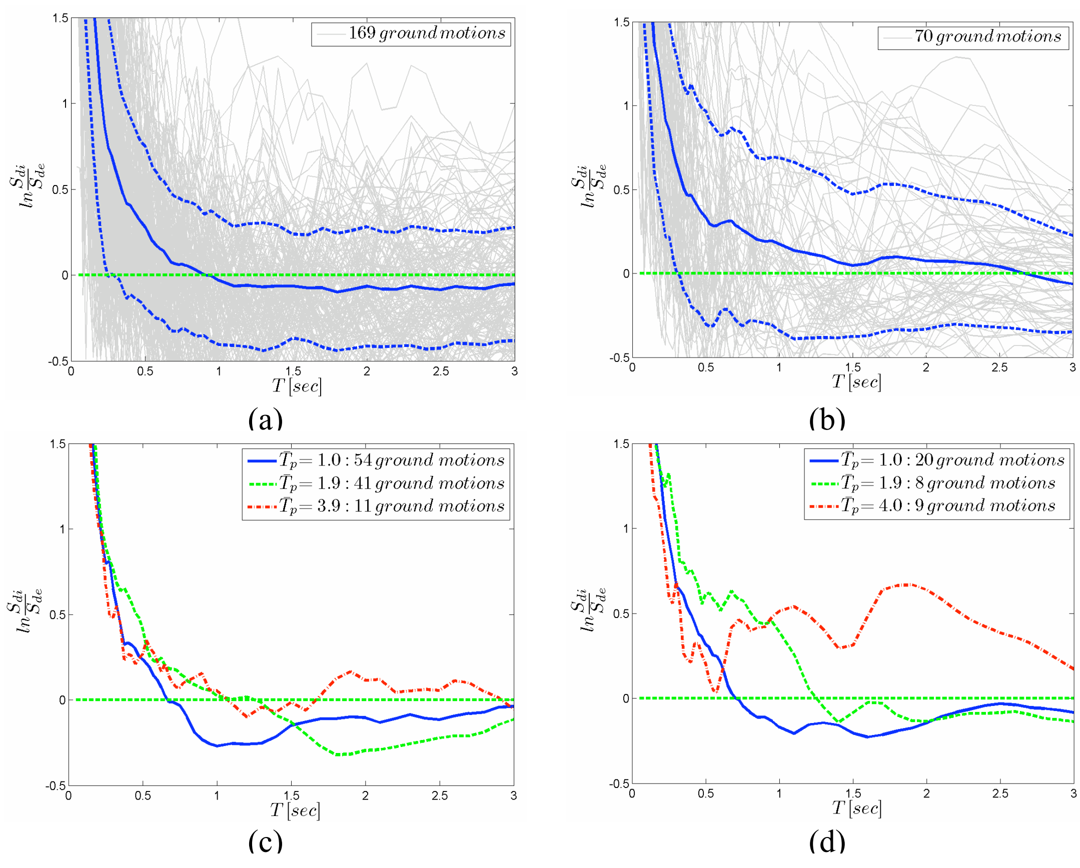

Fig. 4.6 ln(S_{di}/S_{de}) with strength-reduction factor equal to 4 for (a) 169 ordinary ground motions, (b) 70 pulse-like ground motions, (c) mean values of ordinary ground motions grouped by T_p, and (d) mean values of pulse-like ground motions grouped by T_p.

For inelastic responses, T/T_p=0.5 (i.e., a T_p that is twice as long as the elastic period of an oscillator) seems to be the most damaging case because the effectively elongated period drifts toward the peaks of the pulse period, T_p (e.g., Alavi and Krawinkler 2001; Fu 2005; Mavroeidis et al. 2004; Chapter 5). For the ordinary ground motion set, only ground motions with high-pass filter frequency less than or equal to 0.10 Hz are used to plot S_{di}/S_{de} shown in Figure 4.6. In doing so, records with weak signals at long periods are removed, reducing the number of records from 291 to 169 accelerograms.

Figure 4.6a and b shows S_{di}/S_{de} for the ordinary and pulse-like ground motions, respectively. It is clear that the estimated mean (solid lines) and +/- one standard deviation (dotted lines) of $\ln(S_{di}/S_{de})$ of the pulse-like data set is higher for periods that range from 0.5 to 3.0 sec, resulting in a broadband-like modification factor. $\ln(\cdot)$ denotes the natural logarithm of $(\cdot)$ throughout. But Figure 4.6d (for three T_p bins) demonstrates that S_{di}/S_{de} of a near-fault ground motion at a given period can be more precisely predicted if T_p is known. For example, for an oscillator with T = 2 sec, the estimated mean value of $\ln(S_{di}/S_{de})$ is approximately 0.1 for the broadband model (Fig. 4.6b), while it is approximately -0.2 for T_p = 1 or 2 sec and approximately 0.7 for T_p = 4 sec (Fig. 4.6d). As shown in Figure 4.6c, knowing T_p for ordinary ground motions does not significantly help improve the characterization of the inelastic responses of nonlinear oscillators, so it is not useful to identify T_p for non-pulse-like motions (Recall that T_p, the period at the peak of S_v, is defined for even non-pulse-like records).

Another example to illustrate the benefit of considering T_p in characterizing pulse-like, but not ordinary, ground motions is shown in Figure 4.7. The solid lines represent the correlation between $\ln S_a$ at two periods when considering all records. The dotted lines represent the correlation between $\ln S_a$ at two periods (T_1= 2 sec and T_2 versus T_2) for ground motions with T_p values between 3.5 and 4.5 sec. For ordinary ground motions (Fig. 4.7a), we observe that the correlation function does not change whether using all ground motions or only ground motions with T_p close to 4 seconds. As seen in Figure 4.7b, however, the correlation of $\ln S_a$ for all pulse-like ground motions may differ dramatically from the correlation when using ground motions grouped by T_p bin. The correlation function between $\ln S_a$ at two periods can be used to develop the vector-valued PSHA (Bazzurro and Cornell 2002) for the near-fault environment in order to couple with the vector intensity measure (Shome 1999) to improve the probabilistic response prediction of structures.

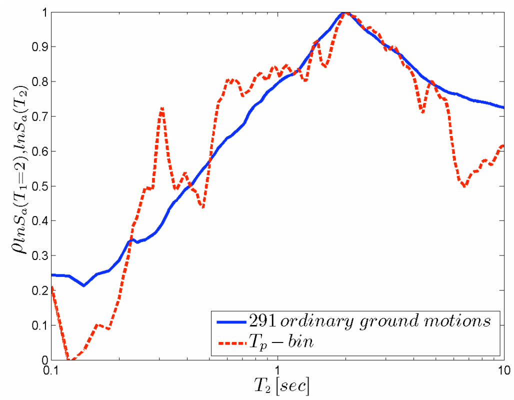

(a)

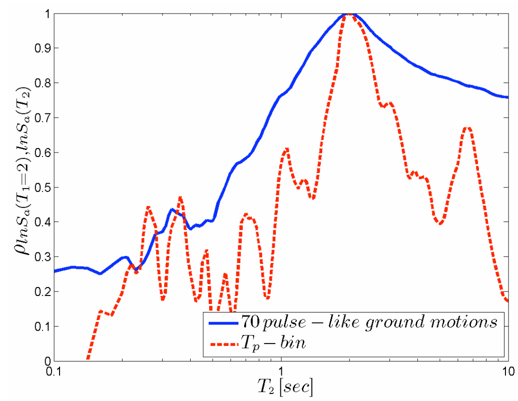

(b)

Fig. 4.7 Correlation of spectral acceleration between two spectral periods, T_1= 2 sec and T_2 versus T_2, when using records with T_p values between 3.5 to 4.5 seconds: (a) ordinary ground motions and (b) pulse-like ground motions.

4.6 PSHA METHOD

4.6.1 PSHA Considering Near-Source Effects

Given the above results that indicate differences between near-source and ordinary ground motions, it would be desirable to modify the PSHA to incorporate these effects in a hazard analysis. In order to clarify the effort needed and to outline the differences for the pulse-like PSHA with the conventional PSHA (Cornell 1968; Frankel et al. 1996; Reiter 1990), we start with the following equation, which underlies the current standard approach for computing the mean annual frequency (MAF, $\lambda_{S_a}(x)$) of exceeding a ground motion parameter, e.g., elastic-pseudo-spectral acceleration (S_a) exceeding an intensity level x:

$$\lambda_{S_a}(x) = \sum_{i=1}^{\#faults} \nu_i \int_{m_w, r_{rup}} \left(G_{S_a|M_w^i, R_{rup}^i}\left(x \mid m_w, r_{rup}\right)\right) \cdot f_{M_w^i, R_{rup}^i}\left(m_w, r_{rup}\right) \cdot dm_w \cdot dr_{rup} \tag{4.1}$$

where ν_i is the mean rate of occurrence of earthquakes on fault i above a minimum threshold magnitude. Uppercase denotes random variables, and lowercase indicates realizations of those random variables throughout this chapter. M_W is the moment magnitude and R_{rup} is the closest distance from the site to the rupture plane. $f_{M_w^i, R_{rup}^i}\left(m_w, r_{rup}\right)$ is the joint probability density function (PDF) of M_w and R_{rup} on fault i. G_{S_a} is the Gaussian complementary cumulative distribution function (CCDF) of the lognormally distributed random variable S_a, which is defined as

$$G_{S_a|M_w^i,R_{rup}^i}\left(x \mid m_w, r_{rup}\right) = 1 - \Phi\left(\frac{\ln x - \propto_{\ln S_a|m_w,r_{rup}}}{\sigma_{\ln S_a|m_w,r_{rup}}}\right) \tag{4.2}$$

where $\Phi(\cdot)$ is the standard Gaussian CDF, and $\propto_{\ln S_a|m_w,r_{rup}}$ and $\sigma_{\ln S_a|m_w,r_{rup}}$ are the conditional mean and standard deviation of the natural logarithm of S_a, as obtained from a ground motion attenuation model (e.g., Abrahamson and Silva 1997).

Building upon the above standard implementation of PSHA, it is now necessary to make several modifications to incorporate the effect of near-fault directivity. As in Somerville et al. (1997), we introduce a directivity parameter (X (or S)·cosθ), where $X = S/L$; S is the projected distance (along the rupture plane) from the epicenter toward the site; L is the fault rupture length; and θ is the azimuth angle between the fault rupture plane and the direction between the epicenter location and the site (Somerville et al. 1997). A similar definition is also available for the non-strike-slip case. In current near-source PSHA software, the location of the hypocenter is treated as random, inducing a distribution on S·cosθ and requiring in effect an additional level of integration. Below for notational simplicity, we denote S·cosθ as Z. In addition, we now propose to condition the prediction of S_a on T_p, and then to integrate over the distribution of possible T_p realizations. In addition, we chose to narrow our attention to pulse-like records because, as we have seen above, they impact linear and nonlinear structural response in predictable ways. Ultimately, this additional integration implies the need to develop an empirical relationship for the likelihood of observing a pulse-like ground motion given ground motion record properties, e.g., M_w, distance, directivity parameters, faulting styles, etc. (P[*pulse*| M_w, *distance*, *directivity parameters*, etc.]). This piece of information is currently under development by Iervolino and Cornell (2007). Once all of the pieces of information have been established, we can incorporate the near-source pulse-like effect into the PSHA using the following equation:

$$\lambda_{S_a}(x) = \lambda_{S_a,non-NS}(x) + \lambda_{S_a,NS}(x) \tag{4.3}$$

where $\lambda_{S_a,non-NS}$ is simply that shown in Equation 4.1 for distance greater than (approximately) 20 km. The MAF of S_a for the near-source case ($\lambda_{S_a,NS}$) is given as follows, where $\lambda_{S_a,NS}$ is separated into two parts: the near-source hazard from the narrowband pulse-like ground motion events ($\lambda_{S_a,NS\&pulse}$), and the near-source hazard due to non-pulse-like records ($\lambda_{S_a,NS\&no\,pulse}$).

For a given fault within R_{rup} < 20 km,

$$\lambda_{S_a,NS}(x) = \lambda_{S_a,NS\&pulse}(x) + \lambda_{S_a,NS\&no\,pulse}(x) \tag{4.4}$$

in which (assuming for simplicity only a single fault):

$$\lambda_{S_a,NS\,\&\,pulse}(x) = \int\limits_{m_w,r_{rup}} \int\limits_{z} P\left(pulse \mid m_w, r_{rup}, z\right) \cdot$$
$$\int\limits_{t_p} G_{S_a|pulse,M_w,R_{rup},Z,T_p}\left(x \mid m_w, r_{rup}, z, t_p\right) \cdot \tag{4.5}$$
$$f_{T_p|Z,M_w,R_{rup}} \cdot f_{Z|M_w,R_{rup}} \cdot dt_p \cdot dz \cdot \left|d\lambda_{M_w,R_{rup}}\left(m_w, r_{rup}\right)\right|$$

$$\lambda_{S_a,NS\,\&\,no\ pulse}(x) = \int\limits_{m_w,r_{rup}} \int\limits_{s\cdot\cos\theta} G_{S_a|M_w,R_{rup},No\ Pulse}\left(x \mid m_w, r_{rup}\right) \cdot$$
$$\left(1 - P\left(pulse \mid m_w, r_{rup}, z\right)\right) \cdot \tag{4.6}$$
$$f_{Z|M_w,R_{rup}} \cdot dz \cdot \left|d\lambda_{M_w,R_{rup}}\left(r_{rup}, m_w\right)\right|$$

Note that $\int\limits_{m_w,r_{rup}} [\square] \cdot \left|d\lambda_{M_w,R_{rup}}\left(m_w, r_{rup}\right)\right| = \nu \cdot \int\limits_{m_w} \int\limits_{r_{rup}} [\square] \cdot f_{M_w,R_{rup}} \cdot dm_w \cdot dr_{rup}$, where $\left|d\lambda_{M_w,R_{rup}}\left(r_{rup}, m_w\right)\right|$ is the absolute value of the joint mean rate of occurrence of events with (loosely speaking) $M_w = m_w$ and $R_{rup} = r_{rup}$ on this near-by fault. dt_p and dz are the integration intervals of the realization values of variable T_p and Z (= $S\cdot\cos\theta$), respectively. $G_{S_a|pulse,M_w,R_{rup},Z,T_p}$ is the Gaussian CCDF of S_a conditioned on M_w, R_{rup}, Z, and T_p (or T/T_p), where T is the period of the oscillator. This narrowband S_a attenuation model is under development by NGA (e.g., Youngs and Chiou 2006). f_{M_w,R_{rup},Z,T_p} is the joint PDF of M_w, R_{rup}, Z, and T_p. Similarly, $f_{M_w,R_{rup},Z}$ is the joint PDF of M_w, R_{rup}, and Z. Using the definition of conditional probability, the joint distribution f_{M_w,R_{rup},Z,T_p} in Equation 4.5 can be broken down as $f_{T_p|M_w,R_{rup},Z} \cdot f_{Z|M_w,R_{rup}} \cdot f_{M_w,R_{rup}}$. However, T_p was shown to depend only on M_w (as cited above); therefore the function $f_{T_p|M_w,R_{rup},Z}$ is reduced to simply $f_{T_p|M_w}$.

To compute $\lambda_{S_a,NS\,\&\,no\ pulse}(x)$ in Equation 4.4, it may be possible to use the same attenuation relationships (for the ordinary ground motions) for R_{rup} < 20 km and $R_{rup} \geq$ 20 km, but this must be confirmed as these R_{rup} < 20 km non-pulse-like motions are likely to have smaller median and standard deviation values than the current S_a attenuation models because they exclude the ground motions within 20 km with the severe pulse-like motions. Youngs and Chiou (2006) are also investigating this issue.

For a fault with $R_{rup} \geq$ 20 km, the conventional PSHA (shown in Eq. 4.1) can be used to compute $\lambda_{S_a,non-NS}(x)$ because large amplitude pulse-like ground motions, while not impossible are not likely there. In effect, we carry out the above three PSHAs—namely $\lambda_{S_a,non-NS}(x), \lambda_{S_a,NS\,\&\,pulse}(x)$, and $\lambda_{S_a,NS\,\&\,no\,pulse}(x)$—and sum them to obtain the site-specific ground motion hazard.

4.6.2 PSHA Disaggregation

In addition to the hazard curves considered above, another common calculation in PSHA is disaggregation (Bazzurro and Cornell 1999; McGuire 1995). Typically, this calculation is used to compute the distribution of magnitudes, distances, and epsilon values contributing to occurrence or exceedance of some ground motion intensity level. In this section, disaggregation equations are developed to also provide the probability that a ground motion intensity level is caused by a pulse-like ground motion, and to provide the distribution of pulse periods associated with those ground motions. This disaggregation is important to structural engineers because it provides a rational basis for selecting representative ground motions (near-fault and non-near-source) to be used in dynamic analyses of a structure.

To compute the probability that a ground motion with S_a *equaling* x is caused by a pulse-like ground motion, the following application of Bayes' theorem can be used.

$$P[pulse \mid S_a = x] = \frac{\Delta\lambda_{S_a,NS\,\&\,pulse}(x)}{\Delta\lambda_{S_a}(x)} \tag{4.7}$$

where $\Delta\lambda_{S_a}(x) = \lambda_{S_a}(x) - \lambda_{S_a}(x + \Delta x)$ and Δx is a small increment of S_a.

Once the probability of experiencing pulse-like motions is known ($P[pulse \mid S_a]$), it would be helpful to know the distribution of associated pulse periods because (as mentioned above) the pulse period will affect the resulting structural responses. The following equation can be used to obtain the PDF of T_p conditioned on S_a equaling x and experiencing pulse motions.

$$\begin{aligned} f_{T_p|S_a=x,pulse} &\propto \frac{P\left[T_p = t_p, S_a = x, pulse\right]}{P\left[S_a = x, pulse\right]} \\ &= \Big\{ \int_{m_w,r_{rup}} \int_z \Delta G_{S_a|M_w,R_{rup},Z,T_p}\left(x \mid m_w, r_{rup}, z, t_p\right) \cdot P\left[pulse \mid m_w, r_{rup}, z\right] \cdot \\ &\qquad f_{T_p|M_w,R_{rup},Z} \cdot f_{Z|M_w,R_{rup}} \cdot dz \cdot \left|d\lambda_{M_w,Rrup}\left(m_w, r_{rup}\right)\right| \Big\} \Big/ \Delta\lambda_{S_a,NS\,\&\,pulse}(x) \end{aligned} \tag{4.8}$$

where $\Delta G_{S_a|\bullet}(x \mid \bullet) = G_{S_a|\bullet}(x \mid \bullet) - G_{S_a|\bullet}(x + \Delta x \mid \bullet)$.

4.7 EXAMPLE

We demonstrate the proposed PSHA framework and the potential effects of near-source effects by considering two hypothetical seismic cases, a firm soil site located R_{rup}= 3 km from a strike-slip fault that produces only characteristic M_w 6.0 events, and another separate example in which the site is 14 km from a fault that produces only M_w 7.5 events. The mean annual rate of the characteristic earthquakes for both cases is assumed to be unity. In both cases, the site location projected onto the fault rupture plane is assumed to be in the middle of the fault. To incorporate directivity parameters, we assume that the epicenter location follows a uniform distribution along the fault. The fault lengths are 8 and 100 kilometers. For non-pulse-like records, we used the Abrahamson and Silva (1997) attenuation relationship. For pulse-like ground motions, a narrowband modification function was estimated from data shown in Figure 4.4. The Harversed sine function was used to fit the normalized residuals by increasing the median value (for $0.5 \leq T/T_p \leq 1.5$); the dispersion was assumed to remain unchanged. The empirical model used to estimate $f_{T_p|M_w}$ follows a lognormal distribution, which is similar to the one shown in Somerville (2003). The estimated median values of T_p ($\hat{T}_p$) for the M_w 6.0 and 7.5 events are 0.7 and 4.7 sec, respectively. The standard deviation of $\ln T_p$ given M_w ($\sigma_{\ln T_p|M_w}$) is 0.7 in both cases. To approximate a continuous distribution, the realizations of T_p are varied from 0.1 to 15 sec using small 0.1 second intervals. Finally, the probability of a pulse occurring at the site given an event that, as used here, was based on early exploratory analyses by Iervolino and Cornell (2007), who found empirically that $P[pulse|\ M_w,\ R_{rup},\ S,\ \theta]= 1/(1+ \exp(-(\ b_0 + b_1 \cdot R_{rup} + b_2 \cdot S + b_3 \cdot \theta + b_4 \cdot (R_{rup} \times \theta) + b_5 \cdot (S \times \theta))))$, with b_0= -4.589, b_1= -3.914, b_2= 4.046, b_3= -4.923, b_4= -2.883, b_5= 4.190.

4.7.1 Uniform Hazard Spectra (UHS)

The target MAF of exceeding S_a is chosen to be 1% in 100 years. The UHS of the two cases are shown in Figure 4.8. The thick solid line represents the UHS using Abrahamson and Silva (1997). The thick dotted line represents the total hazard using the proposed narrowband Equation 4.3. The dashed and dashed-dotted lines represent MAF using Equations 4.5 and 4.6, respectively, i.e., they are the two contributions to the near-source hazard. The broadband directivity attenuation model (Somerville et al. 1997) is also shown (thin dotted lines). When compared to the models of Abrahamson and Silva (1997) and Somerville et al. (1997), the proposed PSHA framework demonstrates a more intuitive picture of how narrowband pulse-like motions will affect the computed ground motion hazard.

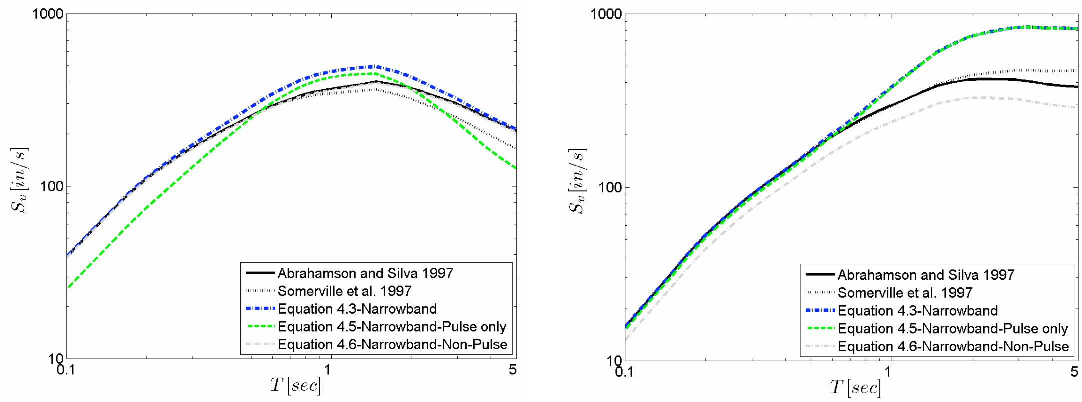

(a) (b)

Fig. 4.8 UHS at MAF of exceeding S_v at 1% in 100 years for (a) M_w 6.0 and (b) M_w 7.5.

Note that in Figure 4.8a the narrowband UHS is equal to the Abrahamson and Silva–based UHS at shorter and longer periods, amplifying it only in a region of T centered on 0.5 to 2 sec. This narrowband effect exists but is not so obvious in Figure 4.8b because the UHS computations are restricted by current attenuation law limitations to T < 5 sec. Periods significantly longer than the expected T_p of 4.7 sec; therefore, they cannot be shown. The UHS shows its largest amplification relative to Abrahamson and Silva (1997) at the T close to $\hat{T}_p$, i.e., 0.7 and 4.7 seconds for M_w 6.0 and 7.5, respectively.

4.7.2 Effect of T_p| M_w Distribution

As the introduction of T_p is what distinguishes this narrowband model from previous broadband models, in this section we explore the role of the conditional distribution of T_p given M_w on the near-source UHS. In the previous section we saw the effect of changes in the median of T_p due to changes in the causative magnitude. In Figure 4.9, we show (for the M_w= 6.0 case) the ratio (amplification factor) of the UHS for the narrowband approach versus that from the simple Abrahamson and Silva (1997) prediction. Note that as $\sigma_{\ln T_p|M_w}$ increases this amplification broadens, has a lower peak, and has a peak at a longer period.

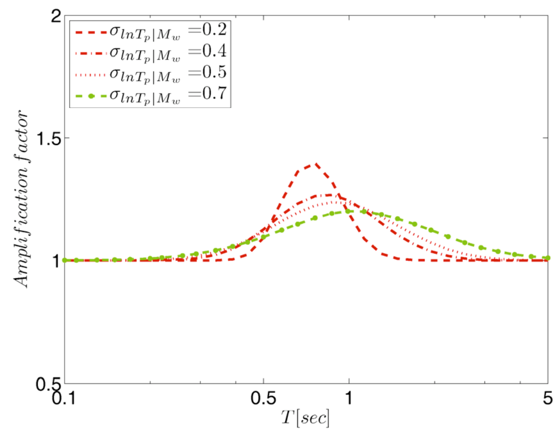

Fig. 4.9 Amplification factor for M_w 6.0 event.

To illustrate more graphically the effect of $\sigma_{\ln T_p|M_w}$ on the UHS, we assume next two different $\sigma_{\ln T_p|M_w}$ values: 0.7 and 0.2. The median value of T_p is 4.7 (for the M_w 7.5 case). In order to help visualize the effect of the narrowband modification, we use here a coarse, discrete, three-mass approximation of the T_p distribution (T_p= 2.3, 4.7, and 7.0 sec). These three T_p values are assigned the appropriate probability mass function obtained from $f_{T_p|M_w}$. For $\sigma_{\ln T_p|M_w}$ = 0.7, the probability mass function for each T_p realization is 0.34, 0.28, and 0.38, respectively. The probability mass function is 0.08, 0.79, and 0.13, respectively, for $\sigma_{\ln T_p|M_w}$ = 0.2.

Noticeably, the smallest T_p realization will be given a very different weight according to how large $\sigma_{\ln T_p|M_w}$ is. This will affect the narrowband amplification at those periods. The UHS using these two three-mass T_p approximations are shown below in Figure 4.10 for the case of one fault producing only M_w 7.5 events.

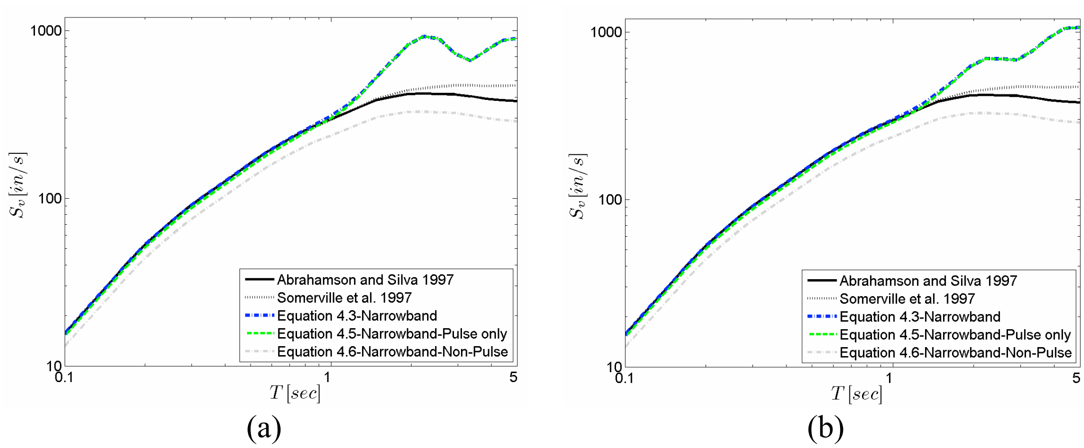

Fig. 4.10 S_v UHS using three T_p realizations for M_w 7.5: (a) with $\sigma_{\ln T_p|M_w}$ = 0.7 (b) with $\sigma_{\ln T_p|M_w}$ = 0.2.

The S_a or S_v amplification relative to Abrahamson and Silva (1997) is shown in Figure 4.11 for three different cases: the S_v amplification for (1) Figure 4.8b, (2) Figure 4.10a, and (3) Figure 4.10b.

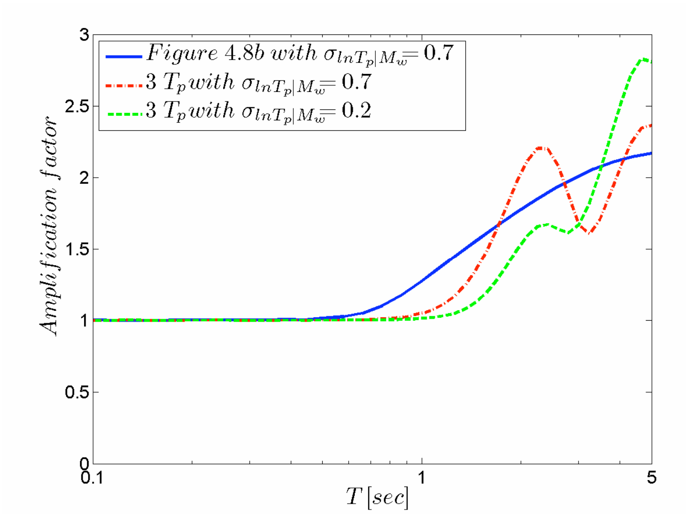

Fig. 4.11 Amplification factor for M_w 7.5 event.

The amplification is calculated as the ratio of S_v from the UHS based on the narrowband modification (Eq. 4.3) to S_v from the UHS that uses only Abrahamson and Silva (1997) for all periods and events. Note that the three-mass representation with $\sigma_{\ln T_p|M_w}$ = 0.7 produces a "lumpy" approximation to the continuous result. As shown in Figures 4.9 and 4.11, the peak amplification value is dictated by the effect of $\sigma_{\ln T_p|M_w}$. The larger the $\sigma_{\ln T_p|M_w}$, the more the shift in the peak amplification to the right (longer period). The smaller the $\sigma_{\ln T_p|M_w}$, the narrower the amplification and the higher the peak. Even with $\sigma_{\ln T_p|M_w}$ = 0.2 there remains, however, a significant amplification of the UHS at $T \approx 2$ sec. Indeed it must be remembered that the UHS is a weighted combination of possible future events. No matter what $\sigma_{\ln T_p|M_w}$ may be, individual spectra observed during these future events will have comparatively narrow response spectra with, potentially, a peak near, approximately, 2 seconds. The lowering and widening of the UHS with increased $\sigma_{\ln T_p|M_w}$ is a product of the UHS "averaging" process.

4.7.3 Disaggregation of PSHA Results

Here we use Equations 4.7 and 4.8 to compute the probability of a pulse and the distribution of T_p values, *conditional* upon $S_a = x$. In Figure 4.12a, conditional distribution of T_p results (Eq. 4.8) are shown for S_a = 0.4g at T = 2 sec using the M_w 7.5 source example case. Similar results are shown in Figure 4.12b for an S_a level of 3.0g. These values of x correspond to annual probabilities of exceedance of 32% and 0.24% for this example case. The probabilities that these values occurred "due to" a pulse are 0.75 and 0.97, respectively (Eq. 4.7). The former S_a level (0.4g) represents an epsilon of about 0.6 relative to the median spectral acceleration predicted by Abrahamson and Silva (1997), which in effect assumes no pulse, while the latter value represents an epsilon of 3.5 if there were no pulse. Figure 4.13 presents similar results for the M_w 6.0 illustration. The levels of 2-second S_a being conditioned upon here are 0.2 and 1.5g. These levels correspond to annual probabilities of 3.6% and 0.086%, respectively; the probabilities that they were associated with a pulse occurrence are 0.08 and 0.23, respectively, and the epsilons are 0.3 and 2.8 relative to Abrahamson and Silva (1997).

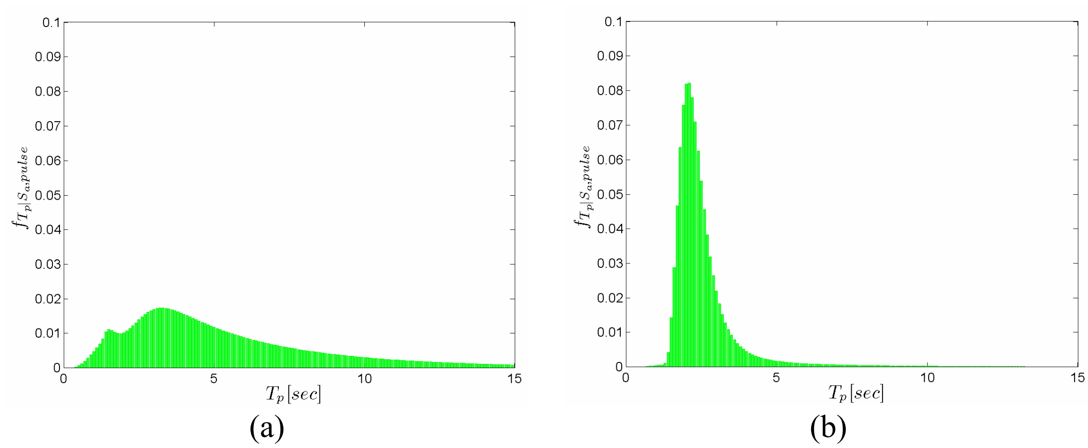

Fig. 4.12 Conditional probability density functions for T_p, given $S_a = x$ and a pulse-like ground motion for 7.5 M_w: (a) S_a= 0.4g and (b) S_a= 3.0g for T= 2 sec.

Based on these no-pulse epsilons, the lower values are not exceedingly rare (given an event), whereas the higher two values are — unless a pulse occurs and its period is such that it induces larger median ground motion amplitudes at the T of interest. Therefore, the occurrence of a larger ground motion amplitude "suggests" that a pulse occurred and increased the median prediction, i.e., the pulse period was not far from the period of interest.

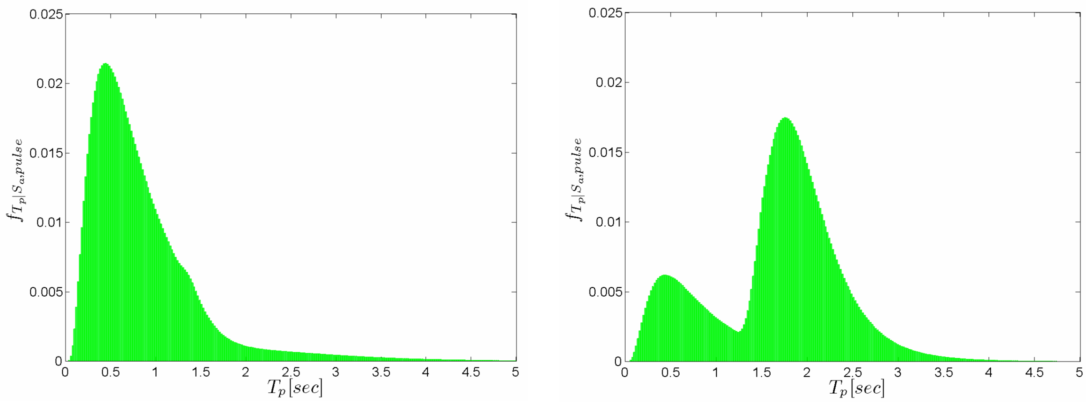

(a) (b)

Fig. 4.13 Conditional probability density functions for T_p, given $S_a = x$ and a pulse-like ground motion for 6.0 M_w: (a) S_a= 0.2g and (b) S_a= 1.5g for T= 2 sec.

These effects dictate in Figures 4.12–4.13 the shapes of the disaggregated T_p distributions, i.e., the conditional distributions given $S_a = x$. The left-hand sides (lower S_a values) are similar in shape to the marginal distributions of T_p (i.e., here, the lognormal distributions given M_w 7.5 or 6.0). The right-hand sides (higher S_a values), on the other hand, show sharp conditional probability mass increases near the period of interest.

It is anticipated that these disaggregation results will be of particular use in guiding the selection of sample ground motion recordings for use in nonlinear dynamic foundation and structural analysis.

4.8 DISCUSSION

This chapter has presented an explicit-pulse-based PSHA method in terms of S_a, elastic spectral acceleration, as the scalar ground motion intensity measure. It appears in the development of the equations as well as in the illustrations. This intensity measure was chosen because it is the conventional and most familiar one. The PSHA then provides conventional uniform hazard spectra as well as insights from the disaggregation by pulse and pulse period that supplement the conventional M_w, R_{rup}, and epsilon disaggregation results. Together these results can be used as much as they are now for near-source sites to aid in the selection and scaling of recordings for use in foundation and structural dynamic analyses, e.g., to estimate the probability distribution of response given an S_a value with a specified mean annual frequency. This may mean scaling to that S_a level a sample of records chosen to reflect the causative magnitude, distance, and epsilon range, plus, now, to reflect the correct fraction of pulse-like records together with their appropriate range of T_p values. In this way the effects of pulse-like records on, for example, nonlinear response (Section 4.5) will be captured and their contribution to the seismic threat ascertained. Analogous to the procedures that have been developed to deal with the (local) peak-valley or "epsilon" effect (Baker and Cornell 2005b; Baker and Cornell 2006b), careful record selection, and/or weighting and/or local regression techniques may all help make the assessment of structural response distributions easier in the near-source case as well, although the dimensionality has been increased to include T_p. These procedures all require disaggregation results. For example at 3.0g intensity with M_w 7.5, if the total ground motions needed are 30 records, engineers will then select 29 (i.e., 0.97×30) pulse-like ground motions with T_p values that approximately match the distribution in Figure 4.12b, and one non-pulse ground motion matching the S_a disaggregation on ε (probably the mean value in this case).

While written for S_a, the PSHA equations (e.g., Eq. 4.3) also hold if S_a is replaced by virtually any other candidate scalar intensity measure (*IM*). In particular, they hold if elastic S_a is replaced by S_{di}, which has been shown (Chapters 2 and 5; see also Luco 2002; Luco and Cornell 2007; Tothong and Luco 2007) to be a very effective *IM*. With S_{di} as the *IM* in the explicit-pulse PSHA, again an attenuation law for pulse-like ground motions would need to be created. The robustness that S_{di} has shown with respect to pulse-like ground motions in the past (e.g., Tothong and Luco 2007) suggests that the (S_{di}-based) epsilon versus T/T_p plots parallel to Figure 4.4 would be significantly different, with the mean lying closer to zero for all T/T_p. This robustness also suggests that the shape of $f_{T_p|pulse,S_{di}}$ would be less sensitive to the ground motion amplitude level and to T_p. All this muting of the pulse effects implies that record selection and scaling should be simpler if S_{di} is used as the *IM*. Some of these same conclusions may also prove true for *IM*s such as $S_{a\text{-}AVG}$, the spectral acceleration averaged over a relevant frequency band. Finally, extension of the explicit-pulse PSHA to a vector *IM* such as $<S_a, \varepsilon>$ or $<S_a, \varepsilon, T_p>$ is also straightforward in principle.

4.9 CONCLUSIONS

A framework is proposed to incorporate accurately the effect of near-source pulse-like ground motions into PSHA. The framework explicitly incorporates the likelihood of experiencing pulse motions and the corresponding distribution of pulse periods, T_p, into the analysis. The PSHA is separated into two parts: non-near-source contribution and the near-source contribution. The former is simply a conventional PSHA. The latter or near-source-contribution is separated further into that due to the event of experiencing a pulse-like motion and that when a pulse is not in evidence. For the pulse case, a new narrowband modification for the ground motion attenuation model needs to be developed. For the non-pulse, but near-source case, the available attenuation models may prove to be adequate.

The direct output of the analysis includes intensity measure hazard curves and uniform hazard spectra, UHS. To improve seismic hazard assessments, disaggregation results provide the conditional distributions of the causative event variables (i.e., ε, M_w, *distance*, P[*pulse*], T_p, etc.) that are associated with a ground motion at a given intensity level. In the same way that M_w, *distance*, and ε disaggregation is provided in standard PSHA, the near-source PSHA framework can provide disaggregation information for P[*pulse*] and T_p distribution for a specified ground motion intensity level. This disaggregation information is important in selecting historical earthquake ground motions for structural analyses because it improves the understanding of earthquakes and their effects on structures. The method is illustrated with elastic spectral acceleration as the intensity measure using a simplified, preliminary model for the narrowband, pulse-like ground motion model. The disaggregation results of P[*pulse*] and the conditional T_p distribution are shown to vary with the intensity level.

Once a PSHA analysis using the proposed procedure is complete and implemented, it will not require additional effort from the engineers. It is simply a modification to, e.g., the USGS hazard maps, together with supplementary information provided by disaggregation regarding the contribution of pulse-like ground motions to the seismic hazard. This extension will improve the usefulness and accuracy of PSHA results at sites that might be subjected to near-source ground motions with pulse-like forward-directivity effects.

5 Structural Performance Assessment under Near-Source Pulse-Like Ground Motions Using Advanced Ground Motion Intensity Measures

5.1 INTRODUCTION

Performance-based seismic evaluation is a process that results in a realistic understanding of the quantified risk due to future earthquakes for a proposed new structure or the upgrade of an existing structure. To evaluate the seismic performance of a structure at a designated site susceptible to *near-source* (or *near-fault*) and/or *ordinary* ground motion records, probabilistic seismic demand analysis (PSDA) can be used to calculate the structural performance information (i.e., mean annual frequency of exceeding a given level of structural responses). PSDA combines a site-specific ground motion hazard curve of a ground motion intensity measure (*IM*) with structural responses from nonlinear dynamic analyses of the given structure. An advanced *IM*, which contains spectral-shape information as well as information about the structure, can be expected to be suitable for selection and scaling records. The desirable properties of an *IM* are the efficiency, the sufficiency, and the scaling robustness. An efficient *IM* is defined as one that results in a relatively small dispersion of structural responses given the level of ground motion intensity (*IM*). A sufficient *IM* is defined as one that renders structural responses *conditionally independent* of ground motion properties (e.g., earthquake moment magnitude (M_w), distance, epsilon, pulse period, etc.) at a given intensity level (epsilon and pulse period are defined below). A sufficient *IM* implies robustness with respect to record selection and scaling. Sufficiency of an *IM* is desirable because it reduces the complexity in both the PSDA calculation as well as the record selection procedure. Lastly, scaling robustness is defined as producing no bias in the responses of scaled records relative to as-recorded ground motions (defined in Chapter 2; see also Luco and Bazzurro 2004; Tothong and Luco 2007).

Pulse-like ground motions are typically very intense and are known to cause severe damage in structures. The characteristics of these motions are different from ordinary records in that they often exhibit a long-period pulse in the velocity-time histories, causing an unusual shape in the response spectrum. Elastic-based *IM*s have been shown to be inefficient and insufficient, and, in particular, to introduce biases when used as a basis for scaling the near-source (or near-fault) pulse-like ground motions (Baker and Cornell 2005b; Luco 2002; Luco and Cornell 2006; Tothong and Luco 2007). This is mainly due to the lack of spectral-shape information (for pseudo-spectral acceleration at or near the first-mode period of the structure, denoted as $S_a(T_1)$ or S_a for short) and the fact that only the *local* shape at the fundamental period of the structure is contained for S_a and epsilon (denoted here as $<S_a, \varepsilon>$). Note that in this chapter, S_{de} is used interchangeably with S_a, simply for direct comparison with S_{di}. Epsilon (ε) is a proxy for measuring the deviation between the S_a of an as-recorded ground motion and the predicted median value from the a ground motion prediction model (i.e., attenuation relationship; for example, Abrahamson and Silva 1997). An inefficient *IM* introduces a large dispersion in responses. In addition, an insufficient *IM* suggests that the conditional probability distribution of responses will depend on how the records are selected, and if this fact is neglected, the results may well be biased.

This study investigates the effectiveness of advanced ground motion *IM*s such as S_{di} (inelastic spectral displacement) and $IM_{1I\&2E}$ (a SRSS combination of inelastic spectral displacement at the first-mode period and the elastic spectral displacement at the second-mode period (Luco 2002; Luco and Cornell 2006). We shall show that the use of these advanced *IM*s leads to efficient and sufficient estimates of the seismic performance of structures (from elastic behavior to global collapse of a structure) even when pulse-like records are used inadvertently; for example, when the site is located away from faults and such records are not anticipated to occur at the site. This apparent missed-selection of record types is intentionally done to investigate the strength of the sufficiency property of an *IM* with respect to the pulse period (T_p, defined below) of the pulse-like record.

The ground motion intensity measure $IM_{1I\&2E}$ is calculated as a function of $S_{di}(T, d_y)$ (where $T = T_1$ and d_y is the yield displacement of an oscillator), $S_{de}(T_2)$, and the elastic participation factors of the first two modes of the structure of interest, i.e.,

$$IM_{1I\&2E} = S_{di}\left(T, d_y\right) \cdot \sqrt{1 + \left[\frac{PF_2^{[2]} \cdot S_{de}\left(T_2\right)}{PF_1^{[2]} \cdot S_{di}\left(T, d_y\right)}\right]^2} \qquad (5.1)$$

where $PF_n^{[2]}$ is the n^{th}-mode *effective* participation factor for interstory drift ratio (i.e., $\Gamma_n \cdot \frac{\phi_{n,i} - \phi_{n,i-1}}{h_i}$) that corresponds to the story of the structure at which $\sqrt{\left[PF_1^{[2]} \cdot S_{di}\left(T, d_y\right)\right]^2 + \left[PF_2^{[2]} \cdot S_{de}\left(T_2\right)\right]^2}$ is maximized (for $\theta_{\max}$; Luco 2002; Luco and Cornell 2006). In the expression for $PF_n^{[2]}$, h_i is the height of the i^{th} story (above the i^{th} floor), $\phi_{n,i}$ is the i^{th}-floor element of the n^{th}-mode shape vector, and Γ_n is the n^{th}-mode participation factor, as defined in Chopra (2001). Note that here we have adopted the equation for $IM_{1I\&2E}$ put forth by Mori et al. (2004), which is slightly different than the original equation proposed by Luco and Cornell (2002; 2006); the latter uses $S_{de}(T_1)$ in the denominator of the square root term, thereby involving three different spectral displacement parameters. In either case, the square root term serves as a higher-mode modification factor for S_{di}.

5.2 MOTIVATION

Near-source pulse-like ground motions, in general, have two characteristics: forward directivity and fling. Forward directivity occurs when a fault rupture propagates toward a site with a rupture velocity close to the shear wave velocity. This phenomenon causes most of the seismic energy from the rupture process to arrive in a single, large, long-period pulse at the beginning of the record in a short span of time (Chen 1995; Hall and Aagaard 1998; Singh 1985; Somerville et al. 1997). The intense velocity pulse is mostly oriented in the fault-normal direction due to the radiation pattern of the shear dislocation on the fault plane (Singh 1985; Somerville et al. 1997). In some cases, the most severe direction can be different from the fault-normal direction (e.g., the ideal fault plane may not locally coincide with the actual fault direction; Mavroeidis and Papageorgiou 2002).

Another important aspect of near-fault ground motions is fling, which is the permanent static displacement in the fault-parallel direction for strike-slip faults or in the fault-normal direction for dip-slip faults (Chen 1995; Hall and Aagaard 1998; Singh 1985). Fling is a result of a permanent ground displacement that generates one-sided velocity pulses, whereas forward directivity is a dynamic phenomenon that produces no permanent ground displacement, and hence two-sided (reversing) velocity pulses (Bray and Rodriguez-Marek 2004; Hall and Aagaard 1998; Hall et al. 1995; Singh 1985). The reversing pulse motion in a fault-normal component is potentially more damaging than the one-sided pulse (Hall and Aagaard 1998; Hall et al. 1995; Ryan and Hall 1998). The standard processing techniques of "raw" strong motions remove parts of the peak shear-wave displacement and essentially the whole static displacement through filtering (Chen 1995; Mavroeidis and Papageorgiou 2002). Given the difference between forward directivity and fling as well as the difficulty in processing the data, it is desirable to treat them separately. This study focuses on the forward directivity from the fault-normal component of near-fault ground motions.

The response of structures subjected to pulse-like motions may be much more damaging than that to ordinary records. The damage due to pulse-like motions is from only a few large displacement excursions (at the beginning of the records of short duration) rather than from a large number of oscillations (Bertero et al. 1978). Hence, records will transmit impulse energy into the structures in a short period of time. Past studies (e.g., Alavi and Krawinkler 2001; Anderson and Bertero 1987; Anderson et al. 1999; Bertero et al. 1978; Cuesta and Aschheim 2001; Fu 2005; Hall and Aagaard 1998; Hall et al. 1995; Iwan 1997; Iwan 1999; Iwan et al. 2000; Luco and Cornell 2006; MacRae et al. 2001; Mavroeidis et al. 2004; Sasani and Bertero 2000; Sinan et al. 2005; Veletsos et al. 1965; Zhang and Iwan 2002a; Zhang and Iwan 2002b) have extensively studied the effects of pulses on structures (either using actual near-fault records or simplified waveforms representing the typical pulse-like nature of near-fault ground motions). Interested readers may find these cited references helpful to provide the fundamental behavior of structures subjected to pulse-like records.

Due to the interest in strong earthquake ground motions (i.e., at a low ground motion hazard level vis-à-vis long-return period motions), pulse-like motions are selected and used as a sufficiency test for the advanced *IM*s considered. This study investigates the effectiveness of the advanced *IM*s and whether or not they can sufficiently characterize the pulse-like motions.

5.3 NEAR-SOURCE PULSE-LIKE GROUND MOTIONS

Near-source pulse-like ground motions are often characterized by intense velocity or displacement pulses with relatively long periods that clearly distinguish them from typical far-field ground motions. Pulse-like records are much different from ordinary records especially when they are observed in the velocity- or displacement- rather than acceleration-time histories. Note though, that not all ground motions at sites that satisfy site-source geometrical configurations exhibit intense velocity pulses. Conversely, forward directivity may occur when geometrical conditions are not satisfied (Bray and Rodriguez-Marek 2004; Mavroeidis and Papageorgiou 2002). It should be noted that, as a result, it is rational to utilize the probability of experiencing a pulse for a near-fault site to quantify the future earthquake hazard. This concept is illustrated in Chapter 4 (see also Tothong et al. 2007) where we perform a site-specific seismic hazard analysis for a site located close to faults.

A particularly important property of pulse-like motions is the pulse period (T_p). Some past investigators (e.g., Bazzurro and Luco 2004; Bray and Rodriguez-Marek 2004; Sinan et al. 2005) have estimated T_p from the duration at which velocity is equal to 10% of the peak velocity. Alavi and Krawinkler (2001) define it as the period associated with the global peak of the velocity spectrum (S_v). Mavroeidis and Papageorgiou (2003) determine T_p such that the S_v of their synthetic records exhibit a peak at about the same peak period observed in the recorded pulse motions. In this study, the T_p is defined as the period associated with the peak of S_v. Note that the correlation between the two T_p definitions is about 0.85 (Bray and Rodriguez-Marek 2004; Sinan et al. 2005).

A database of 70 pulse-like earthquake ground motion records rotated to the fault-normal direction are compiled from records that have been identified as having "distinct" velocity pulses by Mavroeidis and Papageorgiou (2003), Fu and Menun (2004), and Bazzurro and Luco (2004). Bazzurro and Luco (2004) selected records whose location relative to the fault rupture suggested that a velocity pulse is likely to occur, rather than directly identifying a velocity pulse in the record. Accordingly, records have been visually identified based on whether they contained a pulse before including the records in the database. The processed records, in the fault-normal direction, are obtained from the Next Generation Attenuation (NGA) database as of March 2005. All ground motions are recorded on firm soil or rock based on Geomatrix site classes for all faulting styles. The earthquake magnitude, M_w, ranges from 5.6 to 7.6, and the closest distance to rupture ranges from 0.07 to 22 km. The set of 70 pulse-like records is listed in Table A.2.

5.4 STRUCTURES ANALYZED

To study the effect of pulse-like motions, four generic moment-resisting frames designed by Ibarra and Krawinkler (2005) are used for analysis. Each generic frame has a single bay with story stiffnesses and strengths chosen to be representative of typical structures. The peak-oriented hysteretic model considered (Ibarra et al. 2005) is used at the beam ends and at the bases of columns. This model utilizes energy-based deterioration through a cyclic deterioration parameter ($\gamma_{s,c,k,a}$), as well as the following backbone curve parameters: the strain-hardening stiffness ratio (set equal to 3%), which is relative to the elastic stiffness (K_e); the capping ductility (δ_c/δ_y) (set equal to four), which is defined as the displacement at the peak strength (δ_c) divided by the yield displacement (δ_y); and the post-capping stiffness ratio (α_c), relative to K_e. A detailed description of this hysteretic model can be found in (Ibarra et al. 2005). Their hysteretic properties are summarized in Table 5.1 (the backbone for this hysteretic model is illustrated in Chapter 2).

To distinguish among these structures, a four-number code is adopted. The first two numbers indicate the number of stories, and the last two numbers indicate the first-mode period of vibration. The primary structure considered in this chapter has six stories and a first-mode period equal to 1.2 sec; it is referred to as structure 0612. The base shear strength coefficient for this structure is 20% of its total weight. The structural demand parameter considered in this chapter is the peak maximum interstory drift ratio ($\theta_{\max}$; peak response over time and maximum over the height of the structure) because $\theta_{\max}$ has been shown to correlate well with the structural (i.e., joint rotations) and non-structural damage (e.g., partition walls).

Table 5.1 Hysteretic model parameters for generic frames considered in chapter.

Structure code	Number of stories	T_1 [sec]	Ductility capacity (δ_c/δ_y)	Post-capping stiffness ratio (α_c)	Cyclic deterioration parameter ($\gamma_{s,c,k,a}$)
0303	3	0.3	4	-5%	50
0606	6	0.6	4	-10%	∞
0612	6	1.2	4	-5%	50
0909	9	0.9	4	-5%	50

Note that these generic frames are especially sensitive to higher modes because they have been designed to achieve the same story drift ductility under the parabolic lateral load pattern specified in FEMA-356 (2000). This design objective results in a straight-line, first-mode shape function, i.e., the structure will be very flexible in the upper stories. This makes them sensitive to higher-mode excitations. Typically, engineering designed buildings are much stiffer in upper stories, and therefore will be less sensitive to higher modes. The pushover analysis using this parabolic lateral load pattern exhibits a kink at the yield drift level because of the simultaneous yielding of the pre-defined plastic hinges.

5.5 SHORTCOMINGS OF ELASTIC-BASED *IM*s: S_a AND $<S_a, \varepsilon>$

For tall, long-period structures, S_a is neither efficient nor sufficient in explaining the variability in the responses of structures for both *ordinary* (Shome 1999) and *near-source* pulse-like records (Luco 2002; Luco and Cornell 2006; Tothong and Luco 2007). For *ordinary* records, the bias associated with scaling the amplitude of records using S_a can be explained by the effect of *peaks* and *valleys* in the response spectrum vis-à-vis ε. The insufficiency of S_a can be corrected by incorporating ε via either a vector *IM* or detailed record selection (Baker and Cornell 2005a; Baker and Cornell 2006b). Given a level of S_a, epsilon has been shown to capture the average (over a number of records) *local* spectral shape at T_1. Epsilon is efficient and sufficient for *only* ordinary ground motions, largely because the correlation between $\ln S_a$ at T_1 and other periods decays slowly as the period shifts away from T_1 (discussed further in Chapter 6). Therefore, much information (about S_a at other periods) can be gained from knowing S_a and ε at T_1.

Near-source pulse-like ground motions, on the other hand, exhibit "narrowband" spectral shape (Somerville 2003; Tothong et al. 2007, see also Chapter 4). The correlation function between $\ln S_a$, for example, at T_p and other periods drops off rapidly as the period ratio increases for pulse-like records (as compared to ordinary records). For pulse-like motions, Baker and Cornell (2005b) have shown that ε is particularly *insufficient* with respect to the period ratio between T_p and the modal periods of the structure (T_p/T). Previous studies (e.g., Alavi and Krawinkler 2001; Cuesta and Aschheim 2001; Fu 2005; Mavroeidis et al. 2004; and others cited above) have pointed out that the responses of structures subjected to pulse-like motions will depend on T_p/T_1, peak amplitude of the ground motion velocity, number of half-cycle pulses, strength of the structure, and the response of interest.

Given this insufficiency of the elastic-based *IM*s (i.e., S_a, $<S_a, \varepsilon>$), it is interesting to investigate how the advanced *IM*s (such as S_{di} and $IM_{1I\&2E}$) perform under narrowband spectral shape ground motions. The study here considers structural behavior from the elastic range to global dynamic instability (i.e., collapse) of the structures. Collapse is defined as the point at which the IDA (Vamvatsikos and Cornell 2002a) curve of a record becomes flat.

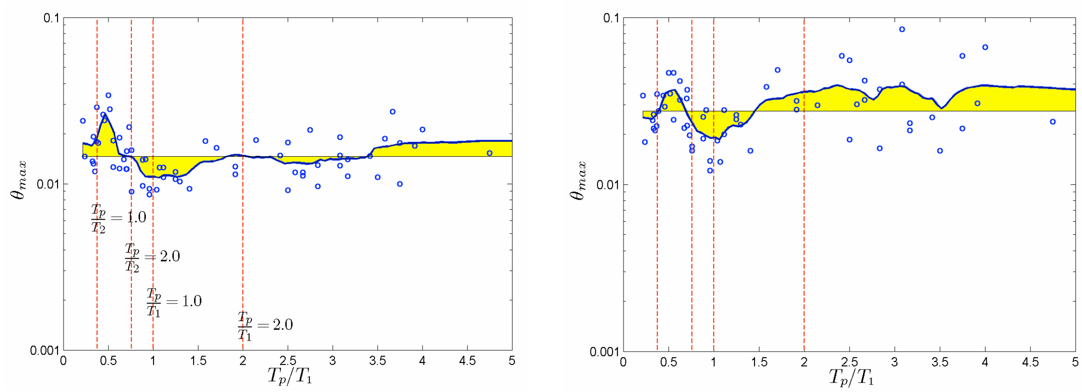

(a) (b)

Fig. 5.1 Dependency of maximum interstory drift ratio, θ_{max}, on T_p/T_1 when records scaled to specified S_{de} (or equivalently S_a) level. Records scaled to produce counted-median story ductility of about (a) 2 and (b) 4. Horizontal lines indicate median (i.e., geometric mean) θ_{max} values.

Figure 5.1 demonstrates the dependency of $\theta_{\max}$ on T_p/T_1 (i.e., it shows that S_a is *insufficient* with respect to T_p/T_1). Each circle denotes the response of each pulse-like record after scaling to a specified intensity level. The thick solid lines indicate the average $\theta_{\max}$ values within a specified window of data (the average is redone at different values of T_p/T_1). This moving-window average (Hastie et al. 2001) is utilized to illustrate the dependency of responses and T_p/T_1. At a low-ductility level, responses are more sensitive to higher modes than at a higher ductility level, and are more influenced by T_p/T_1 less than unity (likely when T_p is close to the T_2 of the structure; see the peak at about T_p/T_1=0.5 in Fig. 5.1a). At a higher ductility level, the nonlinearity of the first-mode contribution becomes significant, and the influence from T_p/T_1>1 is the range of interest.

The sufficiency of $<S_a, \varepsilon>$ with respect to T_p/T_1 was investigated by Baker and Cornell (2005b). They found that $<S_a, \varepsilon>$ is *not* sufficient, and other vector *IM*s (i.e., S_a with spectral ordinate at other periods; Bazzurro and Cornell 2002; Vamvatsikos and Cornell 2004) need to be used. The illustration below shows the insufficiency of $<S_a, \varepsilon>$ with respect to T_p/T_1. The vertical axes show the residuals of ln$\theta_{\max}$ when records are first scaled to a given S_a level, then the responses of the scaled motions are regressed against the ε of each record using linear regression. The residuals are simply the observed minus the predicted values of ln$\theta_{\max}$. If ε is effective in predicting the responses of pulse-like motions, there should be no trend as observed in the S_a. A similar trend (as compared to S_a alone) can, however, be observed when using $\langle S_a, \varepsilon \rangle$.

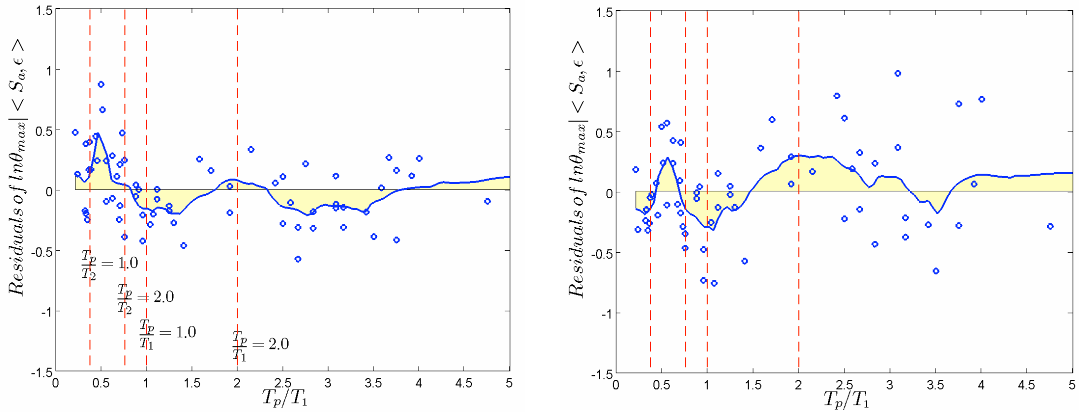

(a) (b)

Fig. 5.2 Residuals of θ_{max} (on S_a and ε) versus T_p/T_1 when records scaled based on S_{de} (or equivalently S_a). Records scaled to produce counted-median story ductility of about (a) 2 and (b) 4.

Again, the responses of a structure conditioned on $\langle S_a, \varepsilon \rangle$ show a dependency on T_p/T_1. This is clearly an *undesirable* feature for the *IM*. This is largely because, for pulse-like motions, response spectra usually exhibit a sharp change in the spectrum making it difficult to simply estimate spectral shape using S_a and the *local* spectral shape at T_1 (vis-à-vis ε). This *insufficiency* of S_a and $\langle S_a, \varepsilon \rangle$ with respect to T_p/T_1 (Fig. 5.1 and Fig. 5.2, respectively) implies that the responses of structures will depend on how records are selected. For example, if records are selected from T_p/T_1 close to unity, the responses will be, on average, smaller than the overall average responses, and vice versa if records are selected from T_p/T_1 of about two (i.e., responses will be, on average, larger than the overall average responses).

5.6 STRUCTURAL RESPONSES USING ADVANCED GROUND MOTION *IM*s

In this section, advanced *IM*s are investigated for their efficiency and sufficiency with respect to pulse-like ground motions. The results are compared with the conventional elastic-based *IM* (i.e., S_a). By design, S_{di} can simply "sense" aggressive or benign[1] behavior of an individual record. Inelastic spectral displacement, S_{di}, can also distinguish between weak and strong structures

[1] Aggressive or benign behavior refers to inelastic displacement ratio (S_{di}/S_{de}, a proxy for spectral shape; discussed in detail in Chapter 3) of ground motion record. Aggressive behavior refers to case when S_{di} is greater than S_{de}, and vice versa for benign behavior.

because the strength will affect the degree of nonlinearity, i.e., whether the effective period of the structure will climb up or down the pulse-like velocity spectra (e.g., Alavi and Krawinkler 2001; Bazzurro and Luco 2006).

Similar to Figure 5.1, records are scaled using S_{di}, $IM_{1E\&2E}$ (which, recall in Chapter 2, is similar to $IM_{1I\&2E}$ but does not reflect inelasticity, i.e., S_{di} is replaced with S_{de}), and $IM_{1I\&2E}$. The results are displayed in Figure 5.3. At the ductility levels of two and four, for example, S_{di} and $IM_{1I\&2E}$ demonstrate their efficiency (smaller dispersion as compared to Figs. 5.1–5.2) and sufficiency with respect to T_p/T_1 (i.e., there is no *obvious* trend between $\theta_{\max}$ and T_p/T_1, at least for T_p/T_1 greater than unity for S_{di}). An exception may be made at a low-ductility level (with T_p/T_1 less than unity) where higher-mode responses may contribute to $\theta_{\max}$ (Fig. 5.3a). As a result, S_{di} may not be sufficient. This insufficiency can be improved by simply using an *IM* that incorporates a higher mode, such as $IM_{1E\&2E}$ and $IM_{1I\&2E}$ (see the reduction in the area of $T_p/T_1<1$ in Fig. 5.3c and d, respectively).

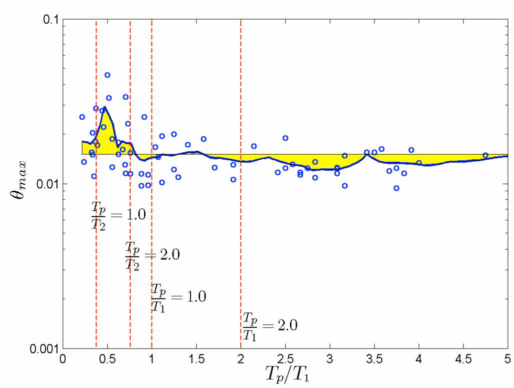

(a) S_{di}

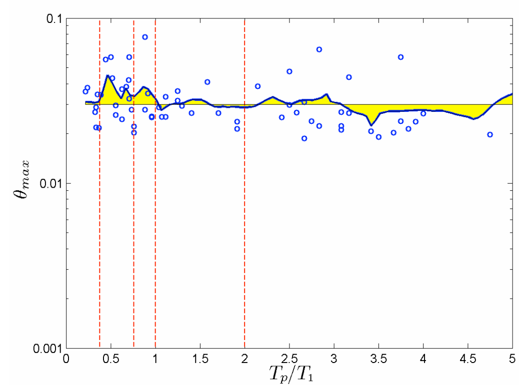

(b) S_{di}

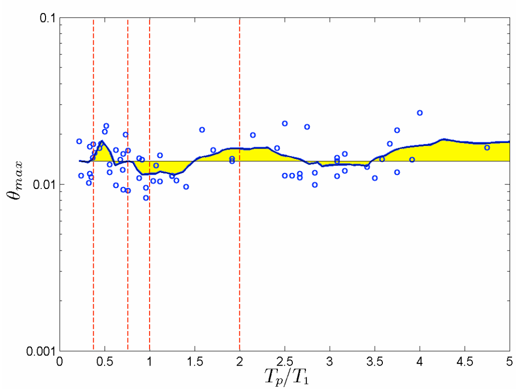

(c) $IM_{1E\&2E}$

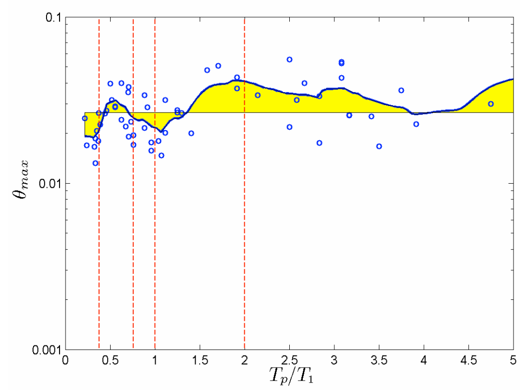

(d) $IM_{1E\&2E}$

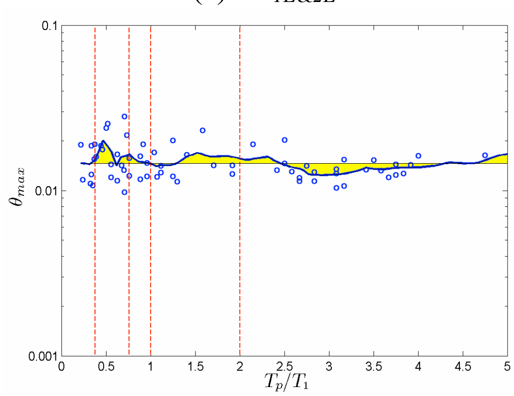

(e) $IM_{1I\&2E}$

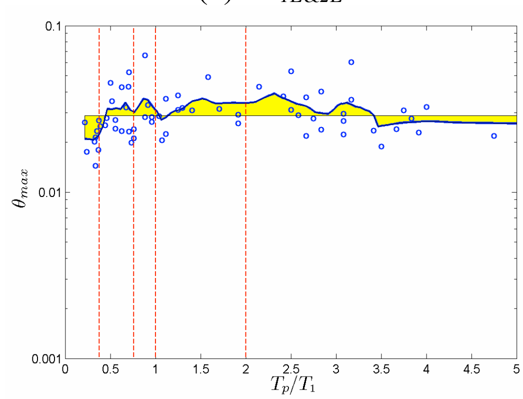

(f) $IM_{1I\&2E}$

Fig. 5.3 Maximum interstory drift ratio versus T_p/T_1 for 0612 structure. Records are scaled using S_{di} (a and b), $IM_{1E\&2E}$ (c and d), and $IM_{1I\&2E}$ (e and f) to produce counted-median $\theta_{\max}$ ductility of about 2 and 4 for each *IM*, respectively. Horizontal lines indicate median (i.e., geometric mean) $\theta_{\max}$ values.

$IM_{1E\&2E}$, by design, does not help reduce the systematic bias at $T_p/T_1>1$, especially at higher ductility levels because of the significant contribution from the first-mode inelasticity to the $\theta_{\max}$ (compare Fig. 5.1b–S_{di} with Fig. 5.3d–$IM_{1E\&2E}$).

Table 5.2 Percentages for area reduction (as a proxy for total bias reduction) for S_{di}, $IM_{1E\&2E}$, and $IM_{1I\&2E}$ relative to that of S_{de} at different counted-median ductility levels.

Structure code	0303			0606		
Median drift ductility	S_{di}	$IM_{1E\&2E}$	$IM_{1I\&2E}$	S_{di}	$IM_{1E\&2E}$	$IM_{1I\&2E}$
1	35	12	39	-10	74	43
2	61	3	60	35	-31	50
4	48	16	47	65	-8	52
6	-28	4	-33	62	-8	47
8	21	8	18	64	9	54

Structure code	0612			0909		
Median drift ductility	S_{di}	$IM_{1E\&2E}$	$IM_{1I\&2E}$	S_{di}	$IM_{1E\&2E}$	$IM_{1I\&2E}$
1	11	57	65	0	53	52
2	37	17	37	-50	11	-25
4	38	4	18	46	-35	46
6	8	-13	28	62	0	46
8	39	37	40	57	-2	39

Table 5.3 Percentages for dispersion reduction in responses for S_{di}, $IM_{1E\&2E}$, and $IM_{1I\&2E}$ relative to that of S_{de} at different counted-median ductility levels.

Structure code	0303			0606		
Median drift ductility	S_{di}	$IM_{1E\&2E}$	$IM_{1I\&2E}$	S_{di}	$IM_{1E\&2E}$	$IM_{1I\&2E}$
1	5	4	12	-8	36	22
2	42	1	43	26	6	39
4	42	4	43	38	3	47
6	26	0	26	36	1	30
8	37	-1	38	39	15	38

Structure code	0612			0909		
Median drift ductility	S_{di}	$IM_{1E\&2E}$	$IM_{1I\&2E}$	S_{di}	$IM_{1E\&2E}$	$IM_{1I\&2E}$
1	-4	48	47	-16	48	35
2	-1	17	26	-20	14	6
4	17	7	26	16	8	26
6	32	-3	11	6	-3	14
8	46	3	11	22	8	24

In terms of the overall bias reduction, Baker and Cornell (2005b) utilize the area (in absolute values) between the moving-average and the median $\theta_{\max}$ value as a statistic. The percentages for the area reduction (relative to that of S_a for S_{di}, $IM_{1E\&2E}$, and $IM_{1I\&2E}$) are 37, 17, and 37% for the median ductility of two and 38, 4, and 18% for the median ductility of four. Overall, the same explanation holds true for other considered structures (see Table 5.2).

In general, S_{di} and $IM_{1I\&2E}$ demonstrate their efficiency (smaller dispersion of the responses) relative to that of S_{de}. At low-ductility levels where higher-mode contributions are considerable, an *IM* incorporating higher mode parameters is necessary, and S_{di} alone is not efficient. Averaging over the buildings, scaling records using S_{di} and $IM_{1I\&2E}$ can reduce dispersion of the response (relative to that of S_{de}) by about -1% (i.e., no reduction is gained) and 26% at the ductility of two and by 17 and 26% at the ductility of four (see Table 5.3). Commonly at low-ductility levels (less than 2), $IM_{1E\&2E}$ shows the largest percentage reduction in the dispersion (except for the 0303 structure where higher modes may not be significant). This dispersion reduction decreases (for $IM_{1E\&2E}$) as the median ductility increases, as expected. The percentage reduction for S_{di}, in general, increases as the median ductility increases. $IM_{1I\&2E}$ tends to reduce the dispersion at both low- and high-ductility levels.

5.6.1 Incremental Dynamic Analyses and Collapse Fragility of Structure Subjected to Pulse-Like Ground Motions

Given the importance of the modal periods of the structure relative to the pulse period, T_p, the records with $T_p/T_1 \geq 2$ are labeled "aggressive case," and the records with T_p/T_1 of about unity are labeled "benign case." Similarly, records with T_p/T_1 of about 0.5 (reflecting the strong higher-mode contribution, see Fig. 5.1) are labeled "higher-mode case." The numbers of records in each case are 28, 13, and 13, respectively. The median response spectra for these records are illustrated in Figure 5.4. In Figure 5.5, the counted-median IDA curves are plotted for the different *IM*s (i.e., S_{de}, S_{di}, $IM_{1E\&2E}$, and $IM_{1I\&2E}$) for the three cases. Collapse fragility curves (i.e., probability of collapse at a given ground motion intensity level, denoted as $P[C|IM]$) of these records are also illustrated in Figure 5.6.

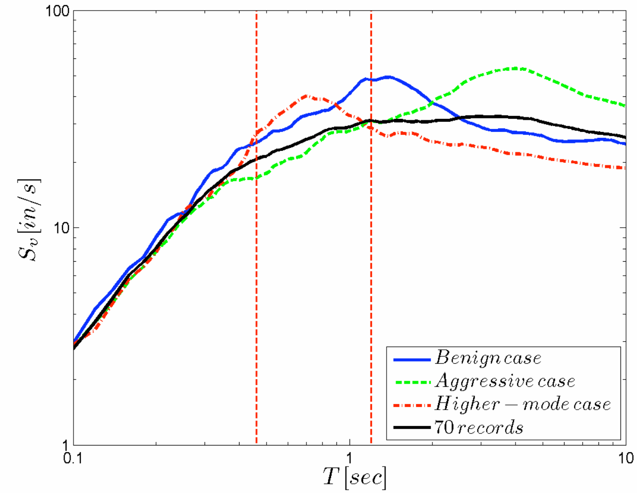

Fig. 5.4 Median response spectra for aggressive, benign, and higher-mode records. Median response spectra of all 70 pulse-like records are also shown for comparison. Vertical dashed lines indicate first- and second-mode periods of structure (i.e., 1.2 and 0.46 sec, respectively).

Note that in this section records (for 3 record sets) are scaled to the same intensity level associated with the counted-median $\theta_{\max}$ of 70 records (and not based on individual record set). Records are scaled to the same intensity level for the ease of comparison among the three record sets (for a given *IM*), as well as the same counted-median $\theta_{\max}$ of 70 records for comparison among *IM*s.

The trend between the median IDA curves and T_p/T_1 for S_{de}, in most cases, is apparent at elastic to global dynamic instability (i.e., collapse) of the structure. First, the benign case shows the smallest counted-median $\theta_{\max}$ values, and the aggressive case shows the largest values at a given intensity level (especially for S_{de} greater than 10). At low S_{de} levels (less than 10), the higher-mode case results in the largest counted-median $\theta_{\max}$ values due to the strong higher-mode contribution. As expected (even in the elastic range), scaling records using S_{de} cannot account for the higher mode responses (Shome 1999). Secondly, the discrepancy between IDA curves (Fig. 5.5a) indicates a larger dispersion in the response when records are scaled using the elastic-based *IM*, i.e., S_{de}.

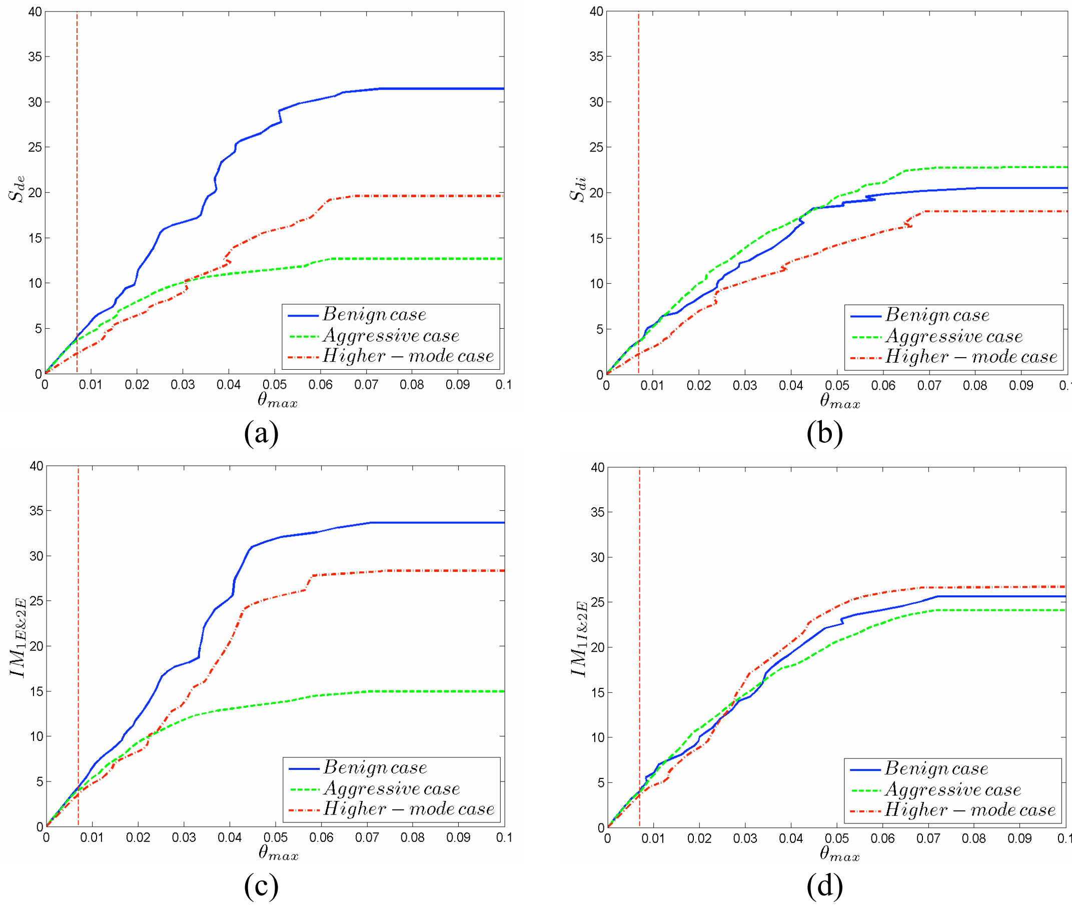

Fig. 5.5 Counted-median IDA curves for aggressive, benign, and higher-mode records when using (a) S_{de}, (b) S_{di}, (c) $IM_{1E\&2E}$, and (d) $IM_{1I\&2E}$ as IM (for 0612 structure). Vertical dashed line indicates (first) yield drift level as determined from static pushover analysis.

As shown in Figure 5.5c, $IM_{1E\&2E}$ can help characterize higher-mode responses at low-intensity levels (i.e., less discrepancy between IDA curves from each case as compared to S_{de} and S_{di} shown in Fig. 5.5a and b, respectively). The median IDA curves, however, diverge as the intensity level increases. This is primarily because $IM_{1E\&2E}$ does not capture the inelasticity of the first mode. S_{di} and $IM_{1I\&2E}$ (Fig. 5.5b and d), on the other hand, can characterize pulse-like effects at high-intensity levels. IDA curves using S_{di} and $IM_{1I\&2E}$ diverge less than in the S_{de} case. Only $IM_{1I\&2E}$, however, can capture both higher-mode contribution at low-intensity and first-mode inelasticity at higher intensity levels. The smaller discrepancy between IDA curves implies the efficiency gained by using these advanced IMs ($IM_{1E\&2E}$ at low-intensity levels, S_{di} at high-intensity levels, and $IM_{1I\&2E}$ from elastic behavior to collapse of the structure).

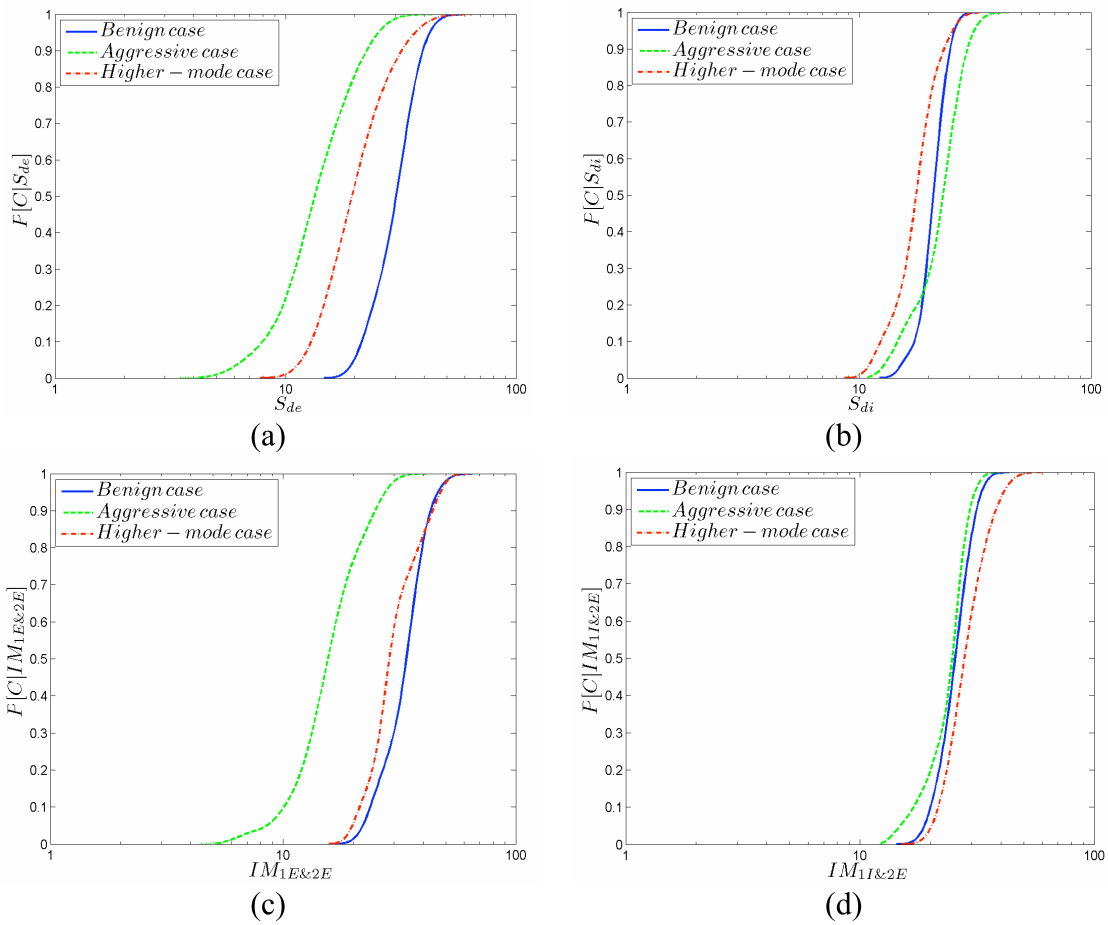

Fig. 5.6 Empirical collapse fragility curves for aggressive, benign, and higher-mode records when using (a) S_{de}, (b) S_{di}, (c) $IM_{1E\&2E}$, and (d) $IM_{1I\&2E}$ as the *IM*.

The dependency of the empirical collapse fragility curves[2], $P[C|IM]$, on T_p/T_1 is also evident when S_{de} is used. The benign set shows the smallest $P[C|S_{de}]$ and the aggressive set shows the largest $P[C|S_{de}]$ at a given intensity level. In contrast to S_{de}, scaling records using S_{di} and $IM_{1I\&2E}$ is normally found to be sufficient relative to T_p/T_1 (less discrepancy between $P[C|IM]$ for different T_p/T_1 record sets). As expected, $IM_{1E\&2E}$ cannot capture the strong inelasticity imposed by the aggressive records (Fig. 5.6c), resulting in $P[C|IM_{1E\&2E}]$ of these records to be different from the other two record sets. Including the first-mode inelastic parameter (i.e., S_{di}) helps ensure the sufficiency property for the aggressive records (see Fig. 5.6d).

By using advanced *IM*s (S_{di} and $IM_{1I\&2E}$), the dependency of responses on T_p/T_1 is less pronounced because these *IM*s will assign a proper scale factor to each pulse-like record.

[2] Empirical collapse fragility curves estimated by smoothing data using a normal kernel function (Hastie et al. 2001).

Aggressive records will be scaled less than the benign records at a specified *IM* level (i.e., median $\theta_{\max}$ level); see Tables 5.4–5.5 for the comparison of the median scale factors of S_{di} and $IM_{1I\&2E}$ relative to those of S_{de}. For higher-mode records, using S_{di} alone can overscale the records (as compared to $IM_{1E\&2E}$ and $IM_{1I\&2E}$). Incorporating the higher-mode factor can help improve the scaling factor assignment to each case of records. These proper scale factors are determined (by using advanced *IM*s) such that records with different spectral shape produce comparable inelastic responses (i.e., achieving approximately the same median drift level). As a result, S_{di} (for first-mode-dominated structures) and $IM_{1I\&2E}$ are *efficient*, *sufficient*, and have *scaling robustness* with respect to pulse-like motions. This scaling robustness of S_{di} and $IM_{1I\&2E}$ relative to pulse-like motions will ultimately simplify the record selection procedure.

Table 5.4 Median (i.e., geometric mean) scaling factor for aggressive, benign, and higher-mode records scaled to target median (of 70 records) $\theta_{\max}$ ductilities for 0612 structure.

Median drift	Benign case		Aggressive case		Higher-mode case	
ductility	2	4	2	4	2	4
S_{de}	0.64	1.14	0.97	1.74	1.30	2.33
S_{di}	0.83	1.85	0.91	1.57	1.54	2.95
$IM_{1E\&2E}$	0.69	1.28	1.01	1.87	1.05	1.96
$IM_{1I\&2E}$	0.88	1.83	0.98	1.64	1.18	2.20

Table 5.5 Ratio of (median) scale factor relative to S_{de} for aggressive, benign, and higher-mode records scaled to target median (of 70 records) $\theta_{\max}$ ductilities for 0612 structure.

Median drift	Benign case		Aggressive case		Higher-mode case	
ductility	2	4	2	4	2	4
S_{di}	1.30	1.63	0.93	0.90	1.18	1.26
$IM_{1E\&2E}$	1.08	1.12	1.03	1.07	0.81	0.84
$IM_{1I\&2E}$	1.38	1.61	1.00	0.94	0.90	0.94

This efficient scaling assignment is illustrated in Figure 5.7 (in terms of peak interstory drift ratio, θ_i, for each record set), which shows that benign and aggressive records generate, on average, $\theta_{\max}$ at the bottom story, while higher-mode records produce $\theta_{\max}$ in the upper story. The $\theta_{\max}$ of the aggressive and benign records are captured by S_{di} because $\theta_{\max}$ are generated at the bottom story (primarily from the first-mode contribution). Therefore, they are scaled such that the median values are close to the target drift level. As expected, S_{di} provides no improvement for the higher-mode records, i.e., θ_i at the top story is larger than the target drift levels (see Fig. 5.7c–d). Note that (for a given *IM*) the target drift levels are determined as the counted-median θ_{max} (of 70 records) associated with the median ductility of 2 and 4. The records in each set are then scaled to the same intensity levels associated with these counted-median θ_{max} levels.

To capture higher modes, $IM_{1E\&2E}$ and $IM_{1I\&2E}$ are used to scale these records. Both *IM*s seem to capture the responses from the higher mode records effectively (see Fig. 5.7e–f). The median responses (i.e., θ_i) of the higher-mode case are close to the target drift levels.

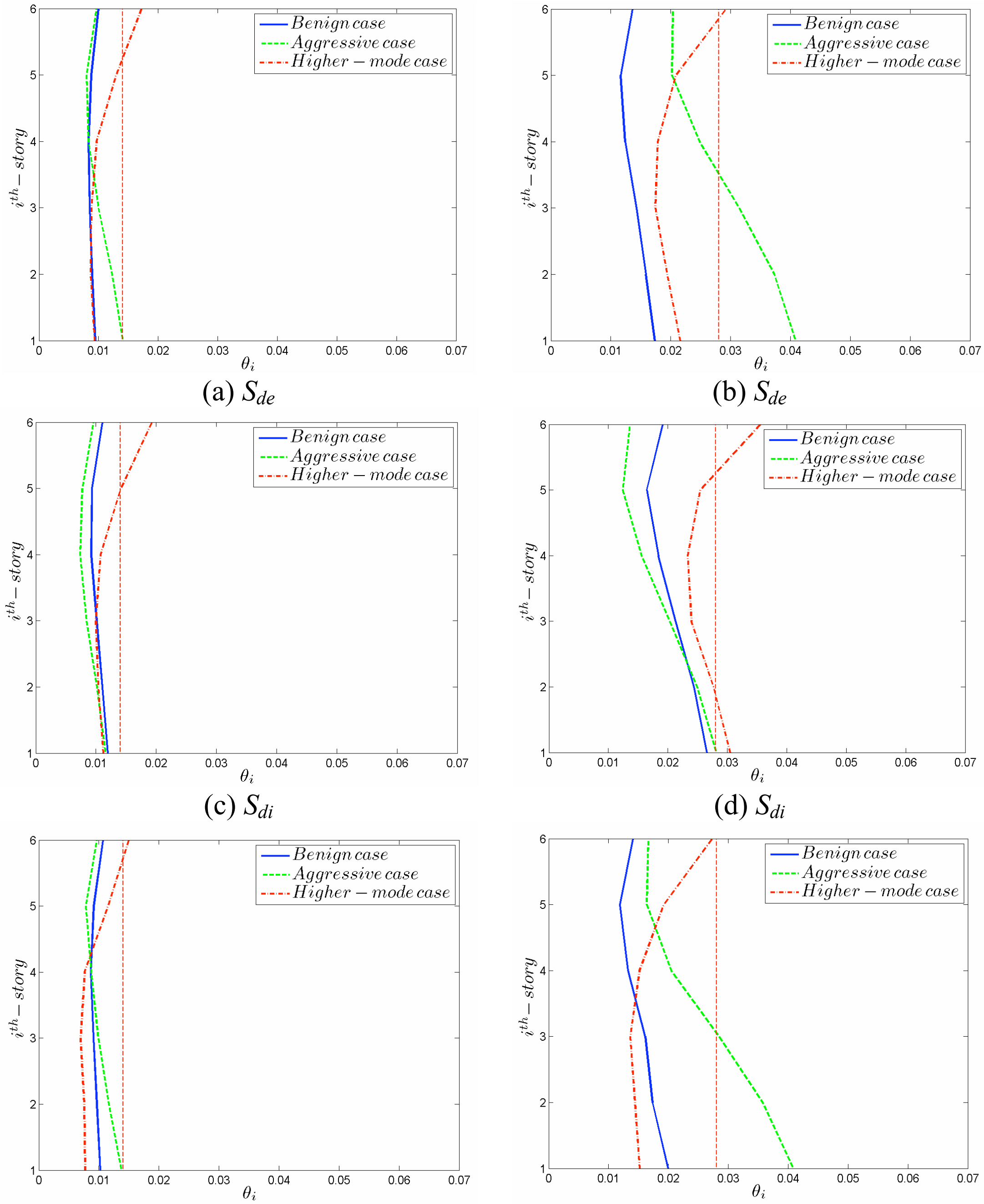

(a) S_{de} (b) S_{de}

(c) S_{di} (d) S_{di}

(e) $IM_{1E\&2E}$ (f) $IM_{1E\&2E}$

Fig. 5.7 Median interstory drift ratio (θ_i) for aggressive, benign, and higher-mode records when using: S_{de} (a and b), S_{di} (c and d), $IM_{1E\&2E}$ (e and f), and $IM_{1I\&2E}$ (g and h) scaled to counted-median $\theta_{\max}$ ductility of 2 and 4. Vertical dashed lines indicate drift ($\theta_{\max}$) levels associated with specified target ductility.

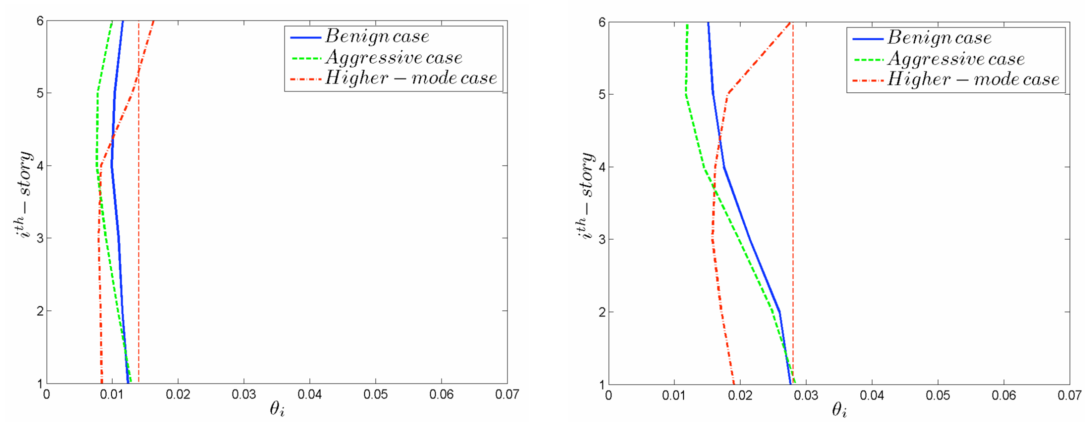

(g) $IM_{1I\&2E}$ (h) $IM_{1I\&2E}$

Fig. 5.7—*continued*

Only the $IM_{1I\&2E}$, however, can capture the responses from the first-mode inelasticity, which can be seen in Figure 5.7g–h where we find that the medians of $\theta_{\max}$ for all three cases are about the same and close to the median (of 70 records) target drift levels. To demonstrate that results displayed previously imply the unbiased response prediction, $\theta_{\max}$ versus the scale factors are plotted in Figure 5.8. Records are scaled to the intensity levels associated with the counted-median (of all 70 records) $\theta_{\max}$ to produce the median ductility of 4. As mentioned previously, using S_{di} or $IM_{1I\&2E}$ can result in scaling robustness (i.e., no statistically significant slope between $\theta_{\max}$ and scale factors). Ground motion records will be scaled more or less (to achieve, on average, the same responses) depending upon their frequency contents relative to important modes of vibration of the structure. As illustrated in Figure 5.8a, structural responses scaled using S_{de} can be biased for aggressive records imposing strong inelasticity on the structure.

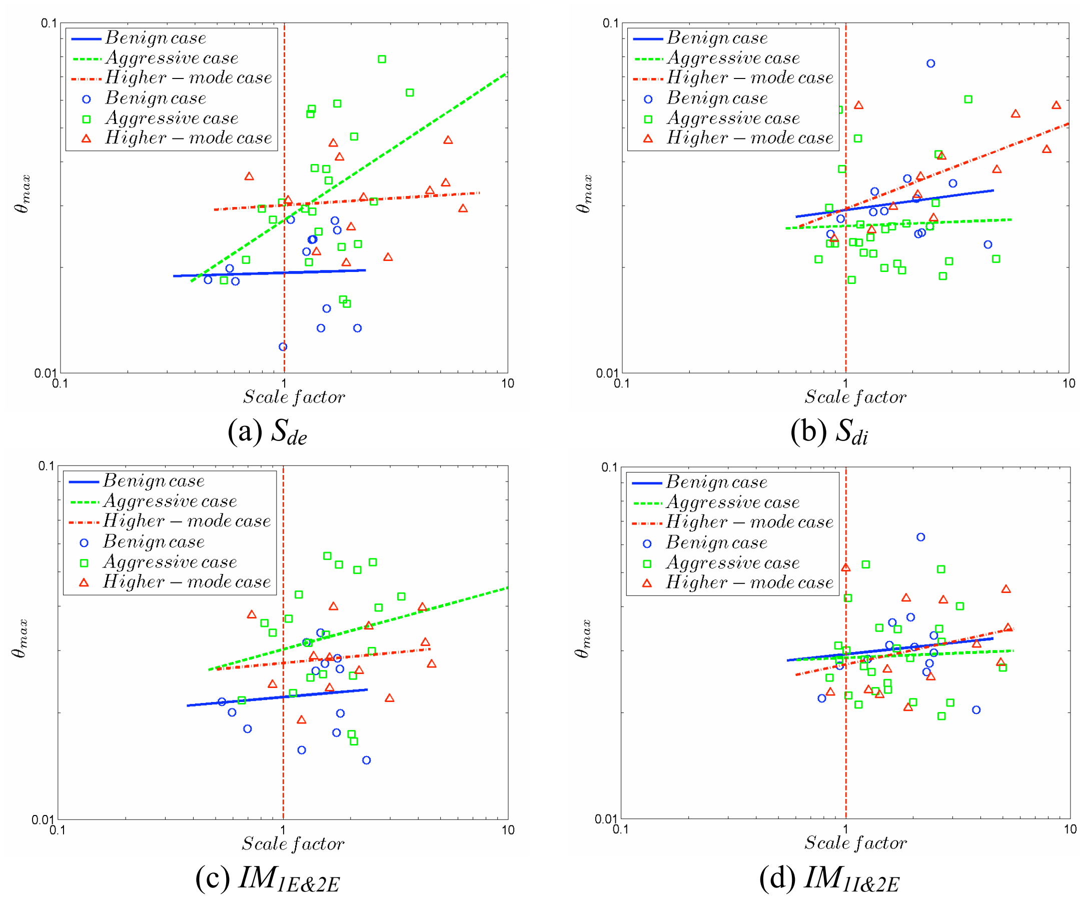

(a) S_{de} (b) S_{di} (c) $IM_{1E\&2E}$ (d) $IM_{1I\&2E}$

Fig. 5.8 Maximum interstory drift ratio (θ_{max}) versus scale factor for records scaled to common value of (a) S_{de}, (b) S_{di}, (c) $IM_{1E\&2E}$, and (d) $IM_{1I\&2E}$. Linear lines show the regression fits. Intersections of dashed vertical lines and fitted lines pinpoint median θ_{max} predicted for unscaled records. Example is for 0612 structure scaled to counted-median ductility (for 70 records) of 4.

On the other hand, using S_{di} alone cannot capture the higher-mode contributions imposed by higher-mode records. Similar to previous findings, a higher-mode factor (i.e., $IM_{1E\&2E}$ and $IM_{1I\&2E}$) is needed to capture higher-mode records in order not to introduce biases in the responses. $IM_{1I\&2E}$ appears to produce unbiased responses when records are scaled to the same intensity level for both first- and higher-mode dominated records. The results shown here bolsters the previous findings on the scaling robustness for S_{di} (for first-mode-dominated responses) and $IM_{1I\&2E}$ for near-source pulse-like records as well as ordinary records (e.g., Chapter 2; see also Tothong and Luco 2007).

5.6.2 Structural Response Hazard Curves

5.6.2.1 PSDA Results Using Aggressive, Benign, and Higher-Mode Records

To completely illustrate the probabilistic response prediction using advanced ground motion *IM*s, the pulse-like records are used to estimate the structural response hazard curves. Probabilistic seismic demand analysis (Chapter 2; see also Tothong and Luco 2007) is utilized as a tool to estimate the MAF of exceeding a specified value of a maximum interstory drift ratio (denoted as $\lambda_{\theta_{\max}}$).

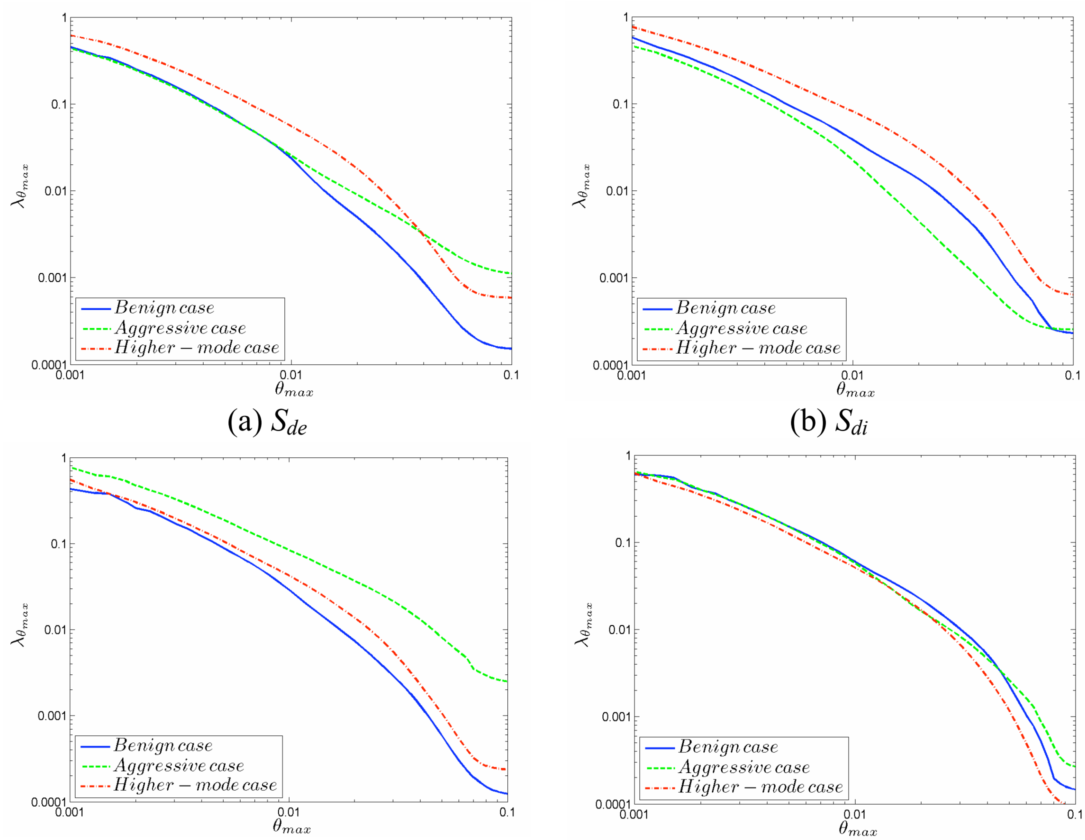

(a) S_{de} (b) S_{di}

(c) $IM_{1E\&2E}$ (d) $IM_{1I\&2E}$

Fig. 5.9 Structural response hazard curves for aggressive, benign, and higher-mode records when using (a) S_{de}, (b) S_{di}, (c) $IM_{1E\&2E}$, and (d) $IM_{1I\&2E}$ as *IM*.

The ground motion hazard is estimated from the Van Nuys site located in Southern California. The directivity effect is not expected at this site, but pulse-like records are intentionally used to illustrate the effectiveness of the advanced *IM*s.

For S_{de}, the structural response hazard curves, $\lambda_{\theta_{\max}}$, vary depending upon which record sets are utilized. Typically, the benign records cause smaller responses and hence may underestimate the MAF of exceeding a specified drift level. Likewise, the aggressive records result in overestimation of the MAF of exceeding a drift level (at least for θ_{max}>2%, see Fig. 5.9a). As mentioned above, the shortcomings of S_{de} and S_{di} are evident when higher-mode contribution is considerable, for example at a low-drift level for long-period structures. S_{de} and S_{di} cannot explain the variability in the responses due to higher modes (see Fig. 5.5a and b, respectively). This insufficient *IM* relative to higher mode in this case will ultimately result in the overestimation of $\lambda_{\theta_{max}}$, especially at low-drift levels (see Fig. 5.9a–b). Including a higher-mode factor can improve the response prediction. $IM_{1E\&2E}$ can capture the higher-mode responses but not the inelastic behavior of the first mode. As a result, $\lambda_{\theta_{max}}$ using $IM_{1E\&2E}$ subjected to the aggressive records is different (i.e., higher) from the other two sets (Fig. 5.9c).

As can be seen in Figure 5.9b and d, the variation of $\lambda_{\theta_{max}}$ among the aggressive, benign, and higher-mode records can be reduced when S_{di} and $IM_{1I\&2E}$ are utilized, as compared to that of S_{de} (Fig. 5.9a). The small differences seen in the figures are merely from the random sampling of a small sample size. The standard error (S.E.) of $\lambda_{\theta_{max}}$ (due to random sampling) can be estimated using the bootstrap technique (Efron and Tibshirani 1993). This is done by re-sampling records from the sample dataset repeatedly with replacement to generate bootstrap samples. Then, each bootstrap sample set will be used to calculate $\lambda_{\theta_{max}}$. The S.E. of $\lambda_{\theta_{max}}$ is simply the standard deviation of the replicated $\lambda_{\theta_{max}}$. The S.E. for $\lambda_{\theta_{max}}$ of these records is simply proportional (by a factor of $\sqrt{40/no.records}$) to those shown in Chapter 2. $\lambda_{\theta_{max}}$ for the three sets of records are not statistically different when using S_{di} (at least not for the higher-mode records) and $IM_{1I\&2E}$.

5.6.2.2 PSDA Results Using 70 Pulse-Like Records

The following comparison is performed when pool (i.e., 70) records are utilized. First, the structural response hazard curves using various *IM*s for ordinary and pulse-like records are compared in Figure 5.10. The structural response hazard curve using $<S_{de}, \varepsilon>$ is also superimposed for comparison. For *ordinary* records, $\lambda_{\theta_{max}}$ using either the advanced *IM*s (S_{di} and $IM_{1I\&2E}$) or the vector *IM*, $<S_{de}, \varepsilon>$, result in approximately the same curve. This statement is also valid for the other structures (see Chapter 2; and also Tothong and Luco 2007).

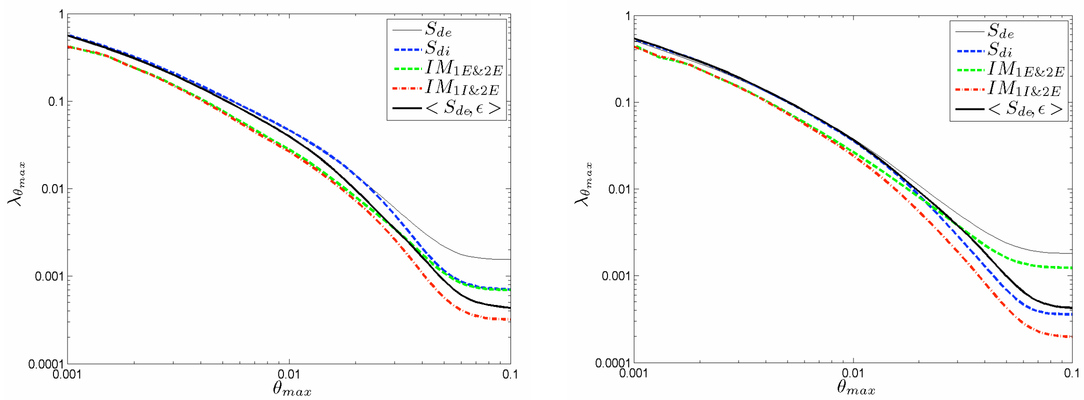

(a) (b)

Fig. 5.10 Structural response hazard curves for 0612 structure using S_{de}, <S_{de}, ε>, S_{di}, $IM_{1E\&2E}$, and $IM_{1I\&2E}$ as IM for (a) 40 ordinary and (b) 70 pulse-like records.

For *near-source* pulse-like records, <S_{de}, ε> is not effective when using records from only a specific T_p/T_1 bin. However, using a broad range of T_p/T_1 records *averages* out the benign and aggressive responses, resulting in a similar $\lambda_{\theta_{\max}}$ result as that of ordinary motions (Fig. 5.10b). The result, in general, may *not* be accurate because selection of T_p/T_1 records should be dictated by the hazard at the site, and using all pools of T_p/T_1 records in that case may not be appropriate. It should be noted that (for S_{de} and < S_{de}, ε >) the result of pool pulse-like records will depend upon the relative number of aggressive and benign records in the dataset. Including parameter T_p with <S_{de}, ε> could help improve the probabilistic response prediction. The conditional (joint) probability density function of T_p and ε at a specified S_{de} level is needed, which can be estimated from the proposed PSHA framework explained in Chapter 4 (see also Tothong et al. 2007). It also explained how one should select records for a site close to faults when S_{de}–based is employed.

To effectively compare the results between ordinary and pulse-like records, the bootstrap technique (explained previously) is performed and illustrated in Figure 5.11. The results can be considered satisfactory when (1) the median value for the MAF of collapse is in the range of 2-3×10^{-4} (based on Fig. 5.10) and (2) the plus/minus one standard error bands of the two sets overlap (or are close) to each other (as a first-order significance test; Hastie et al. 2001).

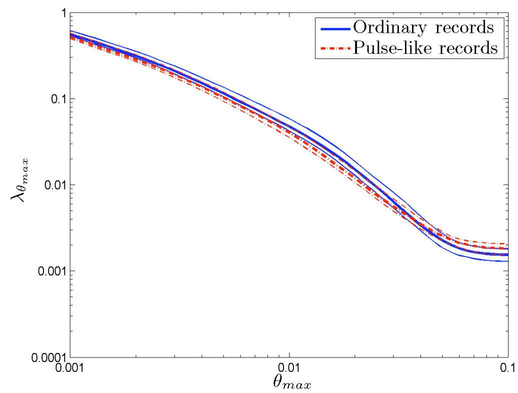

(a) S_{de}

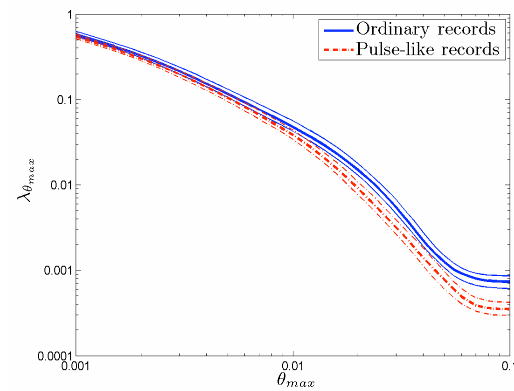

(b) S_{di}

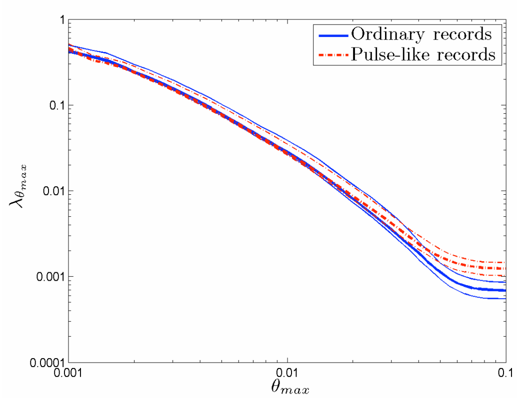

(c) $IM_{1E\&2E}$

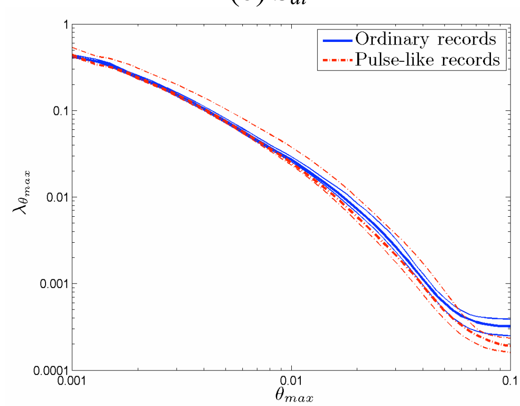

(d) $IM_{1I\&2E}$

Fig. 5.11 Bootstrap results estimating median (heavier lines) and its plus/minus one standard error bands (lighter lines) for structural response hazard curves computed using (a) S_{de}, (b) S_{di}, (c) $IM_{1E\&2E}$, and (d) $IM_{1I\&2E}$ as *IM*. Example is for 0612 structure.

A statistically significant test is reported by the p-values of the difference between the median $\lambda_{\theta_{\max}}$ for the ordinary and pulse-like records. The hypothesis testing on whether the results are indeed an effect of using insufficient *IM*s or simply a variability of record-to-record is due to the small sample size estimation. P-values are determined simply from the bootstrap results determined previously. The statistics here are simply the median ratio of $\lambda_{\theta_{\max}}$ (or simply the mean value of the difference in replicated $\ln \lambda_{\theta_{\max}}$) for near-source and ordinary records. P-values are determined as the probability of t-statistics to be as large as or greater than the observed value (in absolute term) assuming that the underlying mean values of both set are the same. The parameters for the observed statistics are determined from the bootstrap results.

P-values (for all *IM* considered) reporting the difference in the median ratio of $\lambda_{\theta_{\max}}$ between ordinary and pulse-like records are mostly greater than the 5% significant level for the

0612 structure. A small p-value (at 5% significant level) indicates that $\lambda_{\theta_{\max}}$ of the ordinary and pulse-like records are statistically significantly different (assuming the underlying $\lambda_{\theta_{\max}}$ is the same for both record sets). A large p-value (i.e., greater than 5%) indicates the opposite effect, implying the effectiveness (i.e., sufficiency) of the *IM*. Therefore, using either ordinary or pulse-like records produces statistically equivalent nonlinear dynamic analysis results of the structures. This coincidence does not, however, mean that the estimated responses are correct or unbiased, i.e., results using either ordinary or pulse-like records can both be *biased* when a poor choice of (insufficient) *IM* is used (i.e., S_{de} and < S_{de}, ε > subjected to pulse-like motions). The IDA results or drift hazard curves using S_{de} or < S_{de}, ε > will typically depend upon the relative number of aggressive or benign pulse-like records used in the record set. Only the 70 pulse-like record set used in this study coincidently produce such (the same) results as ordinary motions (for the S_{de}–based *IM*s). As shown in previous sections with a careful study on the effect of pulse-like motions by T_p/T_1 bin, the nonlinear dynamic analysis results are significantly different depending upon the relative periods of T_p and the modal periods of the structure. This section deserves noting that selecting the pulse-like motions for a structure can be misleading if records are not selected carefully. It is likely that investigators may conclude the results (subjected to a broad range of T_p/T_1 pulse-like motions) to be approximately the same nonlinear dynamic analysis results as those using ordinary motions when S_{de} or < S_{de}, ε > are used. Using the advanced *IM*s (i.e., S_{di} and $IM_{1I\&2E}$) can produce the same nonlinear dynamic analysis results regardless of the relative number of aggressive or benign records in the pool record set (as illustrated in the previous section).

Overall, using S_{di} (for first-mode-dominated structures) and $IM_{1I\&2E}$ (for structures with significant higher-mode cases) can sufficiently characterize the response due to ordinary and pulse-like records. The higher-mode factor appears to be significant especially at low levels of nonlinearity. The bootstrap results of $\lambda_{\theta_{\max}}$ for ordinary and pulse-like motions indicate that the results are not statistically different (at 5% significant level). P-values are greater than 5% for almost all cases, implying the insignificant difference between ordinary and pulse-like cases. The difference seen is merely the variability of using a small sample size. However, this may be misleading in a case, for example, that $\lambda_{\theta_{\max}}$ of both record sets tend to bias (not correct) the response prediction in the same way, at least for S_{de} and $IM_{1E\&2E}$. For example, S_{de} and $IM_{1E\&2E}$

overestimate the $\lambda_{\theta_{\max}}$ for both ordinary and pulse-like sets, and they are not statistically different from each other.

5.7 DISCUSSIONS

To perform seismic risk analysis of a structure located either close to or away from a fault, the structural analysis results and ground motion hazard at the site need to be combined using PSDA. Even for the close-to-fault case, for S_{di} or *any IM* that is sufficient with respect to the pulse-like property of certain near-field records, only the marginal probability distribution of the *IM* (i.e., ground motion hazard) is needed. For the sufficient *IM*, the structural analysis results (e.g., the IDA statistics or the conditional distribution of $\theta_{\max}$ versus *IM*) using either ordinary or near-source pulse-like records are statistically equivalent. In principle, ordinary or pulse-like records can be selected and used to perform nonlinear dynamic analyses. This property is a clear advantage of using sufficient (with respect to M_w, R_{rup}, ε, and T_p) *IM*s. This, perhaps, unintuitive conclusion does not mean that a site with the potential for experiencing severe pulse-like near-field records is not different from another site where pulses are not expected. For these sufficient *IM*s, the differences between the two sites will show up in the PSHA *IM* hazard curves and not in the response distributions. The challenge becomes to carefully estimate the hazard curves in these two cases. For a non-near-source site, it is necessary to have only the S_{di} attenuation models such as those presented in Chapter 3. For near-source sites where directivity may be an issue, a more extreme modification to familiar PSHA is necessary. This PSHA is described in Chapter 4.

In terms of S_a or other such *insufficient IM*s (as mentioned previously), for near-field sites the larger vector *IM* (S_a, ε, *and* T_p) could be used in conjunction with the disaggregation results of S_a on ε, T_p, and the probability of expecting pulse at a given intensity level. In addition, a detailed record selection would need to be made and nonlinear dynamic analysis performed separately for *ordinary* motions and for *pulse-like* motions with different T_p values. This is because the hazard for the site close to faults will be separated into non-near-source and near-source cases. Therefore, the results need to be combined separately according to the probability of experiencing pulse (analogous to the approach described in Chapter 4). This approach is tedious and likely impractical in all but very special cases. Further selecting records based on ε and T_p would today still be very difficult if not impossible; selecting records based on ε for ordinary ground motions is already problematic when extreme ground motions (i.e., low-hazard ground motions) are needed and scarce. There are not many two or two-plus epsilon records available from the current NGA ground motion databases (http://peer.berkeley.edu/nga/).

Elastic-based *IM*s (such as S_a and $<S_a, \varepsilon>$) cannot capture the sharp change exhibited in the spectral shape of pulse-like motions. S_a and $<S_a, \varepsilon>$ are not sufficient because they predict responses based on the *local* spectral shape at or near T_1. This is acceptable for ordinary records due to the slow decay of the correlation function of $\ln S_a$ between the two periods decays slowly, and the slope of the conditional median spectra of two or more epsilon does not change until the period ratio is about three or more. This issue will be discussed in more detail in Chapter 6.

5.8 CONCLUSIONS

Pulse-like motions are known to cause severe damage to structures depending upon the strength of the structure as well as the relative modal vibration periods of the structure and the dominant period of the pulse-like records (T_p/T_1). To describe strong earthquake records at low-hazard levels, pulse-like records may be selected. This study investigates the effect of pulse-like on structures using advanced *IM*s.

By investigating the relationship between the responses conditioned on S_a or $<S_a, \varepsilon>$ versus T_p/T_1, it is clear that the response of a structure depends on T_p/T_1. Which T_p/T_1 records should be used depends on the seismic hazard at the site. This information varies from site to site and structure to structure. Ignoring the effects of pulse-like records, T_p/T_1, will ultimately bias the results. For example, if the seismic hazard disaggregation suggests that extreme motions are associated with records having T_p/T_1 of about two, but records are selected from a wide range of T_p/T_1, the S_a-based result will underestimate the seismic risk imposed by the hazards.

The results of structural response hazard curves using the elastic-based *IM*s (e.g., S_a and $<S_a, \varepsilon>$) will depend on how records are selected — i.e., conservative results when using aggressive records and unconservative results when using benign records (aggressive records are defined as records tending to cause relatively severe inelastic displacement ratio, S_{di}/S_{de}, and vice versa for benign records). In general, engineers and/or earth scientists do not know in advance whether or not the future record will contain a pulse; thus, ultimately using such records will alter the seismic performance of structures. For example, the median collapse capacity (in terms of *IM*) can be systematically dictated by including a few aggressive or benign pulse-like records into the record set used for analyzing the capacity of the structure.

The results of this study demonstrate that scaling earthquake records using advanced *IM*s (such as S_{di} and $IM_{1I\&2E}$; the latter is for the significant higher-mode contribution structures) subjected to pulse-like records is *efficient*, *sufficient*, and *robust* relative to scaling records. The results are statistically equivalent to the seismic performance values, $\lambda_{\theta_{\max}}$, carried out by using ordinary records. This is mainly because S_{di} can directly capture the sharp change in the pulse-like spectral shape of each record directly. Therefore, the degree of nonlinearity is captured automatically. By scaling records using S_{di} or $IM_{1I\&2E}$ to achieve the same median displacement level (i.e., the same ground motion intensity level), the aggressive records will be scaled less than the benign records, resulting in comparable (median) drift values. The main reason is that S_{di} contains a proxy for the strength of the structure (Alavi and Krawinkler 2001; Bazzurro and Luco 2006).

In addition to M_w, R_{rup}, and ε, inelastic-based *IM*s (i.e., S_{di} or $IM_{1I\&2E}$) are also sufficient with respect to the T_p, an important characteristic of the pulse-like records. This is a clear benefit of implementing the inelastic-based *IM*s. This ultimately implies that a detailed record selection is not necessary. Any ground motion records (any M_w, R_{rup}, ε, or T_p) can be selected and scaled; the conditional response distribution is statistically the same (in other words, the IDA results are the same). The conditional probability distribution of response on M_w, R_{rup}, ε, T_p, and *IM* is statistically equivalent to simply the probability distribution of response conditioned on *IM* alone. The only difference between a site located near a fault or away from a fault is only the (marginal) ground motion hazard curve (this information is illustrated in Chapter 4). With sufficient *IM*s, only the seismic hazard needs to be determined appropriately for a designated site. The conclusions drawn here are based on the generic-frame structures considered, which cover a range of structural configurations (i.e., number of stories, the first-mode period, first- or higher-mode dominated structures). To make a more general conclusion, a number of structures can be analyzed in the same fashion.

6 PSDA: Validation of *IM*-Based Approach by Simulation

6.1 INTRODUCTION

Estimating the seismic risk of a structure at a designated site would be relatively straightforward if earthquake records from all seismic sources in the region had been recorded there for millions of years. With unlimited computational resources, the seismic performance of a structure could be determined easily. Following the same basis, a simulation approach has been utilized to investigate the seismic performance of a structure at a designated site. The approach simply generates earthquake ground motions (thousands or more) from causative earthquake faults in the region for a site of interest. Nonlinear dynamic analyses of the structure are then performed using those simulated records. Assuming that the simulated records are representative of real (as-recorded) motions, the seismic performance evaluation can be easily determined and considered to be the "exact" results. (In this chapter, the term "exact" refers to the results determined using simulated ground motions, and not necessarily the results determined using real ground motions.) Clearly, without sufficient computational power (e.g., super computer), this method seems impractical for practicing engineers (and hence will likely remain within the research community).

Another approach to estimate the seismic performance (in a more efficient way) is to use the ground motion intensity-based (*IM*-based) approach. This approach has been utilized extensively by Cornell and co-workers and is referred to as probabilistic seismic demand analysis (PSDA). The U.S. Nuclear power industry has also used a similar method known as seismic PRAs (probabilistic risk assessments) for more than two decades (Hickman 1983). The advantage of this approach is that it requires far less intensive computing power. The seismic hazard at a site and the nonlinear dynamic analyses of the structures are decoupled. The effects of ground motion characteristics on the structures are assumed to be dependent *only* on the *IM*. Structural responses at a specified *IM* level are assumed to be *conditionally independent* of ground motion characteristics (i.e., earthquake magnitude (M_w), source-to-site distance (R), ground motion epsilon, faulting styles, etc.). As a result, the chosen *IM* is a crucial parameter for this approach.

Various ground motion *IM*s have been proposed in the past, for example, the *advanced* scalar *IM*s (i.e., the inelastic-based *IM*, Luco 2002) and the *vector IM*s (e.g., Bazzurro 1998; Bazzurro and Cornell 2002). The need for the vector *IM* is largely due to the use of the *insufficient* basis-*IM*, meaning the responses of a structure conditioned on *IM* depend upon ground motion record properties (Luco 2002). Using an insufficient *IM*, the results of nonlinear dynamic analysis will depend on how records are selected.

For *ordinary* records, a vector *IM* of S_a and ε (denoted as $<S_a, \varepsilon>$) has been shown to be an improved *IM* as compared to the basis S_a alone in probabilistic response prediction of nonlinear structures (Baker and Cornell 2005a). Note that ground motion epsilon (ε) is a proxy for measuring the deviation between the elastic spectral acceleration (S_a) of an as-recorded ground motion and the predicted (median) value from the ground motion prediction model at a given period (i.e., the attenuation relationship; for example, Abrahamson and Silva 1997). Advanced *IM*s (such as inelastic spectral displacement, S_{di}, and S_{di} with higher-mode mode factor, $IM_{1I\&2E}$) have been shown to be accurate in estimating the seismic performance of structures for both *ordinary* (see Chapter 2, and also Luco and Cornell 2006; Tothong and Luco 2007) and *near-source* pulse-like ground motions (Chapter 5, and also Luco and Cornell 2006; Tothong and Luco 2007). However, the question that remains unanswered is whether the final PSDA results using sufficient *IM*s are the "correct" values. In this study, this question will be investigated by means of simulation. Simulated ground motions will be generated and used as representative realizations of a scenario earthquake.

The objective of this chapter is to validate the structural performance evaluated using the *IM*-based approach (i.e., S_a, $<S_a, \varepsilon>$, and S_{di}) with the results of the simulation approach. The results from the simulation are considered to be "exact" and used as benchmark values against the *IM*-based approach.

6.2 SIMULATED GROUND MOTIONS AND GROUND MOTION HAZARD

6.2.1 Stochastic Ground Motion Model

To simulate earthquake ground motions for this study, a stochastic ground motion model (Stochastic-Method Simulation also known as SMSIM; http://quake.wr.usgs.gov/~boore/) developed by Boore (1983; 2003) is adopted. Other models (e.g., Atkinson and Silva 2000; Wen and Wu 2001) also exist. It is not the focus of this study to compare the results among different models; only Boore's model is considered. This stochastic approach is intended to simulate earthquake time series (accelerograms) using a point-source model with a desired (deterministic) Fourier amplitude spectrum determined from the empirical functional forms in terms of earthquake source, path, site, and instrument or types of motions. A detailed explanation of how to calculate the desired Fourier amplitude can be found in (Boore 2003).

To generate a ground motion, a white noise sequence (independent and identically distributed with a Gaussian distribution) of random variables is generated for a specified duration at a set of discrete time points. The noise is then windowed by applying a modulating function (in Boore's model an exponential window is utilized because Saragoni and Hart (1974) found that it is a good representation of the envelope of accelerograms). The windowed noise is transformed to the frequency domain using a discrete Fourier transform. The noise spectrum is then normalized by the square-root of the mean square amplitude to have, on average, unit amplitude. The normalized spectrum is then multiplied with the desired (or target) amplitude spectrum. The simulated ground motion in the time domain can then be obtained by performing inverse Fourier transform of the modified spectrum. The steps can be repeated to simulate as many ground motions as desired.

6.2.2 Seismic Hazard Analysis

For this exercise, we simplify the seismic threat to a single source that produces earthquakes on a common magnitude. This characteristic earthquake with M_w 6.8 occurs at a source-to-site distance of 18 km from a soil site. The mean rate of occurrence for this characteristic event ($\nu_{M_w,R}$) is assumed to be 1% per annum. The ground motion records for this scenario event are generated using the stochastic simulation method explained previously.

A total of 55,000 records are simulated using the SMSIM program. The ground motion hazard in terms of *IM* (λ_{IM} , i.e., MAF of exceeding an *IM* level) at this site can be simply determined as

$$\lambda_{IM}(x) = P[IM > x \mid event] = \nu_{M_w,R} \cdot \frac{\sum_i I_{IM_i > x}}{Total\ no.of\ records} \tag{6.1}$$

where $I_{IM_i>x}$ is an indicator variable of the i^{th}-record in terms of the *IM*. It is equal to unity if IM_i is greater than x, and zero otherwise. Figure 6.1 illustrates the ground motion hazard curves calculated in terms of S_{de} (at T_1) and S_{di} (T=T_1, d_y=0.364″) which will be used in seismic performance evaluations of a structure in a later section.

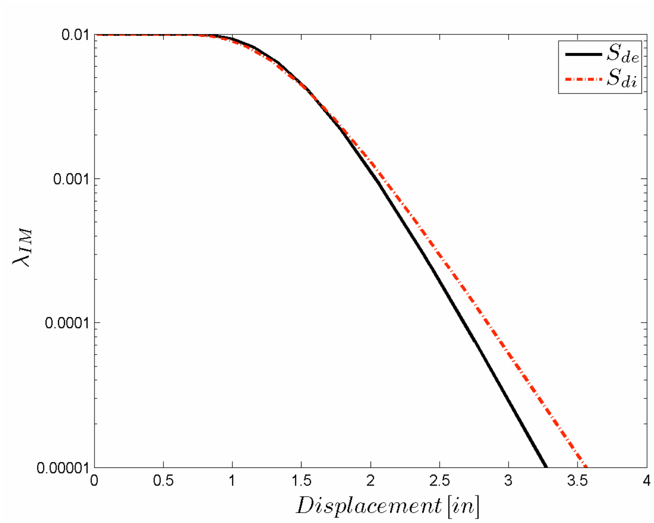

Fig. 6.1 Ground motion hazard curves in terms of S_{de} and S_{di} for structure considered.

6.3 PROBABILISTIC RESPONSE PREDICTION FOR A STRUCTURE

6.3.1 Simulation Approach

To evaluate the seismic performance of structures at a designated site, the uncertainties in the ground motions and nonlinear structures must be considered. Monte-Carlo simulation can be utilized, but this approach requires computationally intensive analyses to evaluate the seismic performance of a structure (e.g., Collins et al. 1996; Han and Wen 1997; Jalayer et al. 2004; Wen 2000). The marginal probability distribution of the response for a site can be directly estimated from nonlinear dynamic analysis results from records generated from the faults in the region. This procedure requires thousands of records to be simulated and analyzed through the structure in order to obtain accurate estimates of the extreme responses and ground motions. To improve the efficiency in the calculation, Wen and co-workers utilize a "de-aggregation" method, which selects only the magnitudes (M_w) and source-to-site distances (R) that contribute most to the performance limit states of interest, but this method is not applicable here as there is only a single magnitude and distance.

An oscillator with a strength-limited bilinear model (Ibarra et al. 2005) is used as an example structure for this study. The chosen structure has a period (T) of 0.9 sec with a yield displacement (d_y) of 0.364 in. The yield displacement is chosen such that the *median* strength-reduction factor (i.e., $\hat{S}_{de}/d_y$) is about 4[1]. The hardening stiffness ratio is 5%, the capping ductility ratio (defined as the displacement at peak strength divided by the yield displacement) is 4, and the post-capping stiffness ratio of -10% is used. The damping ratio equal to 5% is also used for the system. The nonlinear dynamic analyses were performed using Ibarra's model described in Ibarra and Krawinkler (2005) and Ibarra et al. (2005).

Similar to ground motion hazard curves, the structural performance evaluation (i.e., structural response hazard curves, denoted as λ_{EDP}) of a structure can be determined using the 55,000 records directly (*EDP* stands for an engineering demand parameter, the context used at the Pacific Earthquake Engineering Research Center; see e.g., Cornell and Krawinkler (2000); Moehle and Deierlein (2004)). Each simulated record is processed through the structure via nonlinear time-history analysis. The indicator variable, $I_{IM_i>x}$, shown in Equation 6.1 is simply replaced with $I_{EDP_i>x}$ to estimate λ_{EDP}.

Due to the limited number of simulated ground motions, the exact λ_{EDP} is also uncertain because we are interested in very low probabilities. To estimate this variation, at each specified *EDP* value, x, the standard error (S.E.) for λ_{EDP} can be estimated as (as with Bernoulli trials)

$$S.E.\left(\lambda_{EDP}(x)\right) = \nu_{M_w,R} \cdot \sqrt{\frac{\hat{p}\cdot(1-\hat{p})}{Total\,no.of\ records}} \qquad (6.2)$$

where $\hat{p}$ is simply $\sum_i I_{EDP_i>x}/Total\,no.of\ records$. The exact seismic demand hazard curve is shown in Figure 6.2 along with its +/- one standard error bands.

[1] The median strength-reduction factor is determined as the median S_{de} values (at the period of the structure) of the record set divided by the yield displacement.

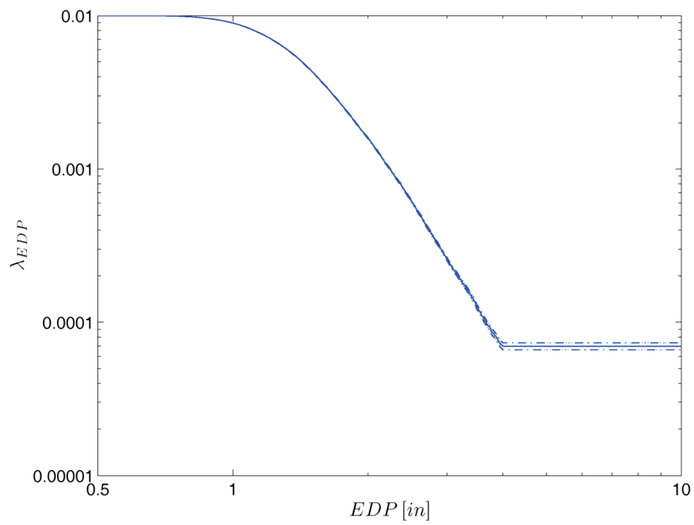

Fig. 6.2 Seismic demand hazard curves determined from simulation approach.

The flat line shown in Figure 6.2 indicates the MAF of collapse for the considered oscillator. The collapse limit state corresponds to a displacement larger than 4 inches (or ductility, S_{di}/d_y, of about 11). This number is based on inspection of the incremental dynamic analysis (IDA) results (shown later) where most IDA curves appear to be flat. In this chapter, this displacement-based collapse limit state is used because a clear definition of collapse needs to be set in order to be consistent when the *IM*-based results are compared with simulation. Out of 55,000 records, there are 384 ground motions that cause the oscillator to collapse (i.e., that cause a displacement greater than 4 in). Hence (Eq. 6.1) the estimated hazard curve becomes flat at 0.01×384/55,000= 0.0000698. This result will be discussed further in the following section. The standard error of estimation of this estimate is approximately (Eq. 6.2) $0.01\times\sqrt{384/55000^2}$ = 0.0000036, or about 5% of the MAF of collapse. Note that this percentage is independent of $\nu_{M_w,R}$; it depends only on the total number of records and $P[EDP>x|\text{ event}]$, which here is about 0.7%. A rule of thumb is that one needs a sample of size n = 100/p to obtain a standard error of 10% of p; therefore even if 10% of all events were collapses, the requisite sample size would be 1000.

6.3.2 *IM*-Based Approach

As seen above, estimation of seismic performance of structures using the simulation method is *not* efficient (i.e., a large number of records are required). To estimate seismic performance with a relatively small number of records, the *IM*-based PSDA can be utilized. $\lambda_{EDP}(x)$ can be calculated as

$$\lambda_{EDP}(x) = \int G_{EDP|IM}(x \mid im) \cdot d\lambda_{IM}(im) \tag{6.3}$$

where $G_{EDP|IM}$ is the Gaussian complementary cumulative distribution function of *EDP* conditioned on *IM* defined as

$$G_{EDP|IM}(x \mid im) = 1 - \Phi\left(\frac{\ln x - \propto_{\ln EDP|im}}{\sigma_{\ln EDP|im}}\right) \tag{6.4}$$

The estimated (conditional) mean and standard deviation of ln*EDP* (denoted $\propto_{\ln EDP|im}$ and $\sigma_{\ln EDP|im}$, respectively) can be estimated from the IDA results at a specified *IM* level. $d\lambda_{IM}(im)$ is the successive difference of the seismic hazard curve, which is equal to $\lambda_{IM}(im) - \lambda_{IM}(im + dim)$, which is approximately the MAF of *IM* = *im*. *dim* is a small increment in the ground motion intensity. Details for this method can be found in Chapter 2 and in Tothong and Luco (2007).

A relatively small number of records (40) is randomly selected from the 55,000 motions. Its median spectra and individual records are shown in Figure 6.3. The median spectra obtained from 55,000 records are also shown for comparison.

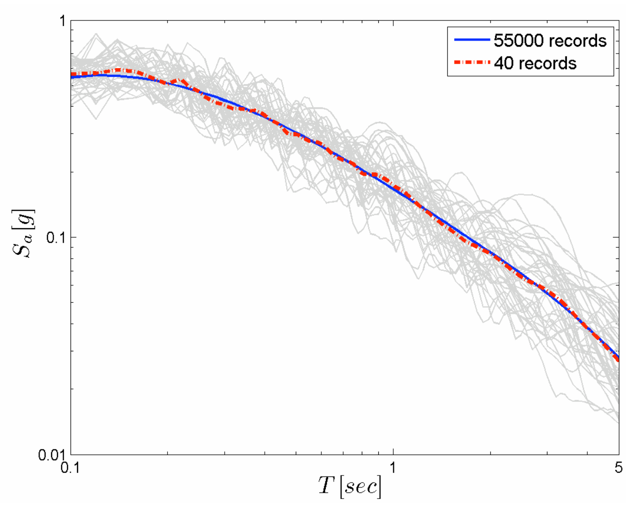

Fig. 6.3 Median and individual response spectra for 40 randomly selected records. Median spectrum for 55,000 records is also shown for comparison.

These 40 records are used to perform nonlinear dynamic analysis using the structure considered. IDA results using S_{de} (or equivalently S_a, where $S_a = (2\pi/T)^2 \times S_{de}$) and S_{di} are shown in Figure 6.4. The circles indicate the intensity levels associated with global dynamic instability of the structure. These IDA results are combined with their seismic hazards to estimate λ_{EDP}.

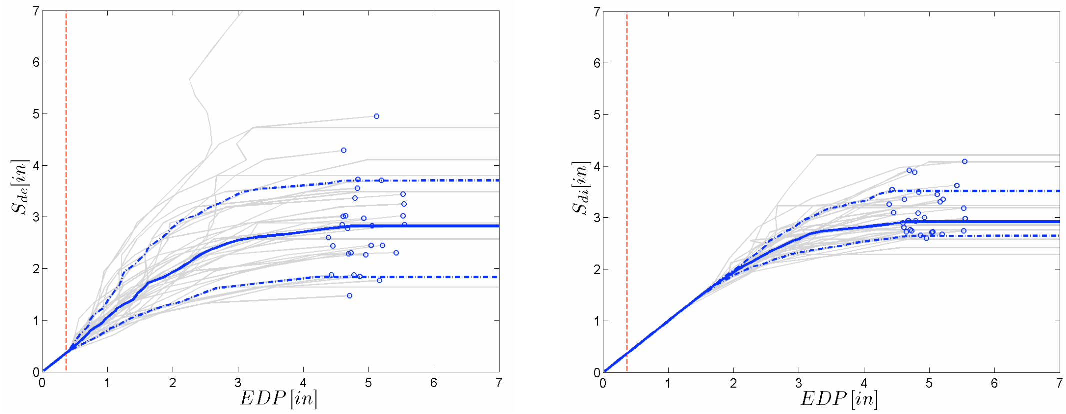

(a) (b)

Fig. 6.4 Median IDA (solid lines) curves and +/- one standard deviation bands (dashed-dotted lines) of 40 records using (a) S_{de} (or equivalently S_a) and (b) S_{di}. Vertical dashed lines indicate yield displacement, d_y, of structure.

For S_{de} or S_a subjected to ordinary records, Baker and Cornell (2005a) have shown that simply using S_a alone in probabilistic response prediction is not sufficient because of the spectral shape associated with ε. At a specified S_{de} or S_a level, *positive* ε records create weaker responses than *negative* ε records. Therefore, response estimation using S_{de} or S_a alone may be biased depending upon which records are selected. Indeed, in principle, to produce IDA using S_{de} as the *IM*, different records are needed at each level because the appropriate epsilon levels are increasing as the *IM* level increases. To overcome this biased estimation, a *vector IM* (i.e., $<S_a, \varepsilon>$) needs to be utilized. The exact λ_{EDP} is used as a basis against that of $<S_a, \varepsilon>$. Using $<S_a, \varepsilon>$ to estimate λ_{EDP}, a slight modification to Equation 6.3 is needed and is shown as follows:

$$\lambda_{EDP}(x) = \int\int G_{EDP|IM,\varepsilon}(x \mid im, e) \cdot f_{\varepsilon|IM}(e \mid im) \cdot de \cdot d\lambda_{IM}(im) \quad (6.5)$$

where $f_{\varepsilon|IM}$ is the conditional probability density function of ε at a specified *IM* level. This probability density function can be directly obtained from seismic hazard disaggregation results.

To implement $<S_a, \varepsilon>$ in estimating λ_{EDP}, two techniques can be utilized: (1) by using regression analysis (via Eq. 6.5) or (2) by selecting records to match the ε distribution at a given S_a level. To illustrate the similarity of these techniques, the collapse fragility *surfaces* (as a function of S_a and ε) are shown in Figure 6.5. The collapse fragility surface for the ε-based selection is demonstrated for an ε value of about 3 (the darker color). As seen in Figure 6.5, the two techniques yield approximately the same prediction for the probability of collapse versus S_{de} (Note, though, that the collapse fragility surface for the regression analysis is extrapolated when S_{de} is greater than 5 in.)

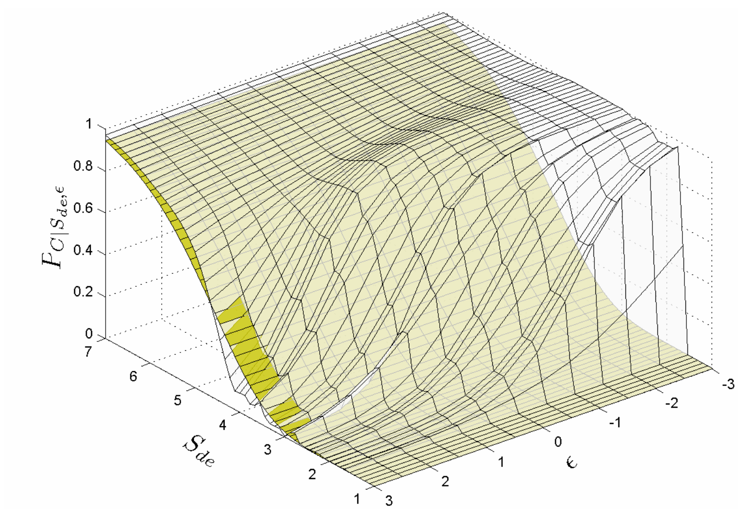

Fig. 6.5 Collapse fragility surface using <S_{de}, ε>: (1) regression analysis (transparent color) and (2) ε-based selection technique with 3ε (solid color).

The probabilistic response prediction using <S_a, ε> is then combined with the hazard curve to estimate the MAF of exceeding a level of responses, λ_{EDP}, (see Fig. 6.6). At a glance, structural performance using S_{de} (S_a) seems to be conservatively estimated, while using <S_a, ε>, in this case, underestimates λ_{EDP} (i.e., unconservative). Only the estimated λ_{EDP} using S_{di} is shown to be accurate.

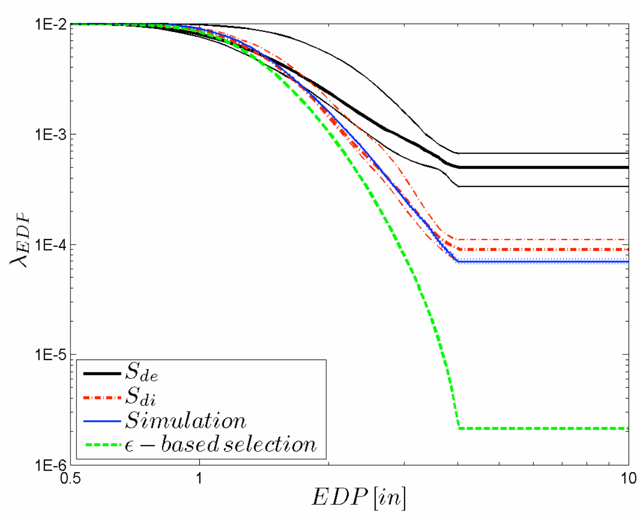

Fig. 6.6 Seismic demand hazard curves, λ_{EDP}, using various methods.

The differences seen between the exact and the estimated λ_{EDP} using S_{di} are merely due to the effect of random sampling with a finite sample size. The standard error (S.E.) bands for λ_{EDP} using the *IM* approach can be estimated using the bootstrap technique (Efron and Tibshirani 1993). The S.E. can be estimated by re-sampling records from the sample dataset repeatedly with replacement to generate bootstrap samples. Then, each bootstrap sample set will be used to calculate λ_{EDP}. The S.E. of λ_{EDP} is simply the standard deviation of the replicate λ_{EDP}.

As mentioned previously, the structure is considered to collapse when the inelastic displacement of the structure is greater than 4 inches. The collapse limit state is crucial for comparing the results between the simulation and *IM*-based approach.

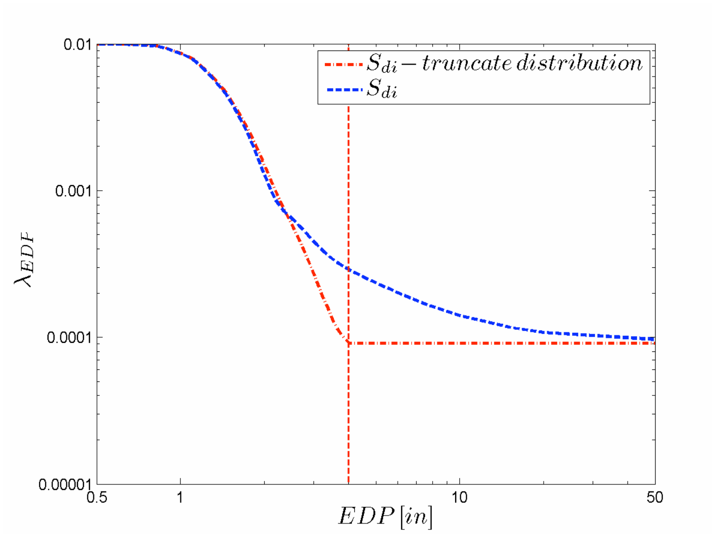

Fig. 6.7 Structural response hazard curves using (1) flat IDA curves as collapse limit state definition and (2) with specified collapse displacement with truncate distribution.

Figure 6.7 demonstrates the structural response hazard curve using Equation 6.3 when collapse is defined as the intensity such that the IDA curve becomes flat (dashed line). The gap between the MAF of collapse (i.e., 10^{-4}) and λ_{EDP} at displacement of, for example, 10 inches is basically the MAF (or probability) of *EDP* exceeding 10 inches and not collapsing. However, from the simulation results, the largest displacement that converges (without collapse) is about 5.3 inches. As a result, an inconsistency may exist when the collapse definition is not explicitly stated. Second, with a specified collapse displacement, the probabilistic response prediction at a specified *IM* level *needs* to be truncated at that collapse displacement. The truncated Gaussian complementary cumulative distribution function of *EDP* conditioned on *IM* ($G^*_{EDP|IM}$) can be calculated as

$$G^*_{EDP|IM}(x \mid im) = \begin{cases} \dfrac{G_{EDP|IM}(x \mid im) - G_{EDP|IM}(collapse\ displacement \mid im)}{1 - G_{EDP|IM}(collapse\ displacement \mid im)} & ; x \leq 4 \\ 0 & ; otherwise \end{cases} \tag{6.6}$$

$G^*_{EDP|IM}$ is used in Equations 6.3 and 6.5 for the scalar and vector IMs, respectively, to estimate λ_{EDP} in Figure 6.6. The estimated statistical parameters (mean and standard deviation) are still determined from all of the data at a specified IM level.

6.4 WHY IS <S_a, ε> NOT EFFECTIVE IN PREDICTING STRUCTURAL RESPONSES FROM SIMULATED GROUND MOTIONS?

The results shown in Figure 6.6 for <S_a, ε> contradicts the conclusion by Baker and Cornell (2005a) for ordinary ground motions. This may be explained by closely investigating the response spectra of simulated records, especially those of the positive ε records (see Fig. 6.8).

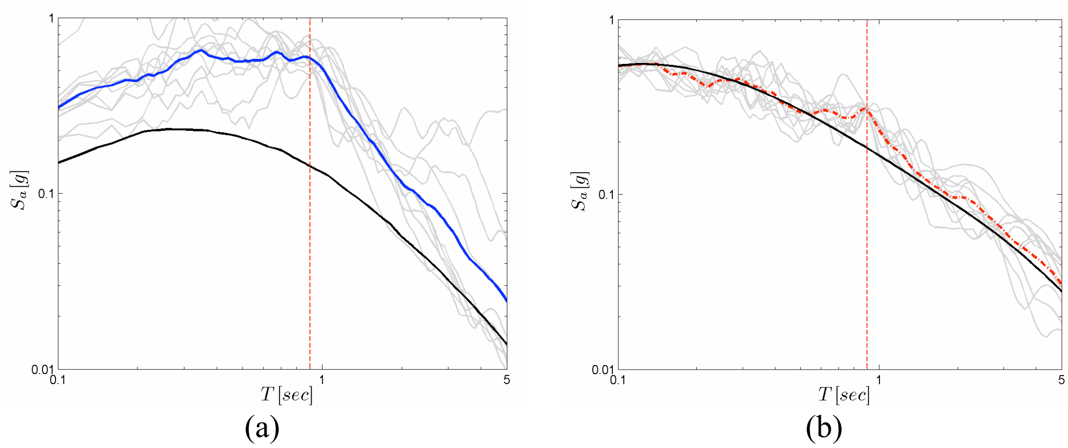

Fig. 6.8 Median and individual response spectra of 10 positive ε (of about 2) records for (a) ordinary and (b) simulated ground motions. Median spectra of all records are also shown for comparison (lower solid lines). Vertical dashed lines indicate natural period of structure, T_1.

The dramatic difference in the spectra of these high positive epsilon spectra can be observed in their (1) median (geometric mean) values of S_a, (2) the standard deviation of lnS_a, and (3) the spectral shape. For as-recorded ground motions, the spectral ordinates decrease slowly as the period ratio from the reference period (T_1 in this case) increases or decreases (as a result, the slope of the spectra from T_1 is approximately the same until the period ratio is about three). For the simulated records, the spectral values drop rapidly with increasing or decreasing period ratio (as a result the slope of the spectra change relatively quickly as the period ratio increases). This rapid change in the slope for the spectra may be the reason why <S_a, ε> is not so effective here in estimating severe nonlinear behavior. Recall that <S_a, ε> predicts the responses based on the *local* slope at T_1. The sharp change in the slope for median spectra of the record set can reduce its effectiveness, a problem of <S_a, ε> also seen with *near-source* pulse-like ground motions. The conditional median spectral shape for the positive ε can also be viewed from the spectral (auto-) correlation function of lnS_a at two periods ($\rho_{\ln S_a(T_i),\ln S_a(T_j)}$). As seen in Figure 6.9, $\rho_{\ln S_a(T_i),\ln S_a(T_j)}$ of as-recorded motions is calculated from the 291 ordinary ground motions used in Chapter 3 (see also Table A.3), and $\rho_{\ln S_a(T_i),\ln S_a(T_j)}$ for simulated records is determined from the 55,000 simulated motions. The correlation function estimated from recorded motions by Baker and Cornell (2006a) is also shown for comparison.

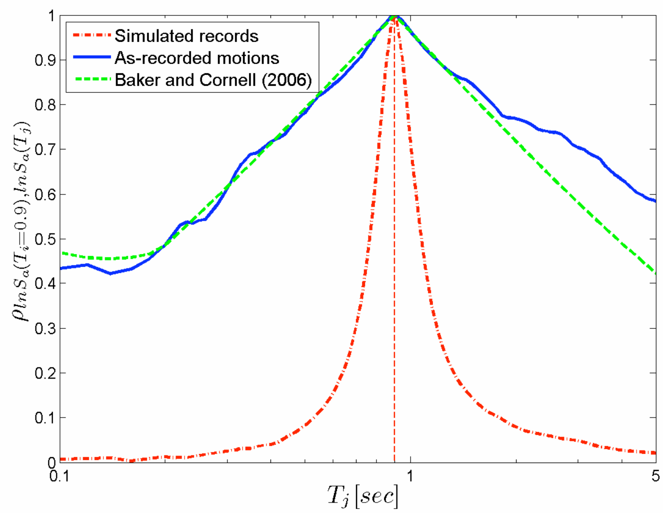

Fig. 6.9 Empirical spectral correlation functions of lnS_a at two periods. Reference period is 0.9 sec (period of structure considered).

The correlation function is valuable because (with a mild assumption that ln$S_a(T_i)$ and ln$S_a(T_j)$ are jointly lognormal) the conditional *median* spectral shape is a function of the spectral correlation function, which is the exponential of

$$E\left[\ln S_a\left(T_j\right) | \varepsilon_{\ln S_a(T_i)}\right] = E\left[\ln S_a\left(T_j\right)\right] + \sigma_{\ln S_a(T_j)} \cdot \rho_{\ln S_a(T_i),\ln S_a(T_j)} \cdot \varepsilon_{\ln S_a(T_i)} \tag{6.7}$$

where $E[\cdot]$ is the expected value of $[\cdot]$. $\sigma_{\ln S_a(T_j)}$ is the standard deviation of ln$S_a(T_j)$. The narrowbanded $\rho_{\ln S_a(T_i),\ln S_a(T_j)}$ seen for the simulated records has also been observed for near-source pulse-like records (see Chapter 4). For this type of ground motion, ε has been shown to be *ineffective* in predicting the responses of the structures (Baker and Cornell 2005b). To demonstrate this ineffectiveness of ε for narrowband-spectral type records, records with ε values of about two are selected for both as-recorded (ordinary) and simulated ground motions at 12 different periods (10 records for each period). The selected T_i's are associated with T_i/T_1 equal to 0.7–1.2 with 0.1 intervals and 1.4–2.4 with 0.2 intervals. The conditional median spectra of these motions are illustrated in Figure 6.10.

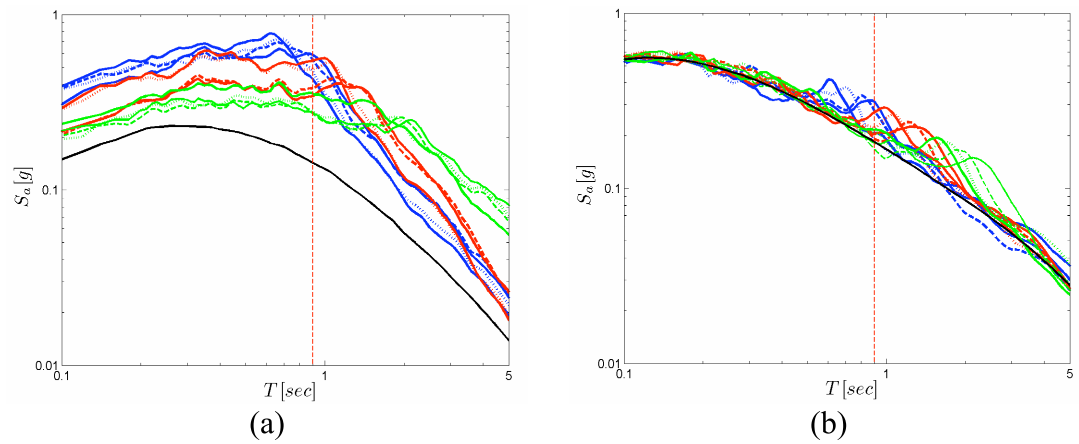

Fig. 6.10 Conditional median spectra for positive ε records at different periods for (a) as-recorded and (b) simulated ground motions. Median spectra of all records also shown for comparison (lower solid lines). Vertical dashed lines indicate period of structure.

The motivation here arises from the near-source pulse-like study (in Chapters 4 and 5) that showed that the responses of a structure depend on the relative periods between the pulse period and the modal periods of the structure (T_p/T_1). Since the simulated records exhibit the narrowband $\rho_{\ln S_a(T_i),\ln S_a(T_j)}$, the responses of the structure may also depend on the relative periods[2]. If so, then <S_a, ε> may not be effective, and the results should provide the explanation seen in Figure 6.6.

Structural responses as a function of (T_i/T_1) for as-recorded and simulated ground motions are shown in the following figures when using S_a and <S_a, ε> (the records are scaled to a counted-median ductility of about four). The moving-window average (Hastie et al. 2001) is superimposed in the figures to emphasize the dependency of responses on T_i/T_1 (solid lines). There is no obvious trend between the residuals of the responses given S_a or <S_a, ε> for as-

[2] Records with the period ratio (T_i/T_1) of about unity tend to create the responses smaller than the average values and vice versa for the period ratio of about two.

recorded ground motions. The strong trend (for the simulated records) between the residuals of *EDP* given S_a or $<S_a, \varepsilon>$ can be clearly observed (see Fig. 6.11b and d, respectively).

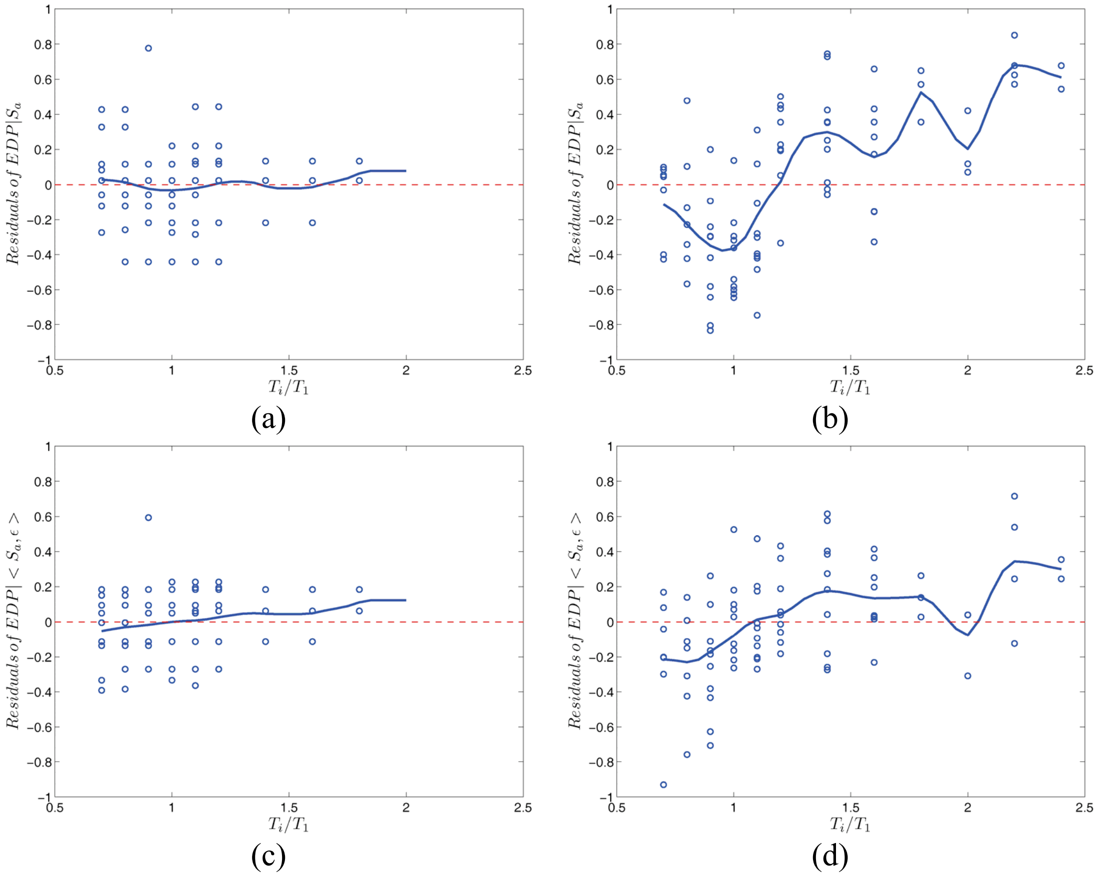

Fig. 6.11 Residuals of responses when using either S_a for (a) as-recorded and (b) simulated ground motions, or $<S_a, \varepsilon>$ for (c) as-recorded and (d) simulated ground motions.

The behavior is similar to that of near-source ground motions (see Chapter 5). As seen in Figure 6.11b and d, the responses obtained from records with periods close to the fundamental period of the structure will, in general, produce responses smaller than records with peaks at periods of about $1.5T_1$ or longer. This observation implies mainly that the inelastic responses of the structures would depend on how the records are selected. Since the S_a and $<S_a, \varepsilon>$ approach will select records with T_i/T_1 of exactly unity, the observed response prediction will be, on average, smaller than it should be (consistent with the results shown in Fig. 6.6). This explanation confirms the ineffectiveness (specifically *insufficiency*) of S_a and $<S_a, \varepsilon>$ with respect to simulated ground motions (with narrowband $\rho_{\ln S_a(T_i),\ln S_a(T_j)}$).

As a result, the spectral correlation function, $\rho_{\ln S_a(T_i),\ln S_a(T_j)}$, or the CMS for positive ε may be used as a guideline to determine the effectiveness of the vector *IM*, $<S_a, \varepsilon>$ for different types of ground motions (e.g., soft-soil, near-source, etc.). For example, if the slope of the $\rho_{\ln S_a(T_i),\ln S_a(T_j)}$ from T_1 is approximately constant until the period ratio of about two or more, then <S_a, ε> may be expected to be effective (e.g., for the ordinary records). With a sharp change in the $\rho_{\ln S_a(T_i),\ln S_a(T_j)}$ near T_1 (or the period ratio less than two), <S_a, ε> may not be effective in predicting the responses of a structure (discussed above and also see Chapter 5).

6.5 DISCUSSIONS

6.5.1 Use of Spectral Correlation Function to Validate Simulated Records and Its Impacts on Engineering Practice

In this section, the possible application of $\rho_{\ln S_a(T_i),\ln S_a(T_j)}$ in practice will be briefly discussed. Often when earthquake records are not available or are limited in number, simulated ground motions will be utilized for the nonlinear dynamic analysis of a structure. Typically, the simulated records will be scaled to the target ground motion intensity level associated with a certain hazard level (e.g., S_a at 2% in 50 years). Presumably, the record set will have epsilon values, on average, of about zero. Simply scaling records to the low-hazard (high-intensity) level, the inelastic responses of a structure are likely to be overestimated due to the effect of *peak* and *valley* (vis-à-vis ε) in the spectral shape at T_1. Ground motion records associated with low hazard usually exhibit a peak in the spectrum by definition (i.e., extreme *elastic* S_a at T_1). Using non-representative records can bias the probabilistic response prediction of a structure (Baker and Cornell 2005a; see also Chapter 2).

To avoid this systematic bias in the response prediction, recent advanced research projects (e.g., Baker and Cornell 2006b) have focused on selecting records based on the likelihood of ε at a specified ground motion hazard level (i.e., disaggregation of S_a on ε). This approach is applicable only to ordinary (as-recorded) motions. For simulated records (with narrow $\rho_{\ln S_a(T_i),\ln S_a(T_j)}$), considering only ε, however, may not be sufficient. Careful attention to the characteristics of the simulated records must be considered. In addition to the marginal mean and standard deviation of lnS_a at a given period, the correlation between lnS_a (at different periods) seems to be even more important because the conditional median spectra, CMS, of the low-hazard ground motions is a function of $\rho_{\ln S_a(T_i),\ln S_a(T_j)}$ (see Eq. 6.7). The effect of $\rho_{\ln S_a(T_i),\ln S_a(T_j)}$ on the inelastic responses of the structures will be illustrated next.

The response parameter considered is the inelastic displacement ratio (S_{di}/S_{de}) defined as the inelastic displacement, S_{di}, of a bilinear oscillator with a 5% hardening stiffness and damping ratios normalized by the elastic displacement, S_{de}, of the same elastic period. This ratio has been shown to provide some information about the shape of the response spectrum (see Chapter 3).

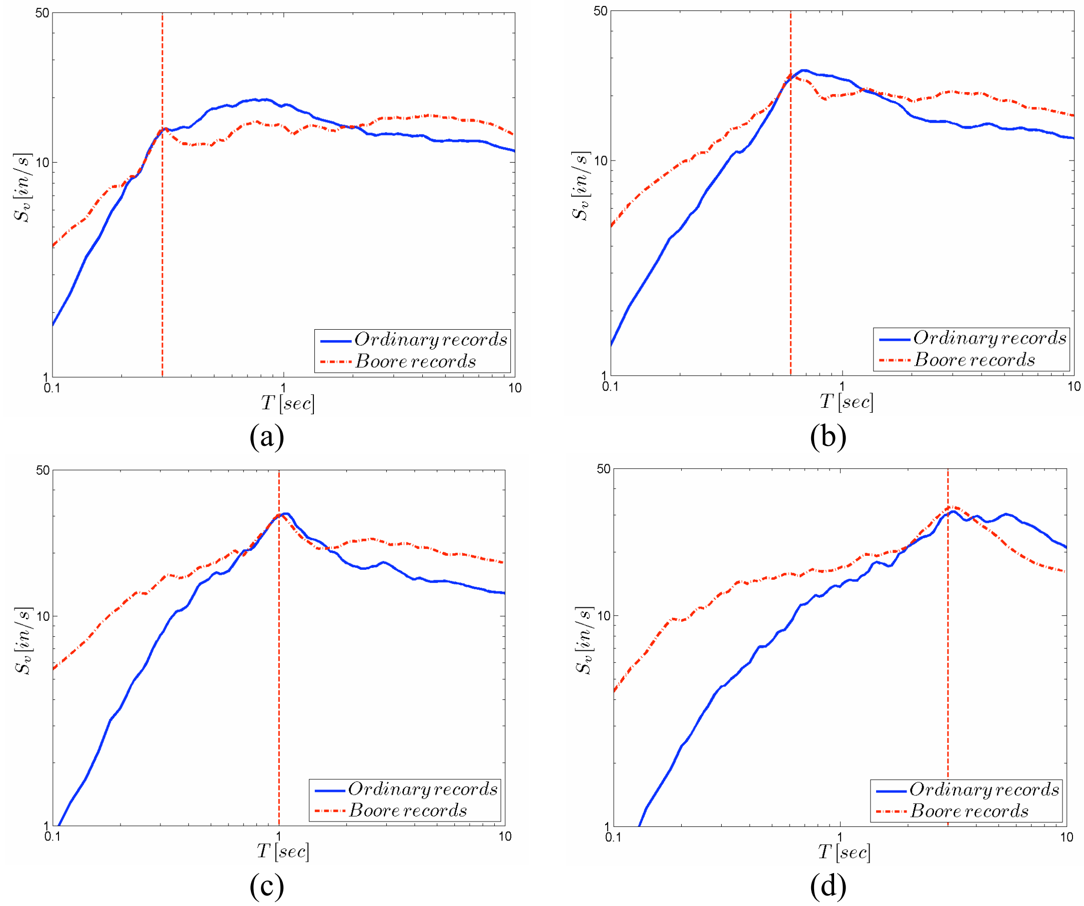

Fig. 6.12 Median response spectra of records with epsilon values of about 1.8 for ordinary and simulated ground motions at (a) 0.3, (b) 0.6, (c) 1.0, and (b) 3.0 sec.

To demonstrate the importance of $\rho_{\ln S_a(T_i),\ln S_a(T_j)}$, 20 records with epsilon values of about 1.8 are selected from ordinary and simulated records for 4 periods (i.e., 0.3, 0.6, 1, and 3 sec). The median response spectra of these records (after scaling to approximately the same intensity level) are shown in Figure 6.12. The difference in median spectral shape between ordinary and simulated records can be easily distinguished. Correspondingly, S_{di}/S_{de} for these sets of records is performed at different yield displacements (d_y). The results are plotted in terms of the median strength reduction ($\hat{R}$, defined as the median S_{de} at the oscillator period divided by d_y). At a specified $\hat{R}$ value, the same d_y is used for all records (for both ordinary and simulated motions). Note that relatively large R values are evaluated to exaggerate the results.

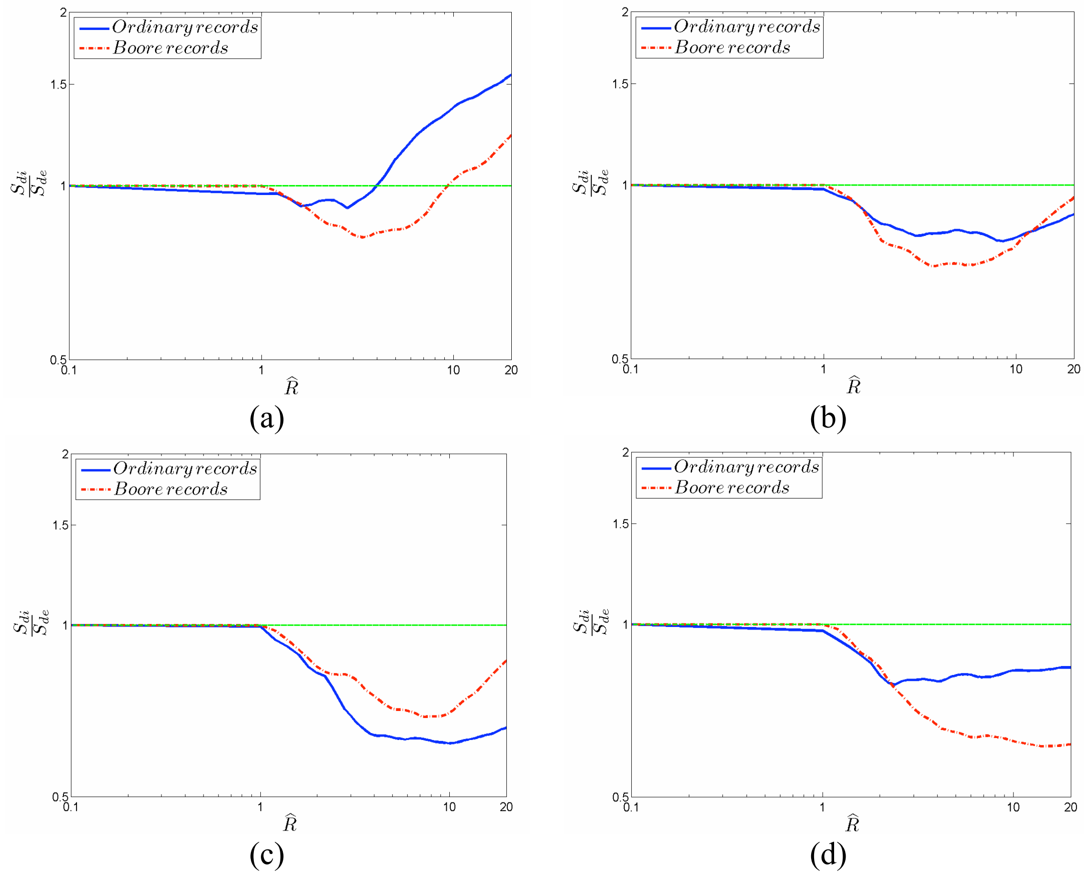

Fig. 6.13 Median inelastic displacement ratio for ordinary and simulated motions as function of $\hat{R}$ for (a) 0.3, (b) 0.6, (c) 1.0, and (d) 3.0 sec.

Comparing Figures 6.12 and 6.13, it is clear that S_{di}/S_{de} captures the (conditional) median spectral shape of the ground motions. The inelastic responses of the structures depend upon the shape of the selected records for nonlinear dynamic analysis. If the CMS of simulated records is narrower than the real (i.e., as-recorded) motions, it is anticipated that its S_{di}/S_{de} should be smaller. Another significant parameter is the difference in the dispersion of ground motions (i.e., $\sigma_{\ln S_a}$). Because simulated records have smaller $\sigma_{\ln S_a}$ than the real records, its CMS will curve back to the median spectra (zero epsilon) faster, resulting in overestimation of S_{di}/S_{de} for relatively weak systems. For example, for a short-period system (T=0.3 sec), the CMS of simulated records has a narrower shape (Fig. 6.12a), thus estimating smaller S_{di}/S_{de} (Fig. 6.13a). For T=0.6 sec, the CMS of simulated records is also narrower than the real ones; therefore, S_{di}/S_{de} for strong systems (small $\hat{R}$ values) is underestimated. However, because of the smaller

$\sigma_{\ln S_a}$ of simulated records, its CMS exceeds that of real motions at periods of 1.3 sec or longer (Fig. 6.12b). As a result, S_{di}/S_{de} of simulated motions becomes larger (overestimates) than that of the real records for relatively weak systems (i.e., large $\hat{R}$ values, see Fig. 6.13b). For T=1.0 sec, the CMS of simulated and real records is relatively close for periods shorter than 1.5 sec (Fig. 6.12c), but the CMS of simulated records exceeds the CMS of the real records, again, because of the smaller $\sigma_{\ln S_a}$. As seen in Figure 6.13c, S_{di}/S_{de} between simulated and real records is very similar for strong systems (small $\hat{R}$ values), but S_{di}/S_{de} obtained from simulated records is larger than that of the real motions for weak systems (large $\hat{R}$ values), consistent with CMS seen in Figure 6.12c. The same explanation holds true for an oscillator with T=3.0 sec. Other possibilities exist, for example, when only the marginal mean and standard deviation of lnS_a are approximately the same, but not the correlation function. It is likely to be the case that the $\rho_{\ln S_a(T_i),\ln S_a(T_j)}$ of simulated motions may be narrower, resulting in underestimation of (i.e., *not* conservative) the inelastic responses of the structures. The user of simulated records should be aware in those situations where as-recorded motions are not available and the low-hazard ground motions are of interest.

As shown above, the median spectra for the positive ε records depend strongly on the shape of the $\rho_{\ln S_a(T_i),\ln S_a(T_j)}$, which can ultimately influence the inelastic responses of the structures. As demonstrated in this section, the influence of the $\rho_{\ln S_a(T_i),\ln S_a(T_j)}$ and $\sigma_{\ln S_a}$ of simulated records can have a large impact on the conditional median spectra, which ultimately influence the S_{di}/S_{de} estimation of the structures. Therefore, in order to use the simulated ground motions in practice, not only should the marginal mean and standard deviation of lnS_a be checked against the real records, but also the $\rho_{\ln S_a(T_i),\ln S_a(T_j)}$ should be validated (which governs the CMS of low-hazard ground motions). As a result, we suggest that the spectral (auto-) correlation function of simulated records should be validated with that of the real records, i.e., an empirical spectral correlation derived from as-recorded ground motions can simply be used (e.g., Baker and Cornell 2006a; Inoue and Cornell 1990).

6.5.2 Definition for Extreme Ground Motions and Considered *IM*

What are rare seismic ground motions? What are their characteristics (i.e., response spectra)? These questions have often been raised by earth scientists and engineers. What should be noted is that the answers to these questions will primarily depend on the *IM* used to determine seismic hazard analysis. For example, the response spectra for the extreme (3ε) *elastic* response and *inelastic* responses are shown in Figure 6.14. With an assumption that lnS_{de} and lnS_{di} are jointly lognormal, the conditional *median* elastic spectra on S_{di} can be calculated as the exponential of

$$E\left[\ln S_a\left(T_j\right) \mid \varepsilon_{\ln S_{di}(T,d_y)}\right] = E\left[\ln S_a\left(T_j\right)\right] + \sigma_{\ln S_a(T_j)} \cdot \rho_{\ln S_{di}(T,d_y),\ln S_a(T_j)} \cdot \varepsilon_{\ln S_{di}(T,d_y)} \tag{6.8}$$

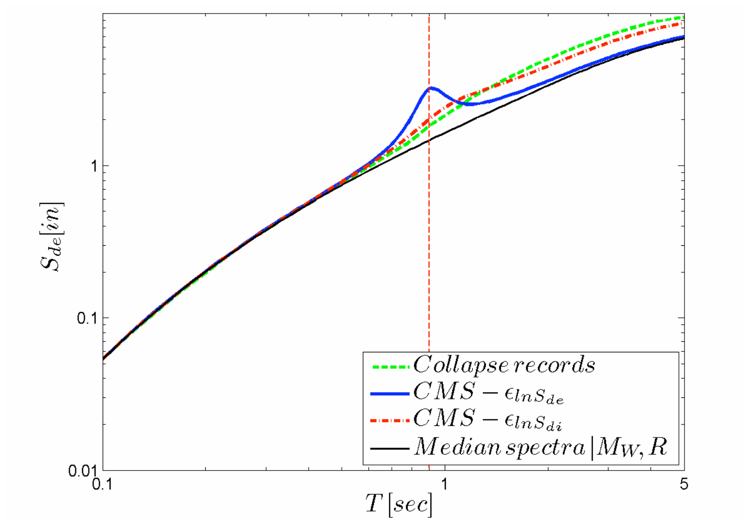

Fig. 6.14 Median response spectra for extreme (i.e., low) hazard ground motion based on S_{de} and S_{di} hazard definition.

Both median spectra are extreme in the sense that they are associated with the same MAF of exceeding a specified intensity level (in terms of S_a or S_{di}). To determine the conditional median spectra for S_{di}, the (cross-) correlation function between lnS_{di} and lnS_{de} (or equivalently lnS_a) needs to be estimated. The median response spectra of records causing collapse (i.e., *EDP* > 4 in.; dashed line) and of 55,000 records (thin solid line) are shown for comparison. The median spectra for the extreme S_{di} are similar to those causing collapse in the structure.

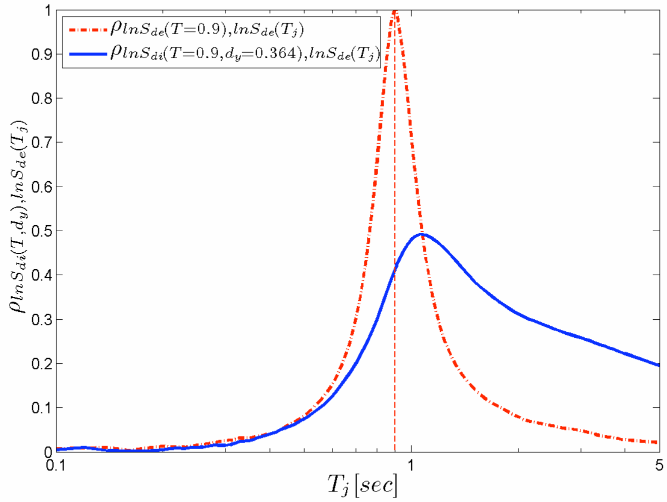

Fig. 6.15 Empirical correlation function between lnS_{di} and lnS_a to be used to derive conditional median (response) spectra for S_{di} *IM*.

The spectral correlation function between lnS_{di} and lnS_{de} (for Boore records) is illustrated in Figure 6.15. It appears that its function is asymmetric because the effective period of the system lengthens as the system behaves inelastically. Therefore, S_{di} is more highly correlated with S_{de} at periods longer than the period of the structure. Another observation is that $\rho_{\ln S_a(T_i),\ln S_a(T_j)}$ is approximately the same as $\rho_{\ln S_{di}(T,d_y),\ln S_{de}(T_j)}$ for periods shorter than the two-thirds period of the inelastic system. This similarity obviously depends on the degree of nonlinearity of S_{di} (see Chapter 3 for more detailed explanation).

6.6 CONCLUSIONS

This chapter focuses on validating seismic response estimation using the *IM*-based approach by comparing such estimates with the results from simulation, which are considered to be the "exact" results. For the simulated ground motions used in this study, *only* S_{di} is shown to be an unbiased estimator. The seismic performances of the structure, λ_{EDP}, are shown to be statistically equivalent to those of the simulation approach. Using S_a or <S_a, ε>, however, yields statistically different results from the simulation method. The former is shown to be bias-high and the latter is bias-low. The bias-high results found when using S_a is due to failure, when the records are chosen randomly to properly represent the ground motion characteristics of records at low ground motion hazard levels. On the other hand, <S_a, ε> underestimates the response prediction largely because the shape of the positive ε records (vis-à-vis the shape of the spectral correlation function) is different from that of typical as-recorded ground motions. The spectral ordinates for positive epsilon records of the simulated records drop off rapidly as the period ratio increases or decreases as compared to the as-recorded motions. This changes the median spectral shape of positive epsilon records rapidly. Given that <S_a, ε> utilizes the shape or the *local* slope at the fundamental period to estimate the responses, it cannot predict well the inelastic responses of a structure with a sharp change in the spectral shape (e.g., *near-source* pulse-like records; see Chapter 5 and simulated motions with a narrowband spectral correlation function). Only S_{di} is shown to be robust in estimating the seismic performance of a structure in any type of earthquake ground motions (at least for the first-mode-dominated structure).

Note that the findings and conclusions drawn in this chapter are primarily based on records generated from a stochastic ground motion model (Boore 1983; Boore 2003). These simulated records have different characteristics, especially the spectral correlation function of lnS_a, as compared to the real (as-recorded) ground motions. The readers should not be discouraged from using <S_a, ε> for actual ground motions. We believe that using S_{di} is, however, a better approach because it is shown to be robust with any type of ground motion considered.

7 Concluding Remarks

7.1 OVERVIEW

This research focused on estimating the seismic performance (or seismic risk) of structures via probabilistic seismic demand analysis (PSDA), i.e., in terms of the MAF of exceeding a specified limit state. The key feature of this method is the choice of the ground motion intensity measure. The selected *IM* can impact the accuracy in estimating the structural response hazard curve, which should be unbiased. In this research, the PSDA framework is applied to study the effectiveness of advanced *IM*s. The results are compared with the elastic-based *IM*s for *ordinary* and *near-source* pulse-like ground motions. Using advanced *IM*s for tall, long-period structures, the probabilistic response prediction shows no dependence on record characteristics (i.e., earthquake magnitude (M_w), closest distance to rupture (R_{rup}), ground motion epsilon (ε), pulse period (T_p), etc.) as well as unbiased estimation when scaling ground motions. One of the disadvantages in implementing the advanced *IM*s in the past has been the computability of the ground motion hazards in terms of these *IM*s. For this reason, one of the focuses of this report was the calculation of ground motion hazards for advanced *IM*s (Chapter 3). The next section summarizes the important findings of this research.

Note that attention in this report has been limited to the prediction of probabilities of structural responses. It will be presumed that many of the conclusions regarding the prediction of structural parameters will carry over to loss estimations (i.e., life-cycle cost analysis).

7.2 PRACTICAL IMPLICATIONS

7.2.1 PSDA Using Advanced Ground Motion *IM*s

PSDA using the *inelastic*-based *IM*s (i.e., S_{di} and $IM_{1I\&2E}$) is implemented in Chapter 2 to demonstrate their effectiveness relative to ground motion parameters such as M_w, source-to-site distance, and ε. Unlike the *elastic*-based *IM*s (such as S_a and a *vector IM*, $<S_a, \varepsilon>$), one of the advantages in using these advanced *IM*s is that ground motion record selection criteria become *less* important to achieve accuracy in estimating the seismic performance of a structure. Sixteen generic frames are used to compare the results between *elastic*- and *inelastic*-based *IM*s. Overall, using S_{di} or $IM_{1I\&2E}$ (the latter is needed for a structure with significant higher-mode contribution) yields statistically the same seismic performance estimations as compared to those of $<S_a, \varepsilon>$ for ordinary records. In addition, the PSDA results using the advanced *IM*s are more stable than the results obtained using $<S_a, \varepsilon>$ from the standpoint that the standard error of the structural performance values subjected to different record sets is much smaller than those of the vector *IM*. All of the problems related to scaling records, biased estimates, responses dependent on record characteristics, etc. are due to the use of *elastic*-based information to estimate *inelastic* results. Only the PSDA results using advanced *IM*s are relatively accurate in terms of probabilistic response prediction subjected to near-source pulse-like motions. The elastic-based *IM*s cannot capture the sharp change in the spectral shape of pulse-like motions; as a result, they should not be used to estimate the seismic performance of structures threatened by such records.

7.2.2 Attenuation Relationships for Advanced Ground Motion *IM*s

To ensure accuracy in estimating the seismic performance of a structure at a designated site, advanced *IM*s (i.e., S_{di} and $IM_{1I\&2E}$) are shown to be *efficient*, *sufficient*, and *robust* with respect to scaling ground motions. Ground motion hazard in terms of the advanced *IM*s, however, needs to be developed. In Chapter 3, ground motion prediction models (i.e., attenuation relationships) in terms of S_{di} and $IM_{1I\&2E}$ as a function of M_w, R_{rup}, fault mechanism, etc. are developed. Currently, the national seismic hazard maps available from the U.S. Geological Survey (USGS; http://earthquake.usgs.gov/research/hazmaps/) and the Southern California Earthquake Center (SCEC; http://www.opensha.org/) only consider S_a. Use of the advanced *IM*s will require that the USGS or SCEC implement attenuation relationships for the advanced *IM*s into the national seismic hazard maps.

7.2.3 PSHA Accounting for Directivity Effect

Due to the concern in estimating seismic hazards at sites located close to faults, past studies (e.g., Somerville et al. 1997) have tried to incorporate directivity effects using a simple monotonic modification (i.e., no significant change in the spectral shape) to existing S_a attenuation models. The proposed framework in Chapter 4 would allow the use of *narrowband* (i.e., where only spectral ordinates near the pulse period, T_p, are modified) attenuation models to be directly implemented in the PSHA. The significance of directly incorporating pulses and T_p explicitly into PSHA is that disaggregation can be performed in terms of the probability of expecting a pulse (given an intensity level) and the probability distribution of the pulse period in addition to M_w, R_{rup}, and ε. The disaggregation results on the probability of experiencing a pulse and T_p can provide basic guidelines for engineers and/or earth scientists to select representative records, as well as the number of pulse motions relative to ordinary motions for a particular site hazard. With increased accuracy in identifying the seismic hazard, seismic risk estimation at a site due to future earthquakes appears to be more accurate. Note though that this detailed record selection is *unnecessary* if sufficient *IM*s (i.e., S_{di} and $IM_{1I\&2E}$) are employed as a basis for scaling records for ordinary and near-source pulse-like ground motions (see Chapter 2 and 5, respectively). However, the hazard analysis for such *IM*s in the near-source awaits their appropriate attenuation law development and this again will require explicit introduction of pulses and T_p to achieve accuracy.

7.2.4 Seismic Performance of Structures Subjected to Pulse-like Ground Motions

As alluded to above, one of the primary goals of this report is to ensure the accuracy of PSDA results subjected to ordinary and near-source pulse-like ground motions. As demonstrated in Chapter 5, PSDA results can be very inaccurate (i.e., biased) if the chosen *IM* is *inefficient*, *insufficient*, and *not* robust relative to scaling records. Generally for ordinary records, S_a has been shown to be insufficient for tall, long-period structures due to its lack of spectral-shape information (Shome 1999). This is due mainly to the effects of peaks and valleys in the spectrum (vis-à-vis ε). Incorporating ε with S_a for near-source records, however, is neither efficient nor sufficient. Using S_{di} and $IM_{1I\&2E}$ has been shown to be accurate in estimating the seismic performance of structures for both *ordinary* and *near-source* pulse-like ground motions. This effectiveness largely implies that detailed record selection is *not* necessary, and records with any

M_w, R_{rup}, ε, and T_p can be selected for nonlinear dynamic analyses. The difference in the structural performance assessment (using advanced *IM*s) for sites located close to and away from the causative faults is solely the marginal ground motion hazard at a site (which varies from site to site and structure to structure). The structural analysis results, e.g., the IDAs, are statistically the same whether ordinary or pulse-like records are applied to the structures when advanced *IM*s are employed.

The inelastic-based *IM*s are very effective because they recognize (1) the relationship between the modal periods of the structures and the pulse period and (2) the strength of the structures. By design for inelastic-based *IM*s, the *effective* period of the oscillator is then determined naturally on a record-to-record basis. As can be seen in Chapter 5, records imposing strong inelasticity to structures will be scaled less than the records imposing weak inelasticity to achieve the same median target displacement level (i.e., the same ground motion intensity level).

7.2.5 Validating the *IM*-Based PSDA with Simulation

In Chapters 2 and 5, PSDA results using inelastic-based *IM*s have been shown to ensure the relative accuracy in estimating the seismic performance of structures for both ordinary and pulse-like ground motions. The "exact" performance values are, however, not known. To overcome this problem, simulated ground motions are generated and used to perform nonlinear dynamic analyses. Determination of the "exact" structural response hazard curve can then be carried out directly and can be used for comparison with the results using the *IM*-based PSDA.

Using S_{di} (as the *IM*) yields results statistically the same as the exact values, but this is not the case for $<S_a, \varepsilon>$. This is largely due to the fact that the spectral autocorrelation function of $\ln S_a$ at two periods of the simulated records drops rapidly (as seen in near-source pulse-like records) as compared to that of real (as-recorded) ground motions. This implies that a spectral autocorrelation function may be used to (1) determine the effectiveness of $<S_a, \varepsilon>$ subjected to certain types of ground motions (e.g., soft soil) and (2) to determine how similar the simulated ground motions are as compared to the real records (in addition to the mean and standard deviation at each period marginally). This condition is crucial when extreme ground motion records are of interest because the conditional median (i.e., geometric mean) spectrum of rare records is a function of the spectral autocorrelation function.

One of the key observations from this study is the use of the spectral autocorrelation function as a way (1) to determine how realistic the simulated ground motions are (as compared to real ground motions) and (2) to determine the effectiveness of $<S_a, \varepsilon>$ for different types of ground motions. This should be implemented as a means to validate the simulated ground motion records.

In recent guidelines (e.g., ATC-40; FEMA-273; Vision-2000; and SAC/FEMA-350), the term "rare seismic events" has been used. What is a rare ground motion? This rare (or extreme) seismic ground motion is typically defined as the 2% in 50 years ground motion intensity level (intensity associated with 2% probability of being exceeded in 50 years). Where alternative *IM*s are used, definition of the extreme ground motions will depend on the *IM* used to determine the seismic hazard, i.e., whether it is an extreme *elastic* (i.e., S_a) or *inelastic* (i.e., S_{di}) intensity. The ground motion characteristics will be different depending upon which *IM* is utilized to determine the seismic hazard. Using *inelastic*-based *IM*s is shown to be accurate in estimating the seismic performance of structures subjected to *ordinary* and *near-source* ground motions as well as the proper extreme motions for inelastic responses of the first-mode-dominated structures.

7.3 LIMITATIONS AND FUTURE RESEARCH

The research presented in this report is based on a number of limiting assumptions and a limited scope. Some of the relevant research areas that should be performed in the future are discussed in the following subsections.

7.3.1 Types of Structures Considered and Modeling Simplification

This research focuses only on the methodology for probabilistic response prediction of a structure considering uncertainties in the ground motions but not in the structural modeling parameters. Although we anticipate that the conclusions would remain unchanged with improved structural modeling and analyses, the following factors should be considered to improve the final predictions of building response:

- This research has not considered (1) the incorporation of partition walls, stairwells, floor slabs, etc., which may increase the stiffness of the structures, (2) improved element models to incorporate axial and shear failure in the column and beam elements, or even local buckling of the web and flange of the element. Consideration of these effects can alter the strength and stiffness of the system especially at or near collapse.

- Other types of structural systems need to be considered in order to draw further conclusions (e.g., braced-frames, shear-wall systems, dual systems, base-isolated structures). The influence of vertical irregularities (due to mass and stiffnesses variation) is not considered.
- Reinforced concrete versus steel structural models: The initial stiffness of reinforced concrete structures is known to be highly uncertain, which may influence the effectiveness of period dependent *IM*s. This may affect the optimal parameters for the chosen *IM*.
- The effect of soil-structure interaction is not considered. The effects of earthquake motion on soil liquefaction and the change in soil properties during strong shaking are not considered. The assumption of a fixed-based foundation may not be appropriate. Settlement of the foundation during strong shaking is not considered.
- The effect of soft-soil sites was not studied. Ground motions in soft-soil sites have been shown to exhibit a narrowband spectrum similar to the spectrum of near-source pulse-like records, which can affect the hazard assessment and structural response.
- The research is limited to analyses of two-dimensional structural models. By modeling structures in 2D, the torsion effect on the responses of interest (e.g., interstory drift of the corner columns) is ignored. It is unclear how a simple *IM* can capture the responses with a significant torsion effect. How records should be scaled and selected remains an open question for 3D structures subjected to bi-directional or even tri-directional shaking. There is no consensus on what response parameters are essential for 3D structures. More research is needed in this area.

7.3.2 Uncertainty in Structural Models and Ground Motion Hazard

In this study, only the aleatory uncertainty in ground motion is considered. This uncertainty is intrinsic in nature and cannot be reduced. Only the best estimates (the mean values) of the structural model and hazard are used. The result is the *mean* (with respect to epistemic uncertainties from the structural and hazard sides) structural response hazard curve. Epistemic uncertainties in the responses of structures and ground motion hazard are not considered. In reality, epistemic uncertainty should also be included to represent the limited accuracy of the structural and hazard analysis procedures and imperfect knowledge of the parameters, modeling, and analyses used in the estimation process. Epistemic uncertainties in both ground motion hazard and structural response parameters can be incorporated with the expense of performing computational intensive analyses (e.g., Monte-Carlo simulations). With a first-order approximation where there is epistemic uncertainty only in the mean estimate and not in that of the variance, a reliability approach may be used to estimate the (first-order) impact of these uncertainties (see e.g., Shome 1999); only the total (aleatory and epistemic in the mean) variance of the model is increased. This epistemic uncertainty can be reduced with more detailed investigations of the problems.

7.3.3 Structural Response of Interest and Loss Estimation

In this research, only the peak maximum interstory drift ratio ($\theta_{\max}$; peak over time and maximum over the height of the structure) is considered, mainly because it is a good indicator of estimating the collapse capacity and maximum plastic deformations in the structure. The interstory drift ratio of each story (θ_i) is, of course, better correlated with the damage (e.g., in partition walls) in a given story. Using $\theta_{\max}$ to estimate the damage in each story may not be suitable. Other structural responses such as peak floor acceleration, residual displacement, and a broader response selection may change the final conclusion. An effective *IM* for displacement-sensitive responses may not be the same as that for acceleration-sensitive responses (Taghavi and Miranda 2003).

In probabilistic loss estimation, a *vector* of response parameters is often required to accurately predict the total loss exceeding a certain value for multiple components. An optimal *IM* for a component *EDP* may not be so for the other *EDP*s. If only the expected annual loss is of interest (and the total losses are a sum of element losses), a separate *IM* for each component can be used to separate the mean annual losses of each component. The results can then be summed. However, if the objective is to compute an estimate of the distribution of the total losses, a joint prediction of all response parameters is needed. Using a vector (i.e., series) *IM* in this case is necessary (i.e., at least two *IM*s are needed: one for acceleration- and the other for displacement-sensitive responses). This implies the need of joint ground motion hazard in terms of the vector

IM. Similar to the joint ground motion hazard, a joint *EDP* hazard can be developed and utilized to estimate each of the component losses as well as the total loss probability distribution.

A search for a robust scalar *IM* for predicting a vector of responses needs to be investigated based on the objective/loss function, which ultimately will vary from structure to structure and site to site. The optimal *IM* will depend on the objective/loss function, which depends on the functionality of the building itself, for example, whether the building will be used for residential, office space, research facilities, storage, hospital, government agency, etc. The optimal *IM* to estimate the total losses for a residential building may not be so for a research facility building equipped with expensive instruments. The *IM* that can predict acceleration-sensitive responses well may be the optimal choice for a building equipped with research facilities.

7.3.4 Ground Motion Attenuation Models and Hazard Analysis

Although the ground motion prediction models (attenuation relationships) for S_{di} and $IM_{1I\&2E}$ (for ordinary records) have been developed in this report, it is desirable to have more than one attenuation model in order to capture the epistemic uncertainty due to the database selection and modeling process. These two *IM*s should also be implemented in the national seismic hazard maps as well as in the openSHA program (http://www.opensha.org/) to make it publicly available.

Based on observations from modal pushover analyses (MPA) and research by the Chopra group (e.g., Chopra and Goel 2002; Han and Chopra 2006), an S_{di} attenuation model for the strength-limited bilinear model developed by the Krawinkler group (e.g., Ibarra et al. 2005) should be developed. It would require two or three additional oscillator parameters, however, making the construction of the attenuation relationship a challenge. By using this hysteresis model to estimate the target displacement in MPA, the response prediction from simplified analysis to estimate severe nonlinear dynamic analysis is considerably improved even at the point of the global dynamic instability (i.e., collapse) of a structure.

In Chapter 4, a PSHA framework incorporating the directivity effect has been proposed. For this framework to be used in practice, a narrowband model of an *IM* (e.g., S_a or S_{di}) needs to be developed. An elastic S_a narrowband model is the subject of ongoing research by the Next Generation Attenuation (NGA 2006) project (e.g., Youngs and Chiou 2006). Ongoing research by the authors is exploring the narrowband model for the inelastic-based *IM*s, i.e., S_{di} and $IM_{1I\&2E}$. With the proposed framework and the narrowband attenuation models, the estimation of seismic hazard and identification at a site is potentially more accurate. This will have an impact in seismic risk analysis, loss estimation, decision-making policy, and future urban planning, which largely depend on the uncertainty inherent in the ground motions.

7.3.5 Multi-Mode-Dominated Structures

For high-rise buildings, there is no consensus on the *IM* for probabilistic response prediction for multi-mode-dominated responses. Using a scalar *IM* for multi-mode dominated structures may not yield a reasonable result. A *vector IM* of the spectral ordinates (i.e., S_{di} for each mode or for each direction of ground shaking) may be more appropriate. If so, the joint ground motion hazard in terms of either multi-mode frequencies (2D) or two-directional shaking (3D) needs to be developed. Due to its superior response prediction, S_{di} may be used as a basis *IM*. The correlation function for $\ln S_{di}$, however, must be developed (either for the average horizontal, randomly oriented horizontal, or orthogonal component). The empirical correlation function for $\ln S_{di}$ has been briefly explored in Chapters 3 and 6 of this report. The simplification from a vector to a scalar *IM* may be made if the loss or objective function is known *a priori*, which depends on the building occupancy type (such as residential buildings, office space, hospital, research facilities with expensive equipment, government agencies, etc.).

7.3.6 Optimal Parameters for Bilinear SDOF Models

In this report, the optimal parameters for a bilinear SDOF model are estimated based on minimizing the dispersion of the collapse capacity of the structure in terms of *IM*. Based on the preliminary study, the optimal choice is the first-mode period of the structure and a yield displacement of about half of the yield displacement estimated from a conventional static pushover analysis. This information is based *only* on the generic frame structures considered, which all have a global ductility capacity of about 4. The optimal yield displacement, theoretically, should be a function of this global ductility. In the limit case, where the ductility capacity is infinite, the optimal yield displacement may simply be the one estimated from the pushover analysis (assuming the P-Δ effect is small). Future research based on a larger database by the Krawinkler group may help parameterize the optimal yield displacement as a function of structural element properties (e.g., global ductility, post-capping stiffness, cyclic deterioration parameters, etc.).

7.4 OVERALL CONCLUSIONS

It appears that the problems from selecting and scaling ground motions are due mainly to the use of elastic information as a basis *IM* to predict nonlinear MDOF responses. By switching to the inelastic-based *IM*s, the assumptions (efficiency, sufficiency, and scaling robustness) used in PSDA are not violated. Advanced (inelastic-based) *IM*s have been shown to be efficient, sufficient, and unbiased when used in estimating the seismic performance of structures susceptible to both ordinary and near-source pulse-like ground motions.

Appendix: Earthquake Ground Motion Records

All earthquake ground motion records used in this report come from the Next Generation Attenuation (NGA) project (http://peer.berkeley.edu/nga/). Column headings match fields provided by NGA. Empty fields are either not available or not applicable for a given record.

A.1 LMSR-N RECORD SET

This record set was compiled by Medina and Krawinkler (2003).

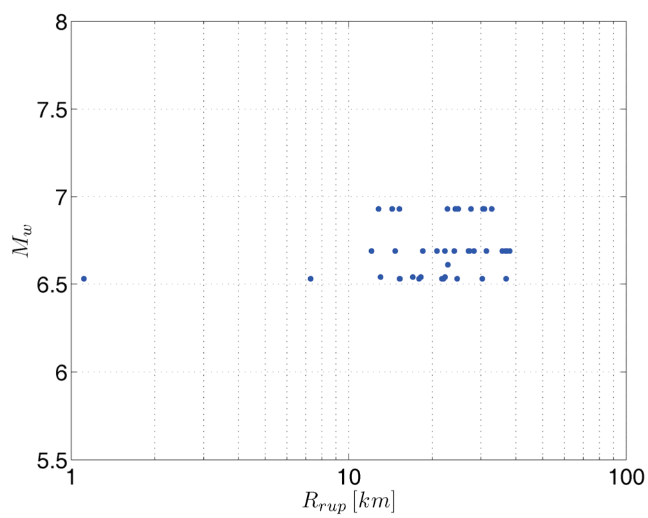

Fig. A.1 Earthquake magnitude and distance range for LMSR-N record set.

Table A.1 Earthquake ground motion properties for LMSR-N record set compiled by Medina and Krawinkler (2003).

#	Record Sequence Number	Earthquake Name	Date	Station Name	Mw	ClstD (km)
1	68	San Fernando	9-Feb-1971	LA - Hollywood Stor FF	6.61	22.77
2	163	Imperial Valley-06	15-Oct-1979	Calipatria Fire Station	6.53	24.60
3	165	Imperial Valley-06	15-Oct-1979	Chihuahua	6.53	7.29
4	167	Imperial Valley-06	15-Oct-1979	Compuertas	6.53	15.30
5	168	Imperial Valley-06	15-Oct-1979	Cucapah	6.53	1.11
6	172	Imperial Valley-06	15-Oct-1979	El Centro Array #1	6.53	21.68
7	175	Imperial Valley-06	15-Oct-1979	El Centro Array #12	6.53	17.94
8	176	Imperial Valley-06	15-Oct-1979	El Centro Array #13	6.53	21.98
9	186	Imperial Valley-06	15-Oct-1979	Niland Fire Station	6.53	36.92
10	188	Imperial Valley-06	15-Oct-1979	Plaster City	6.53	30.33
11	192	Imperial Valley-06	15-Oct-1979	Westmorland Fire Sta	6.53	15.25
12	719	Superstition Hills-02	24-Nov-1987	Brawley Airport	6.54	17.03
13	721	Superstition Hills-02	24-Nov-1987	El Centro Imp. Co. Cent	6.54	18.20
14	724	Superstition Hills-02	24-Nov-1987	Plaster City	6.54	22.24
15	728	Superstition Hills-02	24-Nov-1987	Westmorland Fire Sta	6.54	13.03
16	737	Loma Prieta	18-Oct-1989	Agnews State Hospital	6.93	24.57
17	752	Loma Prieta	18-Oct-1989	Capitola	6.93	15.23
18	767	Loma Prieta	18-Oct-1989	Gilroy Array #3	6.93	12.82
19	768	Loma Prieta	18-Oct-1989	Gilroy Array #4	6.93	14.34
20	770	Loma Prieta	18-Oct-1989	Gilroy Array #7	6.93	22.68
21	772	Loma Prieta	18-Oct-1989	Halls Valley	6.93	30.49
22	777	Loma Prieta	18-Oct-1989	Hollister City Hall	6.93	27.60
23	778	Loma Prieta	18-Oct-1989	Hollister Diff. Array	6.93	24.82
24	787	Loma Prieta	18-Oct-1989	Palo Alto - SLAC Lab	6.93	30.86
25	800	Loma Prieta	18-Oct-1989	Salinas - John & Work	6.93	32.78
26	806	Loma Prieta	18-Oct-1989	Sunnyvale - Colton Ave.	6.93	24.23
27	959	Northridge-01	17-Jan-1994	Canoga Park - Topanga Can	6.69	14.70
28	974	Northridge-01	17-Jan-1994	Glendale - Las Palmas	6.69	22.21
29	987	Northridge-01	17-Jan-1994	LA - Centinela St	6.69	28.30
30	992	Northridge-01	17-Jan-1994	LA - E Vernon Ave	6.69	36.75
31	993	Northridge-01	17-Jan-1994	LA - Fletcher Dr	6.69	27.26
32	995	Northridge-01	17-Jan-1994	LA - Hollywood Stor FF	6.69	24.03
33	996	Northridge-01	17-Jan-1994	LA - N Faring Rd	6.69	20.81
34	1000	Northridge-01	17-Jan-1994	LA - Pico & Sentous	6.69	31.33
35	1003	Northridge-01	17-Jan-1994	LA - Saturn St	6.69	27.01
36	1016	Northridge-01	17-Jan-1994	La Crescenta - New York	6.69	18.50
37	1019	Northridge-01	17-Jan-1994	Lake Hughes #1	6.69	35.81
38	1028	Northridge-01	17-Jan-1994	Leona Valley #2	6.69	37.24
39	1032	Northridge-01	17-Jan-1994	Leona Valley #6	6.69	38.03
40	1048	Northridge-01	17-Jan-1994	Northridge - 17645 Saticoy St	6.69	12.09

Table A.1—*(continued)*

#	Mech	GMX's C3	Max f_{HP}	Min f_{LP}	FileName
1	RV	D	0.20	35.00	SFERN\PEL180
2	SS	D	0.10	40.00	IMPVALL\H-CAL315
3	SS	D	0.05	0.00	IMPVALL\H-CHI012
4	SS	D	0.20	0.00	IMPVALL\H-CMP015
5	SS	D	0.05	0.00	IMPVALL\H-QKP085
6	SS	D	0.10	40.00	IMPVALL\H-E01140
7	SS	D	0.10	40.00	IMPVALL\H-E12230
8	SS	D	0.20	40.00	IMPVALL\H-E13230
9	SS	D	0.10	30.00	IMPVALL\H-NIL090
10	SS	D	0.10	40.00	IMPVALL\H-PLS135
11	SS	D	0.10	40.00	IMPVALL\H-WSM180
12	SS	D	0.10	23.00	SUPERST\B-BRA225
13	SS	D	0.10	40.00	SUPERST\B-ICC000
14	SS	D	0.20	18.00	SUPERST\B-PLS135
15	SS	D	0.10	35.00	SUPERST\B-WSM090
16	RV/OB	D	0.20	30.00	LOMAP\AGW000
17	RV/OB	B	0.20	40.00	LOMAP\CAP090
18	RV/OB	D	0.10	40.00	LOMAP\G03090
19	RV/OB	D	0.20	30.00	LOMAP\G04090
20	RV/OB	B	0.20	40.00	LOMAP\GMR000
21	RV/OB	C	0.20	22.00	LOMAP\HVR000
22	RV/OB	D	0.10	29.00	LOMAP\HCH090
23	RV/OB	D	0.10	33.00	LOMAP\HDA255
24	RV/OB	A	0.20	33.00	LOMAP\SLC270
25	RV/OB	D	0.10	28.00	LOMAP\SJW250
26	RV/OB	D	0.10	40.00	LOMAP\SVL270
27	RV	D	0.05	30.00	NORTHR\CNP196
28	RV	C	0.10	30.00	NORTHR\GLP267
29	RV	D	0.20	30.00	NORTHR\CEN245
30	RV	D	0.10	30.00	NORTHR\VER180
31	RV	D	0.15	30.00	NORTHR\FLE234
32	RV	D	0.20	23.00	NORTHR\PEL090
33	RV	B	0.13	30.00	NORTHR\FAR000
34	RV	D	0.20	46.00	NORTHR\PIC180
35	RV	D	0.10	30.00	NORTHR\STN020
36	RV	C	0.10	30.00	NORTHR\NYA180
37	RV	B	0.12	23.00	NORTHR\L01000
38	RV	B	0.20	23.00	NORTHR\LV2090
39	RV	D	0.20	23.00	NORTHR\LV6090
40	RV	D	0.10	30.00	NORTHR\STC090

A.2 NEAR-SOURCE PULSE-LIKE GROUND MOTION RECORD SET

A database of 70 pulse-like earthquake ground motion records rotated to the fault-normal direction are compiled from records that have been identified as having "distinct" velocity pulses by Mavroeidis and Papageorgiou (2003), Fu and Menun (2004), and Bazzurro and Luco (2004). Bazzurro and Luco (2004) selected records whose location relative to the fault rupture suggested that a velocity pulse is likely to occur, rather than directly identifying a velocity pulse in the record. Accordingly, records have been visually identified based on whether they contained a pulse before including the records into the database. The processed records, in the fault-normal direction, are obtained from the Next Generation Attenuation (NGA) database as of March 2005. All ground motions are recorded on firm soil or rock based on Geomatrix site classes for all faulting styles. The earthquake magnitude, M_w, ranges from 5.6 to 7.6, and the closest distance to rupture ranges from 0.07 to 22 km.

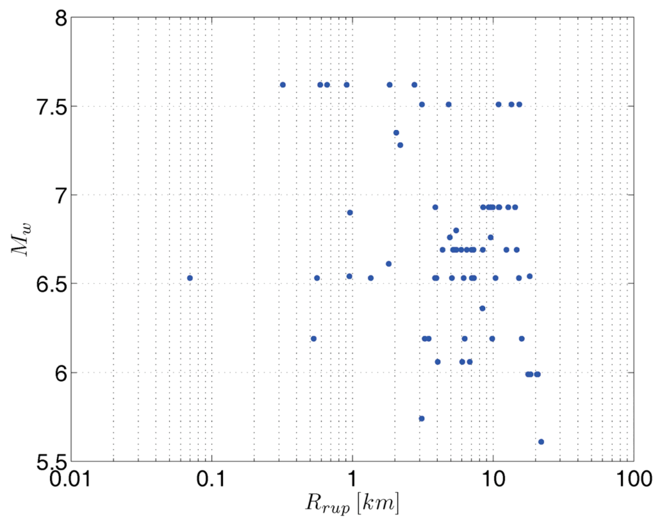

Fig. A.2 Earthquake magnitude and distance range for near-source pulse-like record set.

Table A.2 Earthquake ground motion properties for near-source pulse-like record set.

#	Record Sequence Number	Earthquake Name	Date	Station Name	Mw	ClstD (km)	Mech
1	29	Parkfield	28-Jun-1966	Cholame - Shandon Array #2	6.19	6.28	SS
2	33	Parkfield	28-Jun-1966	Temblor pre-1969	6.19	15.96	SS
3	77	San Fernando	09-Feb-1971	Pacoima Dam (upper left abut)	6.61	1.81	RV
4	126	Gazli, USSR	17-May-1976	Karakyr	6.80	5.46	RV
5	143	Tabas, Iran	16-Sep-1978	Tabas	7.35	2.05	RV
6	150	Coyote Lake	06-Aug-1979	Gilroy Array #6	5.74	3.11	SS
7	161	Imperial Valley-06	15-Oct-1979	Brawley Airport	6.53	10.42	SS
8	170	Imperial Valley-06	15-Oct-1979	EC County Center FF	6.53	7.31	SS
9	171	Imperial Valley-06	15-Oct-1979	EC Meloland Overpass FF	6.53	0.07	SS
10	173	Imperial Valley-06	15-Oct-1979	El Centro Array #10	6.53	6.17	SS
11	179	Imperial Valley-06	15-Oct-1979	El Centro Array #4	6.53	7.05	SS
12	180	Imperial Valley-06	15-Oct-1979	El Centro Array #5	6.53	3.95	SS
13	181	Imperial Valley-06	15-Oct-1979	El Centro Array #6	6.53	1.35	SS
14	182	Imperial Valley-06	15-Oct-1979	El Centro Array #7	6.53	0.56	SS
15	183	Imperial Valley-06	15-Oct-1979	El Centro Array #8	6.53	3.86	SS
16	184	Imperial Valley-06	15-Oct-1979	El Centro Differential Array	6.53	5.09	SS
17	192	Imperial Valley-06	15-Oct-1979	Westmorland Fire Sta	6.53	15.25	SS
18	367	Coalinga-01	02-May-1983	Pleasant Valley P.P. - bldg	6.36	8.41	RV
19	448	Morgan Hill	24-Apr-1984	Anderson Dam (Downstream)	6.19	3.26	SS
20	451	Morgan Hill	24-Apr-1984	Coyote Lake Dam (SW Abut)	6.19	0.53	SS
21	459	Morgan Hill	24-Apr-1984	Gilroy Array #6	6.19	9.86	SS
22	461	Morgan Hill	24-Apr-1984	Halls Valley	6.19	3.48	SS
23	495	Nahanni, Canada	23-Dec-1985	Site 1	6.76	9.60	RV
24	496	Nahanni, Canada	23-Dec-1985	Site 2	6.76	4.93	RV
25	517	N. Palm Springs	08-Jul-1986	Desert Hot Springs	6.06	6.82	RV/OB
26	529	N. Palm Springs	08-Jul-1986	North Palm Springs	6.06	4.04	RV/OB
27	540	N. Palm Springs	08-Jul-1986	Whitewater Trout Farm	6.06	6.04	RV/OB
28	595	Whittier Narrows-01	01-Oct-1987	Bell Gardens - Jaboneria	5.99	17.79	RV/OB
29	615	Whittier Narrows-01	01-Oct-1987	Downey - Co Maint Bldg	5.99	20.82	RV/OB
30	668	Whittier Narrows-01	01-Oct-1987	Norwalk - Imp Hwy, S Grnd	5.99	20.42	RV/OB
31	692	Whittier Narrows-01	01-Oct-1987	Santa Fe Springs - E.Joslin	5.99	18.49	RV/OB
32	721	Superstition Hills-02	24-Nov-1987	El Centro Imp. Co. Cent	6.54	18.20	SS
33	723	Superstition Hills-02	24-Nov-1987	Parachute Test Site	6.54	0.95	SS
34	763	Loma Prieta	18-Oct-1989	Gilroy - Gavilan Coll.	6.93	9.96	RV/OB
35	764	Loma Prieta	18-Oct-1989	Gilroy - Historic Bldg.	6.93	10.97	RV/OB
36	765	Loma Prieta	18-Oct-1989	Gilroy Array #1	6.93	9.64	RV/OB
37	766	Loma Prieta	18-Oct-1989	Gilroy Array #2	6.93	11.07	RV/OB
38	767	Loma Prieta	18-Oct-1989	Gilroy Array #3	6.93	12.82	RV/OB
39	768	Loma Prieta	18-Oct-1989	Gilroy Array #4	6.93	14.34	RV/OB
40	779	Loma Prieta	18-Oct-1989	LGPC	6.93	3.88	RV/OB

Table A.2—*(continued)*

#	GMX's C3	X or Y	θ or ϕ [degree]	T_p [sec]	Max f_{HP}	Min f_{LP}	FileName
1	D	1.00	4.74	0.67			PARKF\C02065
2	A	1.00	10.43	0.40	0.20	14.70	PARKF\TMB_051_FN
3	A	0.80	7.53	1.34	0.50	35.00	SFERN\PUL_195_FN
4	A	1.00	3.15	1.06	0.05	38.00	GAZLI\GAZ_177_FN
5	A	0.32	0.58	4.70	0.05		TABAS\TAB-TR
6	A	0.62	16.99	0.91	0.20	25.00	COYOTELK\G06_246_FN
7	D	0.76	10.54	4.80	0.10	40.00	IMPVALL\H-BRA_233_FN
8	D	0.55	18.15	3.70	0.10	35.00	IMPVALL\H-ECC_233_FN
9	D	0.39	5.37	3.00	0.10	40.00	IMPVALL\H-EMO_233_FN
10	D	0.50	17.53	6.10	0.10	40.00	IMPVALL\H-E10_233_FN
11	D	0.53	11.49	3.70	0.10	40.00	IMPVALL\H-E04_233_FN
12	D	0.55	4.68	3.40	0.10	40.00	IMPVALL\H-E05_233_FN
13	D	0.55	0.78	3.30	0.10	40.00	IMPVALL\H-E06_233_FN
14	D	0.55	4.80	3.20	0.10	40.00	IMPVALL\H-E07_233_FN
15	D	0.55	11.52	4.20	0.10	40.00	IMPVALL\H-E08_233_FN
16	D	0.53	14.55	3.70	0.10	40.00	IMPVALL\H-EDA_233_FN
17	D	0.76	3.04	4.60	0.10	40.00	IMPVALL\H-WSM_233_FN
18	D	0.21	4.61	1.10	0.20	20.00	COALINGA\H-PVB_047_FN
19	D	0.61	11.12	0.45	0.10	30.00	MORGAN\AND_058_FN
20	A	0.91	0.40	0.75	0.10	39.00	MORGAN\CYC_058_FN
21	A	0.98	0.95	1.15	0.10	27.00	MORGAN\G06_058_FN
22	C	0.02	6.74	0.84	0.20	26.00	MORGAN\HVR_058_FN
23	A	0.10	79.91	3.40	0.05	62.50	NAHANNI\S1_070_FN
24	A	0.47	30.77	0.55	0.10	62.50	NAHANNI\S2_070_FN
25	D	0.66	37.43	0.42	0.50	40.00	PALMSPR\DSP_197_FN
26	D	0.73	14.47	0.91	0.23	20.00	PALMSPR\NPS_197_FN
27	C	0.71	32.40	0.53	0.15	40.00	PALMSPR\WWT_197_FN
28	D	0.03	24.36	0.62	0.25	25.00	WHITTIER\A-JAB_190_FN
29	D	0.03	14.02	0.81	0.25	30.00	WHITTIER\A-DWN_190_FN
30	D	0.03	15.12	0.60	0.15	40.00	WHITTIER\A-NOR_190_FN
31	D	0.03	21.45	0.26	0.35	25.00	WHITTIER\A-EJS_190_FN
32	D	0.90	8.31	1.50	0.10	38.00	SUPERST\B-ICC_037_FN
33	D	0.80	3.40	1.90	0.12	20.00	SUPERST\B-PTS_037_FN
34	B	0.81	12.96	0.39	0.20	35.00	LOMAP\GIL_038_FN
35	D	0.81	19.54	1.29	0.20	38.00	LOMAP\GOF_038_FN
36	A	0.81	12.45	0.40	0.20	50.00	LOMAP\G01_038_FN
37	D	0.81	16.18	1.56	0.20	31.00	LOMAP\G02_038_FN
38	D	0.81	19.32	0.47	0.10	33.00	LOMAP\G03_038_FN
39	D	0.81	23.02	1.50	0.20	28.00	LOMAP\G04_038_FN
40	A	0.81	5.32	0.75	0.10	80.00	LOMAP\LGP_038_FN

Table A.2—*(continued)*

#	Record Sequence Number	Earthquake Name	Date	Station Name	Mw	ClstD (km)	Mech
41	802	Loma Prieta	18-Oct-1989	Saratoga - Aloha Ave	6.93	8.50	RV/OB
42	803	Loma Prieta	18-Oct-1989	Saratoga - W Valley Coll.	6.93	9.31	RV/OB
43	1642	Sierra Madre	28-Jun-1991	Cogswell Dam - Right Abutment	5.61	22.00	RV
44	821	Erzican, Turkey	13-Mar-1992	Erzincan	6.69	4.38	SS
45	879	Landers	28-Jun-1992	Lucerne	7.28	2.19	SS
46	959	Northridge-01	17-Jan-1994	Canoga Park - Topanga Can	6.69	14.70	RV
47	960	Northridge-01	17-Jan-1994	Canyon Country - W Lost Cany	6.69	12.44	RV
48	982	Northridge-01	17-Jan-1994	Jensen Filter Plant	6.69	5.43	RV
49	1004	Northridge-01	17-Jan-1994	LA - Sepulveda VA Hospital	6.69	8.44	RV
50	1013	Northridge-01	17-Jan-1994	LA Dam	6.69	5.92	RV
51	1044	Northridge-01	17-Jan-1994	Newhall - Fire Sta	6.69	5.92	RV
52	1045	Northridge-01	17-Jan-1994	Newhall - W Pico Canyon Rd.	6.69	5.48	RV
53	1050	Northridge-01	17-Jan-1994	Pacoima Dam (downstr)	6.69	7.01	RV
54	1052	Northridge-01	17-Jan-1994	Pacoima Kagel Canyon	6.69	7.26	RV
55	1063	Northridge-01	17-Jan-1994	Rinaldi Receiving Sta	6.69	6.50	RV
56	1084	Northridge-01	17-Jan-1994	Sylmar - Converter Sta	6.69	5.35	RV
57	1085	Northridge-01	17-Jan-1994	Sylmar - Converter Sta East	6.69	5.19	RV
58	1086	Northridge-01	17-Jan-1994	Sylmar - Olive View Med FF	6.69	5.30	RV
59	1106	Kobe, Japan	16-Jan-1995	KJMA	6.90	0.96	SS
60	1148	Kocaeli, Turkey	17-Aug-1999	Arcelik	7.51	13.49	SS
61	1158	Kocaeli, Turkey	17-Aug-1999	Duzce	7.51	15.37	SS
62	1161	Kocaeli, Turkey	17-Aug-1999	Gebze	7.51	10.92	SS
63	1171	Kocaeli, Turkey	17-Aug-1999	Sakarya	7.51	3.12	SS
64	1176	Kocaeli, Turkey	17-Aug-1999	Yarimca	7.51	4.83	SS
65	1492	Chi-Chi, Taiwan	20-Sep-1999	TCU052	7.62	0.66	RV/OB
66	1503	Chi-Chi, Taiwan	20-Sep-1999	TCU065	7.62	0.59	RV/OB
67	1505	Chi-Chi, Taiwan	20-Sep-1999	TCU068	7.62	0.32	RV/OB
68	1510	Chi-Chi, Taiwan	20-Sep-1999	TCU075	7.62	0.91	RV/OB
69	1511	Chi-Chi, Taiwan	20-Sep-1999	TCU076	7.62	2.76	RV/OB
70	1549	Chi-Chi, Taiwan	20-Sep-1999	TCU129	7.62	1.84	RV/OB

Table A.2—*(continued)*

#	GMX's C3	X or Y	θ or ϕ [degree]	T_p [sec]	Max f_{HP}	Min f_{LP}	FileName
41	D	0.81	11.53	1.69	0.10	38.00	LOMAP\STG_038_FN
42	D	0.81	15.65	1.15	0.10	38.00	LOMAP\WVC_038_FN
43	A	0.07	89.22	0.29	0.50	23.00	SMADRE\chan1_152_FN
44	D	0.31	1.95	2.30	0.10		ERZIKAN\ERZ_032_FN
45	A	0.66	20.24	4.50	0.08	60.00	LANDERS\LCN_239_FN
46	D	0.41	56.34	2.05	0.05	30.00	NORTHR\CNP_032_FN
47	C	0.81	6.42	0.67	0.10	30.00	NORTHR\LOS_032_FN
48	B	0.81	13.70	2.90	0.20		NORTHR\JEN_032_FN
49	D	0.72	26.01	0.85	0.08	50.00	NORTHR\0637_032_FN
50	A	0.81	16.04	1.34	0.12		NORTHR\LDM_032_FN
51	D	0.81	3.99	1.25	0.12	23.00	NORTHR\NWH_032_FN
52	B	0.81	10.99	2.30	0.10	30.00	NORTHR\WPI_032_FN
53	A	0.81	1.46	0.44	0.16	23.00	NORTHR\PAC_032_FN
54	B	0.81	5.41	0.88	0.14	23.00	NORTHR\PKC_032_FN
55	B	0.81	18.30	1.06	0.09	30.00	NORTHR\RRS_032_FN
56	D	0.81	13.29	3.00			NORTHR\SCS_032_FN
57	B	0.81	12.18	3.10			NORTHR\SCE_032_FN
58	D	0.81	6.32	2.58	0.12	23.00	NORTHR\SYL_032_FN
59	B	0.30	7.83	0.85	0.05		KOBE\KJM_140_FN
60	B	0.35	19.92	9.20	0.07	50.00	KOCAELI\ARC_184_FN
61	D	0.65	17.40	3.80		15.00	KOCAELI\DZC_163_FN
62	A	0.34	23.87	4.30	0.08	25.00	KOCAELI\GBZ_184_FN
63	B	0.24	3.56	5.70			KOCAELI\SKR090
64	D	0.14	13.92	3.80	0.07	50.00	KOCAELI\YPT_180_FN
65	A	0.39	6.59	6.70	0.04	50.00	CHICHI\TCU052_278_FN
66	D	0.38	5.99	4.50	0.06	50.00	CHICHI\TCU065_272_FN
67	A	0.39	7.01	9.00	0.03	50.00	CHICHI\TCU068_280_FN
68	D	0.36	4.05	4.40	0.04	50.00	CHICHI\TCU075_271_FN
69	D	0.32	0.05	3.20	0.10	50.00	CHICHI\TCU076_271_FN
70	D	0.29	3.75	4.10	0.03	50.00	CHICHI\TCU129_271_FN

A.3 ORDINARY GROUND MOTION RECORD SET

These earthquake ground motion records were to develop a S_{di} attenuation relationship in Chapter 3. The maximum closest distance to rupture (R_{rup}) was limited to 95 km to avoid the potential effects of (regionally differing) anelastic attenuation on spectral shape. Near-source ground motions with forward-directivity effects were largely excluded by restricting the R_{rup} to be greater than 15 km (SEAOC 1999). Free-field-like ground motions recorded on deep, stiff soil from all faulting styles were collected from the NGA database; we used Geomatrix-C1 (Instrument Housing) classes I, A, and B, and Geomatrix-C3 (Geotechnical Subsurface Characteristics) classes C and D. One randomly oriented (i.e., arbitrary) horizontal component was selected. This record set comprises 291 strong earthquake ground motions from 28 historical earthquakes with M_w ranging from 5.65 to 7.90.

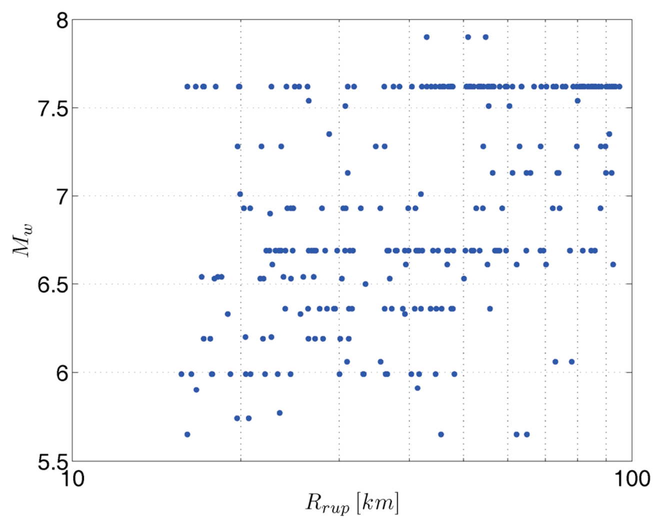

Fig. A.3 Earthquake magnitude and distance range for ordinary record set.

Table A.3 Earthquake ground motion properties for ordinary record set.

#	Record Sequence Number	Earthquake Name	Date	Station Name	Mw	ClstD (km)
1	28	Parkfield	28-Jun-1966	Cholame - Shandon Array #12	6.19	17.64
2	51	San Fernando	09-Feb-1971	2516 Via Tejon PV	6.61	55.20
3	58	San Fernando	09-Feb-1971	Cedar Springs Pumphouse	6.61	92.59
4	65	San Fernando	09-Feb-1971	Gormon - Oso Pump Plant	6.61	46.78
5	68	San Fernando	09-Feb-1971	LA - Hollywood Stor FF	6.61	22.77
6	92	San Fernando	09-Feb-1971	Wheeler Ridge - Ground	6.61	70.23
7	93	San Fernando	09-Feb-1971	Whittier Narrows Dam	6.61	39.45
8	94	San Fernando	09-Feb-1971	Wrightwood - 6074 Park Dr	6.61	62.23
9	122	Friuli, Italy-01	06-May-1976	Codroipo	6.50	33.40
10	131	Friuli, Italy-02	15-Sep-1976	Codroipo	5.91	41.39
11	138	Tabas, Iran	16-Sep-1978	Boshrooyeh	7.35	28.79
12	140	Tabas, Iran	16-Sep-1978	Ferdows	7.35	91.14
13	152	Coyote Lake	06-Aug-1979	SJB Overpass, Bent 3 g.l.	5.74	20.67
14	154	Coyote Lake	06-Aug-1979	San Juan Bautista, 24 Polk St	5.74	19.70
15	163	Imperial Valley-06	15-Oct-1979	Calipatria Fire Station	6.53	24.60
16	166	Imperial Valley-06	15-Oct-1979	Coachella Canal #4	6.53	50.10
17	172	Imperial Valley-06	15-Oct-1979	El Centro Array #1	6.53	21.68
18	175	Imperial Valley-06	15-Oct-1979	El Centro Array #12	6.53	17.94
19	176	Imperial Valley-06	15-Oct-1979	El Centro Array #13	6.53	21.98
20	186	Imperial Valley-06	15-Oct-1979	Niland Fire Station	6.53	36.92
21	188	Imperial Valley-06	15-Oct-1979	Plaster City	6.53	30.33
22	266	Victoria, Mexico	09-Jun-1980	Chihuahua	6.33	18.96
23	267	Victoria, Mexico	09-Jun-1980	Cucapah	6.33	25.57
24	268	Victoria, Mexico	09-Jun-1980	SAHOP Casa Flores	6.33	39.30
25	288	Irpinia, Italy-01	23-Nov-1980	Brienza	6.90	22.56
26	302	Irpinia, Italy-02	23-Nov-1980	Rionero In Vulture	6.20	22.69
27	303	Irpinia, Italy-02	23-Nov-1980	Sturno	6.20	20.39
28	316	Westmorland	26-Apr-1981	Parachute Test Site	5.90	16.66
29	322	Coalinga-01	02-May-1983	Cantua Creek School	6.36	24.02
30	323	Coalinga-01	02-May-1983	Parkfield - Cholame 12W	6.36	55.77
31	324	Coalinga-01	02-May-1983	Parkfield - Cholame 1E	6.36	43.68
32	326	Coalinga-01	02-May-1983	Parkfield - Cholame 2WA	6.36	44.72
33	328	Coalinga-01	02-May-1983	Parkfield - Cholame 3W	6.36	45.70
34	329	Coalinga-01	02-May-1983	Parkfield - Cholame 4AW	6.36	47.57
35	334	Coalinga-01	02-May-1983	Parkfield - Fault Zone 1	6.36	41.99
36	335	Coalinga-01	02-May-1983	Parkfield - Fault Zone 10	6.36	31.62
37	336	Coalinga-01	02-May-1983	Parkfield - Fault Zone 11	6.36	28.52
38	337	Coalinga-01	02-May-1983	Parkfield - Fault Zone 12	6.36	29.34
39	338	Coalinga-01	02-May-1983	Parkfield - Fault Zone 14	6.36	29.48
40	339	Coalinga-01	02-May-1983	Parkfield - Fault Zone 15	6.36	29.38

Table A.3—*(continued)*

#	Mech	GMX's C3	Max f_{HP}	Min f_{LP}	FileName
1	SS	D	0.20	20.00	PARKF\C12050
2	RV	C	0.20	20.00	SFERN\PVE065
3	RV	C	0.10	20.00	SFERN\CSP216
4	RV	C	0.10	23.00	SFERN\OPP000
5	RV	D	0.20	35.00	SFERN\PEL180
6	RV	D	0.10	23.00	SFERN\WRP090
7	RV	D	0.10	20.00	SFERN\WND143
8	RV	D	0.20	30.00	SFERN\WTW025
9	RV	D	0.10	25.00	FRIULI\A-COD000
10	RV	D	0.10	25.00	FRIULI\B-COD270
11	RV	C	0.13	20.00	TABAS\BOS-T1
12	RV	D	0.13	20.00	TABAS\FER-T1
13	SS	D	0.23	60.00	COYOTELK\SJ3337
14	SS	D	0.20	20.00	COYOTELK\SJB303
15	SS	D	0.10	40.00	IMPVALL\H-CAL315
16	SS	D	0.20	40.00	IMPVALL\H-CC4135
17	SS	D	0.10	40.00	IMPVALL\H-E01230
18	SS	D	0.10	40.00	IMPVALL\H-E12140
19	SS	D	0.20	40.00	IMPVALL\H-E13140
20	SS	D	0.10	40.00	IMPVALL\H-NIL360
21	SS	D	0.10	40.00	IMPVALL\H-PLS045
22	SS	D	0.20	27.00	VICT\CHI192
23	SS	D	0.20	44.00	VICT\QKP085
24	SS	C	0.20	28.00	VICT\SHP010
25	NORMAL	D	0.20	30.00	ITALY\A-BRZ270
26	NORMAL	C	0.20	30.00	ITALY\B-VLT000
27	NORMAL	C	0.21	23.00	ITALY\B-STU000
28	SS	D	0.10	33.00	WESTMORL\PTS315
29	RV	D	0.20	23.00	COALINGA\H-CAK360
30	RV	D	0.20	21.00	COALINGA\H-C12360
31	RV	D	0.20	20.00	COALINGA\H-C01000
32	RV	D	0.20	22.00	COALINGA\H-C02000
33	RV	C	0.20	21.00	COALINGA\H-C03000
34	RV	C	0.20	20.00	COALINGA\H-C4A090
35	RV	D	0.20	21.00	COALINGA\H-COW090
36	RV	D	0.20	24.00	COALINGA\H-Z10000
37	RV	D	0.20	21.00	COALINGA\H-Z11000
38	RV	C	0.20	20.00	COALINGA\H-PRK180
39	RV	C	0.10	23.00	COALINGA\H-Z14090
40	RV	D	0.20	20.00	COALINGA\H-Z15000

Table A.3—*(continued)*

#	Record Sequence Number	Earthquake Name	Date	Station Name	Mw	ClstD (km)
41	340	Coalinga-01	02-May-1983	Parkfield - Fault Zone 16	6.36	27.67
42	341	Coalinga-01	02-May-1983	Parkfield - Fault Zone 2	6.36	38.95
43	342	Coalinga-01	02-May-1983	Parkfield - Fault Zone 3	6.36	37.22
44	345	Coalinga-01	02-May-1983	Parkfield - Fault Zone 7	6.36	31.21
45	348	Coalinga-01	02-May-1983	Parkfield - Gold Hill 1W	6.36	36.15
46	355	Coalinga-01	02-May-1983	Parkfield - Gold Hill 6W	6.36	47.88
47	359	Coalinga-01	02-May-1983	Parkfield - Vineyard Cany 1E	6.36	26.38
48	366	Coalinga-01	02-May-1983	Parkfield - Vineyard Cany 6W	6.36	40.92
49	463	Morgan Hill	24-Apr-1984	Hollister Diff Array #1	6.19	26.43
50	464	Morgan Hill	24-Apr-1984	Hollister Diff Array #3	6.19	26.43
51	465	Morgan Hill	24-Apr-1984	Hollister Diff Array #4	6.19	26.43
52	466	Morgan Hill	24-Apr-1984	Hollister Diff Array #5	6.19	26.43
53	467	Morgan Hill	24-Apr-1984	Hollister Diff. Array	6.19	26.43
54	470	Morgan Hill	24-Apr-1984	San Juan Bautista, 24 Polk St	6.19	27.15
55	474	Morgan Hill	24-Apr-1984	Saratoga - WVC NE Corner	6.19	28.06
56	520	N. Palm Springs	08-Jul-1986	Hesperia	6.06	72.97
57	522	N. Palm Springs	08-Jul-1986	Indio	6.06	35.57
58	532	N. Palm Springs	08-Jul-1986	Rancho Cucamonga - FF	6.06	78.09
59	535	N. Palm Springs	08-Jul-1986	San Jacinto - Valley Cemetary	6.06	30.97
60	544	Chalfant Valley-01	20-Jul-1986	Bishop - LADWP South St	5.77	23.47
61	548	Chalfant Valley-02	21-Jul-1986	Benton	6.19	21.92
62	549	Chalfant Valley-02	21-Jul-1986	Bishop - LADWP South St	6.19	17.17
63	551	Chalfant Valley-02	21-Jul-1986	Convict Creek	6.19	31.19
64	556	Chalfant Valley-02	21-Jul-1986	McGee Creek - Surface	6.19	30.11
65	595	Whittier Narrows-01	01-Oct-1987	Bell Gardens - Jaboneria	5.99	17.79
66	605	Whittier Narrows-01	01-Oct-1987	Canyon Country - W Lost Cany	5.99	48.18
67	607	Whittier Narrows-01	01-Oct-1987	Carson - Catskill Ave	5.99	33.19
68	608	Whittier Narrows-01	01-Oct-1987	Carson - Water St	5.99	30.03
69	615	Whittier Narrows-01	01-Oct-1987	Downey - Co Maint Bldg	5.99	20.82
70	616	Whittier Narrows-01	01-Oct-1987	El Monte - Fairview Av	5.99	15.67
71	621	Whittier Narrows-01	01-Oct-1987	Glendora - N Oakbank	5.99	22.11
72	624	Whittier Narrows-01	01-Oct-1987	Huntington Beach - Lake St	5.99	44.58
73	626	Whittier Narrows-01	01-Oct-1987	LA - 116th St School	5.99	23.29
74	645	Whittier Narrows-01	01-Oct-1987	LB - Orange Ave	5.99	24.54
75	650	Whittier Narrows-01	01-Oct-1987	La Puente - Rimgrove Av	5.99	17.75
76	664	Whittier Narrows-01	01-Oct-1987	N Hollywood - Coldwater Can	5.99	33.11
77	667	Whittier Narrows-01	01-Oct-1987	Northridge - 17645 Saticoy St	5.99	41.69
78	668	Whittier Narrows-01	01-Oct-1987	Norwalk - Imp Hwy, S Grnd	5.99	20.42
79	672	Whittier Narrows-01	01-Oct-1987	Pacoima Kagel Canyon USC	5.99	36.29
80	673	Whittier Narrows-01	01-Oct-1987	Panorama City - Roscoe	5.99	36.55

Table A.3—*(continued)*

#	Mech	GMX's C3	Max f_{HP}	Min f_{LP}	FileName
41	RV	C	0.20	26.00	COALINGA\H-Z16000
42	RV	D	0.20	25.00	COALINGA\H-Z02090
43	RV	D	0.10	22.00	COALINGA\H-COH090
44	RV	C	0.20	30.00	COALINGA\H-Z07090
45	RV	D	0.20	22.00	COALINGA\H-PG1090
46	RV	C	0.20	30.00	COALINGA\H-PG6000
47	RV	C	0.20	24.00	COALINGA\H-PV1000
48	RV	C	0.20	27.00	COALINGA\H-VC6090
49	SS	D	0.20	30.00	MORGAN\HD1255
50	SS	D	0.10	30.00	MORGAN\HD3345
51	SS	D	0.10	30.00	MORGAN\HD4345
52	SS	D	0.20	30.00	MORGAN\HD5255
53	SS	D	0.20	23.00	MORGAN\HDA255
54	SS	D	0.10	21.00	MORGAN\SJB213
55	SS	D	0.20	30.00	MORGAN\WNE270
56	RV/OB	D	0.20	25.00	PALMSPR\HES002
57	RV/OB	D	0.10	35.00	PALMSPR\INO225
58	RV/OB	D	0.20	40.00	PALMSPR\CLJ000
59	RV/OB	D	0.20	31.00	PALMSPR\H06360
60	SS	D	0.10	20.00	CHALFANT\B-LAD270
61	SS	D	0.10	40.00	CHALFANT\A-BEN270
62	SS	D	0.10	40.00	CHALFANT\A-LAD180
63	SS	C	0.10	30.00	CHALFANT\A-CVK000
64	SS	C	0.10	50.00	CHALFANT\A-MCG270
65	RV/OB	D	0.10	25.00	WHITTIER\A-JAB297
66	RV/OB	C	0.23	22.50	WHITTIER\A-LOS270
67	RV/OB	D	0.18	25.00	WHITTIER\A-CAT090
68	RV/OB	D	0.20	25.00	WHITTIER\A-WAT180
69	RV/OB	D	0.20	30.00	WHITTIER\A-DWN180
70	RV/OB	D	0.13	25.00	WHITTIER\A-FAI270
71	RV/OB	D	0.23	25.00	WHITTIER\A-OAK170
72	RV/OB	D	0.17	25.00	WHITTIER\A-HNT360
73	RV/OB	D	0.20	30.00	WHITTIER\A-116270
74	RV/OB	D	0.12	25.00	WHITTIER\A-OR2010
75	RV/OB	D	0.18	25.00	WHITTIER\A-RIM015
76	RV/OB	C	0.20	25.00	WHITTIER\A-CWC180
77	RV/OB	D	0.23	25.00	WHITTIER\A-STC090
78	RV/OB	D	0.15	45.00	WHITTIER\A-NOR360
79	RV/OB	D	0.23	25.00	WHITTIER\A-KAG315
80	RV/OB	D	0.20	25.00	WHITTIER\A-RO2180

Table A.3—*(continued)*

#	Record Sequence Number	Earthquake Name	Date	Station Name	Mw	ClstD (km)
81	683	Whittier Narrows-01	01-Oct-1987	Pasadena - Old House Rd	5.99	19.17
82	701	Whittier Narrows-01	01-Oct-1987	Terminal Island - S Seaside	5.99	40.36
83	705	Whittier Narrows-01	01-Oct-1987	West Covina - S Orange Ave	5.99	16.32
84	719	Superstition Hills-02	24-Nov-1987	Brawley Airport	6.54	17.03
85	720	Superstition Hills-02	24-Nov-1987	Calipatria Fire Station	6.54	27.00
86	721	Superstition Hills-02	24-Nov-1987	El Centro Imp. Co. Cent	6.54	18.20
87	722	Superstition Hills-02	24-Nov-1987	Kornbloom Road (temp)	6.54	18.48
88	726	Superstition Hills-02	24-Nov-1987	Salton Sea Wildlife Refuge	6.54	25.88
89	729	Superstition Hills-02	24-Nov-1987	Wildlife Liquef. Array	6.54	23.85
90	733	Loma Prieta	18-Oct-1989	APEEL 2E Hayward Muir Sch	6.93	52.68
91	736	Loma Prieta	18-Oct-1989	APEEL 9 - Crystal Springs Res	6.93	41.03
92	737	Loma Prieta	18-Oct-1989	Agnews State Hospital	6.93	24.57
93	739	Loma Prieta	18-Oct-1989	Anderson Dam (Downstream)	6.93	20.26
94	754	Loma Prieta	18-Oct-1989	Coyote Lake Dam (Downst)	6.93	20.80
95	757	Loma Prieta	18-Oct-1989	Dumbarton Bridge West End FF	6.93	35.52
96	761	Loma Prieta	18-Oct-1989	Fremont - Emerson Court	6.93	39.85
97	772	Loma Prieta	18-Oct-1989	Halls Valley	6.93	30.49
98	773	Loma Prieta	18-Oct-1989	Hayward - BART Sta	6.93	54.15
99	776	Loma Prieta	18-Oct-1989	Hollister - South & Pine	6.93	27.93
100	778	Loma Prieta	18-Oct-1989	Hollister Diff. Array	6.93	24.82
101	783	Loma Prieta	18-Oct-1989	Oakland - Outer Harbor Wharf	6.93	74.26
102	784	Loma Prieta	18-Oct-1989	Oakland - Title & Trust	6.93	72.20
103	786	Loma Prieta	18-Oct-1989	Palo Alto - 1900 Embarc.	6.93	30.81
104	790	Loma Prieta	18-Oct-1989	Richmond City Hall	6.93	87.87
105	799	Loma Prieta	18-Oct-1989	SF Intern. Airport	6.93	58.65
106	800	Loma Prieta	18-Oct-1989	Salinas - John & Work	6.93	32.78
107	806	Loma Prieta	18-Oct-1989	Sunnyvale - Colton Ave.	6.93	24.23
108	826	Cape Mendocino	25-Apr-1992	Eureka - Myrtle & West	7.01	41.97
109	827	Cape Mendocino	25-Apr-1992	Fortuna - Fortuna Blvd	7.01	19.95
110	836	Landers	28-Jun-1992	Baker Fire Station	7.28	87.94
111	838	Landers	28-Jun-1992	Barstow	7.28	34.86
112	841	Landers	28-Jun-1992	Boron Fire Station	7.28	89.69
113	848	Landers	28-Jun-1992	Coolwater	7.28	19.74
114	850	Landers	28-Jun-1992	Desert Hot Springs	7.28	21.78
115	855	Landers	28-Jun-1992	Fort Irwin	7.28	62.98
116	860	Landers	28-Jun-1992	Hemet Fire Station	7.28	68.66
117	862	Landers	28-Jun-1992	Indio - Coachella Canal	7.28	54.25
118	884	Landers	28-Jun-1992	Palm Springs Airport	7.28	36.15
119	888	Landers	28-Jun-1992	San Bernardino - E & Hospitality	7.28	79.76
120	900	Landers	28-Jun-1992	Yermo Fire Station	7.28	23.62

Table A.3—*(continued)*

#	Mech	GMX's C3	Max f_{HP}	Min f_{LP}	FileName
81	RV/OB	C	0.23	25.00	WHITTIER\A-OLD090
82	RV/OB	D	0.20	25.00	WHITTIER\A-SSE252
83	RV/OB	D	0.23	25.00	WHITTIER\A-SOR225
84	SS	D	0.10	23.00	SUPERST\B-BRA225
85	SS	D	0.23	20.00	SUPERST\B-CAL225
86	SS	D	0.10	38.00	SUPERST\B-ICC090
87	SS	D	0.15	23.00	SUPERST\B-KRN360
88	SS	D	0.20	30.00	SUPERST\B-WLF315
89	SS	D	0.10	50.00	SUPERST\B-IVW090
90	RV/OB	D	0.20	30.00	LOMAP\A2E000
91	RV/OB	C	0.20	40.00	LOMAP\A09137
92	RV/OB	D	0.20	30.00	LOMAP\AGW000
93	RV/OB	D	0.20	40.00	LOMAP\AND340
94	RV/OB	C	0.10	30.00	LOMAP\CLD195
95	RV/OB	D	0.05	23.00	LOMAP\DUMB357
96	RV/OB	D	0.10	31.00	LOMAP\FMS090
97	RV/OB	C	0.20	22.00	LOMAP\HVR090
98	RV/OB	D	0.20	36.00	LOMAP\HWB310
99	RV/OB	D	0.10	23.00	LOMAP\HSP090
100	RV/OB	D	0.10	33.00	LOMAP\HDA255
101	RV/OB	D	0.10	23.00	LOMAP\CH12000
102	RV/OB	D	0.20	44.00	LOMAP\TIB290
103	RV/OB	D	0.20	30.00	LOMAP\PAE055
104	RV/OB	D	0.20	29.00	LOMAP\RCH280
105	RV/OB	D	0.20	31.00	LOMAP\SFO000
106	RV/OB	D	0.10	28.00	LOMAP\SJW250
107	RV/OB	D	0.10	32.00	LOMAP\SVL360
108	RV	D	0.16	23.00	CAPEMEND\EUR090
109	RV	D	0.07	23.00	CAPEMEND\FOR090
110	SS	D	0.10	23.00	LANDERS\BAK050
111	SS	D	0.07	23.00	LANDERS\BRS000
112	SS	D	0.07	23.00	LANDERS\BFS090
113	SS	D	0.10	30.00	LANDERS\CLW-LN
114	SS	D	0.07	23.00	LANDERS\DSP000
115	SS	C	0.07	23.00	LANDERS\FTI090
116	SS	D	0.16	23.00	LANDERS\H05000
117	SS	D	0.10	23.00	LANDERS\IND000
118	SS	D	0.07	23.00	LANDERS\PSA090
119	SS	D	0.10	50.00	LANDERS\HOS090
120	SS	D	0.07	23.00	LANDERS\YER360

Table A.3—*(continued)*

#	Record Sequence Number	Earthquake Name	Date	Station Name	Mw	ClstD (km)
121	942	Northridge-01	17-Jan-1994	Alhambra - Fremont School	6.69	36.77
122	944	Northridge-01	17-Jan-1994	Anaheim - W Ball Rd	6.69	68.62
123	945	Northridge-01	17-Jan-1994	Anaverde Valley - City R	6.69	38.00
124	948	Northridge-01	17-Jan-1994	Arcadia - Campus Dr	6.69	41.41
125	950	Northridge-01	17-Jan-1994	Baldwin Park - N Holly	6.69	47.98
126	951	Northridge-01	17-Jan-1994	Bell Gardens - Jaboneria	6.69	44.11
127	961	Northridge-01	17-Jan-1994	Carson - Catskill Ave	6.69	50.38
128	964	Northridge-01	17-Jan-1994	Compton - Castlegate St	6.69	47.04
129	965	Northridge-01	17-Jan-1994	Covina - S Grand Ave	6.69	57.51
130	966	Northridge-01	17-Jan-1994	Covina - W Badillo	6.69	53.45
131	968	Northridge-01	17-Jan-1994	Downey - Co Maint Bldg	6.69	46.74
132	971	Northridge-01	17-Jan-1994	Elizabeth Lake	6.69	36.55
133	974	Northridge-01	17-Jan-1994	Glendale - Las Palmas	6.69	22.21
134	978	Northridge-01	17-Jan-1994	Hollywood - Willoughby Ave	6.69	23.07
135	979	Northridge-01	17-Jan-1994	Huntington Bch - Waikiki	6.69	69.50
136	980	Northridge-01	17-Jan-1994	Huntington Beach - Lake St	6.69	77.45
137	981	Northridge-01	17-Jan-1994	Inglewood - Union Oil	6.69	42.20
138	984	Northridge-01	17-Jan-1994	LA - 116th St School	6.69	41.17
139	986	Northridge-01	17-Jan-1994	LA - Brentwood VA Hospital	6.69	22.50
140	987	Northridge-01	17-Jan-1994	LA - Centinela St	6.69	28.30
141	988	Northridge-01	17-Jan-1994	LA - Century City CC North	6.69	23.41
142	991	Northridge-01	17-Jan-1994	LA - Cypress Ave	6.69	30.70
143	993	Northridge-01	17-Jan-1994	LA - Fletcher Dr	6.69	27.26
144	995	Northridge-01	17-Jan-1994	LA - Hollywood Stor FF	6.69	24.03
145	998	Northridge-01	17-Jan-1994	LA - N Westmoreland	6.69	26.73
146	1000	Northridge-01	17-Jan-1994	LA - Pico & Sentous	6.69	31.33
147	1003	Northridge-01	17-Jan-1994	LA - Saturn St	6.69	27.01
148	1006	Northridge-01	17-Jan-1994	LA - UCLA Grounds	6.69	22.49
149	1008	Northridge-01	17-Jan-1994	LA - W 15th St	6.69	29.74
150	1009	Northridge-01	17-Jan-1994	LA - Wadsworth VA Hospital North	6.69	23.60
151	1010	Northridge-01	17-Jan-1994	LA - Wadsworth VA Hospital South	6.69	23.60
152	1015	Northridge-01	17-Jan-1994	LB - Rancho Los Cerritos	6.69	51.89
153	1017	Northridge-01	17-Jan-1994	La Habra - Briarcliff	6.69	59.62
154	1024	Northridge-01	17-Jan-1994	Lakewood - Del Amo Blvd	6.69	56.92
155	1025	Northridge-01	17-Jan-1994	Lancaster - Fox Airfield Grnd	6.69	52.12
156	1026	Northridge-01	17-Jan-1994	Lawndale - Osage Ave	6.69	39.91
157	1031	Northridge-01	17-Jan-1994	Leona Valley #5 - Ritter	6.69	37.80
158	1032	Northridge-01	17-Jan-1994	Leona Valley #6	6.69	38.03
159	1035	Northridge-01	17-Jan-1994	Manhattan Beach - Manhattan	6.69	39.29
160	1038	Northridge-01	17-Jan-1994	Montebello - Bluff Rd.	6.69	45.03

Table A.3—*(continued)*

#	Mech	GMX's C3	Max f_{HP}	Min f_{LP}	FileName
121	RV	D	0.12	25.00	NORTHR\ALH360
122	RV	D	0.23	30.00	NORTHR\WBA000
123	RV	D	0.20	46.00	NORTHR\ANA090
124	RV	D	0.23	30.00	NORTHR\CAM279
125	RV	D	0.23	30.00	NORTHR\NHO270
126	RV	D	0.13	30.00	NORTHR\JAB310
127	RV	D	0.20	30.00	NORTHR\CAT090
128	RV	D	0.20	30.00	NORTHR\CAS270
129	RV	C	0.20	30.00	NORTHR\GRA344
130	RV	D	0.20	30.00	NORTHR\BAD000
131	RV	D	0.20	23.00	NORTHR\DWN360
132	RV	D	0.16	46.00	NORTHR\ELI180
133	RV	C	0.10	30.00	NORTHR\GLP267
134	RV	D	0.13	30.00	NORTHR\WIL180
135	RV	D	0.20	30.00	NORTHR\WAI200
136	RV	D	0.20	23.00	NORTHR\HNT090
137	RV	D	0.16	23.00	NORTHR\ING090
138	RV	D	0.16	23.00	NORTHR\116360
139	RV	D	0.08	50.00	NORTHR\0638-285
140	RV	D	0.20	30.00	NORTHR\CEN245
141	RV	D	0.14	23.00	NORTHR\CCN360
142	RV	C	0.13	30.00	NORTHR\CYP143
143	RV	D	0.15	30.00	NORTHR\FLE234
144	RV	D	0.20	23.00	NORTHR\PEL090
145	RV	D	0.20	30.00	NORTHR\WST000
146	RV	D	0.20	46.00	NORTHR\PIC090
147	RV	D	0.10	30.00	NORTHR\STN110
148	RV	D	0.08	25.00	NORTHR\UCL090
149	RV	C	0.13	30.00	NORTHR\W15090
150	RV	D	0.08	50.00	NORTHR\5082A-325
151	RV	D	0.08	50.00	NORTHR\5082-235
152	RV	D	0.16	23.00	NORTHR\LBR000
153	RV	C	0.20	30.00	NORTHR\BRC000
154	RV	D	0.20	30.00	NORTHR\DEL090
155	RV	D	0.15	25.00	NORTHR\LAN090
156	RV	D	0.13	30.00	NORTHR\LOA092
157	RV	C	0.20	23.00	NORTHR\LV5000
158	RV	D	0.20	23.00	NORTHR\LV6360
159	RV	C	0.05	30.00	NORTHR\MAN090
160	RV	D	0.10	30.00	NORTHR\BLF296

Table A.3—*(continued)*

#	Record Sequence Number	Earthquake Name	Date	Station Name	Mw	ClstD (km)
161	1039	Northridge-01	17-Jan-1994	Moorpark - Fire Sta	6.69	24.76
162	1043	Northridge-01	17-Jan-1994	Neenach - Sacatara Ck	6.69	51.85
163	1047	Northridge-01	17-Jan-1994	Newport Bch - Newp & Coast	6.69	84.54
164	1053	Northridge-01	17-Jan-1994	Palmdale - Hwy 14 & Palmdale	6.69	41.67
165	1056	Northridge-01	17-Jan-1994	Phelan - Wilson Ranch	6.69	85.90
166	1057	Northridge-01	17-Jan-1994	Playa Del Rey - Saran	6.69	31.74
167	1059	Northridge-01	17-Jan-1994	Port Hueneme - Naval Lab.	6.69	51.79
168	1070	Northridge-01	17-Jan-1994	San Gabriel - E Grand Ave	6.69	39.31
169	1077	Northridge-01	17-Jan-1994	Santa Monica City Hall	6.69	26.45
170	1079	Northridge-01	17-Jan-1994	Seal Beach - Office Bldg	6.69	64.76
171	1088	Northridge-01	17-Jan-1994	Terminal Island - S Seaside	6.69	57.20
172	1092	Northridge-01	17-Jan-1994	Ventura - Harbor & California	6.69	58.00
173	1093	Northridge-01	17-Jan-1994	Villa Park - Serrano Ave	6.69	77.56
174	1094	Northridge-01	17-Jan-1994	West Covina - S Orange Ave	6.69	51.71
175	1097	Northridge-01	17-Jan-1994	Wrightwood - Nielson Ranch	6.69	81.69
176	1155	Kocaeli, Turkey	17-Aug-1999	Bursa Tofas	7.51	60.43
177	1160	Kocaeli, Turkey	17-Aug-1999	Fatih	7.51	55.48
178	1166	Kocaeli, Turkey	17-Aug-1999	Iznik	7.51	30.74
179	1179	Chi-Chi, Taiwan	20-Sep-1999	CHK	7.62	63.53
180	1180	Chi-Chi, Taiwan	20-Sep-1999	CHY002	7.62	24.98
181	1181	Chi-Chi, Taiwan	20-Sep-1999	CHY004	7.62	47.34
182	1183	Chi-Chi, Taiwan	20-Sep-1999	CHY008	7.62	40.44
183	1192	Chi-Chi, Taiwan	20-Sep-1999	CHY023	7.62	81.28
184	1203	Chi-Chi, Taiwan	20-Sep-1999	CHY036	7.62	16.06
185	1204	Chi-Chi, Taiwan	20-Sep-1999	CHY039	7.62	31.88
186	1209	Chi-Chi, Taiwan	20-Sep-1999	CHY047	7.62	24.14
187	1215	Chi-Chi, Taiwan	20-Sep-1999	CHY058	7.62	59.80
188	1217	Chi-Chi, Taiwan	20-Sep-1999	CHY060	7.62	68.86
189	1221	Chi-Chi, Taiwan	20-Sep-1999	CHY065	7.62	83.43
190	1223	Chi-Chi, Taiwan	20-Sep-1999	CHY067	7.62	83.56
191	1225	Chi-Chi, Taiwan	20-Sep-1999	CHY070	7.62	83.61
192	1228	Chi-Chi, Taiwan	20-Sep-1999	CHY076	7.62	42.16
193	1233	Chi-Chi, Taiwan	20-Sep-1999	CHY082	7.62	36.11
194	1236	Chi-Chi, Taiwan	20-Sep-1999	CHY088	7.62	37.48
195	1238	Chi-Chi, Taiwan	20-Sep-1999	CHY092	7.62	22.70
196	1241	Chi-Chi, Taiwan	20-Sep-1999	CHY096	7.62	82.26
197	1243	Chi-Chi, Taiwan	20-Sep-1999	CHY100	7.62	53.46
198	1246	Chi-Chi, Taiwan	20-Sep-1999	CHY104	7.62	18.04
199	1247	Chi-Chi, Taiwan	20-Sep-1999	CHY107	7.62	50.62
200	1252	Chi-Chi, Taiwan	20-Sep-1999	ESL	7.62	44.54

Table A.3—*(continued)*

#	Mech	GMX's C3	Max f_{HP}	Min f_{LP}	FileName
161	RV	D	0.16	23.00	NORTHR\MRP180
162	RV	D	0.12	46.00	NORTHR\NEE180
163	RV	D	0.12	46.00	NORTHR\NEW090
164	RV	C	0.20	46.00	NORTHR\PHP000
165	RV	D	0.20	46.00	NORTHR\PHE090
166	RV	D	0.10	30.00	NORTHR\SAR000
167	RV	D	0.14	23.00	NORTHR\PTH090
168	RV	D	0.10	30.00	NORTHR\GRN270
169	RV	D	0.14	23.00	NORTHR\STM360
170	RV	D	0.16	46.00	NORTHR\SEA000
171	RV	D	0.13	30.00	NORTHR\SSE330
172	RV	D	0.10	25.00	NORTHR\VEN360
173	RV	D	0.10	30.00	NORTHR\SER270
174	RV	D	0.10	30.00	NORTHR\SOR315
175	RV	C	0.24	46.00	NORTHR\WWN180
176	SS	D	0.02	50.00	KOCAELI\BUR000
177	SS	C	0.01	50.00	KOCAELI\FAT090
178	SS	D	0.07	25.00	KOCAELI\IZN090
179	RV/OB	D	0.14	20.00	CHICHI\CHK-N
180	RV/OB	D	0.03	50.00	CHICHI\CHY002-W
181	RV/OB	D	0.03	40.00	CHICHI\CHY004-W
182	RV/OB	D	0.03	40.00	CHICHI\CHY008-W
183	RV/OB	D	0.03	30.00	CHICHI\CHY023-W
184	RV/OB	D	0.03	50.00	CHICHI\CHY036-N
185	RV/OB	D	0.02	40.00	CHICHI\CHY039-E
186	RV/OB	D	0.03	50.00	CHICHI\CHY047-N
187	RV/OB	D	0.03	23.00	CHICHI\CHY058-N
188	RV/OB	D	0.03	30.00	CHICHI\CHY060-E
189	RV/OB	D	0.02	33.00	CHICHI\CHY065-E
190	RV/OB	D	0.02	40.00	CHICHI\CHY067-W
191	RV/OB	D	0.02	24.00	CHICHI\CHY070-N
192	RV/OB	D	0.03	50.00	CHICHI\CHY076-E
193	RV/OB	D	0.03	50.00	CHICHI\CHY082-N
194	RV/OB	D	0.04	33.00	CHICHI\CHY088-E
195	RV/OB	D	0.05	50.00	CHICHI\CHY092-W
196	RV/OB	D	0.03	50.00	CHICHI\CHY096-W
197	RV/OB	D	0.02	50.00	CHICHI\CHY100-W
198	RV/OB	D	0.05	50.00	CHICHI\CHY104-N
199	RV/OB	D	0.02	50.00	CHICHI\CHY107-W
200	RV/OB	C	0.15	25.00	CHICHI\ESL-E

Table A.3—*(continued)*

#	Record Sequence Number	Earthquake Name	Date	Station Name	Mw	ClstD (km)
201	1255	Chi-Chi, Taiwan	20-Sep-1999	HWA	7.62	55.59
202	1258	Chi-Chi, Taiwan	20-Sep-1999	HWA005	7.62	47.58
203	1259	Chi-Chi, Taiwan	20-Sep-1999	HWA006	7.62	47.86
204	1260	Chi-Chi, Taiwan	20-Sep-1999	HWA007	7.62	56.30
205	1261	Chi-Chi, Taiwan	20-Sep-1999	HWA009	7.62	56.06
206	1262	Chi-Chi, Taiwan	20-Sep-1999	HWA011	7.62	53.19
207	1263	Chi-Chi, Taiwan	20-Sep-1999	HWA012	7.62	56.65
208	1264	Chi-Chi, Taiwan	20-Sep-1999	HWA013	7.62	54.32
209	1265	Chi-Chi, Taiwan	20-Sep-1999	HWA014	7.62	55.24
210	1266	Chi-Chi, Taiwan	20-Sep-1999	HWA015	7.62	51.12
211	1267	Chi-Chi, Taiwan	20-Sep-1999	HWA016	7.62	52.18
212	1268	Chi-Chi, Taiwan	20-Sep-1999	HWA017	7.62	51.11
213	1269	Chi-Chi, Taiwan	20-Sep-1999	HWA019	7.62	55.59
214	1270	Chi-Chi, Taiwan	20-Sep-1999	HWA020	7.62	44.54
215	1276	Chi-Chi, Taiwan	20-Sep-1999	HWA027	7.62	51.62
216	1277	Chi-Chi, Taiwan	20-Sep-1999	HWA028	7.62	53.84
217	1278	Chi-Chi, Taiwan	20-Sep-1999	HWA029	7.62	54.29
218	1279	Chi-Chi, Taiwan	20-Sep-1999	HWA030	7.62	46.95
219	1285	Chi-Chi, Taiwan	20-Sep-1999	HWA036	7.62	43.80
220	1286	Chi-Chi, Taiwan	20-Sep-1999	HWA037	7.62	46.20
221	1288	Chi-Chi, Taiwan	20-Sep-1999	HWA039	7.62	45.89
222	1289	Chi-Chi, Taiwan	20-Sep-1999	HWA041	7.62	47.76
223	1290	Chi-Chi, Taiwan	20-Sep-1999	HWA043	7.62	58.05
224	1292	Chi-Chi, Taiwan	20-Sep-1999	HWA045	7.62	63.43
225	1294	Chi-Chi, Taiwan	20-Sep-1999	HWA048	7.62	51.41
226	1295	Chi-Chi, Taiwan	20-Sep-1999	HWA049	7.62	50.76
227	1296	Chi-Chi, Taiwan	20-Sep-1999	HWA050	7.62	53.27
228	1297	Chi-Chi, Taiwan	20-Sep-1999	HWA051	7.62	53.56
229	1299	Chi-Chi, Taiwan	20-Sep-1999	HWA054	7.62	43.01
230	1300	Chi-Chi, Taiwan	20-Sep-1999	HWA055	7.62	47.46
231	1306	Chi-Chi, Taiwan	20-Sep-1999	HWA2	7.62	55.59
232	1311	Chi-Chi, Taiwan	20-Sep-1999	ILA005	7.62	87.20
233	1312	Chi-Chi, Taiwan	20-Sep-1999	ILA006	7.62	85.07
234	1316	Chi-Chi, Taiwan	20-Sep-1999	ILA012	7.62	88.18
235	1318	Chi-Chi, Taiwan	20-Sep-1999	ILA014	7.62	80.67
236	1324	Chi-Chi, Taiwan	20-Sep-1999	ILA030	7.62	85.62
237	1327	Chi-Chi, Taiwan	20-Sep-1999	ILA035	7.62	93.43
238	1328	Chi-Chi, Taiwan	20-Sep-1999	ILA036	7.62	89.98
239	1330	Chi-Chi, Taiwan	20-Sep-1999	ILA039	7.62	86.11
240	1342	Chi-Chi, Taiwan	20-Sep-1999	ILA055	7.62	90.30

Table A.3—*(continued)*

#	Mech	GMX's C3	Max f_{HP}	Min f_{LP}	FileName
201	RV/OB	D	0.15	50.00	CHICHI\HWA-N
202	RV/OB	D	0.05	40.00	CHICHI\HWA005-W
203	RV/OB	D	0.06	50.00	CHICHI\HWA006-N
204	RV/OB	D	0.02	30.00	CHICHI\HWA007-E
205	RV/OB	D	0.05	50.00	CHICHI\HWA009-N
206	RV/OB	D	0.02	30.00	CHICHI\HWA011-N
207	RV/OB	D	0.06	40.00	CHICHI\HWA012-N
208	RV/OB	D	0.02	50.00	CHICHI\HWA013-E
209	RV/OB	D	0.02	20.00	CHICHI\HWA014-N
210	RV/OB	D	0.02	50.00	CHICHI\HWA015-N
211	RV/OB	D	0.05	50.00	CHICHI\HWA016-N
212	RV/OB	D	0.02	50.00	CHICHI\HWA017-N
213	RV/OB	D	0.02	50.00	CHICHI\HWA019-E
214	RV/OB	C	0.02	50.00	CHICHI\HWA020-N
215	RV/OB	D	0.03	40.00	CHICHI\HWA027-N
216	RV/OB	D	0.02	50.00	CHICHI\HWA028-N
217	RV/OB	D	0.12	50.00	CHICHI\HWA029-N
218	RV/OB	D	0.02	50.00	CHICHI\HWA030-E
219	RV/OB	D	0.02	30.00	CHICHI\HWA036-N
220	RV/OB	D	0.04	30.00	CHICHI\HWA037-E
221	RV/OB	C	0.03	40.00	CHICHI\HWA039-E
222	RV/OB	D	0.02	30.00	CHICHI\HWA041-E
223	RV/OB	D	0.05	40.00	CHICHI\HWA043-E
224	RV/OB	C	0.02	40.00	CHICHI\HWA045-N
225	RV/OB	D	0.05	50.00	CHICHI\HWA048-W
226	RV/OB	D	0.02	40.00	CHICHI\HWA049-W
227	RV/OB	D	0.05	50.00	CHICHI\HWA050-N
228	RV/OB	D	0.02	40.00	CHICHI\HWA051-W
229	RV/OB	D	0.06	30.00	CHICHI\HWA054-N
230	RV/OB	D	0.04	40.00	CHICHI\HWA055-W
231	RV/OB	D	0.20	50.00	CHICHI\HWA2-E
232	RV/OB	D	0.02	30.00	CHICHI\ILA005-N
233	RV/OB	D	0.02	30.00	CHICHI\ILA006-N
234	RV/OB	D	0.05	20.00	CHICHI\ILA012-N
235	RV/OB	D	0.03	30.00	CHICHI\ILA014-N
236	RV/OB	D	0.02	20.00	CHICHI\ILA030-N
237	RV/OB	D	0.05	20.00	CHICHI\ILA035-E
238	RV/OB	D	0.05	40.00	CHICHI\ILA036-N
239	RV/OB	D	0.03	20.00	CHICHI\ILA039-E
240	RV/OB	D	0.05	30.00	CHICHI\ILA055-N

Table A.3—*(continued)*

#	Record Sequence Number	Earthquake Name	Date	Station Name	Mw	ClstD (km)
241	1343	Chi-Chi, Taiwan	20-Sep-1999	ILA056	7.62	92.04
242	1345	Chi-Chi, Taiwan	20-Sep-1999	ILA061	7.62	78.55
243	1346	Chi-Chi, Taiwan	20-Sep-1999	ILA062	7.62	73.22
244	1348	Chi-Chi, Taiwan	20-Sep-1999	ILA064	7.62	72.33
245	1349	Chi-Chi, Taiwan	20-Sep-1999	ILA066	7.62	70.35
246	1402	Chi-Chi, Taiwan	20-Sep-1999	NST	7.62	38.43
247	1431	Chi-Chi, Taiwan	20-Sep-1999	TAP043	7.62	91.19
248	1433	Chi-Chi, Taiwan	20-Sep-1999	TAP047	7.62	84.46
249	1469	Chi-Chi, Taiwan	20-Sep-1999	TCU011	7.62	75.17
250	1470	Chi-Chi, Taiwan	20-Sep-1999	TCU014	7.62	92.70
251	1480	Chi-Chi, Taiwan	20-Sep-1999	TCU036	7.62	19.84
252	1481	Chi-Chi, Taiwan	20-Sep-1999	TCU038	7.62	25.44
253	1482	Chi-Chi, Taiwan	20-Sep-1999	TCU039	7.62	19.90
254	1484	Chi-Chi, Taiwan	20-Sep-1999	TCU042	7.62	26.32
255	1498	Chi-Chi, Taiwan	20-Sep-1999	TCU059	7.62	17.13
256	1500	Chi-Chi, Taiwan	20-Sep-1999	TCU061	7.62	17.19
257	1502	Chi-Chi, Taiwan	20-Sep-1999	TCU064	7.62	16.62
258	1526	Chi-Chi, Taiwan	20-Sep-1999	TCU098	7.62	47.67
259	1539	Chi-Chi, Taiwan	20-Sep-1999	TCU113	7.62	31.07
260	1557	Chi-Chi, Taiwan	20-Sep-1999	TTN001	7.62	56.56
261	1559	Chi-Chi, Taiwan	20-Sep-1999	TTN003	7.62	94.99
262	1560	Chi-Chi, Taiwan	20-Sep-1999	TTN004	7.62	66.87
263	1567	Chi-Chi, Taiwan	20-Sep-1999	TTN012	7.62	81.67
264	1569	Chi-Chi, Taiwan	20-Sep-1999	TTN014	7.62	63.53
265	1573	Chi-Chi, Taiwan	20-Sep-1999	TTN020	7.62	50.69
266	1574	Chi-Chi, Taiwan	20-Sep-1999	TTN022	7.62	53.34
267	1575	Chi-Chi, Taiwan	20-Sep-1999	TTN023	7.62	54.29
268	1579	Chi-Chi, Taiwan	20-Sep-1999	TTN027	7.62	76.13
269	1581	Chi-Chi, Taiwan	20-Sep-1999	TTN031	7.62	56.30
270	1583	Chi-Chi, Taiwan	20-Sep-1999	TTN033	7.62	59.43
271	1586	Chi-Chi, Taiwan	20-Sep-1999	TTN041	7.62	45.35
272	1589	Chi-Chi, Taiwan	20-Sep-1999	TTN045	7.62	61.16
273	1592	Chi-Chi, Taiwan	20-Sep-1999	TTN048	7.62	79.69
274	1628	St Elias, Alaska	28-Feb-1979	Icy Bay	7.54	26.46
275	1629	St Elias, Alaska	28-Feb-1979	Yakutat	7.54	80.00
276	1740	Little Skull Mtn,NV	29-Jun-1992	Station #1-Lathrop Wells	5.65	16.06
277	1742	Little Skull Mtn,NV	29-Jun-1992	Station #3-Beaty	5.65	45.59
278	1743	Little Skull Mtn,NV	29-Jun-1992	Station #4-Pahrump 2	5.65	62.21
279	1744	Little Skull Mtn,NV	29-Jun-1992	Station #5-Pahrump 1	5.65	64.94
280	1766	Hector Mine	16-Oct-1999	Baker Fire Station	7.13	64.79

Table A.3—*(continued)*

#	Mech	GMX's C3	Max f_{HP}	Min f_{LP}	FileName
241	RV/OB	D	0.05	30.00	CHICHI\ILA056-N
242	RV/OB	C	0.02	40.00	CHICHI\ILA061-N
243	RV/OB	C	0.02	40.00	CHICHI\ILA062-W
244	RV/OB	C	0.02	40.00	CHICHI\ILA064-W
245	RV/OB	C	0.02	50.00	CHICHI\ILA066-W
246	RV/OB	C	0.03	50.00	CHICHI\NST-E
247	RV/OB	D	0.02	20.00	CHICHI\TAP043-E
248	RV/OB	D	0.02	22.00	CHICHI\TAP047-N
249	RV/OB	C	0.03	30.00	CHICHI\TCU011-N
250	RV/OB	D	0.02	25.00	CHICHI\TCU014-N
251	RV/OB	D	0.02	40.00	CHICHI\TCU036-N
252	RV/OB	D	0.05	20.00	CHICHI\TCU038-N
253	RV/OB	D	0.02	50.00	CHICHI\TCU039-N
254	RV/OB	D	0.05	50.00	CHICHI\TCU042-N
255	RV/OB	D	0.03	30.00	CHICHI\TCU059-E
256	RV/OB	D	0.04	50.00	CHICHI\TCU061-E
257	RV/OB	D	0.02	50.00	CHICHI\TCU064-E
258	RV/OB	C	0.02	50.00	CHICHI\TCU098-E
259	RV/OB	D	0.03	50.00	CHICHI\TCU113-N
260	RV/OB	D	0.03	30.00	CHICHI\TTN001-N
261	RV/OB	D	0.03	20.00	CHICHI\TTN003-N
262	RV/OB	D	0.04	20.00	CHICHI\TTN004-N
263	RV/OB	D	0.02	20.00	CHICHI\TTN012-E
264	RV/OB	D	0.02	20.00	CHICHI\TTN014-N
265	RV/OB	D	0.02	23.00	CHICHI\TTN020-N
266	RV/OB	D	0.02	20.00	CHICHI\TTN022-N
267	RV/OB	D	0.02	30.00	CHICHI\TTN023-E
268	RV/OB	C	0.03	30.00	CHICHI\TTN027-N
269	RV/OB	D	0.03	30.00	CHICHI\TTN031-E
270	RV/OB	D	0.02	30.00	CHICHI\TTN033-N
271	RV/OB	D	0.03	40.00	CHICHI\TTN041-W
272	RV/OB	D	0.05	30.00	CHICHI\TTN045-N
273	RV/OB	D	0.03	20.00	CHICHI\TTN048-N
274	RV	D	0.04	23.00	STELIAS\059v2180
275	RV	D	0.04	23.00	STELIAS\059v2279
276	NORMAL	D	0.10	33.00	SKULLMT\Lsm1000
277	NORMAL	C	0.10	33.00	SKULLMT\Lsm3270
278	NORMAL	D	0.10	33.00	SKULLMT\Lsm4000
279	NORMAL	D	0.10	33.00	SKULLMT\Lsm5270
280	SS	D	0.07	23.00	HECTOR\32075140

Table A.3—*(continued)*

#	Record Sequence Number	Earthquake Name	Date	Station Name	Mw	ClstD (km)
281	1768	Hector Mine	16-Oct-1999	Barstow	7.13	61.20
282	1776	Hector Mine	16-Oct-1999	Desert Hot Springs	7.13	56.40
283	1783	Hector Mine	16-Oct-1999	Fort Irwin	7.13	65.89
284	1789	Hector Mine	16-Oct-1999	Hesperia - 4th & Palm	7.13	89.87
285	1791	Hector Mine	16-Oct-1999	Indio - Coachella Canal	7.13	73.55
286	1792	Hector Mine	16-Oct-1999	Indio - Riverside Co Fair Grnds	7.13	74.00
287	1794	Hector Mine	16-Oct-1999	Joshua Tree	7.13	31.06
288	1810	Hector Mine	16-Oct-1999	Mecca - CVWD Yard	7.13	91.96
289	2107	Denali, Alaska	03-Nov-2002	Carlo (temp)	7.90	50.94
290	2111	Denali, Alaska	03-Nov-2002	R109 (temp)	7.90	43.00
291	2113	Denali, Alaska	03-Nov-2002	TAPS Pump Station #09	7.90	54.78

Table A.3—*(continued)*

#	Mech	GMX's C3	Max f_{HP}	Min f_{LP}	FileName
281	SS	D	0.08	46.00	HECTOR\23559090
282	SS	D	0.10	46.00	HECTOR\12149360
283	SS	C	0.07	23.00	HECTOR\32577090
284	SS	C	0.10	46.00	HECTOR\23583090
285	SS	D	0.12	23.00	HECTOR\12026090
286	SS	D	0.10	46.00	HECTOR\12543090
287	SS	C	0.07	46.00	HECTOR\22170090
288	SS	C	0.07	46.00	HECTOR\11625090
289	SS	C	0.04	30.00	DENALI\5595-090
290	SS	D	0.05	40.00	DENALI\5596-090
291	SS	D	0.10	40.00	DENALI\ps09013

REFERENCES

Next generation attenuation of ground motions (NGA) project. (2006). http://peer.berkeley.edu/nga/ (Accessed 10/10/2006).

Aagaard, B. T., Hall, J. F., and Heaton, T. H. (2000). "Sensitivity study of near-source ground motion," *Proceedings of the 12th World Conference on Earthquake Engineering*, New Zealand Society for Earthquake Engineering, Upper Hutt, New Zealand.

Aagaard, B. T., Hall, J. F., and Heaton, T. H. (2001). "Characterization of near-source ground motions with earthquake simulations," *Earthquake Spectra*, **17**(2): 177-207.

Abrahamson, N. A. (2000). "Effects of rupture directivity on probabilistic seismic hazard analysis," *Proceedings of the Sixth International Conference on Seismic Zonation: Managing Earthquake Risk in the 21st Century*, Palm Springs, CA, 12-15 November 2000: 6 pp.

Abrahamson, N. A., and Silva, W. J. (1997). "Empirical response spectral attenuation relations for shallow crustal earthquakes," *Seismological Research Letters*, **68**(1): 94-127.

Akkar, S., and Bommer, J. J. (2006). "Influence of long-period filter cut-off on elastic spectral displacements," *Earthquake Engineering & Structural Dynamics*, **35**(9): 1145-1165.

Alavi, B., and Krawinkler, H. (2001). "Effects of near-field ground motion on frame structures," John A. Blume Earthquake Engineering Center, Report No.138, Department of Civil and Environmental Engineering, Stanford University, Stanford, CA: 301 pp. http://blume.stanford.edu/Blume/TRList.htm (Accessed 05/31/2006).

Anderson, J. C., and Bertero, V. V. (1987). "Uncertainties in establishing design earthquakes," *Journal of Structural Engineering*, **113**(8): 1709-1724.

Anderson, J. C., Bertero, V. V., and Bertero, R. D. (1999). "Performance improvement of long period building structures subjected to severe pulse-type ground motions," Pacific Earthquake Engineering Research Center, PEER Report 1999/09, University of California, Berkeley: 229 pp.

ATC-40. (1996). "Methodology for seismic evaluation and retrofit of existing concrete buildings," *Applied Technology Council*, Redwood City, CA.

Atkinson, G. M., and Silva, W. (2000). "Stochastic modeling of California ground motions," *Bulletin of the Seismological Society of America*, **90**(2): 255-274.

Baker, J. W. (2007). "Quantitative classification of near-fault ground motions using wavelet analysis," *Bulletin of the Seismological Society of America*: (In review).

Baker, J. W., and Cornell, C. A. (2005a). "A vector-valued ground motion intensity measure consisting of spectral acceleration and epsilon," *Earthquake Engineering & Structural Dynamics*, **34**(10): 1193-1217.

Baker, J. W., and Cornell, C. A. (2005b). "Vector-valued ground motion intensity measures for probabilistic seismic demand analysis," John A. Blume Earthquake Engineering Center, Report No. 150, Stanford University, Stanford, CA: 321 pp. http://blume.stanford.edu/Blume/TRList.htm (Accessed 05/31/2006).

Baker, J. W., and Cornell, C. A. (2006a). "Correlation of response spectral values for multicomponent ground motions," *Bulletin of the Seismological Society of America*, **96**(1): 215-227.

Baker, J. W., and Cornell, C. A. (2006b). "Spectral shape, epsilon and record selection," *Earthquake Engineering & Structural Dynamics*, **35**(9): 1077-1095. http://dx.doi.org/10.1002/eqe.571

Baker, J. W., and Cornell, C. A. (2006c). "Which spectral acceleration are you using?," *Earthquake Spectra*, **22**(2): 293-312.

Bates, D. M., and Watts, D. G. (1988). *Nonlinear regression analysis and its applications*, New York, Wiley, c1988, 365 pp

Bazzurro, P. (1998). "Probabilistic seismic demand analysis," *Ph.D. Report*, Department of Civil and Environmental Engineering, Stanford University, Stanford, CA, 329 pp. http://www.stanford.edu/group/rms/ (Accessed 10/10/2006).

Bazzurro, P., and Cornell, C. A. (1999). "Disaggregation of seismic hazard," *Bulletin of the Seismological Society of America*, **89**(2): 501-520.

Bazzurro, P., and Cornell, C. A. (2002). "Vector-valued probabilistic seismic hazard analysis (VPSHA)," *Proceedings of the 7th U.S. National Conference on Earthquake Engineering, Paper No. 61*, 1276038 (EQ) call no. CF 61, Boston, Massachusetts.

Bazzurro, P., and Luco, N. (2004). "Parameterization of non-stationary acceleration time histories," Lifelines Program Project 1G00 Addenda, Pacific Earthquake Engineering Research (PEER) Center, University of California, Berkeley, CA: 83 pp. http://peer.berkeley.edu/lifelines/LL-CEC/reports/final_reports/1G00-FR_pt2.pdf (Accessed 10/10/2006).

Bazzurro, P., and Luco, N. (2006). "Damage potential of near-source ground motion records," *Proceedings of the 8th U.S. National Conference on Earthquake Engineering*, San Francisco, CA, 18-22 April, 2006: 10 pp.

Bazzurro, P., Sjoberg, B., Luco, N., Silva, W., and Darragh, R. (2004). "Effects of strong motion processing procedures on time histories, elastic and inelastic spectra," *Workshop on Strong-Motion Record Processing, The Consortium of Organizations for Strong-Motion Observation Systems (COSMOS)*, Richmond, CA, May 26-27 2004: 39 pp.

Benjamin, J. R., and Cornell, C. A. (1970). *Probability, statistics, and decision for civil engineers*, McGraw Hill, Inc. New York, 684 pp

Bertero, V. V., Mahin, S. A., and Herrera, R. A. (1978). "Aseismic design implications of near-fault San Fernando earthquake records," *Earthquake Engineering and Structural Dynamics*, **6**(1): 31-42.

Boore, D. M. (1983). "Stochastic simulation of high-frequency ground motions based on seismological models of the radiated spectra," *Bulletin of the Seismological Society of America*, **73**(6A): 1865-1894.

Boore, D. M. (2003). "Simulation of ground motion using the stochastic method," *Pure and applied geophysics*, **160**(3): 635-676.

Boore, D. M. (2005). "Erratum: Equations for estimating horizontal response spectra and peak acceleration from western north American earthquakes: A summary of recent work," *Seismological Research Letters*, **76**(3): 368-369.

Boore, D. M., and Bommer, J. J. (2005). "Processing of strong-motion accelerograms: Needs, options and consequences," *Soil Dynamics and Earthquake Engineering*, **25**(2): 93-115.

Bozorgnia, Y., Hachem, M. M., and Campbell, K. W. (2006). "Attenuation of inelastic and damage spectra," *Proceedings of the 8th U.S. National Conference on Earthquake Engineering*, San Francisco, CA, 18-22 April 2006: 11 pp.

Bray, J. D., and Rodriguez-Marek, A. (2004). "Characterization of forward-directivity ground motions in the near-fault region," *Soil Dynamics and Earthquake Engineering*, **24**(11): 815-828.

Chakraborti, A., and Gupta, V. K. (2005). "Scaling of strength reduction factors for degrading elasto-plastic oscillators," *Earthquake Engineering & Structural Dynamics*, **34**(2): 189-206.

Chen, X. (1995). "Near-field ground motion from the Landers earthquake," (Chapter 2: Nature of the near-field ground motion), EERL 95-02, Earthquake Engineering Research Laboratory, California Institute of Technology, Pasadena, CA: 169 pp.

Chintanapakdee, C., and Chopra, A. K. (2003). "Evaluation of the modal pushover analysis procedure using vertically "Regular" And irregular generic frames," Earthquake Engineering Research Center Report No. EERC-2003/03, University of California, Berkeley, CA: 213.

Chopra, A. K. (2001). *Dynamics of structures: Theory and applications to earthquake engineering*, Second Edition, Prentice Hall, Englewood Cliffs, New Jersey: 844.

Chopra, A. K., and Chintanapakdee, C. (2004). "Inelastic deformation ratios for design and evaluation of structures: Single-degree-of-freedom bilinear systems," *Journal of Structural Engineering*, **130**(9): 1309-1319.

Chopra, A. K., and Goel, R. K. (2002). "A modal pushover analysis procedure for estimating seismic demands for buildings," *Earthquake Engineering & Structural Dynamics*, **31**(3): 561-582.

Collins, K. R., Wen, Y., and Foutch, D. A. (1996). "Dual-level seismic design: A reliability-based methodology," *Earthquake Engineering & Structural Dynamics*, **25**(12): 1433-1467.

Cornell, C. A. (1968). "Engineering seismic risk analysis," *Bulletin of the Seismological Society of America*, **58**(5): 1583-1606.

Cornell, C. A. (1996a). "Calculating building seismic performance reliability: A basis for multi-level design norms," *Proceedings of the 11th World Conference on Earthquake Engineering, Paper No. 2122*, Acapulco, Mexico, 8 pp.

Cornell, C. A. (1996b). "Reliability-based earthquake-resistant design: The future," *Proceedings of the Eleventh World Conference on Earthquake Engineering, Paper No. 2166*, Acapulco, Mexico, 11 pp.

Cornell, C. A., and Krawinkler, H. (2000). "Progress and challenges in seismic performance assessment," *PEER Center News*, **3**(2) http://peer.berkeley.edu/news/2000spring/index.html (Accessed 10/10/2006).

Cuesta, I., and Aschheim, M. A. (2001). "Isoductile strengths and strength-reduction factors of elasto-plastic SDOF systems subjected to simple waveforms," *Earthquake Engineering & Structural Dynamics*, **30**(7): 1043-1059. http://dx.doi.org/10.1002/eqe.51

Efron, B., and Tibshirani, R. J. (1993). *An introduction to the bootstrap*, Chapman & Hall/CRC, New York: 436 pp.

Fajfar, P. (2000). "A nonlinear analysis method for performance-based seismic design," *Earthquake Spectra*, **16**(3): 573-592.

Farrow, K. T., and Kurama, Y. C. (2004). "SDOF displacement ductility demands based on smooth ground motion response spectra," *Engineering Structures*, **26**(12): 1713-1733.

FEMA-273. (1997). "NEHRP guidelines for the seismic rehabilitation of building," *Building Seismic Safety Council*, Federal Emergency Management Agency, Washington, D.C.

FEMA-350. (2000). "Recommended seismic design criteria for new steel moment-frame buildings," *SAC Joint Venture*, Federal Emergency Management Agency, Washington, D.C.

FEMA-355. (2000). "State of the art report on systems performance of steel moment frames subject to earthquake ground shaking," *SAC Joint Venture*, Federal Emergency Management Agency, Washington, D.C.

FEMA-356. (2000). "Prestandard and commentary for the seismic rehabilitation of buildings," *SAC Joint Venture*, Federal Emergency Management Agency, Washington, D.C.

Foutch, D. A., and Shi, S. (1998). "Effects of hysteresis type on the seismic response of buildings," *Proceedings of the 6th U.S. National Conference on Earthquake Engineering*, call no. CF 10, Seattle, Washington, 12 pp.

Frankel, A. D., Mueller, C., Barnhard, T., Perkins, D., Leyendecker, E. V., Dickman, N., Hanson, S., and Hopper, M. (1996). "National seismic-hazard maps : Documentation June 1996, open-file report 96-532," U.S. Geological Survey: 41 pp. http://earthquake.usgs.gov/research/hazmaps/publications/hazmapsdoc/Junedoc.pdf (Accessed 10/10/2006).

Frankel, A. D., Mueller, C. S., Barnhard, T. P., Leyendecker, E. V., Wesson, R. L., Harmsen, S. C., Klein, F. W., Perkins, D. M., Dickman, N. C., Hanson, S. L., and Hopper, M. G. (2000). "USGS national seismic hazard maps," *Earthquake Spectra*, **16**(1): 1-19.

Fu, Q. (2005). "Modeling and prediction of fault-normal near-field ground motions and structural response," *Ph.D. Report*, Department of Civil and Environmental Engineering, Stanford University, Stanford, CA: 231 pp.

Fu, Q., and Menun, C. (2004). "Seismic-environment-based simulation of near-fault ground motions," *Proceedings of the 13th World Conference on Earthquake Engineering, Paper No. 322*, Vancouver, BC Canada, August 1-6.

Goel, R. K., and Chopra, A. K. (2004). "Evaluation of modal and FEMA pushover analyses: SAC buildings," *Earthquake Spectra*, **20**(1): 225-254.

Hall, J. F. (1998). "Seismic response of steel frame buildings to near-source ground motions," *Earthquake Engineering & Structural Dynamics*, **27**(12): 1445-1464.

Hall, J. F., and Aagaard, B. T. (1998). "Fundamentals of the near-source problem," *Proceedings of the 5th Caltrans Seismic Research Workshop: California Department of Transportation Engineering Service Center*, call no 630/C25/1998, Sacramento, CA, June 16-18: 10 pp.

Hall, J. F., Heaton, T. H., Halling, M. W., and Wald, D. J. (1995). "Near-source ground motion and its effects on flexible buildings," *Earthquake Spectra*, **11**(4): 569-605.

Han, S. W., and Chopra, A. K. (2006). "Approximate incremental dynamic analysis using the modal pushover analysis procedure," *Earthquake Engineering & Structural Dynamics*, **35**(15): 1853-1873. DOI: 10.1002/eqe.605.

Han, S. W., and Wen, Y. K. (1997). "Method of reliability-based seismic design. I: Equivalent nonlinear systems," *Journal of Structural Engineering*, **123**(3): 256-263.

Haselton, C. B., and Baker, J. W. (2006). "Ground motion intensity measures for collapse capacity prediction: Choice of optimal spectral period and effect of spectral shape," *Proceedings of the 8th U.S. National Conference on Earthquake Engineering*, San Francisco, CA, 18-22 April, 2006: 10 pp.

Hastie, T., Tibshirani, R., and Friedman, J. (2001). *The elements of statistical learning* 2 ed., Springer-Verlag: 536 pp.

Hickman, J. W. (1983). "PRA procedures guide: A guide to the performance of probabilistic risk assessments for nuclear power plants," NUREG/CR-2300, Vol. II, Office of Nuclear Regulatory Research, U.S. Nuclear Regulatory Commission, Washington, D.C.:

Ibarra, L. F., and Krawinkler, H. (2005). "Global collapse of frame structures under seismic excitations," John A. Blume Earthquake Engineering Center, Report No. 152, Department of Civil and Environmental Engineering, Stanford University, Stanford, CA: 324 pp. http://blume.stanford.edu/Blume/TRList.htm (Accessed 05/31/2006).

Ibarra, L. F., Medina, R. A., and Krawinkler, H. (2005). "Hysteretic models that incorporate strength and stiffness deterioration," *Earthquake Engineering & Structural Dynamics*, **34**(12): 1489-1511.

Iervolino, I., and Cornell, C. A. (2007). "Prediction of the occurrence of velocity pulses in near-fault ground motions," (In preparation).

Inoue, T., and Cornell, C. A. (1990). "Seismic hazard analysis of multi-degree-of-freedom structures," Reliability of Marine Structures Program, Report No. RMS-8, Department of Civil and Environmental Engineering, Stanford University, Stanford, CA: 70 pp.

Iwan, W. D. (1997). "Drift spectrum: Measure of demand for earthquake ground motions," *Journal of Structural Engineering*, **123**(4): 397-404. http://link.aip.org/link/?QST/123/397/1

Iwan, W. D. (1999). "Implications of near-fault ground motion for structural design," *U.S.-Japan Workshop on Performance-Based Earthquake Engineering Methodology for Reinforced Concrete Building Structures*, PEER Report 1999/10, Maui, Hawaii, 17-25 pp.

Iwan, W. D., Huang, C.-T., and Guyader, A. C. (2000). "Important features of the response of inelastic structures to near-field ground motion," *Proceedings of the 12th World Conference on Earthquake Engineering, Paper No. 1740*, Auckland, New Zealand, January 2000: 8 pp.

Jalayer, F. (2003). "Direct probabilistic seismic analysis: Implementing non-linear dynamic assessments," *Ph.D. Report*, Department of Civil and Environmental Engineering, Stanford University, Stanford, CA: 244 pp. http://www.stanford.edu/group/rms/ (last accessed 31 May 2006).

Jalayer, F., Beck, J. L., Porter, K. A., and Hall, J. F. (2004). "Effects of ground motion uncertainty on predicting the response of an existing RC frame structure," *Proceedings of the 13th World Conference on Earthquake Engineering, Paper No. 2007*, Vancouver, Canada, 1-6 August 2004: 14 pp.

Joyner, W. B., and Boore, D. M. (1982). "Prediction of earthquake response spectra," U.S. Geological Survey, call no. 415/J69/1982:

Kennedy, R. P., Short, S. A., Merz, K. L., Tokarz, F. J., Idriss, I. M., Power, M. S., and Sadigh, K. (1984). "Engineering characterization of ground motion - task i: Effects of characteristics of free-field motion on structural response," U.S. Nuclear Regulatory Commission, NUREG/CR-3805, Division of Engineering Technology, Office of Nuclear Regulatory Research, Washington, D.C.:

Lawson, R. S. (1996). "Site-dependent inelastic seismic demands," *Ph.D. Report*, Department of Civil and Environmental Engineering, Stanford University, Stanford, CA: 224 pp.

Loh, C.-H., Wu, T.-C., and Huang, N. E. (2001). "Application of the empirical mode decomposition-Hilbert spectrum method to identify near-fault ground-motion characteristics and structural responses," *Bulletin of the Seismological Society of America*, **91**(5): 1339-1357.

Luco, N. (2002). "Probabilistic seismic demand analysis, SMRF connection fractures, and near-source effects," *Ph.D. Report*, Department of Civil and Environmental Engineering, Stanford University, Stanford, CA: 260 pp. http://www.stanford.edu/group/rms/ (Accessed 05/31/2006).

Luco, N., and Bazzurro, P. (2004). "Effects of earthquake record scaling on nonlinear structural response," Report for Pacific Earthquake Engineering Research (PEER) Center, Lifelines Program Project 1G00 Addenda: 64 pp. http://peer.berkeley.edu/lifelines/LL-CEC/reports/final_reports/1G00-FR.pdf (Accessed 07/30/2006).

Luco, N., and Cornell, C. A. (2006). "Structure-specific scalar intensity measures for near-source and ordinary earthquake ground motions," *Earthquake Spectra*: (Accepted for publication).

Luco, N., and Cornell, C. A. (2007). "Structure-specific scalar intensity measures for near-source and ordinary earthquake ground motions," *Earthquake Spectra*: (In press).

Luco, N., Manuel, L., Baldava, S., and Bazzurro, P. (2005). "Correlation of damage of steel moment-resisting frames to a vector-valued set of ground motion parameter," *Proceedings of the 9th International Conference on Structural Safety and Reliability (ICOSSAR05)*, Rome, Italy, 19-23 June 2005: 8 pp.

MacRae, G. A., Morrow, D. V., and Roeder, C. W. (2001). "Near-fault ground motion effects on simple structures," *Journal of Structural Engineering*, **127**(9): 996-1004.

Mavroeidis, G. P., Dong, G., and Papageorgiou, A. S. (2004). "Near-fault ground motions, and the response of elastic and inelastic single-degree-of-freedom (SDOF) systems," *Earthquake Engineering & Structural Dynamics*, **33**(9): 1023-1049.

Mavroeidis, G. P., and Papageorgiou, A. S. (2002). "Near-source strong ground motion: Characteristics and design issues," *Proceedings of the 7h U.S. National Conference on Earthquake Engineering*, Boston, Massachusetts.

Mavroeidis, G. P., and Papageorgiou, A. S. (2003). "A mathematical representation of near-fault ground motions," *Bulletin of the Seismological Society of America*, **93**(3): 1099-1131.

McCullagh, P., and Nelder, J. A. (1990). *Generalized linear models*, Second Edition, Chapman & Hall/CRC, 532 pp

McGuire, R. K. (1995). "Probabilistic seismic hazard analysis and design earthquakes: Closing the loop," *Bulletin of the Seismological Society of America*, **85**(5): 1275-1284.

McGuire, R. K., and Cornell, C. A. (1974). "Seismic structural response risk analysis, incorporating peak response regressions on earthquake magnitude and distance," Report No. 74-51, Dept. of Civil Engineering, Massachusetts Institute of Technology, Cambridge, MA: 371 pp.

Medina, R. A., and Krawinkler, H. (2003). "Seismic demands for nondeteriorating frame structures and their dependence on ground motions," John A. Blume Earthquake Engineering Center, Report No. 144, Department of Civil and Environmental Engineering, Stanford University, Stanford, CA: 347 pp. http://blume.stanford.edu/Blume/TRList.htm (accessed 05/31/2006).

Miranda, E. (2000). "Inelastic displacement ratios for structures on firm sites," *Journal of Structural Engineering*, **126**(10): 1150-1159.

Miranda, E. (2001). "Estimation of inelastic deformation demands of SDOF systems," *Journal of Structural Engineering*, **127**(9): 1005-1012.

Miranda, E., and Bertero, V. V. (1994). "Evaluation of strength reduction factors for earthquake-resistant design," *Earthquake Spectra*, **10**(2): 357-379.

Moehle, J. P., and Deierlein, G. G. (2004). "A framework methodology for performance-based earthquake engineering," *Proceedings of the 13th World Conference on Earthquake Engineering*, Vancouver, Canada, 1-6 August 2004: 13 pp.

Mori, Y., Yamanaka, T., Luco, N., Nakashima, M., and Cornell, C. A. (2004). "Predictors of seismic demand of SMRF buildings considering post-elastic mode shape," *Proceedings of the 13th World Conference on Earthquake Engineering, Paper No. 632*, Vancouver, Canada, 1-6 August 2004: 15 pp.

Nassar, A. A., and Krawinkler, H. (1991). "Seismic demands for SDOF and MDOF systems," John A. Blume Earthquake Engineering Center Report No. 95, Stanford University, Stanford, CA: http://blume.stanford.edu/Blume/TRList.htm (Accessed 10/10/2006).

Qi, X., and Moehle, J. P. (1991). "Displacement design approach for reinforced concrete structures subjected to earthquakes," Earthquake Engineering Research Center Report No. EERC 91/02, 0271-0323, University of California, Berkeley, CA:

Reiter, L. (1990). *Earthquake hazard analysis: Issues and insights*, Columbia University Press, New York, 254 pp.

Riddell, R., Garcia, J. E., and Garces, E. (2002). "Inelastic deformation response of SDOF systems subjected to earthquakes," *Earthquake Engineering & Structural Dynamics*, **31**(3): 515-538.

Ruiz-García, J., and Miranda, E. (2003). "Inelastic displacement ratios for evaluation of existing structures," *Earthquake Engineering & Structural Dynamics*, **32**(8): 1237-1258.

Ruiz-García, J., and Miranda, E. (2005). "Performance-based assessment of existing structures accounting for residual displacements," John A. Blume Earthquake Engineering Center Report No. 153, Stanford University, Stanford, CA: http://blume.stanford.edu/Blume/TRList.htm (Accessed 10/10/2006).

Ryan, K., and Hall, J. F. (1998). "Aspects of building response to near-source ground motions," *Proceedings of the Structural Engineering World Wide, Paper No. T162-5*, Elsevier Science, Oxford, U.K.

Saragoni, G. R., and Hart, G. C. (1974). "Simulation of artificial earthquakes," *Earthquake Engineering and Structural Dynamics*, **2**(3): 249-267.

Sasani, M., and Bertero, V. V. (2000). "Importance of severe pulse-type ground motions in performance-based engineering: Historical and critical review," *Proceedings of the 12th World Conference on Earthquake Engineering*, Auckland, New Zealand, 30 January - 4 February.

SEAOC. (1999). "Recommended lateral force requirements and commentary," *Structural Engineers Association of California*, Sacramento, CA.

Sewell, R. T. (1989). "Damage effectiveness of earthquake ground motion: Characterizations based on the performance of structures and equipment," *Ph.D. Report*, Department of Civil and Environmental Engineering, Stanford University, Stanford, CA: 619 pp. http://www.stanford.edu/group/rms/ (Accessed 10/10/2006).

Shome, N. (1999). "Probabilistic seismic demand analysis of nonlinear structures," *Ph.D. Report*, Department of Civil and Environmental Engineering, Stanford University, Stanford, CA: 320 pp. http://www.stanford.edu/group/rms/ (Accessed 10/01/2006).

Silva, W. (2003). "Strong ground motion database CDs (similar to peer database, http://peer.Berkeley.Edu/smcat/)." Personal Communication (Accessed 10/10/2006).

Sinan, A., Ufuk, Y., and Polat, G. (2005). "Drift estimates in frame buildings subjected to near-fault ground motions," *Journal of Structural Engineering*, **131**(7): 1014-1024.

Singh, J. P. (1985). "Earthquake ground motions: Implications for designing structures and reconciling structural damage," *Earthquake Spectra*, **1**(2): 239-270.

Somerville, P. G. (2003). "Magnitude scaling of the near fault rupture directivity pulse," *Journal of Physics of the Earth and Planetary Interiors*, **137**(1-4): 201-212.

Somerville, P. G., Smith, N., Graves, R., and Abrahamson, N. (1997). "Modification of empirical strong ground motion attenuation relations to include the amplitude and duration effects of rupture directivity," *Seismological Research Letters*, **68**(1): 199-222.

Taghavi, S., and Miranda, E. (2003). "Response assessment of nonstructural building elements," Pacific Earthquake Engineering Research Center, PEER Report 2003/05, University of California, Berkeley: 96 pp.

Tothong, P., and Cornell, C. A. (2006). "An empirical ground motion attenuation relation for inelastic spectral displacement," *Bulletin of the Seismological Society of America*, **96**(6): 2146-2164.

Tothong, P., Cornell, C. A., and Baker, J. W. (2007). "Explicit-directivity-pulse inclusion in probabilistic seismic hazard analysis," *Earthquake Spectra*: (In preparation).

Tothong, P., and Luco, N. (2007). "Probabilistic seismic demand analysis using advanced ground motion intensity measures," *Earthquake Engineering & Structural Dynamics*: (In press in the special issue: Seismic Reliability Analysis of Structures).

Vamvatsikos, D. (2002). "Seismic performance, capacity and reliability of structures as seen through incremental dynamic analysis," *Ph.D. Report*, Department of Civil and Environmental Engineering, Stanford University, Stanford, CA: 152 pp. http://www.stanford.edu/group/rms/ (Accessed 10/10/2006).

Vamvatsikos, D., and Cornell, C. A. (2002a). "Incremental dynamic analysis," *Earthquake Engineering & Structural Dynamics*, **31**(3): 491-514.

Vamvatsikos, D., and Cornell, C. A. (2002b). "Practical estimation of the seismic demand and capacity of oscillators with multi-linear static pushovers through incremental dynamic analysis," *Proceedings of the 7th U.S. National Conference on Earthquake Engineering*, call no. CF 61, Boston, MA, 21-25 July 2002: 10 pp.

Vamvatsikos, D., and Cornell, C. A. (2004). "Investigating the influence of elastic spectral shape on the limit-state capacities of a 9-story building through IDA," *Proceedings of the 13th World Conference on Earthquake Engineering, Paper No. 1463*, Vancouver, BC Canada.

Veletsos, A. S., and Newmark, N. M. (1960). "Effect of inelastic behavior on the response of simple systems to earthquake motions," *Proceeding of the 2nd World Conference on Earthquake Engineering*, Tokyo, Japan, 895-912 pp.

Veletsos, A. S., Newmark, N. M., and Chepalati, C. V. (1965). "Deformation spectra for elastic and elastoplastic systems subjected to ground shock and earthquake motion," *Proceeding of the 3rd World Conference on Earthquake Engineering*, Wellington, New Zealand, 663-682 pp.

Vision-2000. (1995). "A framework for performance based design," *Structural Engineers Association of California (SEAOC)*, Volumes I-III, Sacramento, CA.

Wald, D. J., and Heaton, T. H. (1998). "Forward and inverse modeling of near-source ground motions for use in engineering response analysis," *Proceedings of the American Society of Civil Engineering, Paper T162-1*, San Francisco, CA.

Wen, Y. K. (2000). "Reliability and performance based design," *The 8th ASCE Specialty Conference on Probabilistic Mechanics and Structural Reliability, PMC2000-YKW*, University of Notre Dame, South Bend, Indiana, 21 pp.

Wen, Y. K., and Wu, C. L. (2001). "Uniform hazard ground motions for mid-America cities," *Earthquake Spectra*, **17**(2): 359-384.

Younan, A., Banon, H., Marshall, P., Crouse, C. B., and Cornell, C. A. (2001). "An overview of the ISO seismic guidelines," *Proceedings of the offshore Technology Conference*, Houston, Texas.

Youngs, R., and Chiou, B. (2006). Personal Communications.

Zhang, Y., and Iwan, W. D. (2002a). "Active interaction control of tall buildings subjected to near-field ground motions," *Journal of Structural Engineering*, **128**(1): 69-79. http://link.aip.org/link/?QST/128/69/1

Zhang, Y., and Iwan, W. D. (2002b). "Protecting base-isolated structures from near-field ground motion by tuned interaction damper," *Journal of Engineering Mechanics*, **128**(3): 287-295. http://link.aip.org/link/?QEM/128/287/1

PEER REPORTS

PEER reports are available from the National Information Service for Earthquake Engineering (NISEE). To order PEER reports, please contact the Pacific Earthquake Engineering Research Center, 1301 South 46th Street, Richmond, California 94804-4698. Tel.: (510) 665-3405; Fax: (510) 665-3420.

PEER 2006/11 *Probabilistic Seismic Demand Analysis Using Advanced Ground Motion Intensity Measures, Attenuation Relationships, and Near-Fault Effects.* Polsak Tothong and C. Allin Cornell. March 2007.

PEER 2006/10 *Application of the PEER PBEE Methodology to the I-880 Viaduct.* Sashi Kunnath. February 2007.

PEER 2006/09 *Quantifying Economic Losses from Travel Forgone Following a Large Metropolitan Earthquake.* James Moore, Sungbin Cho, Yue Yue Fan, and Stuart Werner. November 2006.

PEER 2006/08 *Vector-Valued Ground Motion Intensity Measures for Probabilistic Seismic Demand Analysis*. Jack W. Baker and C. Allin Cornell. October 2006.

PEER 2006/07 *Analytical Modeling of Reinforced Concrete Walls for Predicting Flexural and Coupled–Shear-Flexural Responses*. Kutay Orakcal, Loenardo M. Massone, and John W. Wallace. October 2006.

PEER 2006/06 *Nonlinear Analysis of a Soil-Drilled Pier System under Static and Dynamic Axial Loading.* Gang Wang and Nicholas Sitar. November 2006.

PEER 2006/05 *Advanced Seismic Assessment Guidelines.* Paolo Bazzurro, C. Allin Cornell, Charles Menun, Maziar Motahari, and Nicolas Luco. September 2006.

PEER 2006/04 *Probabilistic Seismic Evaluation of Reinforced Concrete Structural Components and Systems.* Tae Hyung Lee and Khalid M. Mosalam. August 2006.

PEER 2006/03 *Performance of Lifelines Subjected to Lateral Spreading.* Scott A. Ashford and Teerawut Juirnarongrit. July 2006.

PEER 2006/02 *Pacific Earthquake Engineering Research Center Highway Demonstration Project.* Anne Kiremidjian, James Moore, Yue Yue Fan, Nesrin Basoz, Ozgur Yazali, and Meredith Williams. April 2006.

PEER 2006/01 *Bracing Berkeley. A Guide to Seismic Safety on the UC Berkeley Campus.* Mary C. Comerio, Stephen Tobriner, and Ariane Fehrenkamp. January 2006.

PEER 2005/16 *Seismic Response and Reliability of Electrical Substation Equipment and Systems.* Junho Song, Armen Der Kiureghian, and Jerome L. Sackman. April 2006.

PEER 2005/15 *CPT-Based Probabilistic Assessment of Seismic Soil Liquefaction Initiation.* R. E. S. Moss, R. B. Seed, R. E. Kayen, J. P. Stewart, and A. Der Kiureghian. April 2006.

PEER 2005/14 *Workshop on Modeling of Nonlinear Cyclic Load-Deformation Behavior of Shallow Foundations.* Bruce L. Kutter, Geoffrey Martin, Tara Hutchinson, Chad Harden, Sivapalan Gajan, and Justin Phalen. March 2006.

PEER 2005/13 *Stochastic Characterization and Decision Bases under Time-Dependent Aftershock Risk in Performance-Based Earthquake Engineering.* Gee Liek Yeo and C. Allin Cornell. July 2005.

PEER 2005/12 *PEER Testbed Study on a Laboratory Building: Exercising Seismic Performance Assessment.* Mary C. Comerio, editor. November 2005.

PEER 2005/11 *Van Nuys Hotel Building Testbed Report: Exercising Seismic Performance Assessment.* Helmut Krawinkler, editor. October 2005.

PEER 2005/10 *First NEES/E-Defense Workshop on Collapse Simulation of Reinforced Concrete Building Structures.* September 2005.

PEER 2005/09 *Test Applications of Advanced Seismic Assessment Guidelines.* Joe Maffei, Karl Telleen, Danya Mohr, William Holmes, and Yuki Nakayama. August 2006.

PEER 2005/08 *Damage Accumulation in Lightly Confined Reinforced Concrete Bridge Columns.* R. Tyler Ranf, Jared M. Nelson, Zach Price, Marc O. Eberhard, and John F. Stanton. April 2006.

PEER 2005/07 *Experimental and Analytical Studies on the Seismic Response of Freestanding and Anchored Laboratory Equipment.* Dimitrios Konstantinidis and Nicos Makris. January 2005.

PEER 2005/06 *Global Collapse of Frame Structures under Seismic Excitations*. Luis F. Ibarra and Helmut Krawinkler. September 2005.

PEER 2005//05 *Performance Characterization of Bench- and Shelf-Mounted Equipment.* Samit Ray Chaudhuri and Tara C. Hutchinson. May 2006.

PEER 2005/04 *Numerical Modeling of the Nonlinear Cyclic Response of Shallow Foundations.* Chad Harden, Tara Hutchinson, Geoffrey R. Martin, and Bruce L. Kutter. August 2005.

PEER 2005/03 *A Taxonomy of Building Components for Performance-Based Earthquake Engineering.* Keith A. Porter. September 2005.

PEER 2005/02 *Fragility Basis for California Highway Overpass Bridge Seismic Decision Making*. Kevin R. Mackie and Bozidar Stojadinovic. June 2005.

PEER 2005/01 *Empirical Characterization of Site Conditions on Strong Ground Motion.* Jonathan P. Stewart, Yoojoong Choi, and Robert W. Graves. June 2005.

PEER 2004/09 *Electrical Substation Equipment Interaction: Experimental Rigid Conductor Studies.* Christopher Stearns and André Filiatrault. February 2005.

PEER 2004/08 *Seismic Qualification and Fragility Testing of Line Break 550-kV Disconnect Switches.* Shakhzod M. Takhirov, Gregory L. Fenves, and Eric Fujisaki. January 2005.

PEER 2004/07 *Ground Motions for Earthquake Simulator Qualification of Electrical Substation Equipment.* Shakhzod M. Takhirov, Gregory L. Fenves, Eric Fujisaki, and Don Clyde. January 2005.

PEER 2004/06 *Performance-Based Regulation and Regulatory Regimes.* Peter J. May and Chris Koski. September 2004.

PEER 2004/05 *Performance-Based Seismic Design Concepts and Implementation: Proceedings of an International Workshop.* Peter Fajfar and Helmut Krawinkler, editors. September 2004.

PEER 2004/04 *Seismic Performance of an Instrumented Tilt-up Wall Building.* James C. Anderson and Vitelmo V. Bertero. July 2004.

PEER 2004/03 *Evaluation and Application of Concrete Tilt-up Assessment Methodologies.* Timothy Graf and James O. Malley. October 2004.

PEER 2004/02 *Analytical Investigations of New Methods for Reducing Residual Displacements of Reinforced Concrete Bridge Columns.* Junichi Sakai and Stephen A. Mahin. August 2004.

PEER 2004/01 *Seismic Performance of Masonry Buildings and Design Implications.* Kerri Anne Taeko Tokoro, James C. Anderson, and Vitelmo V. Bertero. February 2004.

PEER 2003/18 *Performance Models for Flexural Damage in Reinforced Concrete Columns.* Michael Berry and Marc Eberhard. August 2003.

PEER 2003/17 *Predicting Earthquake Damage in Older Reinforced Concrete Beam-Column Joints.* Catherine Pagni and Laura Lowes. October 2004.

PEER 2003/16 *Seismic Demands for Performance-Based Design of Bridges.* Kevin Mackie and Božidar Stojadinovic. August 2003.

PEER 2003/15 *Seismic Demands for Nondeteriorating Frame Structures and Their Dependence on Ground Motions.* Ricardo Antonio Medina and Helmut Krawinkler. May 2004.

PEER 2003/14 *Finite Element Reliability and Sensitivity Methods for Performance-Based Earthquake Engineering.* Terje Haukaas and Armen Der Kiureghian. April 2004.

PEER 2003/13 *Effects of Connection Hysteretic Degradation on the Seismic Behavior of Steel Moment-Resisting Frames.* Janise E. Rodgers and Stephen A. Mahin. March 2004.

PEER 2003/12 *Implementation Manual for the Seismic Protection of Laboratory Contents: Format and Case Studies.* William T. Holmes and Mary C. Comerio. October 2003.

PEER 2003/11 *Fifth U.S.-Japan Workshop on Performance-Based Earthquake Engineering Methodology for Reinforced Concrete Building Structures.* February 2004.

PEER 2003/10 *A Beam-Column Joint Model for Simulating the Earthquake Response of Reinforced Concrete Frames.* Laura N. Lowes, Nilanjan Mitra, and Arash Altoontash. February 2004.

PEER 2003/09 *Sequencing Repairs after an Earthquake: An Economic Approach.* Marco Casari and Simon J. Wilkie. April 2004.

PEER 2003/08 *A Technical Framework for Probability-Based Demand and Capacity Factor Design (DCFD) Seismic Formats*. Fatemeh Jalayer and C. Allin Cornell. November 2003.

PEER 2003/07 *Uncertainty Specification and Propagation for Loss Estimation Using FOSM Methods.* Jack W. Baker and C. Allin Cornell. September 2003.

PEER 2003/06 *Performance of Circular Reinforced Concrete Bridge Columns under Bidirectional Earthquake Loading.* Mahmoud M. Hachem, Stephen A. Mahin, and Jack P. Moehle. February 2003.

PEER 2003/05 *Response Assessment for Building-Specific Loss Estimation.* Eduardo Miranda and Shahram Taghavi. September 2003.

PEER 2003/04 *Experimental Assessment of Columns with Short Lap Splices Subjected to Cyclic Loads*. Murat Melek, John W. Wallace, and Joel Conte. April 2003.

PEER 2003/03 *Probabilistic Response Assessment for Building-Specific Loss Estimation.* Eduardo Miranda and Hesameddin Aslani. September 2003.

PEER 2003/02 *Software Framework for Collaborative Development of Nonlinear Dynamic Analysis Program.* Jun Peng and Kincho H. Law. September 2003.

PEER 2003/01 *Shake Table Tests and Analytical Studies on the Gravity Load Collapse of Reinforced Concrete Frames.* Kenneth John Elwood and Jack P. Moehle. November 2003.

PEER 2002/24 *Performance of Beam to Column Bridge Joints Subjected to a Large Velocity Pulse.* Natalie Gibson, André Filiatrault, and Scott A. Ashford. April 2002.

PEER 2002/23 *Effects of Large Velocity Pulses on Reinforced Concrete Bridge Columns.* Greg L. Orozco and Scott A. Ashford. April 2002.

PEER 2002/22 *Characterization of Large Velocity Pulses for Laboratory Testing.* Kenneth E. Cox and Scott A. Ashford. April 2002.

PEER 2002/21 *Fourth U.S.-Japan Workshop on Performance-Based Earthquake Engineering Methodology for Reinforced Concrete Building Structures*. December 2002.

PEER 2002/20 *Barriers to Adoption and Implementation of PBEE Innovations.* Peter J. May. August 2002.

PEER 2002/19 *Economic-Engineered Integrated Models for Earthquakes: Socioeconomic Impacts.* Peter Gordon, James E. Moore II, and Harry W. Richardson. July 2002.

PEER 2002/18 *Assessment of Reinforced Concrete Building Exterior Joints with Substandard Details.* Chris P. Pantelides, Jon Hansen, Justin Nadauld, and Lawrence D. Reaveley. May 2002.

PEER 2002/17 *Structural Characterization and Seismic Response Analysis of a Highway Overcrossing Equipped with Elastomeric Bearings and Fluid Dampers: A Case Study.* Nicos Makris and Jian Zhang. November 2002.

PEER 2002/16 *Estimation of Uncertainty in Geotechnical Properties for Performance-Based Earthquake Engineering.* Allen L. Jones, Steven L. Kramer, and Pedro Arduino. December 2002.

PEER 2002/15 *Seismic Behavior of Bridge Columns Subjected to Various Loading Patterns.* Asadollah Esmaeily-Gh. and Yan Xiao. December 2002.

PEER 2002/14 *Inelastic Seismic Response of Extended Pile Shaft Supported Bridge Structures.* T.C. Hutchinson, R.W. Boulanger, Y.H. Chai, and I.M. Idriss. December 2002.

PEER 2002/13 *Probabilistic Models and Fragility Estimates for Bridge Components and Systems.* Paolo Gardoni, Armen Der Kiureghian, and Khalid M. Mosalam. June 2002.

PEER 2002/12 *Effects of Fault Dip and Slip Rake on Near-Source Ground Motions: Why Chi-Chi Was a Relatively Mild M7.6 Earthquake.* Brad T. Aagaard, John F. Hall, and Thomas H. Heaton. December 2002.

PEER 2002/11 *Analytical and Experimental Study of Fiber-Reinforced Strip Isolators*. James M. Kelly and Shakhzod M. Takhirov. September 2002.

PEER 2002/10 *Centrifuge Modeling of Settlement and Lateral Spreading with Comparisons to Numerical Analyses***.** Sivapalan Gajan and Bruce L. Kutter. January 2003.

PEER 2002/09 *Documentation and Analysis of Field Case Histories of Seismic Compression during the 1994 Northridge, California, Earthquake.* Jonathan P. Stewart, Patrick M. Smith, Daniel H. Whang, and Jonathan D. Bray. October 2002.

PEER 2002/08 *Component Testing, Stability Analysis and Characterization of Buckling-Restrained Unbonded Braces™.* Cameron Black, Nicos Makris, and Ian Aiken. September 2002.

PEER 2002/07 *Seismic Performance of Pile-Wharf Connections.* Charles W. Roeder, Robert Graff, Jennifer Soderstrom, and Jun Han Yoo. December 2001.

PEER 2002/06 *The Use of Benefit-Cost Analysis for Evaluation of Performance-Based Earthquake Engineering Decisions*. Richard O. Zerbe and Anthony Falit-Baiamonte. September 2001.

PEER 2002/05 *Guidelines, Specifications, and Seismic Performance Characterization of Nonstructural Building Components and Equipment*. André Filiatrault, Constantin Christopoulos, and Christopher Stearns. September 2001.

PEER 2002/04 *Consortium of Organizations for Strong-Motion Observation Systems and the Pacific Earthquake Engineering Research Center Lifelines Program: Invited Workshop on Archiving and Web Dissemination of Geotechnical Data, 4–5 October 2001*. September 2002.

PEER 2002/03 *Investigation of Sensitivity of Building Loss Estimates to Major Uncertain Variables for the Van Nuys Testbed.* Keith A. Porter, James L. Beck, and Rustem V. Shaikhutdinov. August 2002.

PEER 2002/02 *The Third U.S.-Japan Workshop on Performance-Based Earthquake Engineering Methodology for Reinforced Concrete Building Structures*. July 2002.

PEER 2002/01 *Nonstructural Loss Estimation: The UC Berkeley Case Study.* Mary C. Comerio and John C. Stallmeyer. December 2001.

PEER 2001/16 *Statistics of SDF-System Estimate of Roof Displacement for Pushover Analysis of Buildings.* Anil K. Chopra, Rakesh K. Goel, and Chatpan Chintanapakdee. December 2001.

PEER 2001/15 *Damage to Bridges during the 2001 Nisqually Earthquake.* R. Tyler Ranf, Marc O. Eberhard, and Michael P. Berry. November 2001.

PEER 2001/14 *Rocking Response of Equipment Anchored to a Base Foundation.* Nicos Makris and Cameron J. Black. September 2001.

PEER 2001/13 *Modeling Soil Liquefaction Hazards for Performance-Based Earthquake Engineering*. Steven L. Kramer and Ahmed-W. Elgamal. February 2001.

PEER 2001/12 *Development of Geotechnical Capabilities in OpenSees.* Boris Jeremi . September 2001.

PEER 2001/11 *Analytical and Experimental Study of Fiber-Reinforced Elastomeric Isolators*. James M. Kelly and Shakhzod M. Takhirov. September 2001.

PEER 2001/10 *Amplification Factors for Spectral Acceleration in Active Regions.* Jonathan P. Stewart, Andrew H. Liu, Yoojoong Choi, and Mehmet B. Baturay. December 2001.

PEER 2001/09 *Ground Motion Evaluation Procedures for Performance-Based Design.* Jonathan P. Stewart, Shyh-Jeng Chiou, Jonathan D. Bray, Robert W. Graves, Paul G. Somerville, and Norman A. Abrahamson. September 2001.

PEER 2001/08 *Experimental and Computational Evaluation of Reinforced Concrete Bridge Beam-Column Connections for Seismic Performance*. Clay J. Naito, Jack P. Moehle, and Khalid M. Mosalam. November 2001.

PEER 2001/07 *The Rocking Spectrum and the Shortcomings of Design Guidelines.* Nicos Makris and Dimitrios Konstantinidis. August 2001.

PEER 2001/06 *Development of an Electrical Substation Equipment Performance Database for Evaluation of Equipment Fragilities*. Thalia Agnanos. April 1999.

PEER 2001/05 *Stiffness Analysis of Fiber-Reinforced Elastomeric Isolators.* Hsiang-Chuan Tsai and James M. Kelly. May 2001.

PEER 2001/04 *Organizational and Societal Considerations for Performance-Based Earthquake Engineering.* Peter J. May. April 2001.

PEER 2001/03 *A Modal Pushover Analysis Procedure to Estimate Seismic Demands for Buildings: Theory and Preliminary Evaluation.* Anil K. Chopra and Rakesh K. Goel. January 2001.

PEER 2001/02 *Seismic Response Analysis of Highway Overcrossings Including Soil-Structure Interaction.* Jian Zhang and Nicos Makris. March 2001.

PEER 2001/01 *Experimental Study of Large Seismic Steel Beam-to-Column Connections.* Egor P. Popov and Shakhzod M. Takhirov. November 2000.

PEER 2000/10 *The Second U.S.-Japan Workshop on Performance-Based Earthquake Engineering Methodology for Reinforced Concrete Building Structures.* March 2000.

PEER 2000/09 *Structural Engineering Reconnaissance of the August 17, 1999 Earthquake: Kocaeli (Izmit), Turkey.* Halil Sezen, Kenneth J. Elwood, Andrew S. Whittaker, Khalid Mosalam, John J. Wallace, and John F. Stanton. December 2000.

PEER 2000/08 *Behavior of Reinforced Concrete Bridge Columns Having Varying Aspect Ratios and Varying Lengths of Confinement.* Anthony J. Calderone, Dawn E. Lehman, and Jack P. Moehle. January 2001.

PEER 2000/07 *Cover-Plate and Flange-Plate Reinforced Steel Moment-Resisting Connections.* Taejin Kim, Andrew S. Whittaker, Amir S. Gilani, Vitelmo V. Bertero, and Shakhzod M. Takhirov. September 2000.

PEER 2000/06 *Seismic Evaluation and Analysis of 230-kV Disconnect Switches.* Amir S. J. Gilani, Andrew S. Whittaker, Gregory L. Fenves, Chun-Hao Chen, Henry Ho, and Eric Fujisaki. July 2000.

PEER 2000/05 *Performance-Based Evaluation of Exterior Reinforced Concrete Building Joints for Seismic Excitation.* Chandra Clyde, Chris P. Pantelides, and Lawrence D. Reaveley. July 2000.

PEER 2000/04 *An Evaluation of Seismic Energy Demand: An Attenuation Approach.* Chung-Che Chou and Chia-Ming Uang. July 1999.

PEER 2000/03 *Framing Earthquake Retrofitting Decisions: The Case of Hillside Homes in Los Angeles.* Detlof von Winterfeldt, Nels Roselund, and Alicia Kitsuse. March 2000.

PEER 2000/02 *U.S.-Japan Workshop on the Effects of Near-Field Earthquake Shaking.* Andrew Whittaker, ed. July 2000.

PEER 2000/01 *Further Studies on Seismic Interaction in Interconnected Electrical Substation Equipment.* Armen Der Kiureghian, Kee-Jeung Hong, and Jerome L. Sackman. November 1999.

PEER 1999/14 *Seismic Evaluation and Retrofit of 230-kV Porcelain Transformer Bushings*. Amir S. Gilani, Andrew S. Whittaker, Gregory L. Fenves, and Eric Fujisaki. December 1999.

PEER 1999/13 *Building Vulnerability Studies: Modeling and Evaluation of Tilt-up and Steel Reinforced Concrete Buildings.* John W. Wallace, Jonathan P. Stewart, and Andrew S. Whittaker, editors. December 1999.

PEER 1999/12 *Rehabilitation of Nonductile RC Frame Building Using Encasement Plates and Energy-Dissipating Devices.* Mehrdad Sasani, Vitelmo V. Bertero, James C. Anderson. December 1999.

PEER 1999/11 *Performance Evaluation Database for Concrete Bridge Components and Systems under Simulated Seismic Loads.* Yael D. Hose and Frieder Seible. November 1999.

PEER 1999/10 *U.S.-Japan Workshop on Performance-Based Earthquake Engineering Methodology for Reinforced Concrete Building Structures.* December 1999.

PEER 1999/09 *Performance Improvement of Long Period Building Structures Subjected to Severe Pulse-Type Ground Motions*. James C. Anderson, Vitelmo V. Bertero, and Raul Bertero. October 1999.

PEER 1999/08 *Envelopes for Seismic Response Vectors.* Charles Menun and Armen Der Kiureghian. July 1999.

PEER 1999/07 *Documentation of Strengths and Weaknesses of Current Computer Analysis Methods for Seismic Performance of Reinforced Concrete Members.* William F. Cofer. November 1999.

PEER 1999/06 *Rocking Response and Overturning of Anchored Equipment under Seismic Excitations.* Nicos Makris and Jian Zhang. November 1999.

PEER 1999/05 *Seismic Evaluation of 550 kV Porcelain Transformer Bushings.* Amir S. Gilani, Andrew S. Whittaker, Gregory L. Fenves, and Eric Fujisaki. October 1999.

PEER 1999/04 *Adoption and Enforcement of Earthquake Risk-Reduction Measures.* Peter J. May, Raymond J. Burby, T. Jens Feeley, and Robert Wood.

PEER 1999/03 *Task 3 Characterization of Site Response General Site Categories*. Adrian Rodriguez-Marek, Jonathan D. Bray, and Norman Abrahamson. February 1999.

PEER 1999/02 *Capacity-Demand-Diagram Methods for Estimating Seismic Deformation of Inelastic Structures: SDF Systems.* Anil K. Chopra and Rakesh Goel. April 1999.

PEER 1999/01 *Interaction in Interconnected Electrical Substation Equipment Subjected to Earthquake Ground Motions.* Armen Der Kiureghian, Jerome L. Sackman, and Kee-Jeung Hong. February 1999.

PEER 1998/08 *Behavior and Failure Analysis of a Multiple-Frame Highway Bridge in the 1994 Northridge Earthquake.* Gregory L. Fenves and Michael Ellery. December 1998.

PEER 1998/07 *Empirical Evaluation of Inertial Soil-Structure Interaction Effects.* Jonathan P. Stewart, Raymond B. Seed, and Gregory L. Fenves. November 1998.

PEER 1998/06 *Effect of Damping Mechanisms on the Response of Seismic Isolated Structures.* Nicos Makris and Shih-Po Chang. November 1998.

PEER 1998/05 *Rocking Response and Overturning of Equipment under Horizontal Pulse-Type Motions.* Nicos Makris and Yiannis Roussos. October 1998.

PEER 1998/04 *Pacific Earthquake Engineering Research Invitational Workshop Proceedings, May 14–15, 1998: Defining the Links between Planning, Policy Analysis, Economics and Earthquake Engineering.* Mary Comerio and Peter Gordon. September 1998.

PEER 1998/03 *Repair/Upgrade Procedures for Welded Beam to Column Connections.* James C. Anderson and Xiaojing Duan. May 1998.

PEER 1998/02 *Seismic Evaluation of 196 kV Porcelain Transformer Bushings.* Amir S. Gilani, Juan W. Chavez, Gregory L. Fenves, and Andrew S. Whittaker. May 1998.

PEER 1998/01 *Seismic Performance of Well-Confined Concrete Bridge Columns.* Dawn E. Lehman and Jack P. Moehle. December 2000.